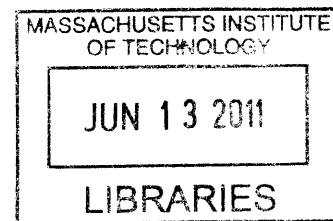# Automated reaction mechanism generation:
Data collaboration, Heteroatom implementation, and Model validation

by

Michael Richard Harper, Jr.

B.S. in Chemical Engineering

University of California, Berkeley (2005)

M.S. in Chemical Engineering Practice

Massachusetts Institute of Technology (2007)

Submitted to the Department of Chemical Engineering in partial fulfillment of the

requirements for the degree of

DOCTOR OF PHILOSOPHY IN CHEMICAL ENGINEERING

at the

MASSACHUSETTS INSTITUTE OF TECHNOLOGY

June 2011

Signature of Author:

)epartment of Chemical Engineering

, Date: May 10, 2011

Certified by: _

William H. Green

Hoyt C. Hottel Professor of Chemical Engineering

Thesis Supervisor

Accepted by: _____

· William M. Deen

Carbon P. Dubbs Professor of Chemical Engineering

Chairman, Committee for Graduate Students

1

Automated Reaction Mechanism Generation:
Data Collaboration, Heteroatom Implementation and Model Validation

by

Michael R. Harper Jr.

Submitted to the Department of Chemical Engineering on May 10, 2011
in Partial Fulfillment of the Requirements for the Degree of
Doctor of Philosophy in Chemical Engineering

ABSTRACT

Nearly two-thirds of the United States' transportation fuels are derived from non-renewable fossil fuels. This demand of fossil fuels requires the United States to import ~ 60% of its total fuel consumption. Relying so heavily on foreign oil is a threat to national security, not to mention that burning all of these fossil fuels produces increased levels of CO_2, a greenhouse gas that contributes to global warming. This is not a sustainable model. The United States government has recently passed legislation that requires greenhouse gas emissions to be reduced to 80% of the 2005 level by the year 2050. Furthermore, new legislation under the Energy Independence and Security Act (EISA) requires that 36 billion gallons of renewable fuel be blended into transportation fuel by 2022. Solving these types of problems will require the fuel industry to shift away from petroleum fuels to biomass-derived oxygenated hydrocarbon fuels. These fuels are generated through different biological pathways, using different "bugs." The question of which fuel molecules should we be burning, and thus, which bugs should we be engineering, arises. To answer that question, a detailed understanding of the fuel chemistry under a wide range of operating conditions, *i.e.* temperature, pressure, fuel equivalence ratio, and fuel percentage, must be known.

Understanding any fuel chemistry fully requires significant collaboration: experimental datasets that span a range of temperatures, pressures, and equivalence ratios, high-level *ab initio* quantum chemistry calculations for single species and reactions, and a comprehensive reaction mechanism and reactor model that utilizes the theoretical calculations to make predictions. A shortcoming in any of these three fields limits the knowledge gained from the others. This thesis addresses the third field of the collaboration, namely constructing accurate reaction mechanisms for chemical systems.

In this thesis, reaction mechanisms are constructed automatically using a software package Reaction Mechanism Generator (RMG) that has been developed in the Green Group over the last decade. The predictive capability of any mechanism depends on the parameters employed. For kinetic models, these parameters consist of species thermochemistry and reaction rate coefficients. Many parameters have been reported in the literature, and it would be beneficial if RMG would utilize these values instead of relying on estimation routines purely. To this end, the PrIMe Warehouse C/H/O chemistry has been validated and a means of incorporating said data in the RMG database has been implemented. Thus, all kinetic models built by RMG may utilize the community's reported thermochemical parameters.

A kinetic model is evaluated by how accurately it can predict experimental data. In this thesis, it was shown that the RMG software, with the PrIMe Warehouse data collaboration, constructs validated kinetic models by using RMG to predict the pyrolysis and combustion chemistry of the four butanol isomers. The kinetic model has been validated against many unique datasets, including: pyrolysis experiments in a flow reactor, opposed-flow and doped methane diffusion flames, jet-stirred reactors, shock tube and rapid compression machine experiments, and low-pressure and atmospheric premixed laminar flames. The mechanism predicts the datasets remarkably well across all operating conditions, including: speciation data within a factor of three, ignition delays within a factor of two, and laminar burning velocities within 20% of the experimental measurements. This accurate, comprehensively-validated kinetic model for the butanol isomers is valuable itself, and even more so as a demonstration of the state-of-the-art in predictive chemical kinetics.

Although the butanol kinetic model was validated against many datasets, the model contained no nitrogen-containing species, and also had limited pathways for benzene formation. These limitations were due to the RMG software, as RMG was initially written with only carbon, hydrogen, and oxygen chemistry in mind. While this functionality has been sufficient in modeling the combustion of hydrocarbons, the ability to make predictions for other chemical systems, $e.g.$ nitrogen, sulfur, and silicon compounds, with the same tools is desired. As part of this thesis, the hardcoded C/H/O functional groups were removed from the source code and database, enabling our RMG software to model heteroatom chemistry. These changes in the RMG software also allows for robust modeling of aromatic compounds.

The future in the transportation sector is uncertain, particularly regarding which fuels our engines will run on. Understanding the elementary chemistry of combustion will be critical in efficiently screening all potential fuel alternatives. This thesis demonstrates one method of understanding fuel chemistry, through detailed reaction mechanisms constructed automatically using the RMG software. Specifically, a method for data collaboration between the RMG software and the PrIMe Warehouse has been established, which will facilitate collaboration between researchers working on combustion experiments, theory, and modeling. The RMG software's algorithm of mechanism construction has been validated by comparing the RMG-generated model predictions for the combustion of the butanol isomers against many unique datasets from the literature; many new species thermochemistry and reaction rate kinetics were calculated and this validation shows RMG to be a capable tool in constructing reaction mechanisms for combustion. Finally, the RMG source code and database have been updated, to allow for robust modeling of heteroatom and aromatic chemistry; these two features will be especially important for future modeling of combustion systems as they relate to the formation of harmful pollutants such as NO_x and soot.

Thesis Supervisor: William H. Green
Title: Professor of Chemical Engineering

DEDICATION

I dedicate this thesis to my parents, Michael and Jennette Harper.

ACKNOWLEDGEMENTS

Thank you also to the rest of the Green Group. I can say with 100% sincerity that I enjoyed coming into the office each day, looking forward to "pushing back the frontiers of science" with you. I enjoyed everything about the group dynamic, from our afternoon tea breaks (which invariably morphed into impromptu RMG debugging meetings), to our social events at the Muddy and CBC, to our open and constructive criticism-friendly group meetings (of which my presentations benefitted tremendously).

I would also like to thank my UROP students Mary Machado, Enrique Cintron, Eugenio de Hoyos, and Billy Boettcher for all of their hard work and patience.

Thank you to Barb Balkwill for always making sure the Green Group ran smoothly. Whether I needed a reimbursement for travel, snacks for group meeting, or simply someone to chat with about the weather, Barb always greeted me with a smile!

Thank you to Suzanne, Mary, Iris, Katie, and Fran for all of their support over the years.

Thank you to D. Wayne Blaylock, Chris Marton, and Jon McMullen. You have contributed the most to my personal development over the past six years: I'm now aware of other beverages besides Corona, my tummy no longer hurts, ... and my answer would still be "it is," primarily because of our friendship.

Thank you Kevin Fowler for being a true friend, and for joining me in supporting the Celtics ("Big Baby for 3 out of a timeout?"), Bruins ("most anticlimactic overtime game-winning goal ever") , and Re-vo-lu-tion (clap, clap, clap-clap-clap). Thank you Dan and Erin for our years of friendship, for our lunch-time companionship, and for calling Monopoly on brick (I was just about to build a settlement!).

Thank you Jeff and Lily (and Pudgie), Ryan Hartman, Jason Orcutt, and Nick Zaborenko (I'm all in), Richard (you Rapscallion), David Couling (my A+ blood donation brother), and Kristin Vicari (I'll just use my other Starbucks gift card). My last six years would not have been as memorable without you.

Thank you Mom and Dad for showing me the meaning of hard work, integrity, and sacrifice. Thank you Mom for all of the care packages ... does my graduating mean I won't be receiving any more? I can continue with my schooling. Thank you Laura (aka Bum) for always checking up on me, for being my "I'll be walking for the next 10 minutes and thought I'd bother you instead of being bored" phone call, and for sending lots of Roxy pictures! Thank you to the rest of my family, especially Grandpa Harper and Grandpa and Grandma Hornbrook, for all of your love and support.

Finally, thank you to my fiancée, Jennifer Seto. Thank you for putting up with me, for taking care of me, for always listening to my RMG and butanol rants, and for loving me for who I am, your moreso. I cannot wait to begin our lives together.

TABLE OF CONTENTS

CHAPTER 1
INTRODUCTION

Predictive modeling is ubiquitous in our everyday lives. Some common examples:

- A meteorologist predicting the weekly weather forecast
- An online website predicting the price of airline tickets from Logan International Airport to LA/Ontario International Airport
- Fantasy sports websites predicting the outcome of the NCAA March Madness
- The Mayans predicting the end of the world to be December 21, 2012

In each scenario, a human supplies inputs to a model and interprets the output in order to make a decision. The models can be rudimentary – my "gut feeling" tells me these teams will advance to the Sweet Sixteen – or extremely sophisticated – 10,000 simulations of the games in question have been simulated and Team X is predicted to defeat Team Y 73% of the time. In all cases, the model's predictive ability is limited by the assumptions built within the model – there is no perfect model – and the parameters employed by the model, many of which are very rough estimates.

Although many individuals would prefer a more accurate and robust model for predicting the round-by-round winners of the NCAA March Madness bracket, what most individuals should be interested in is a tool to determine what alternative fuel source will be utilized in the year 2050.

1.1   UNITED STATES TRANSPORTATION FUEL STATISTICS

Nearly two-thirds of the United States' transportation fuels are derived from non-renewable fossil fuels [1]. This demand of fossil fuels requires the United States to import ~ 60% of its total fuel consumption. Relying so heavily on foreign oil is a threat to national security, not to mention that burning all of these fossil fuels produces increased levels of CO_2, a greenhouse gas that contributes to global warming. This is not a sustainable model.

The United States government has recently passed legislation that requires greenhouse gas emissions to be reduced to 80% of the 2005 level by the year 2050. Furthermore, new legislation under the Energy Independence and Security Act (EISA) requires that 36 billion gallons of renewable fuel be blended into transportation fuel by 2022. Solving these types of problems will require the fuel industry to shift away from petroleum fuels to biomass-derived oxygenated hydrocarbon fuels. These fuels are generated through different biological pathways, using different "bugs." The question of which fuel molecules should we be burning, and thus, which bugs should we be engineering, arises. To answer that question, a detailed understanding of the fuel chemistry under a wide range of operating conditions – temperature, pressure, fuel equivalence ratio, fuel percentage – must be known.

1.2 KINETIC MODELING

Understanding the chemistry of any fuel under real engine conditions is non-trivial. In any combustion process, thousands of species may be generated, most of which are very short-lived and cannot be detected in situ. These thousands of species participate in hundreds of thousands of reactions. To model an engine, one must not only have an accurate engine model describing the fluid mechanics of the system, but also a reliable chemistry model that accurately describes the fuel's decomposition and the products' formation; accurate product formation rates are particularly important when considering the production of soot or NO_x. In the chemistry model, each reaction requires kinetic parameters and each species requires thermodynamic and transport properties. Ideally, each of these parameters could be found in a database. However, a typical fuel chemistry model will only have a handful of "known" parameters and the remainder must be estimated in some fashion.

1.3 PREDICTIVE VERSUS "POSTDICTIVE" MODELING

These unknown parameters can be estimated in many ways.

- Optimization: One could optimize the model's parameters to a particular set of validation targets. The advantage of this method is that the model is likely to predict the training datasets to within the solver's tolerance. This method is also advantageous for interpolation. However, the drawback is there are no guarantees

the optimized parameters will extrapolate well, that is, accurately predict new datasets. Moreover, the optimized parameters may have no chemical basis to them.

- Experimental measurements: A batch-scale experiment may be run, at operating conditions similar to an engine, such that the measured observable is sensitive only to one rate coefficient. Data analysis would yield a thermochemical parameter, valid over the operating conditions tested. The advantage of this method is the parameter has a chemical basis, and may thus be extended to similar reacting systems. The drawback is that not all thermochemical parameters may be measured in a laboratory. Even if all parameters could be determined experimentally, the design and operation of these experiments would be extremely expensive and time-consuming. Thus, it would be infeasible to estimate every parameter in this fashion.

- Theoretical calculations: *Ab initio* quantum chemistry calculations may be run for many different species and reactions. Two advantages are that the computed parameters would have a chemical basis, but more importantly, these theoretical calculations can address the parameters not determinable in an experiment. One drawback is that the quantum chemistry calculations' runtime scales as a high power of the number of atoms; thus, although all species thermochemistry and reaction kinetics can be calculated from first-principles, it would be infeasible to calculate every parameter.

The first two examples are common in "postdictive" modeling: obtain a best-fit parameter from a single set of experiments and employ it in a reactive chemical model. This method of determining the parameters in reaction mechanisms is fine, so long as the simulated reaction conditions remain within the range of conditions of the experiment. The potential problems arise when someone unfamiliar with how that single thermochemical parameter was determined uses it out of context. Many reaction rate coefficients are measured as relative ratios, k_1/k_2. Thus, if one knows k_2 then k_1 is also known. So, applying k_2 at conditions outside of its valid range will result in an incorrect k_1. However, the same study may treat k_1 and k_2 as constraints in an optimization routine, in order to compute k_3, and now one single extrapolated k_2 has introduced bias in two

other thermochemical parameters. This sort of problem is propagated throughout the kinetics literature.

Conversely, predictive modeling computes all thermochemical parameters from first-principles. Thus, when the parameter is employed outside of the study which reported it, the chemistry is still valid and any resulting estimated parameters will not be biased. Although this method is preferred, its implementation is not yet tractable, for the reasons mentioned before. However, if one could utilize the known thermochemical parameters computed from first-principles to estimate the unknown parameters in an efficient manner, one could rapidly construct kinetic models which are fairly accurate.

1.4   THESIS OUTLINE

This thesis discusses predictive modeling for reacting chemical systems. Before making predictions, a model must be generated. Equally important when generating the kinetic mechanism is the algorithm implemented and the thermochemical database employed. The proposed models must then be validated against known data sets; the more expansive and unique the dataset, the more reliable the model.

Chapter 2 discusses different techniques for constructing a kinetic model for a reacting chemical system. Of the methods discussed, more focus will be given for an automated software package Reaction Mechanism Generator, or RMG, as this was the technique employed in this thesis. The advantages and limitations of the software package, as of January 2006, will be discussed.

Chapter 3 discusses the union of the RMG software with the Process Informatics Model (PrIMe), an online kinetic model analysis tool and data depository for the combustion community. Through this collaboration, the amount of "known" thermochemical data RMG employs in its estimation routines is enhanced significantly. The most important aspect in the RMG database collaborating with the PrIMe depository was the selection of a unique species identifier, the International Chemical Identifier, or InChI. Using the InChI, the PrIMe C/H/N/O species catalog was validated and cleaned of duplicates.

16

Chapter 4 discusses the improvements made to the RMG "H-Abstraction" reaction family. Utilizing the RMG collaboration with PrIMe, hundreds of H-Abstraction reactions were identified as requiring resolution – RMG's predicted kinetics were drastically different from the PrIMe Warehouse's stored kinetics. Using conventional transition state theory, where the partition functions and zero-point energies were computed using the CBS-QB3 calculations, 54 reaction rate coefficients were computed and added to the RMG database and PrIMe Warehouse.

Chapter 5 discusses the application of the RMG software package to a practical system, the pyrolysis and combustion of 1-butanol. 1-Butanol is a candidate gasoline additive; to understand the gasoline/1-butanol fuel blend's chemistry better, the chemistry of 1-butanol must be known. This requires detailed chemistry across a wide range of temperatures, pressures, and equivalence ratios. The proposed 1-butanol model is validated against several distinct datasets.

Chapter 6 extends the 1-butanol model to include the other butanol isomers: 2-, iso-, and tert-butanol; iso-butanol is also a candidate gasoline additive. Studying the butanol system, regardless of its industrial applications, is chemically interesting: butanol is the smallest alcohol system to contain a primary, secondary, and tertiary alcohol. Thus, the knowledge gained by constructing a validated kinetic model for each isomer may be applied to any general alcohol compound. Given the many uncertainties in the future regarding fuels, engines, emissions, etc., it is equally beneficial to have a general understanding of alcohol chemistry as it is to have butanol-specific chemistry.

Chapter 7 discusses improvements to the RMG software and algorithm that this thesis has contributed. In particular, the ability of the RMG software to handle carbon, hydrogen, and oxygen reacting systems has been expanded to sulfur and silicon, continuing with the hardcoded functional groups. Utilizing the knowledge gained from hardcoding these two elements, a methodology is implemented to remove all element-based hardcoding within the RMG software. This allows a RMG user to model any chemistry they desire. Further

improvements were made to the RMG software to enable the modeling of aromatic chemistry.

Chapter 8 summarizes this thesis' contributions and discusses the near- and long-term application of an automated reaction mechanism generation software package.

CHAPTER 2
CONSTRUCTING REACTION MECHANISMS

The scientific community has been constructing mechanisms for reacting chemical systems for over one hundred years. Until the last 20 years or so, many of the models were constructed in a "postdictive" fashion, by hand; it is now commonplace to build predictive kinetic models, using computer-aided tools.

2.1   REACTION MECHANISM GENERATION BY HAND

One of the earliest, and well-known, examples is the Michaelis-Menten kinetics model [2], Equation (2.1). In the Michaelis-Menten model, it is assumed that the formation of product is an irreversible step and that the product does not bind to the enzyme.

$$E + S \underset{k_{-1}}{\overset{k_1}{\leftrightarrow}} ES \overset{k_2}{\rightarrow} E + P \tag{2.1}$$

Assuming that the total enzyme concentration is constant over time, and that the bound enzyme is in pseudo-steady state, the initial rate of product formation as a function of initial substrate concentration can be predicted, given one knows the values of k_1, k_{-1}, and k_2. Alternatively, one could use a Lineweaver-Burk plot [3] to extract the values of k_2 and k_1/k_{-1} from experimental measurements of initial rate of formation of product as a function of initial substrate concentration. However, not all enzyme kinetics obey this model. Plotting the initial rate of product formation versus initial substrate concentration for some systems, e.g. oxygen binding to hemoglobin, yields a sigmoid curve; Hill recognized the assumption of non-cooperative binding to be incorrect [4], and postulated a model to determine the degree of cooperativity of any system. Additional assumptions can be relaxed from the Michaelis-Menten and Hill equations to predict new experimental data better, although making experiment-by-experiment corrections to the model is normally done by hand.

Another classic example of constructing reaction mechanisms by hand is the Rice-Herzfeld mechanism [5] for free radical chemistry. One example is given in Equation (2.2).

$$C_2H_6 \rightarrow CH_3 + CH_3$$
$$CH_3 + C_2H_6 \rightarrow C_2H_5 + CH_4$$
$$C_2H_5 \rightarrow C_2H_4 + H \qquad\qquad (2.2)$$
$$H + C_2H_6 \rightarrow C_2H_5 + H_2$$
$$C_2H_5 + C_2H_5 \rightarrow C_4H_{10}$$
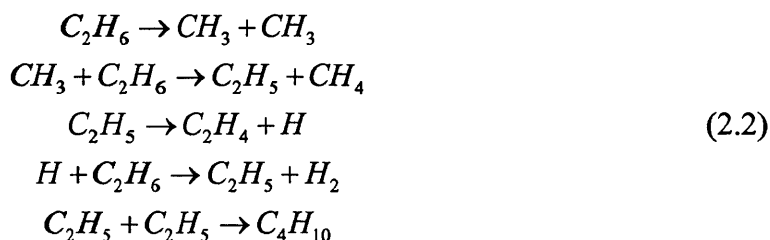
The general procedure of the Rice-Herzfeld mechanism is chain initiation (bond fission), chain propagation (hydrogen abstractions and β-scissions), and chain termination (radical recombination). Assuming the radicals are in pseudo-steady-state, one can then predict the rate of product formation and/or rate of reactant depletion, assuming the kinetic rate coefficients are known. Of course, the primary assumption in this model is that the radicals are in pseudo-steady-state, thus limiting the model's predictive capabilities at short times. Moreover, obtaining kinetics in this fashion requires a detailed knowledge of the chemical system; leaving out any single reaction in the above proposed mechanism would dramatically change the overall rate coefficient expression for the system, leading to inaccurate estimates for the desired specific rate coefficient.

Although both reaction mechanism examples discussed above are widely applicable, especially considering the time it takes to write down the mechanism, it is difficult to know which model modifications to make in the event the model does not predict the data accurately. The answer, assuming the system is kinetically-limited, is that at least one of the reaction rate coefficients is incorrect. Taking the Rice-Herzfeld example from above, the most likely rate coefficient to be incorrect is that for reactions 6-∞; by not including a reaction in a mechanism, the user is inherently estimating the corresponding k(T,P) to be zero.

Although building large, detailed reaction mechanisms by hand seems daunting, two notable exceptions in the combustion community is the work out of Lawrence Livermore National Laboratory (particularly Dr. Charles Westbrook and Dr. William Pitz) and the Combustion Chemistry Center at NUI Galway (particularly Dr. Henry Curran and Prof. John Simmie). Some of the more recent references for the LLNL mechanisms may be found here [6-9]; a complete list of published mechanisms is available at their website

[10]. Some of the more recent references for the NUI Galway mechanisms may be found here [11-14]; a complete list of published mechanisms is available at their website [15]. The general approach of each of these groups has been to start with the smallest system possible: hydrogen oxidation. The mechanism is created by hand, using a list of rules and kinetics. The proposed model is validated by comparing its predictions with experimental data. The sensitive parameters are adjusted, to within reason, to make the model's predictions satisfactory. The next smallest system, e.g. methane oxidation, is approached in the same way, building off the already known mechanism for hydrogen oxidation. This process is continued to at least C_4 chemistry. With a small-molecule foundation, any larger species may now be explored. The idea is to find reaction pathways from the starting species X to the species in the C_4 mechanism; once the C_4 chemistry is reached, the proposed mechanism's predictions can be validated against experiments, and the sensitive parameters can be tuned to make the model's predictions match the experimental results. This approach allows rapid development of validated kinetic models for new fuel species.

One drawback of this "postdictive" approach is that the adjusted sensitive parameters are only valid for the operating conditions of the experiments. Given that many of the unimolecular reactions' kinetics are expressed as high-pressure-limit rate coefficients, $k_\infty(T)$, and that most of the experiments were not run under the high-pressure-limit, tuning these parameters to a limited dataset should surely cause skepticism when using the model to make predictions at pressures significantly different from those used to validate the model. The other disadvantage of constructing models by hand is that many reaction's rate coefficients are estimated to be $k(T,P)$ = zero. Although these models, particularly those of the LLNL, have thousands of species, the ratio of reactions to species is usually no greater than 5. This implies that there are not many cross-reactions between the primary fuel's radical chemistry with the smaller C_4 chemistry. As mentioned previously, the goal of the mechanism generation by hand procedure is to get from the starting fuel to the known C_4 chemistry; once these two are connected, there is little incentive to continue exploring potential pathways because the kinetics of the proposed pathways may simply be tuned to match the experimental data.

The Combustion Kinetics Laboratory of the University of Southern California, led by Prof. Hai Wang, also constructs detailed reaction mechanisms by hand. Two mechanisms in particular from the Combustion Kinetics Laboratory are the USC-Mech II reaction mechanism for high-temperature chemistry for $H_2/CO/C_1-C_4$ compounds [16] and the JetSurF project [17]. It must be noted that these mechanisms do not have "tuned" parameters, in order to match particular validation datasets, and the source of each thermochemical parameter in the mechanism is well-documented; the latter point is especially critical and, unfortunately, nearly-unique among research groups that publish detailed reaction mechanisms.

The hierarchical idea of creating a solid C_4 (or similar) base chemistry, and then constructing pathways from any starting fuel molecule to this known small-molecule chemistry, is quite ingenious and is a good approach of solving reacting chemical systems. However, with the recent advancements in computing power, one would hope that the computer could be exploited in finding these pathways.

2.2   AUTOMATED REACTION MECHANISM GENERATION

Writing a Rice-Herzfeld mechanism by hand, even for moderately small molecules, is a tedious, time-consuming, and error-prone process. As the size of the molecule increases, the number of potential pathways and thus the number of possible intermediate species grows exponentially. Fortunately, with the advances in computing capabilities, constructing these reaction mechanisms through automation is realizable.

Several groups have constructed computer software packages for the purpose of automating the construction of reaction mechanisms for hydrocarbon oxidation. A brief list of some of the software packages, their developers, and their published manuscripts follows.

- EXGAS: This open-source software package has been developed in the Battin-Leclerc group in Nancy (France) since the 1980's [18]; some recent publications may be found here [19-21]. The EXGAS software algorithm has three major

22

components: the C_0-C_2 database (consisting of the validated small-molecule chemistry), THERGAS (a computer software package to estimate species thermochemistry), and KINGAS (a computer software package to estimate reaction rate coefficients). The mechanism is constructed by starting with the initial species of interest and the C_0-C_2 database in the mechanism. One generation of reactions and species is proposed from all species already present in the mechanism. A second generation of reactions and species is then proposed, from all species now present in the mechanism. This process continues for as many generations as the user desires. What limits the number of generations explored is the number of resulting species, which affects the runtime and therefore applicability in reactor model simulations. One technique the group employs to navigate this species limitation is species lumping, e.g. the species shown in Figure 2-1 would all be lumped into one species with the mechanism. Until recently, the entire EXGAS database was hardcoded into the software. Recent work has focused on updating their mechanism generation algorithm to allow for an external database.

Figure 2-1: An example of a set of species that would be lumped into a single species within an EXGAS simulation.

- MAMOX: This software package was developed in the Ranzi group in Milan (Italy) since the mid 1990's [22]; some recent publications may be found here [23-25]. This software is not available for academic researchers.

- REACTION: This software package was developed by Edward Blurock in the mid 1990's [26]; some recent publications may be found here [27-29].

- MOLEC: This software package was developed by Yuswan Muharam in Prof. Warnatz's group at the University of Heidelberg (Germany) [30].

- NETGEN: This software package was developed by Broadbelt, Stark, and Klein [31-33]. One of the unique aspects of this software was the convergence criteria: ranking the proposed species and terminating the simulation based on this species flux, in stark contrast to the generation model approach of EXGAS. More details of this general algorithm will be presented in the next section.

- The Laboratory for Chemical Technology at the University of Gent (Belgium) also employs reaction mechanism software in analyzing pyrolysis data obtained in their bench-scale and pilot plant facilities. The software is not available to academic users.

- Structure-oriented lumping: This method of constructing reaction mechanisms was developed by Quann and Jaffe [34-36], then of Mobil Research and Development. Given that the compounds of interest contained many heavy-atoms and multiple functional groups, a lumping procedure was utilized where the number and type of each functional group for every molecule is identified regardless of the stereochemistry. These structure-oriented species then react against a set of reaction template rules to form reactions and intermediate species.

- KUCRS: This software package, Knowledge-basing Utilities for Complex Reaction Systems, was developed in Prof. Akira Miyoshi's group at the University of Tokyo (Japan) [37-40]. The software provides its own C_0-C_2 base chemistry and utilizes the THERM software [41] to estimate species' thermochemistry via a group-additivity approach. Reactions' rate coefficients are estimated based on the specific reaction type and these estimates are located in an external database; however, adding a new reaction type to the software also requires changing the source code.

Several companies have proprietary software of this type, e.g. The Dow Chemical Company and ExxonMobil. A review on the (then) current automatic kinetic model generation software packages for hydrocarbon oxidation, including many from the above list, was written by Pierucci and Ranzi [42].

A recent software development in automated reaction pathway construction and analysis is the Rule Input Network Generator, or RING, software developed by Rangarajan, Bhan, and Daoutidis [43]. The software program uses reaction template rules to find pathways from the user-specified input to the user-desired products. The algorithm terminates once all options have been explored; note: the reaction rules have constraints which allow the termination to be achieved. Also of particular note is the user-friendly input and output

files. Presently, there are no kinetics associated with any of the pathways, but that is a work-in-progress.

All of the previous software packages mentioned above focused solely on the oxidation of hydrocarbon and oxygenated hydrocarbon species. One software package that generates reaction mechanisms for elements other than C/H/O is from Prof. Linda Broadbelt's group, where they are interested in silicon-containing species [44-46].

Lastly, this review on automated mechanism generation would be remiss without mentioning the many efforts that are being put forth in atmospheric chemistry, particularly the collaboration between the IUPAC Subcommittee for Gas Kinetic Data Evaluation [47] and the Master Chemical Mechanism [48].

2.3   REACTION MECHANISM GENERATOR (RMG)

Another automated tool for generating detailed kinetic models is the software package "Reaction Mechanism Generator," or RMG. The RMG software has been developed in the Green Group at MIT for the last decade [49-56]. The essential aspects of the algorithm are as follows.

The user specifies the input parameters: temperature, pressure, species concentrations, and some form of termination criterion; the termination criterion is either a desired reactant conversion or reaction time. The species is entered in the form of a graph. All species supplied in the input file are known as "core" (or significant) species. The RMG software then applies its ~35 reaction family templates against all species in the core to make "edge" species; types of reactions that may occur are: A → products, A + A → products, A + B → products, etc. All of the newly formed species are "edge" (or not yet significant) species; the reactions connecting the core species to the edge species are labeled "edge" reactions. The RMG software then solves this system of ordinary differential equations (ODEs) for an isothermal, isobaric batch reactor model, over a given time step. RMG then evaluates the flux of all edge species, defined as dC_i/dt where C_i is the concentration of species i. The largest edge species' flux is compared against a "minimum flux," defined as the core's characteristic flux (root mean squared average of

all core species' flux) multiplied by the user-specified tolerance. If the edge species' flux is greater than the minimum flux, the edge species is brought into the core, and the algorithm continues. This process of expanding the network is known as a rate-based procedure [57]. This iterative loop continues until the flux of all edge species' is below the minimum flux. Then, the simulated reaction time (or reactant conversion) is compared against the user-defined criterion. If the criterion is not met, the system of ODEs is solved for a longer time step, and the edge fluxes are evaluated and compared against the minimum flux, Figure 2-2. This algorithm continues until both criteria are satisfied. A reaction mechanism, in the form of a CHEMKIN chem.inp file, is then output to the user.
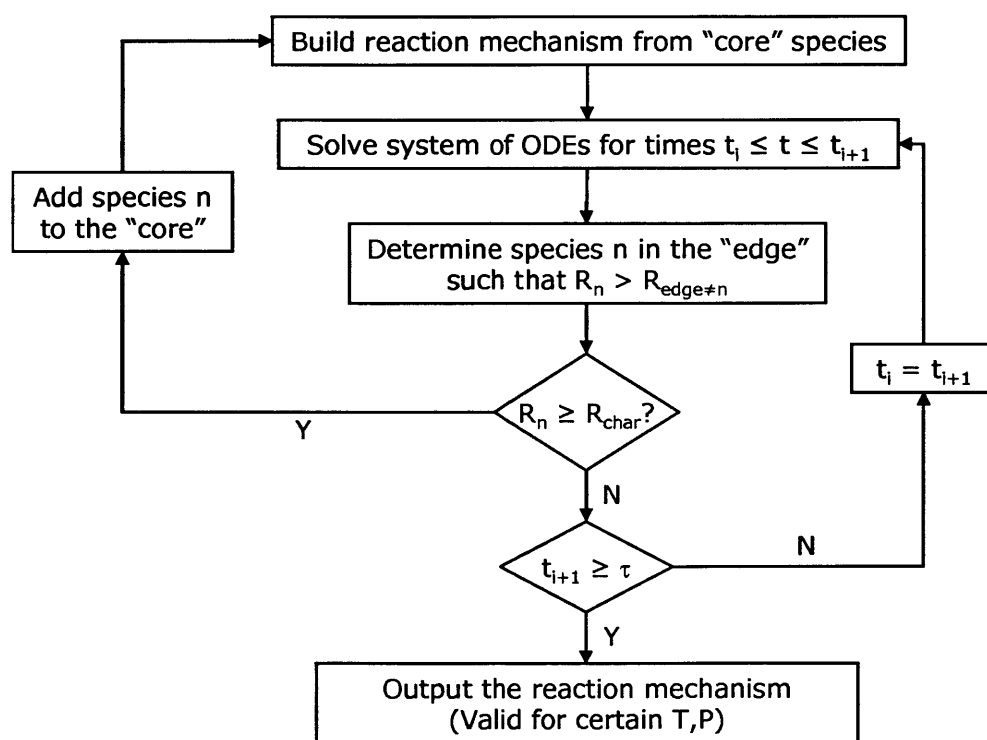
Figure 2-2: Skeletal outline of a RMG pressure-independent algorithm

For each species created in the mechanism, the thermodynamic parameters – the enthalpy of formation and entropy at 298 K, and the heat capacity at 300, 400, 500, 600, 800, 1000, and 1500 K – are needed. When estimating these parameters, RMG first searches its own database; if the species was found, the known parameters would be employed. It should be noted that as of January 2006, RMG contained exactly three species in its own

thermodynamic database: H atom, H_2, and C_2O_2 (O=C=C=O). If the species was not found, estimation routines using the Benson group additivity approach [58] would be employed. An example of this method is shown in Figure 2-3.
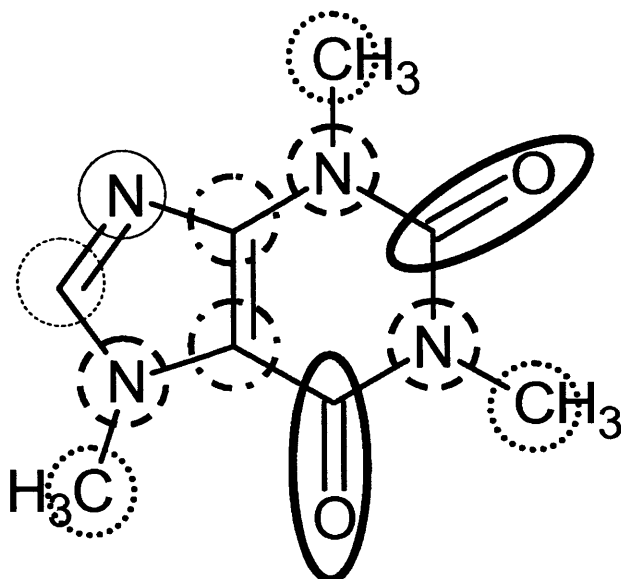
Figure 2-3: Example of deconstructing a molecule into its functional groups: cyclic ketone (thick solid line), cyclic tertiary amine (thick dashed line), methyl (dotted line), cyclic =C< (dash-dotted line), cyclic =N- (solid line), and cyclic =CH- (dashed line) functional groups.

A similar approach would be taken for estimating the kinetics of every reaction proposed within the algorithm. RMG would first check its internal database for the exact structure of the reaction; if present, the stored kinetics would be employed. It should be noted that as of January 2006, the only reactions listed in the internal RMG database were those of the Leeds methane oxidation mechanism [59]. If the exact reaction was not found, RMG would employ estimation routines, based on the "reactive" function groups. This estimation routine involves traversing a set of trees as deeply as possible. Once the deepest nodes have been identified, RMG checks its database for the kinetics matching that set of nodes. If there is no value, RMG traverses up the tree until a known value is found. The advantage of this traversing down (and then possibly back up) the tree is that a value will always be found. The drawback is that this estimation method can give very approximate kinetics, to the point that the predicted activation barrier is significantly lower than the endothermicity. However, other than hardcoding a few sanity checks – ensure the activation energy is greater than or equal to the endothermicity, and that the

total rate coefficient does not exceed the collision limit – it is difficult to know *a priori* which reactions, or functional groups within a reaction family, need further refinement. This idea of validating the RMG database will be discussed further in 0, where the RMG "H_Abstraction" reaction family template will be used as a test case.

The assumptions in the algorithm primarily deal with the types of chemistry that may be modeled. For example, as of January 2006, the only elements that RMG would recognize in any input or database file were carbon, hydrogen, and oxygen. The reason for this was two-fold: only C/H/O chemistry existed in the database, and some C/H/O chemistry was hardcoded into the software. The hardcoded software involved the internal definitions of functional groups, e.g. "Cs," "Cd," "Ct," etc. What these three functional groups represent are a carbon with four single bonds, a carbon with one double bond and two single bonds, and a carbon with one triple and one single bond; see Figure 2-4.
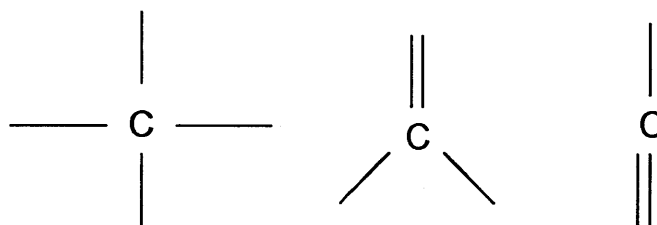
Figure 2-4: Examples of hardcoded functional groups within the RMG software: Cs, Cd, and Ct (from left to right)

The primary reason these functional groups exist in the software is due to their being present in the RMG database: instead of listing elements in each chemgraph definition, some are populated with functional groups (or in the likely event, a set of functional groups). It must be noted that the RMG software, fashioned with these hardcoded functional groups, built validated models for the combustion of hydrocarbons: the software and database were consistent. However, as the RMG developers hope to expand the range of chemistry available to users, this scheme is not robust. Adding a new element, e.g. silicon, would require an experienced RMG developer to implement all of the necessary hardcoded functional groups in the software and database. Furthermore, a multi-valence element, e.g. nitrogen, would not be straightforward to implement, even for an experienced RMG developer. As RMG deals with free-radical chemistry, the carbon, hydrogen, and oxygen elements have a single valency, that is, the maximum number of

connections to the element is equal to the maximum number of hydrogens that can be attached to the element; in the Ph.D. thesis of Robert Ashcraft, he refers to these as "bonding electrons" [54]. Elements like nitrogen, sulfur, and phosphorous do not obey this single valency rule.

Another important assumption of the RMG software involves the representation and handling of aromatics. If a user wished to generate a reaction mechanism for a species containing aromaticity, e.g. benzene, the bond connectivity would need to be specified using the (Johannes) Thiele nomenclature, using a "B" bond to represent the resonance structure. While the internal nomenclature is sufficient, the RMG software lacked the ability to recognize aromatic species automatically; thus, if a user entered benzene using the Kekule structure, RMG could not convert this to the benzene "B" bonds and would therefore not use the most accurate thermochemistry or reaction rate coefficients. Addressing both of the aforementioned issues – generic heteroatom chemistry and aromatic chemistry – will be discussed in 0.

Regardless of what chemistry the user is modeling with RMG, the limiting factor is the database. Foremost, it would be beneficial to validate as many thermochemical parameters in the RMG database as possible. No matter what routine is employed when estimating the thermochemistry parameters, the adage of "garbage in, garbage out" is always applicable. Furthermore, it would be beneficial if RMG did not have to employ its estimation routines as often, i.e. that more species thermochemistry and reaction rate coefficients from the literature were stored in the RMG database. Both of these issues can be addressed by comparing RMG's current database values with those published in the literature. Fortunately, massive combustion chemistry data, such as those discussed in the next Chapter, are now housed in online databases that are amenable to automated mining.

CHAPTER 3
DATA COLLABORATION:
MINING AND CONTRIBUTING TO THE PrIMe WAREHOUSE

3.1   THE NECESSITY OF DATA COLLABORATION

The accuracy of any reaction mechanism is dictated by the thermodynamic, kinetic, and transport parameters employed in the model. As mentioned previously, a typical RMG simulation will create $O(10^4)$ species and $O(10^5)$ reactions. The RMG software needs the thermodynamic and transport parameters for each species, and the kinetic rate expression for each reaction in order to make species concentration estimates for any reaction conditions. Unfortunately, most of this thermochemical information has never been measured: many of the species proposed by RMG are very short-lived radicals, making it exceptionally difficult to measure a property such as the enthalpy of formation.

Since RMG cannot know exactly the thermochemical information for each species and reaction created within a mechanism, estimation routines must be employed. The estimation routines, as employed within the RMG software, utilize the known chemistry that is housed in the RMG database. In theory, the RMG database should have all known species thermochemistry, reaction rate coefficients, and documentation detailing the source of the stored values. In reality, the RMG database stores a small percentage of the hydrocarbon and oxygenated hydrocarbon literature's peer-reviewed thermochemistry parameters, in addition to "in-house" quantum calculations performed by previous members of the Green Group.

Many issues exist regarding expanding the RMG database: Where should the data come from? How reliable is the data? How can the reported data be converted to the RMG database syntax? Equally important questions are: Where do our current thermochemical parameters come from and how reliable are they? Once these questions are answered, the biggest hurdle in populating the RMG database with the literature's peer-reviewed values may be addressed: How can one automate this entire process?

3.2   ONLINE THERMOCHEMISTRY DATABASES

Fortunately, several agencies have already addressed (to a large extent) the question of where should the data come from. Several online databases exist, including the NIST Chemistry WebBook [60] and the NIH PubChem Project [61], which house the community's raw and evaluated data. With any database, especially those with tens of thousands of entries, there are bound to be a few unintentional mistakes, e.g. the thermochemistry for species A is actually associated with species B. Although difficult to detect on a single data entry level, it would be useful if a tool existed that suggested data entries to double-check for consistency.

Another example of an online thermochemical database is the Process Informatics Model (PrIMe) Warehouse [62, 63]. This project began in 2004 and has been administered primarily by Prof. Michael Frenklach of the University of California, Berkeley of the Mechanical Engineering department. The mission of PrIMe is two-fold:

- House the combustion community's raw data: The PrIMe Warehouse would store all thermochemistry information supplied to it. Furthermore, working groups would periodically review the raw data in order to make recommendations on evaluated data, that is, thermochemical parameters the PrIMe project recommends users to implement in constructing reaction models.
- Data collaboration: The PrIMe project would also have tools to support users constructing and validating kinetic models for any fuel in any reactor set-up. The PrIMe project would also offer optimization routines to identify the active parameters, or those parameters which most effect the model's predictions, for any model.

The PrIMe Warehouse is structured in multiple repositories: bibliography, reactions, species, models, etc. Within each repository are a "catalog" directory and a "data" directory. The "catalog" directory contains files which define different types of data entries, for the specific catalog; e.g. within the species catalog are files for methane, ethane, propane, etc. The "data" directory contains files which store information about

the corresponding file in the "catalog" directory; e.g. the data associated with methane includes all thermochemistry and transport property estimates. In theory, only one file in the "catalog" directory will represent each entry, i.e. there is only one methane identifier. There can be multiple (and in theory, infinite) files in the "data" directory for each entry, i.e. every distinct measurement for the enthalpy of formation of methane at 298 K will be stored.

The PrIMe Warehouse was initially populated with the raw data stored in the NIST Chemistry WebBook, with the support of Tom Allison. This initialization had its benefits – approximately 10,000 species thermochemistry and 16,000 reaction rate coefficients were transferred – and its drawbacks – the errors that existed in the NIST Chemistry WebBook now existed in the PrIMe Warehouse, not to mention the additional errors that were introduced via the translation procedure. Regardless of the handful of errors, the PrIMe Warehouse contained a vast amount of thermochemical data, many of which are not present in the RMG database. It would be beneficial for RMG to have access to this information when constructing kinetic models.

3.3   SELECTING A COMMON LANGUAGE

In order for the RMG software to collaborate with the PrIMe Warehouse, there must be a form of communication between the two. The RMG software represents a species using a labeled graph (Figure 3-1): the nodes are labeled with a one-or-two letter string to represent an element and an integer to represent the number of free electrons associated with that node, and the arcs are labeled with a one letter string to represent the bond strength between the two nodes. In RMG, this labeled graph is commonly referred to as a ChemGraph (or adjacency list). Within the RMG software, this ChemGraph is a unique species identifier: no distinct set of species will have the same ChemGraph and no ChemGraph can represent more than one species. In RMG's current representation, it cannot distinguish between stereoisomers, e.g. diastereomers (cis- and trans-isomers) or enantiomers (R- vs. S-compounds).

```
1 C 0 {2,S}
2 C 0 {1,S} {3,S}
3 C 0 {2,S} {4,S}
4 C 0 {3,S} {5,S}
5 O 0 {4,S}
```

Figure 3-1: RMG's representation of the species n-buatnol

In the PrIMe Warehouse, the unique species identifier is the primeID (Figure 3-2): a nine character string starting with the lower-case letter "s" and followed by an 8 digit long number (base 10). The number has no meaning, other than acting as a counter; all new species added to the Warehouse are assigned the lowest number not already in use.

With two very distinct species identifiers already employed, a common language must be selected. Creating and storing a ChemGraph for each species in the PrIMe Warehouse is not sensible. Firstly, the ChemGraph is not a commonly-used species identifier, thus whenever a new species is added to the PrIMe Warehouse, the user would be expected to add the ChemGraph representation as well. Furthermore, if the RMG software ever changed the syntax of its unique species identifier, the definitions stored in the PrIMe Warehouse would become obsolete. Lastly, it is well-known to the RMG developers that the most time-consuming portion of any RMG simulation (excluding external executable calls, e.g. solving pressure-dependent networks) is ChemGraph comparisons. Thus, having an identifier that scales better than $O(N^2)$, where N is the number of atoms in the species, would be preferred.

The primeID is a nine character string: string comparisons scale as $O(N)$ and thus would be much more efficient than comparing ChemGraphs. However, adding a primeID to each ChemGraph generated within RMG is also not feasible. Firstly, there are only ~11,000 species in the PrIMe Warehouse, whereas a typical RMG simulation can make ~40,000 unique species; some species would thus not be assigned a primeID. Moreover, this implementation would require user intervention: someone would have to make a database, by hand, which assigned each primeID a ChemGraph. This is problematic because the process would be error-prone, not to mention RMG's search of this database

for the proper primeID would involve searching via ChemGraph, the species identifier that we are trying to avoid when identifying the same species. Furthermore, if a species in the PrIMe Warehouse were ever removed, e.g. it was determined it was a duplicate species, one would need to be alerted of this update and manually update the RMG database. Lastly, just like the RMG ChemGraph, the primeID is not a universally-recognized species identifier, thus making it difficult for someone unfamiliar with RMG and/or PrIMe to quickly read or contribute to the database.

```
<?xml version="1.0" encoding="utf-8" ?>
<copyright>©primekinetics.org 2005</copyright>
<preferredKey group="prime" type="formula">C4H10O</preferredKey>
<chemicalIdentifier>
<name source="©NIST" type="CASRegistryNumber">71-36-3</name>
<name source="©NIST" type="formula">C4H10O</name>
<name source="©NIST">n-C4H9OH</name>
<name source="©NIST">1-butanol</name>
<name source="©NIST">1-butyl alcohol</name>
<name source="©NIST">1-hydroxybutane</name>
<name source="©NIST">alcool butylique</name>
<name source="©NIST">butan-1-ol</name>
<name source="©NIST">butanol</name>
<name source="©NIST">butanolen</name>
<name source="©NIST">butanolo</name>
<name source="©NIST">butyl alcohol</name>
<name source="©NIST">butyl hydroxide</name>
<name source="©NIST">butylowy alkohol</name>
<name source="©NIST">butyric alcohol</name>
<name source="©NIST">ccs 203</name>
<name source="©NIST">hemostyp</name>
<name source="©NIST">methylolpropane</name>
<name source="©NIST">n-butan-1-ol</name>
<name source="©NIST">n-butanol</name>
<name source="©NIST">n-butanolbutanolen</name>
<name source="©NIST">n-butyl alcohol</name>
<name source="©NIST">n-c4h9oh</name>
<name source="©NIST">na 1120</name>
<name source="©NIST">nba</name>
<name source="©NIST">propylcarbinol</name>
<name source="©NIST">propylmethanol</name>
<name source="©NIST">rcra waste number u031</name>
<name source="©NIST">un 1120</name>
<name type="InChI">InChI=1/C4H10O/c1-2-3-4-5/h5H,2-4H2,1H3</name>
</chemicalIdentifier>
<chemicalComposition>
<atom symbol="C">4</atom>
<atom symbol="H">10</atom>
<atom symbol="O">1</atom>
</chemicalComposition>
</chemicalSpecies>
```

Figure 3-2: PrIMe's representation of the species n-butanol

The goal then is to select a unique species identifier that is both human friendly, primarily regarding its prevalent use in the scientific and engineering communities, and computer interpretable. Other options available at the time, and which were already present in a majority of the species entries the PrIMe Warehouse were: the IUPAC name, the molecular formula, the CAS Registry Number, and an ASCII interpretation of the species structure, e.g. tert-butanol might be represented as HOC(CH3)3.

The IUPAC name is a canonical (one-to-one) species identifier. However, converting a ChemGraph to an IUPAC name on-the-fly would not be straightforward. Furthermore, RMG's limitations of representing stereoisomers, and it's representation of certain species (e.g. carbon monoxide, with a double-bond between the carbon and oxygen and a set of free electrons on the carbon), would further restrict the ability of properly converting a ChemGraph to an IUPAC name.

The molecular formula, although fast to generate and compare against other species, is not a canonical species identifier. Imagine all of the C_4H_8 isomers: 1-butene, (E)-2-butene, (Z)-2-butene, iso-butene (or 2-methylpropene), cyclobutane, methyl cyclopropane, etc.

Although the CAS Registry Number is nearly a one-to-one species identifier, there are some instances of one CAS Registry Number being assigned to multiple species, and one species being assigned multiple CAS Registry Numbers. Additionally, there is not a CAS Registry Number for all species. Moreover, converting from a ChemGraph to a CAS Registry Number on-the-fly would not be straightforward.

Other options available at the time were the InChI (International Chemical Identifier) and SMILES (simplified molecular input line entry specification) strings. Both claim to represent species unambiguously. However, both identifiers cannot currently represent molecules of differing electronic states, spin states, vibrational states, or phases. Of these features, it is particularly desirable to distinguish between different spin states, e.g. the singlet and triplet states of methylene. Although the SMILES are more human-readable,

they are not canonical, whereas the InChI string is canonical. Thus, it was decided to use the InChI string as the unique chemical identifier (Figure 3-3).

InChI=1/C4H10O/c1-2-3-4-5/h5H,2-4H2,1H3

Figure 3-3: InChI's representation of the species n-butanol

With the InChI selected as the common language, it thus became necessary to teach both RMG and PrIMe how to converse in the new language.

3.4 TEACHING RMG TO SPEAK INCHI

An InChI can be automatically generated by a free, open-source, stand-alone software package provided by IUPAC and NIST. The stand-alone software requires a "standard" input file be supplied in order to generate an InChI, none of which match the ChemGraph or primeID nomenclature. One of these standard files is a MDL Molfile (.mol extension), Figure 3-4. I typically use the free software package ChemSketch to generate MDL Molfiles with 2-d geometry estimates. The basis of the MDL Molfile is a list of atoms (labeled with its Cartesian coordinates, element symbol, etc.) and a list of bonds (listing each bond, including the two atoms that are connected to that bond and the bond strength). Fortunately, RMG already has this information, with the exception of the Cartesian coordinates. However, these can all be set to (0,0,0) as the InChI executable does not interpret the Cartesian coordinates; some software packages that utilize the MDL Molfiles do use the coordinates in order to display the molecule visually.

A function was written in the Species class of the RMG source code (/jing/chem/Species.java) which converts a ChemGraph to a MDL Molfile. There are no restrictions on the element symbol or bond connectivity; there is a maximum number of atoms (99) and bonds (99) that is hardcoded into the algorithm, though this is easily resolved. In fact, unique MDL Molfiles are written for species of differing spin state; the only drawback is that no visualization software, nor the InChI executable, can currently utilize this information. For future work in this regard, please see the Recommendations section of this chapter.

ACD/Labs12061009462D

```
 5 4 0 0 0 0 0 0 0 0 1 V2000
   7.7396 -11.7457   0.0000 C  0 0 0 0 0 0 0 0 0 0 0 0
   9.0696 -11.7457   0.0000 C  0 0 0 0 0 0 0 0 0 0 0 0
   9.7346 -12.8975   0.0000 C  0 0 0 0 0 0 0 0 0 0 0 0
  11.0646 -12.8975   0.0000 C  0 0 0 0 0 0 0 0 0 0 0 0
  11.7296 -14.0493   0.0000 O  0 0 0 0 0 0 0 0 0 0 0 0
  1 2 1 0 0 0 0
  2 3 1 0 0 0 0
  3 4 1 0 0 0 0
  4 5 1 0 0 0 0
M  END
```

Figure 3-4: MDL Molfile's 2-dimensional representation of the species n-butanol

This feature is available as a stand-alone module of RMG, or can be called within a RMG simulation. If the user desires the InChI to be generated, RMG writes the MDL Molfile to disk, calls the InChI executable passing the MDL file as input, and generates the InChI standard output files. The output file is then read by the RMG software and the InChI is extracted. On the other hand, if the user wishes to convert an InChI to a ChemGraph, that feature is provided as a stand-alone code as well.

At one point in time, I thought using the InChI string as the unique identifier within RMG would be beneficial, especially for species comparison purposes. It seemed reasonable that comparing a string would be much faster than comparing a ChemGraph. However, after implementing the InChI string as the check for species uniqueness (this check comes after comparing molecular formulas, as is the case for the ChemGraph comparison), the overall runtime of the RMG simulation increased drastically. I determined that although the string comparison of the InChIs was much faster in comparison to ChemGraph comparisons, the time spent generating the InChI far outweighed the time saved by comparing strings instead of ChemGraphs. This thought

could be re-visited in the future, if the runtime of any of the following processes are decreased significantly:

- the InChI stand-alone executable
- the construction of the MDL Molfile
- the reading of the standard InChI output file

Likewise, if the InChI generation could be performed in parallel with other processes, e.g. RMG's estimating the thermodynamic and transport properties of the species, using the InChI as RMG's unique species identifier would be worthwhile.

Presently, the InChI is generated for all "core" species at the end of a RMG simulation (if the user so desires). This string can be used in searching external databases for thermochemistry parameters, or for the unique species ID in a therm.dat CHEMKIN input file. One feature the Reaction Design software package CHEMKIN-MFC [64] offers is a mechanism merging feature. A user may supply a list of mechanisms to the software, and if each species' thermochemistry is labeled with a unique species string, e.g. InChI or SMILES, the software can automatically merge the mechanisms.

3.5   TEACHING PRIME TO SPEAK INCHI

Each species in the PrIMe Warehouse has its unique species identifier: the primeID. However, many of the species data entries contain much more information that this; see Figure 3-2 for an example. For instance, it is not uncommon for each species to have its molecular formula, CAS Registry Number, IUPAC name, chemical composition, other common names, chemical structure as written in an ASCII string, etc. Thus, although the InChI string was not originally present in the database, each species file gave a user many clues regarding its true identity.

Since teaching the PrIMe database required populating the database by hand, it was convenient to first attempt a computer-aided approach. Initially, Greg Magoon of the Green Group used the CAS Registry Number as the initial species key. Many external databases (to RMG and PrIMe) have the CAS Registry Number labeled with each of their species entries. Two such databases are the NIST WebBook and the NIH PubChem Project. Furthermore, each of them also had InChI strings assigned to many of their

species entries. The following algorithm was written to resolve as many PrIMe species as possible, via automation.

- Grab the single CAS Registry Number from each species entry in the PrIMe Warehouse. If multiple, or no, CAS Registry Number existed, the algorithm was terminated immediately for that species.
- The single CAS Registry Number was then entered into the WebBook and PubChem search engines. If this search returned a single hit, the entry was explored for its InChI string. If a single InChI string existed, it was extracted.
- The InChI string from the PubChem database was then compared with the InChI string from the WebBook database. If they were exactly the same (including the auxiliary information), then the search was considered a success and the PrIMe species was labeled with the appropriate InChI string.

Of the 11,000 species in the PrIMe Warehouse, ~4,400 species were labeled with an InChI automatically. However, that left ~6,600 species entries that required resolution.

The initial purpose of this InChI population was to allow RMG to mine the PrIMe database for thermochemistry parameters. Since RMG could only handle species containing C, H, and O atoms, I initially restricted the resolution of the species catalog to those types of species. The element N was also included, as this was the next element to be added to RMG. Of the remaining 6,600 species, ~2,000 of them were C/H/N/O only containing species. Thus, these ~2,000 needed to be manually populated with InChIs.

As I mentioned before, many of the species have additional information within their species file. These are clues into what species the file is meant to represent. Determining which species each entry actually meant relied on how much information was given in the species file itself, and on how many reactions / models / etc. it was involved in. For instance, if the species had the following information in its file – propane, C_3H_8, $CH_2=CH_2-CH_3$, $CH_3CH_2CH_3$ – I could be fairly confident that the species was propane despite the one incorrect structure. However, I still checked each of the reactions that referenced it, making sure each of the reactions was marking the species correctly, and

that the "propane" species was indeed propane. However, for those hundreds of species entries which only contained the molecular formula, additional information in the form of which reactions they participated in was also available. For example, one of the PrIMe species entries (e.g. s00004601) only contained the molecular formula C_4H_8, leaving me with many options to choose from. However, searching the PrIMe reactions catalog for entries containing s00004601 also gave me a list of reactions which this species participates in, the kinetics for each of these reactions, and the source of this kinetics. With these references, I tracked down the reaction associated with the reported kinetics and determined the identity of the C_4H_8 species. If all reaction references pointed to the same C_4H_8 isomer, I concluded that isomer to be the identity of the s00004601 data entry and labeled it with the appropriate InChI. If the references pointed to multiple C_4H_8 isomers, each InChI was temporarily stored with the species file; this labeling of species with multiple InChI strings was performed on my local computer, and not in the PrIMe Warehouse. By having multiple InChI strings, I was declaring to myself that this species entry was not yet resolved. This process was performed for each of the ~2,000 "needed to be resolved" C/H/N/O PrIMe species data entries.

In the process of identifying the ~2000 unresolved C/H/N/O PrIMe species data entries, another problem arose: some of the bibliography data entries were incorrect. Any error in the PrIMe Warehouse needs to be resolved. However, an error in the bibliography catalog is more critical than an error in any other catalog as every "data" entry in the PrIMe Warehouse is linked to one of the files in the bibliography "catalog." Thus, before any further work with the PrIMe Warehouse, including the collaboration with RMG, could be pursued, the PrIMe Warehouse bibliography catalog needed to cleaned and validated.

3.6 CLEANING THE PrIME WAREHOUSE: BIBLIOGRAPHY CATALOG

As mentioned previously, PrIMe was originally populated with the NIST WebBook data. However, duplicates, typos, etc. exist in the WebBook database, meaning they initially existed in the PrIMe Warehouse. Furthermore, with no unique identifier for species, reactions, bibliography, etc., there was no check when adding new entries to the Warehouse. For example, if a user wanted to input the species thermochemistry for

methane, the PrIMe Warehouse would have created a new primeID for this species "methane" without first checking whether methane already existed.

Every file in the PrIMe warehouse is linked to a bibliography file. Thus, the natural starting point in cleaning the PrIMe database of duplicates was the bibliography database. A protocol for searching the bibliography database was established. The first step involved automated checking, using search criteria of author's last name, journal publication year, and journal publication pages as fields to compare for each file. A script was written in collaboration with Dr. Zoran Djurisic which compared the author's last name, year of publication, and page number of each entry against every other entry. If all three were the same, the duplicate search was considered a success and the two data entries were saved to a file. After this initial search, 848 bibliography entries were determined to be potential duplicates of one another. I then went through this list by hand, determining which of the entries were actual duplicates of one another. This process involved obtaining each potential duplicate's reference and confirming the information in the bibliography data entry was correct. Once all entries were validated, the process of identifying actual duplicate entries was straightforward to determine. In some cases, multiple files were flagged as potential duplicates because of errors in the files present in the PrIMe Warehouse. In other cases, the author published two consecutive articles in the same issue of a journal, e.g. the first article spanned pages 872-879 and the second spanned 879-888. The bibliography duplicate search found the same page number in both instances (page 879) and thus labeled it a potential duplicate. At the conclusion of this work, 384 bibliography entries were determined to be duplicates. I decided which entries to keep and which to place in the attic (i.e. remove from the Warehouse).

The entire PrIMe Warehouse was then searched to determine which non-bibliography files were linked to the duplicate bibliography files. For each file, the link to the duplicate file was broken and then reestablished to the correct bibliographic reference. In total, there were ~270 reconnections; many of the duplicate files were not linked to any other PrIMe file. These 270 updated files were resubmitted to the PrIMe Warehouse, the

400 duplicate bibliography entries were placed into PrIMe's attic (obsolete folder), and the duplicate's respective primeIDs were retired. By placing a file into the attic, PrIMe restricts automated code from accessing its content; however, a human-user can peruse the file without restriction.

Although one might hope the entire bibliography catalog to be clean and free of duplicates, that is not necessarily so. One caveat of this work is that we had to assume the information stored in each bibliography entry was correct. Thus, this work produced a clean bibliography catalog, assuming the data stored in each entry is correct. Future work relating to the cleaning of the bibliography catalog should involve labeling each data entry with a unique identifier, the Digital Object Identifier (DOI). The difficulty in automating this process could be licensing and security restrictions; e.g. searching for each of the >19,000 bibliography DOIs via SciFinder using MIT's license would not be possible, as the use of automated scripts are strictly prohibited.

3.7   CLEANING THE PRIME WAREHOUSE: C/H/N/O SPECIES CATALOG

With the bibliography database void of duplicates (to the best of our abilities), the next step was pruning duplicates from the species database. The protocol for searching for duplicates in the species database paralleled that for searching for duplicates in the bibliography catalog. Search criteria of chemical formula, number of unique elements, and total number of atoms were chosen. Of the ~10,900 species files, ~5,800 potential duplicates were identified. Since the number of potential species duplicates was an order of magnitude greater than the potential bibliography duplicates, the problem was divided into smaller subcategories. Since all combustion researchers are interested in molecules made of carbon, hydrogen, nitrogen, and oxygen (C/H/N/O species), files containing only those elements were placed into the first subcategory to be checked for duplicates.

The PrIMe species database has ~5,400 C/H/N/O species, ~4,800 of which were marked as potential duplicates. Checking 4,800 potential duplicates by hand seemed tedious and error-prone, so another method of identifying potential duplicates was established. With my work on adding an InChI string to each C/H/N/O species complete, it was decided to

test the utility of the InChI by using it as the only search criteria in identifying potential duplicate species. One disadvantage of using the InChI in checking for potential duplicates is that some false positives will be identified since PrIMe has species of varying electronic, spin, and vibrational states stored in the database; PrIMe also stores the same species for different phases. The improvement InChI offers is the benefit of eliminating many of the false positives generated from the initial search. For example, imagine a species with the molecular formula $C_{10}H_{10}$. With six degrees of unsaturation, dozens of legitimate isomers could be imagined. Moreover, the initial search criteria would mark all of them as potential duplicates. With InChI's structured layers, none of these would be flagged.

A duplicate check, using only the InChI string, produced 343 potential duplicates in the C/H/N/O species database, an order of magnitude smaller than the 4,800 duplicates marked using the method mentioned previously. This reduction in potential duplicates demonstrates the robustness of using the InChI string as the unique species identifier. The reasons for the ~400 duplicate species were many:

- The PrIMe Warehouse contained the same species entry multiple times. As mentioned previously, there was no standard identifier to check against when submitting a species to the PrIMe Warehouse: how could a duplicate of methane be identified with only the primeID acting as the unique species identifier.
- The species were distinct, however the limitations of the InChI string (e.g. the inability to distinguish between different phases of the same species) caused the search to return a false positive.
- The species file contained multiple InChIs; the reason for this was mentioned previously, in that I could not narrow down that particular data entry to a single species, based on the information provided in the PrIMe Warehouse.

With this more manageable number, the process of checking for duplicates by hand continued. The results of the duplicate species check produced 129 sets of duplicate species. For the duplicates, I again decided which data entries to keep in the Warehouse and which to place in the attic. Another script was written, which replaced all "speciesLink" entries from the duplicated species to the now-unique species.

Although no duplicates now exist in the corrected C/H/N/O species database, all this work assumes the chemical composition (which was used to generate the initial list of C/H/N/O species) is correct. There are certainly instances where the chemical composition does not match the species formula. However, the script did not account (and could not account) for these errors.

3.8   VALIDATING C/H/O THERMODYNAMICS DATA

With all C/H/O species in the PrIMe database having an InChI string and RMG's source code allowing it to generate ChemGraphs from InChI strings, a preliminary thermodynamics data consistency check was performed. For every C/H/O species in PrIMe containing thermodynamic data, the InChI string and data were sent to RMG. Using the InChI string, RMG constructed a ChemGraph, from which the species thermodynamic properties were estimated using Benson's group additivity. The two sets of data were then compared; if the difference in enthalpy of formation was greater than 5 kcal/mol, or the difference in entropy or heat capacity differed by more than 2 cal/mol/K, the species was flagged as having statistically different values. These tolerances were selected based on reaction rate coefficients' sensitivity to them. A difference less than the stated numbers would produce an error in the rate constant of less than an order of magnitude; this error would be indistinguishable in comparison to the error generated by software in generating the mechanism.

Preliminary results showed a 50% pass rate; about half of the 500 C/H/O species in PrIMe with thermodynamic data differed significantly from RMG's estimates. Not surprisingly, most of these flagged species were due to RMG's inability to accurately predict the thermochemistry of fused-rings, e.g. polycyclic aromatic hydrocarbons, a flaw known to the RMG developers. However, a handful of functional groups, e.g. a ring-system including a carbonyl group, consistently resulted in species being marked statistically different. Greg Magoon of the Green Group resolved these discrepancies, and presented the work at the 2008 International Combustion Symposium [ref. needed]. In some cases, the RMG prediction was poor; in others, Greg found the PrIMe database to have typos. In some instances, the thermochemistry was correct, but the species it was

assigned to was not (i.e. the thermochemistry for 1-butyl was originally assigned to the 2-butyl species in the PrIMe Warehouse). For other discrepancies, Greg determined the entropy was miscalculated because the external rotational symmetry number was not computed correctly.

3.9 *FUTURE WORK AND RECOMMENDATIONS*

New experimental and theoretical thermochemistry information, particularly as it relates to the combustion community, is published every week. Looking at the small picture, particularly how it relates to the RMG database, most of these new measurements and calculations will never be utilized in the RMG database for the reason that there is no communal portal from which to access all of this information. The question of how to make this information available to the entire community in a quick, efficient manner arises.

On a separate note: I am part of a Subcommittee for the InChI software, whose plan is to address expanding the InChI's capabilities. Presently, the group has agreed to expand the InChI string to represent species of differing electronic spin; potential future work includes representing transition states. If successful on the transition state representation, there would be a simple string notation to describe the 3- and 4-member ring transition state for the isomerization of 1-butyl to 2-butyl radical. The working group's purpose is to devise how the unique spin states should be represented in the InChI string, and in the input/output files of the InChI executable. This will assist RMG in distinguishing species of the type:

- Methylene: singlet vs. triplet
- Molecular oxygen: single vs. triplet
- Biradicals (in particular those formed from ring opening reactions) : singlet vs. triplet

For all cases, it is important to know the spin of the species, as the thermochemistry and kinetics will be very different. In particular, for the last case, the singlet molecule may

46

undergo an intramolecular radical recombination, forming a cyclic compound. However, the triplet species may not, as the reaction is spin-forbidden.

In RMG currently, multi-radical species are handled differently, depending on where the unpaired electrons are. If the unpaired electrons are localized to the same atom (e.g. methylene), RMG denotes that by putting a "2" in the electron field of that atom's line in the ChemGraph. By default, RMG assumes all "2" electrons are the triplet state, and would thus be labeled "2T." A singlet state only occurs if the user specifies so in the input file, or the database. If a species has single unpaired electrons on different atoms (e.g. the product of a ring opening reaction), RMG makes no assumptions about the spin and treats each unpaired electron equivalently when computing thermochemistry or kinetics. However, as mentioned previously, this is technically incorrect when considering the possibly of intramolecular radical recombination (i.e. ring closing) reactions.

CHAPTER 4
RESOLVING THE HYDROGEN ABSTRACTION REACTION FAMILY

The estimated thermochemistry from RMG's algorithm depends on the availability and reliability of the data employed in its estimation routines. For thermochemistry, each heavy atom (or in some cases, set of heavy atoms) is assigned a function group. This functional group then contributes to the overall molecule's enthalpy, entropy, and heat capacity. Summing all contributions from all groups yields the RMG-predicted thermochemistry parameters. The functional groups defined in RMG's database come primarily from the work of Benson, who compiled experimental thermochemical data for numerous hydrocarbon and oxygenated hydrocarbon species. After defining functional groups, e.g. R-CH₃, Benson performed regression analysis on the data in order to assign "best-fit" values for each functional group, for each thermochemistry property of interest. In general, estimating thermochemistry for hydrocarbons and oxygenated hydrocarbons, using Benson's group additivity scheme, is fairly reliable, i.e. +/- 5 kcal/mol uncertainty in the predicted enthalpy at 298K and +/- 2 cal/mol/K uncertainty in the predicted entropy at 298K and heat capacity over the temperature range 300 to 1500K.

When considering the estimation routines employed by RMG for predicting kinetic rate coefficients, the reliability is less certain. The general algorithm for estimating kinetics is through averaging "similar" numbers, when the exact number is not available. This routine can be particularly troubling as the number of averages increases. One example would be in the intra_H_migration family, where one of the trees distinguishes the size of the transition state: If the kinetics for a 3-membered ring is desired, but only kinetics for 5-membered rings exist, the averaging scheme will utilize those numbers. Thus, it is not uncommon for the predicted activation energy for a 3-membered ring (which is highly strained) to have a relatively low activation barrier.

To access the validity of the RMG database, the predicted values for a set of species was compared to the reported values from an online thermochemical database, the PrIMe

(Process Informatics Model) Warehouse. The set of species and reactions chosen, the algorithm of comparing the two sets of data, and the resolution of any discrepancies is described in the following sections.

A list of all C/H/O species was compiled (~3600 species); the criterion for this was the chemical composition. Next, each reaction file was checked for the PrIMe species IDs. If all of the species IDs were determined to be C/H/O species, the reaction was labeled as C/H/O reaction and all of its kinetics (there can be multiple kinetics reported for the same reaction) were then stored. There are ~3000 reactions and ~6000 kinetics in the PrIMe Warehouse that are C/H/O only.

Each of the ~3000 reactions was then passed to a script. The species for each reaction was read in; since all of these C/H/O species have an InChI, the InChI was extracted from the file. RMG then converted the InChI to a ChemGraph. Once all InChIs were converted to ChemGraphs, the ChemGraphs were then sent to another RMG module, PopulateReactions. This module reads in a list of species and determines all ways they can react with themselves, by themselves, and with every other species in the file. Of course, this is based on the rules RMG has in its database. Each of the generated reactions was compared to the reaction of interest. If the structure returned from PopulateReactions matched the structure sent in from the PrIMe Warehouse, the RMG kinetics were stored with the PrIMe kinetics. The result of these series of scripts was a list of ~3000 reactions, with RMG and PrIMe kinetics stored with each one.

To determine the accuracy of the two methods, the k(T) was plotted from 300-1500K (this was arbitrary, but is supposed to represent the valid temperature range for all RMG data, in general). If the k(T) from the two methods differed by more than 2 orders of magnitude for any temperature, the reaction was flagged for further inspection. Of the 6,000 kinetics in the PrIMe Warehouse, 2,000 were flagged because of discrepant data. Given the large number of potential discrepancies, a smaller subset was chosen to address for my thesis: the H-Abstraction reaction family. This family was selected for a few reasons: (1) these types of reactions are not pressure-dependent, so there was no need to

worry about whether the experiments were in the high-pressure limit or not; (2) the H-abstraction reaction family in RMG is one of the more heavily populated families, and we have more confidence in these values; (3) H-abstractions are prevalent under almost all experimental operating conditions (pressure, temperature, equivalence ratio, fuel percentage) for any fuel; and (4) the transition state structures are relatively easy to converge in quantum chemistry packages, e.g. Gaussian 03. Of the ~2,000 discrepant kinetics, >300 were from the H-abstraction reaction family.

These 54 kinetic rate expressions are now in the RMG database, and should be a good, validated dataset for which group additivity scheme for reactions may be employed. (training set). Furthermore, the recommendations for the 80 kinetics will be submitted to the PrIMe Warehouse as part of the data compilation. However, it is also hoped that these will be the evaluated kinetics (rk00000000.xml) that PrIMe would recommend to any user. Presently, there are ~300 kinetics that PrIMe recommends, most of which are the reactions and kinetics from the GRI-Mech 3.0 mechanism.

4.1 COMPUTATIONAL METHODS

The entire catalog of reactions in the PrIMe Warehouse was searched for those reactions containing only carbon, hydrogen, and oxygen-containing species; this was done in an automated fashion, using the primekinetics MATLAB portal. Each reaction's reactants and products were then exported to the RMG software and the kinetics was estimated for every possible reaction between A and B (e.g. A decomposition / isomerization, B decomposition / isomerization, and every cross reaction between A and B, according to the RMG reaction family templates). These estimated kinetics were compared against those stored in the PrIMe Warehouse. A reaction was marked for further inspection if the kinetics differed by more than one order of magnitude at any temperature between 300 and 1500 K; at the time of this study, no PrIMe reaction xml file contained a valid temperature range, so 300 – 1500 K was assumed. This long list was reduced to include only Hydrogen abstraction reactions. It is this list of 334 reactions that set the scope of the present study.

For 54 of the 334 reactions, the geometry, single-point energy, and frequencies of each reactant, product, and transition state were computed using the CBS-QB3 method [65-68]; these were performed in the Gaussian 03 software suite [69]. The frequencies computed with Density Functional Theory (DFT) at the B3LYP/CBSB7 level were scaled by a factor 0.99 [70]. The rate coefficient was then computed using conventional transition state theory, Equation (2.3).

$$k = \kappa(T) \frac{k_B T}{hC^\circ} \exp\left(-\frac{G_{TS} - \sum G_{reactants}}{RT}\right) \tag{2.3}$$

k_B, h, and R are the Boltzmann, Planck, and universal gas constant, respectively, T is the absolute temperature, C° is the standard-state concentration (assumed to be P_{ref} / RT where $P_{ref} = 1$ atm), and G_i is the Gibbs free energy of species i. $\kappa(T)$ is the tunneling correction; an asymmetric Eckart correction [71] is employed in this study and was calculated using the methodology presented by Johnston and Heicklen [72], with their Equation (15) replaced by the formula given in Equation (2.4), as noted by Garrett and Truhlar [73]. The TST calculations were performed in the software package CANTHERM [74].

$$2\pi b = \frac{2\sqrt{(\xi - 1)\alpha_1 + \alpha_2}}{\alpha_1^{-1/2} + \alpha_2^{-1/2}} \tag{2.4}$$

The Gibbs free energy is computed using the species' enthalpy and entropy, where these quantities are computed from the species' partition functions. The rigid rotor harmonic oscillator (RRHO) approximation is applied for the vibrational partition function, with 1-dimensional hindered rotor corrections for the low-frequency torsional modes. For each low-frequency torsion, 37 constrained optimizations were performed using DFT at the B3LYP/6-31G(d) level, rotating the dihedral angle in 10° increments. The potential energy was fit to a fifth-order Fourier series, Equation (2.5). This form of the potential energy, along with the reduced moment of inertia $I^{(2,3)}$ of the optimized geometry [75], was substituted into the Schrodinger equation; the Schrodinger equation was solved using a Galerkin method, with assumed basis functions of the form $\exp(-in\phi)$. The lowest 200 energies were calculated and substituted into the canonical partition function; the evaluation of this partition function replaced what the RRHO approximation would otherwise compute for the

low-frequency torsional mode. These hindered rotor corrections were calculated in CANTHERM.

$$V(\phi) = \sum_{m=0}^{5} A_m \cos(m\phi) + B_m \sin(m\phi) \qquad (2.5)$$

The rate coefficient was computed over the temperature range 300 – 2500 K, in increments of 200 K. The parameters for the modified Arrhenius expression were calculated using least-squares regression. The modified Arrhenius parameters for the reported 54 reactions were computed in this fashion.

4.2   RATE COEFFICIENT EVALUATIONS AND RECOMMENDATIONS

The computed total rate coefficients, fit to $k(T) = A (T / 1000 \text{ K})^n \exp(-E_A/RT)$, are reported in Table 1. The reactions are discussed in detail below.

Table 1: Summary of the 54 reaction rate coefficients computed in this study. The Arrhenius parameters are for the form $k(T) = A \, (T / 1000K)^n \exp(-E_A/RT)$ where A and E_A have the units $cm^3 \, mol^{-1} \, s^{-1}$ and $kcal \, mol^{-1}$, respectively.

#	Reaction String	A	n	E_A	Valid Temperature Range		Source
1	CH3O + CH(CH3)3 = C(CH3)3 + CH3OH	2.629E+11	1.837	1.348	300	- 2500	Present Study
		2.000E+11	0.000	4.093	464	- 533	Bercés et al.
		1.000E+11	0.000	4.093	464	- 533	Kerr et al.
		3.980E+11	0.000	2.404	383	- 423	Batt et al.
		2.290E+10	0.000	2.881	300	- 1500	Tsang
2	CH3O + (CH3)2CHCH(CH3)2 = (CH3)2CCH(CH3)2 + CH3OH	7.723E+10	2.204	0.620	300	- 2500	Present Study
		4.000E+08	0.000	0.000	373	373	Alcock et al.
3	CH3 + CH(CH3)3 = CH2CH(CH3)2 + CH4	1.855E+11	4.152	7.955	300	- 2500	Present Study
		1.450E+13	0.000	16.293	770	- 855	Konar et al.
		1.212E+11	3.650	7.153	300	- 2500	Tsang
		7.590E+11	0.000	11.564	300	- 855	Zhang et al.
		4.813E+11	3.650	7.146	800	- 950	Goos et al.
4	CH3 + CH3CH2CH2CH3 = CH2CH2CH2CH3 + CH4	2.649E+11	4.133	8.031	300	- 2500	Present Study
		3.006E+12	0.000	13.591	980	- 1060	Yampolskii
5	CH3 + CH3(CH2)3CH3 = CH2(CH2)3CH3 + CH4	2.061E+11	4.144	7.991	300	- 2500	Present Study
		1.000E+09	0.000	0.000	813	813	Blackmore et al.
6	CH3 + CH3(CH2)6CH3 = CH2(CH2)6CH3 + CH4	4.858E+11	4.116	8.131	300	- 2500	Present Study
		1.600E+09	0.000	0.000	813	813	Blackmore et al.
7	CH3 + CH3CH2CH2CH3 = CH3CHCH2CH3 + CH4	1.789E+11	3.808	6.255	300	- 2500	Present Study
		1.708E+12	0.000	10.490	980	- 1060	Yampolskii
		3.648E+11	0.000	9.307	399	- 434	Sway
8	CH3 + CH(CH3)3 = C(CH3)3 + CH4	1.361E+11	3.498	5.042	300	- 2500	Present Study
		3.240E+12	0.000	12.896	770	- 885	Konar et al.
		1.660E+12	0.000	11.405	903	- 1070	Yampolskii et al.
		1.349E+11	0.000	8.031	399	- 434	Sway
		2.170E+10	3.460	4.590	300	- 2500	Tsang
		1.410E+11	0.000	8.067	300	- 855	Zhang et al.

#	Reaction	A	n	Ea	T low		T high	Reference
9	CH3(CH2)3CH3 + H = H2 + CH3CHCH2CH2CH3	1.449E+13	2.630	4.309	300	-	2500	Present Study
		1.960E+14	0.000	7.948	753	-	773	Baldwin et al.
10	CH3(CH2)3CH3 + H = H2 + CH3CH2CHCH2CH3	1.511E+13	2.630	4.232	300	-	2500	Present Study
		9.790E+13	0.000	7.948	753	-	773	Baldwin et al.
11	CH3CH2CH(CH3)2 + H = H2 + CH3CHCH(CH3)2	1.559E+13	2.263	4.641	300	-	2500	Present Study
		9.790E+13	0.000	7.948	753	-	773	Baldwin et al.
12	CH3CH2CH(CH3)2 + H = H2 + CH3CH2C(CH3)2	1.822E+13	1.974	2.869	300	-	2500	Present Study
		5.110E+13	0.000	6.021	753	-	773	Baldwin et al.
13	cyC3H6 + H = H2 + cyC3H5	8.503E+13	2.097	10.824	300	-	2500	Present Study
		1.620E+14	0.000	11.703	358	-	550	Marshall et al.
		3.981E+13	0.000	11.592	628	-	729	Marshall et al.
14	cyCH2CH2O + H = H2 + cyCHCH2O	1.467E+13	2.430	8.478	300	-	2500	Present Study
		2.000E+13	0.000	8.306	830	-	1200	Lifshitz et al.
		8.000E+13	0.000	9.677	297	-	753	Baldwin et al.
15	CH(CH3)3 + CH2OH = CH3OH + C(CH3)3	2.349E+10	4.075	7.428	300	-	2500	Present Study
		2.297E+10	2.760	10.789	300	-	2500	Tsang
16	CH3CH2CH3 + CH2OH = CH3OH + CH3CHCH3	6.482E+10	4.319	9.349	300	-	2500	Present Study
		4.263E+10	2.950	11.988	300	-	2500	Tsang
17	C3H6 + C2H5 = C2H6 + aC3H5	5.427E+10	4.408	5.026	300	-	2500	Present Study
		6.920E+10	0.000	5.186	490	-	510	Löser et al.
		7.061E+10	3.500	6.637	300	-	2500	Tsang
18	C3H6 + iC3H7 = C3H8 + aC3H5	2.096E+10	4.710	4.558	300	-	2500	Present Study
		5.010E+09	0.000	7.650	494	-	580	Szirovicza et al.
		6.619E+10	4.000	8.067	300	-	2500	Tsang
		7.943E+10	0.000	4.708	490	-	510	Löser et al.
19	C3H6 + tC4H9 = iC4H10 + aC3H5	3.963E+09	4.959	3.643	300	-	2500	Present Study
		1.508E+10	4.900	7.948	300	-	2500	Tsang
20	C2H3 + C2H6 = C2H5 + C2H4	1.806E+11	3.870	2.973	300	-	2500	Present Study
		1.500E+13	0.000	9.995	1200	-	1700	Hidaka et al.
		4.848E+12	3.300	10.491	300	-	2500	Tsang et al.
		1.120E+11	0.000	4.809	480	-	520	Scherzer et al.

21	C2H3 + CH(CH3)3 = C(CH3)3 + C2H4	2.210E+11	2.939	1.676	300	-	2500	Present Study
		3.010E+10	0.000	0.000	600		600	Slagle et al. upper bound
		2.170E+10	3.460	2.603	300	-	2500	Tsang
22	C2H3 + CH(CH3)3 = CH2CH(CH3)2 + C2H4	4.060E+11	3.840	3.995	300	-	2500	Present Study
		1.212E+11	3.650	5.166	300	-	2500	Tsang
23	CH(CH3)3 + C2H5 = C2H6 + CH2CH(CH3)2	8.253E+10	4.398	9.185	300	-	2500	Present Study
		1.237E+11	3.650	9.140	300	-	2500	Tsang
24	CH(CH3)3 + CH2CH2CH3 = CH3CH2CH3 + CH2CH(CH3)2	1.009E+11	4.451	9.054	300	-	2500	Present Study
		1.237E+11	3.650	9.140	300	-	2500	Tsang
25	CH(CH3)3 + CH2(CH2)2CH3 = CH3(CH2)2CH3 + CH2CH(CH3)2	1.302E+11	4.386	9.311	300	-	2500	Present Study
26	C6H5OH + H = H2 + C6H5O	3.916E+12	2.124	7.077	300	-	2500	Present Study
		1.150E+14	0.000	12.399	1000	-	1150	He et al.
		1.150E+14	0.000	12.399	1000	-	1150	Baulch et al.
27	HOC(CH3)3 + H = H2 + OC(CH3)3	4.341E+13	2.535	8.008	300	-	2500	Present Study
		1.690E+13	0.000	5.305	843	-	963	Oganesyan et al.
28	CH2O + aC3H5 = C3H6 + HCO	2.094E+11	4.600	11.393	300	-	2500	Present Study
		6.335E+13	1.900	18.181	300	-	2500	Tsang
29	CH2O + CH3OO = CH3OOH + HCO	1.369E+11	4.371	6.512	300	-	2500	Present Study
		1.200E+06	0.000	0.000	410		410	Selby et al.
		1.990E+12	0.000	11.664	300	-	2500	Tsang et al.
30	CH2O + nC3H7 = C3H8 + HCO	1.543E+11	4.118	4.378	300	-	2500	Present Study
		1.000E+11	0.000	7.789	333	-	363	Knoll et al.
		1.510E+12	2.900	5.862	300	-	2500	Tsang
	C3H7CHO + nC3H7 = C3H8 + C3H7CO	1.995E+11	0.000	6.700	464	-	573	Kerr et al.
		1.000E+11	0.000	6.600	273	-	529	Forgeteg et al.
31	CH2O + C2H3 = C2H4 + HCO	5.276E+11	2.828	1.610	300	-	2500	Present Study
		1.459E+12	2.810	5.862	300	-	2500	Tsang et al.
		1.740E+11	0.000	4.133	480	-	520	Scherzer et al.
		3.161E+11	4.210	1.620	300	-	2500	Zhang et al.
32	CH2O + OC(CH3)3 = HOC(CH3)3 + HCO	7.522E+10	2.985	-0.629	300	-	2500	Present Study
		7.079E+12	0.000	4.613	399	-	434	Al Akeel et al.

33	C2H5OC2H5 + C2H5OCH2CH2 = C2H5OC2H5 + C2H5OCHCH3	6.890E+10	4.778	3.941	300	-	2500	Present Study
		2.510E+12	0.000	12.896	763	-	798	Foucaut et al.
34	C2H5OC2H5 + H = H2 + C2H5OCHCH3	1.180E+13	2.341	3.101	300	-	2500	Present Study
		7.400E+12	0.000	3.239	250	-	620	Faubel et al.
35	C2H5OC2H5 + H = H2 + C2H5OCH2CH2	2.556E+13	2.348	8.427	300	-	2500	Present Study
36	C2H5OH + CH3 = CH4 + CH3CHOH	1.475E+11	3.828	5.753	300	-	2500	Present Study
		1.600E+06	0.000	0.000	423		423	Bansal et al.
		3.980E+11	0.000	9.697	403	-	523	Gray et al.
		3.448E+08	18.510	-9.408	300	-	600	Xu et al.
		2.568E+11	3.370	7.634	600	-	3000	Xu et al.
37	C2H5OH + H = H2 + CH3CHOH	1.146E+13	2.345	3.717	300	-	2500	Present Study
		1.300E+10	0.000	0.000	423		423	Bansal et al.
		4.400E+12	0.000	4.570	295	-	700	Aders et al.
		6.964E+12	2.530	3.420	300	-	3000	Park et al.
38	iC4H10 + OC(CH3)3 = HOC(CH3)3 + iC4H9	1.116E+11	3.763	1.241	300	-	2500	Present Study
		1.040E+11	0.000	6.219	283	-	343	Brokenshire et al.
	neo-C5H12 + OC(CH3)3 = HOC(CH3)3 + CH2C(CH3)3	1.605E+13	0.000	7.750	399	-	434	Sway et al.
39	iC4H9OOH + CH3O = CH3OH + iC4H9OO	5.810E+10	2.223	0.829	300	-	2500	Present Study
		4.220E+09	0.000	0.000	373		373	Kirsch et al.
40	iC4H9OOH + CH3 = CH4 + iC4H9OO	7.565E+10	3.154	1.369	300	-	2500	Present Study
		6.810E+16	0.000	17.048	501	-	528	Mulder et al.
41	CH3C(=O)OCH3 + CH3 = CH4 + CH3C(=O)OCH2	3.073E+10	4.745	6.870	300	-	2500	Present Study
		1.580E+11	0.000	11.902	393	-	553	Ferguson et al.
		2.750E+11	0.000	11.227	389	-	497	Arthur et al.
42	CH3C(=O)OCH3 + CH3 = CH4 + CH2C(=O)OCH3	3.733E+10	4.157	6.418	300	-	2500	Present Study
		2.000E+11	0.000	9.856	393	-	553	Ferguson et al.
		1.480E+11	0.000	10.253	389	-	497	Arthur et al.
		1.620E+11	0.000	10.253	386	-	505	Arthur et al.
43	C6H5C2H5 + HO2 = H2O2 + C6H5CHCH3	2.004E+10	5.141	6.242	300	-	2500	Present Study
		2.650E+11	0.000	11.286	600	-	1000	Baulch et al.
		1.650E+08	0.000	0.000	773		773	Scott et al.

44	C6H5C2H5 + H = H2 + C6H5CHCH3	1.037E+13	2.368	4.002	300	-	2500	Present Study
		3.160E+13	0.000	5.007	773	-	1020	Ebert et al.
		2.510E+12	5.500	0.334	1250	-	1680	Müller-Markgraf et al.
		1.450E+12	0.000	0.000	773		773	Baulch et al.
		6.100E+11	0.000	0.000	773		773	Ellis et al.
		3.300E+13	2.000	5.345	500	-	1500	Ellis et al.
45	C6H5C2H5 + H = H2 + C6H5CH2CH2	1.520E+13	2.438	8.633	300	-	2500	Present Study
		2.277E+13	1.500	7.410	500	-	1500	Ellis et al.
		1.250E+11	0.000	0.000	773		773	Ellis et al.
46	C6H5OCH3 + CH3 = CH4 + C6H5OCH2	5.048E+10	4.251	6.253	300	-	2500	Present Study
		5.010E+11	0.000	10.491	453	-	539	Mulcahy et al.
47	p-CH3C6H4CH3 + H = H2 + p-CH2C6H4CH3	8.853E+12	2.782	5.084	300	-	2500	Present Study
		3.980E+14	0.000	8.365	1000	-	1800	Hippler et al.
48	C6H5CH3 + aC3H5 = C3H6 + C6H5CH2	1.284E+10	5.019	12.952	300	-	2500	Present Study
		2.820E+11	0.000	17.207	850	-	950	Akers et al.
		1.000E+11	0.000	15.995	653	-	784	Louw
		3.980E+12	0.000	17.203	850	-	950	Throssell
49	C6H5OH + cyC5H5 = cyC5H6 + C6H5O	1.508E+10	4.647	9.771	300	-	2500	Present Study
		2.670E+14	0.000	25.235	1060	-	1160	Lovell et al.
50	C2H5OCHO + C2H5 = C2H6 + C2H5OCO	2.919E+10	3.855	6.561	300	-	2500	Present Study
		7.940E+10	0.000	7.789	370	-	521	Thynne
51	C2H5OCHO + CH3 = CH4 + C2H5OCO	1.072E+11	3.994	5.930	300	-	2500	Present Study
		3.160E+10	0.000	8.210	370	-	521	Thynne
	CH3OCHO + CH3 = CH4 + CH3OCHO	7.940E+10	0.000	9.000	382	-	510	Thynne
		5.010E+11	0.000	10.290	400	-	519	Donovan et al.
		5.983E+11	3.320	10.010	298	-	2500	Good et al.
52	cyC6H12 + CH3 = CH4 + cyC6H11	3.043E+11	3.977	6.150	300	-	2500	Present Study
		8.510E+11	0.000	8.862	373	-	473	Al-Niami et al.
		1.350E+12	0.000	9.538	399	-	434	Sway
53	cyC6H10 + C2H5 = C2H6 + cyCHCHCHCH2CH2CH2	9.341E+10	3.843	3.559	300	-	2500	Present Study
		1.108E+12	0.000	9.200	298	-	500	James et al.

54	C3H6 + CH3O = CH3OH + aC3H5	8.283E+11	2.878	2.278	300	-	2500	Present Study
		6.367E+10	2.950	11.982	300	-	2500	Tsang (reported)
		2.175E+11	0.000	4.570	300	-	2500	Tsang (intended)
	H2 + CH3O = CH3OH + H	1.260E+11	4.000	4.910	300	-	2000	Jodkowski et al.
	CH4 + CH3O = CH3OH + CH3	6.200E+11	5.000	5.580	300	-	2000	Jodkowski et al.

4.2.1 CH3O + CH(CH3)3 = C(CH3)3 + CH3OH

4.2.2 CH3O + (CH3)2CHCH(CH3)2 = (CH3)2CCH(CH3)2 + CH3OH
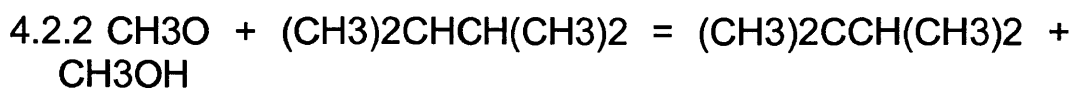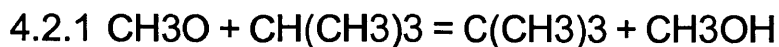
The abstraction from a tertiary carbon of 2-methylpropane and 2,3-dimethylbutane by methoxy radical was investigated. The two rate coefficients calculated in this study are within a factor of 2.5 of each other over the temperature range 300 – 2500 K, with the reaction involving 2-methylpropane computed to be the faster of the two reactions despite having half as many tertiary C-H's.

Bercés and Trotman-Dickenson [76] report kinetics over the temperature range 463.5 – 533 K H abstraction from the tertiary carbon of 2-methylpropane by methoxy; the reported expression was $\log_{10}(k\,/\,cm^3\,mol^{-1}\,s^{-1}) = 11.30 \pm 0.24 - (4100 \pm 600\ cal\ mol^{-1})/2.3RT$ where the uncertainties correspond to one standard deviation. The reported value was obtained using a seven-step mechanism for 2-methylpropane decomposition in the presence of dimethyl peroxide and di-tert-butyl peroxide, the measured flow rates of 2-methylpropane, ethane, and dimethyl ether, and literature values for the kinetics of methyl self-recombination, methyl recombination with methoxy radical, and methyl abstracting from the tertiary carbon of 2-methylpropane. The mechanism does not contain any decomposition channels for tert-butyl radical, nor does it propose formation of the iso-butyl radical. This number was revised by Kerr and Moss [77], noting an overestimate of 0.3 in the previously-reported $\log_{10}A$. In a review by Tsang [78], the value reported assumes the kinetics reported by Kerr and Moss for H abstraction from 2-methylpropane by methoxy to be the total H abstraction rate coefficient. Tsang then utilizes the kinetics of H abstraction from 2,2-dimethylpropane by methoxy [79] to isolate the abstraction from primary carbons, thereby estimating the kinetics for the abstraction from tertiary carbons. Tsang recommends an uncertainty of ten in the rate coefficient over the temperature range 300 – 1500 K. Batt and Rattray [80] report the total rate coefficient of methoxy radical abstracting from 2-methylpropane over the temperature range 383 – 423 K. The reported value, $\log_{10}(k\,/\,cm^3\,mol^{-1}\,s^{-1}) =$

60

$11.6 \pm 0.6 - (2.4 \pm 1.1 \text{ kcal mol}^{-1})/2.3RT$, comes from the thesis of G. N. Robinson. This rate coefficient was determined from a competitive study of methoxy radical reacting with 2-methylpropane and molecular oxygen. Their reported rate coefficient for $CH_3O + O_2 = HO_2 + CH_2O$ is consistent with the evaluated rate coefficient of Atkinson et al. [81]; the value reported by Batt and Rattray is larger by only 5 – 40% over the temperature range 383 – 423 K.

Our calculation is in good agreement (a factor of two) with the value reported by Batt and Rattray, Figure 4-1. Our k(T) is significantly larger (greater than a factor of 10) than those of Kerr and Moss, and so also of Tsang's value based on Kerr and Moss.

Normally, Arrhenius A factors for hydrogen transfers between polyatomics are approximately $3 \times 10^{11} \text{ cm}^3 \text{ mol}^{-1} \text{ s}^{-1}$, while A factors for H-abstractions by a diatomic are slightly higher. Tsang's recommendation extrapolates to an unusually small H-abstraction rate coefficient at high temperature, while our calculation gives an unexpectedly high rate coefficient at high temperature, comparable to Tully et al.'s measured rate coefficient for H abstraction from the tertiary carbon of 2-methylpropane by OH [82]. It is not obvious why our calculations would overestimate the A factor; however, we note that the independent hindered rotor approximation may be inaccurate, and also that methoxy radical is a Jahn-Teller molecule, so the simple RRHO approximation may be inaccurate as well.

The only kinetics reported for methoxy radical abstracting from the tertiary carbons of 2,3-dimethylbutane is from Alcock and Mile [83]. This value is cited within the paper as a "literature value," though no reference is cited. Searching the literature for kinetics of 2,3-dimethylbutane + RO reactions was unsuccessful. The rate coefficient of H abstraction from the tertiary carbon of 2-methylpropane by methoxy as reported by Bercés and Trotman-Dickenson, the only source at the time of Alcock and Mile's publication, is a factor of two larger than the estimate reported by Alcock and Mile.

Neither the experiments nor the calculations are compelling. It appears safe to assume the true rate coefficient lies between Tsang's estimate and our calculation. In the absence of more information, we recommend our calculations, with an uncertainty of 10.
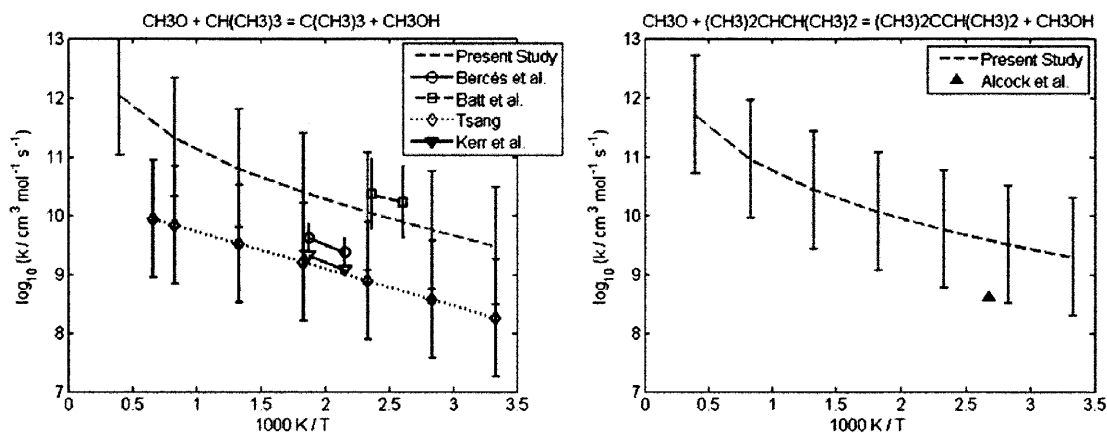
Figure 4-1: Rate coefficient for abstraction from the tertiary carbon of 2-methylpropane (left) and 2,3-dimethylbutane (right) by methoxy radical.

Methyl + Primary C-H

$$4.2.3 \quad CH(CH3)3 + CH3 = CH4 + CH2CH(CH3)2$$

$$4.2.4 \quad CH3(CH2)2CH3 + CH3 = CH4 + CH2(CH2)2CH3$$

$$4.2.5 \quad CH3(CH2)3CH3 + CH3 = CH4 + CH2(CH2)3CH3$$

$$4.2.6 \quad CH3(CH2)6CH3 + CH3 = CH4 + CH2(CH2)6CH3$$
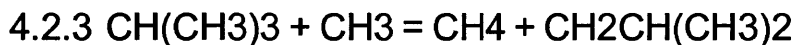
The H abstraction from the primary carbons of 2-methylpropane, n-butane, n-pentane, and n-octane by methyl radical was investigated. Over the temperature range 300 – 2500 K, the four computed rate coefficients agree with one another to within a factor of 2.5; the abstraction from n-octane has the largest computed rate coefficient and abstraction from 2-methylpropane has the smallest.

Konar et al. [84] measured the rate coefficient for H abstraction from the primary carbons of 2-methylpropane by methyl over the temperature range 770 – 855 K. The value was determined from fitting parameters in their proposed reaction

mechanism to their experimental data on the pyrolysis of 2-methylpropane. Tsang recommended the rate coefficient [78] to be equal to 1.5 times the rate coefficient of H abstraction from a primary carbon of propane by methyl [85]. Zhang and Back recommend a rate coefficient over the temperature range 300 – 855 K [86]. Their reported value is based on the current literature's (at that time, 1990) value for the total abstraction rate, the experimental branching ratio between tertiary and primary hydrogen abstraction as reported by Jackson et al. [87] and Konar et al. [84], and the (then) recent measurements of Ahonkhai et al. on the branching ratio of H abstraction from ethylene by methyl relative to H abstraction from 2-methylpropane by methyl [88]. Goos et al. report a rate coefficient for this reaction from 800 – 950 K, based on 2-methylpropane pyrolysis experiments utilizing CO_2-laser induced heating [89]; it should be noted that the expression reported by the NIST Chemical Kinetics Database for the kinetics from Goos et al. is for abstraction from the tertiary carbon, not the primary carbons. The value reported by Goos et al. uses the form of the rate coefficient reported by Tsang, with the temperature-independent pre-exponential factor increased by a factor 3.97 to match the measured speciation data. It should be noted that the rate coefficient reported by Goos et al. is a factor of four greater than the other three rate coefficients mentioned here from 800 – 950 K; the other values are within 20% of each other over this temperature range.

Our calculations are in good agreement with the estimates of Konar et al., Tsang, and Zhang and Back, see Figure 4-2; our calculations are a factor four slower than those of Goos et al. One may ask how this reaction failed the check discussed in Section 4.1. One reason is due to the error in the NIST Database for the Goos et al. rate coefficient, as this error was propagated to the PrIMe Warehouse. Another reason is the extrapolated k(T) value for each kinetics expression at T = 300 K: ignoring the incorrect Goos et al. expression, there is a difference of nearly three orders of magnitude between the evaluated Konar et al. and Tsang k(T) expressions.

Figure 4-2: Rate coefficient for H abstraction from the primary carbon of 2-methylpropane by methyl radical.

Yampolskii reports the rate coefficient for H abstraction from the primary carbons of n-butane by methyl over the temperature range 980-1060 K [90]; he assumed the rate coefficient is equal to the rate coefficient of H abstraction from the primary carbons of ethane by methyl [91]. It should be noted that the expression reported by the NIST Chemical Kinetics Database is the per-H rate coefficient, not the total. We recommend our calculation for H abstraction from the primary carbons of n-butane by methyl, which is in good agreement with the value reported by Yampolskii, Figure 4-3, since they give k(T) over a broader temperature range.

Blackmore and Hinshelwood report the rate coefficient for H abstraction from the primary carbons of n-pentane and n-octane by methyl at 813 K [92]. The rate coefficients were determined by fitting the parameters of a reaction mechanism to the experimental pyrolysis data; the concentration of each respective hydrocarbon

was measured in the presence and absence of nitric oxide. Our calculations for H abstraction from the primary carbons of n-pentane and n-octane by methyl are in good agreement with the Blackmore and Hinshelwood estimates, Figure 4-3. We recommend use of our k(T), which cover a broad temperature range.

Overall, there is excellent agreement on CH_3 + alkanes = R + CH_4. The experimental data is mostly consistent, and our quantum calculations closely agree with the experimental consensus. We estimate the uncertainty in the calculated k(T) for reactions 3-6 reported here to be a factor of three.
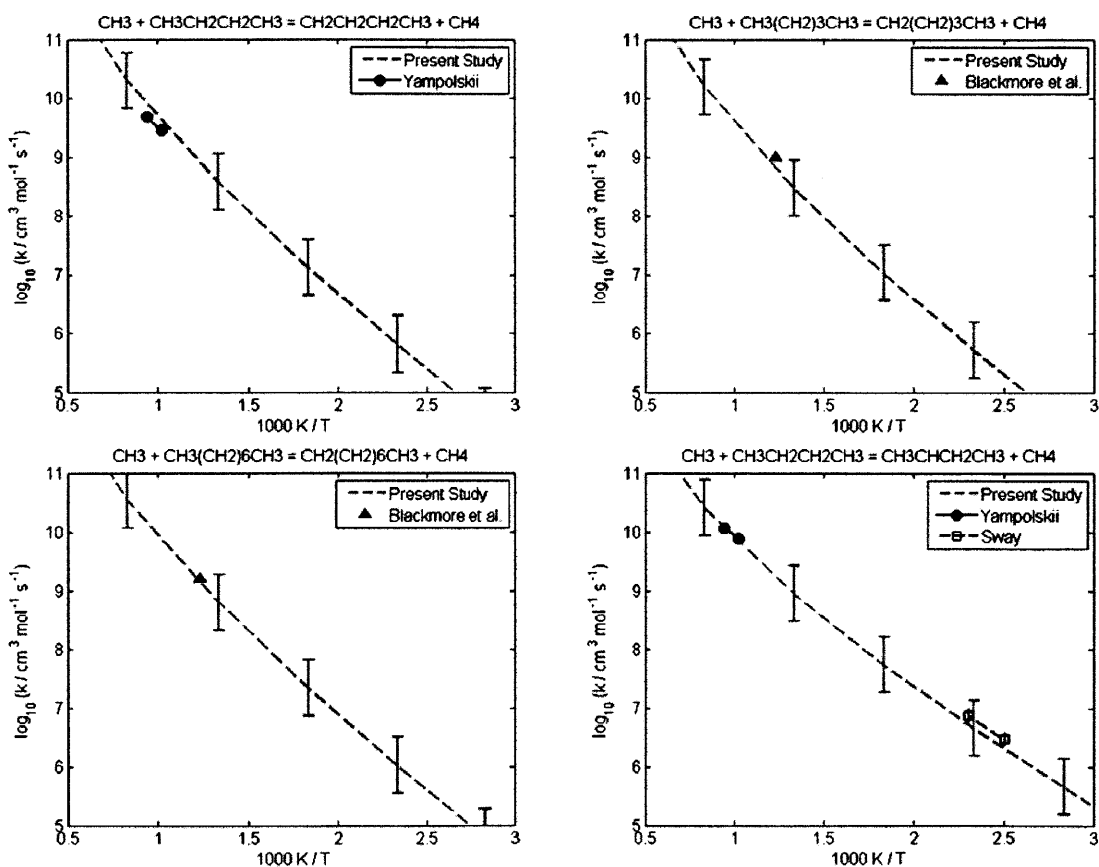
Figure 4-3: Rate coefficient for the abstraction from the primary carbons of n-butane (top-left), n-pentane (top-right), and n-octane (bottom-left), and from the secondary carbons of n-butane (bottom-right) by methyl radical.

Methyl + Secondary C-H

4.2.7 CH3CH2CH2CH3 + CH3 = CH4 + CH3CHCH2CH3

The abstraction from the primary carbons of n-butane by methyl radical was discussed in Sections 4.2.4. This section extends the previous discussion to include abstraction from secondary (n-butane) carbons by methyl radical.

Yampolskii reports the rate coefficient for H abstraction from the secondary carbons of n-butane by methyl over the temperature range 980-1060 K [90]; the rate coefficient is calculated by subtracting the estimated rate coefficient of abstraction from the primary carbons from the total measured butane abstraction rate coefficient. It should be noted that the expression reported by the NIST Chemical Kinetics Database is the per-H rate coefficient, not the total. Sway estimated the kinetics between 399 and 434 K by fitting parameters to a proposed butane decomposition mechanism [93]; di-tert-butyl ether was the source of methyl radicals, and the rate coefficient was in reference to the kinetics of methyl recombination. The reported per-H rate coefficient is $\log_{10}(k\ /\ cm^3\ mol^{-1}\ s^{-1}) = 10.96 \pm 0.10 - (38.94 \pm 1.20\ kJ\ mol^{-1}\ /\ 2.3RT)$. It should be noted that the expression reported by the NIST Chemical Kinetics Database is the total abstraction from n-butane by methyl radical.

We recommend our calculation for H abstraction from the secondary carbons of n-butane by methyl, which is in good agreement with all available data, Figure 4-3. The estimated uncertainty is a factor of three.

Methyl + Tertiary C-H

4.2.8 CH(CH3)3 + CH3 = CH4 + C(CH3)3

Konar et al. [84] measured the rate coefficient for H abstraction from the tertiary carbon of 2-methylpropane by methyl over the temperature range 770 – 855 K. The value was determined from fitting parameters in their proposed reaction mechanism to their 2-methylpropane pyrolysis experimental data. Tsang evaluated the rate coefficient for this reaction over the temperature range 300 – 2500 K [78]. Tsang assumed the total abstraction rate coefficient to be the value reported by Kerr and Parsonage [94]. The rate coefficient for abstraction from the three primary carbons

66

was assumed to be 1.5 times greater than the rate coefficient for H abstraction from the two primary carbons of propane by methyl [85]; the tertiary rate coefficient was thus the difference between the total and estimated primary rate coefficient, with the constraint that the temperature-dependent pre-exponential factor be equal to the temperature-dependent pre-exponential factor for H abstraction from the secondary carbon of propane by methyl [85]. Zhang and Back report a rate coefficient over the temperature range 300 – 855 K. Their reported value is based on the current literature's (at that time) value for the total abstraction rate, the experimental branching ratio between tertiary and primary hydrogen abstraction as reported by Jackson et al. [87] and Konar et al. [84], and their evaluation of an average total abstraction rate over the temperature range 500 – 855 K. Sway estimated the kinetics between 399 and 434 K by fitting parameters to a proposed 2-methylpropane decomposition mechanism [93]; di-tert-butyl ether was the source of methyl radicals, and the rate coefficient was in reference to the kinetics of methyl recombination. The reported per-H rate coefficient is $\log_{10}(k / cm^3 \, mol^{-1} \, s^{-1}) = 11.13 \pm 0.20 - (33.60 \pm 2.30 \, kJ \, mol^{-1} / 2.3RT)$. It should be noted that the expression reported by the NIST Chemical Kinetics Database is the total abstraction from iso-butane by methyl radical. Yampolskii and Tsikhlinski estimate the total abstraction from 2-methylpropane by methyl radical [95]; it should be noted that the NIST Chemical Kinetics Database assigns their reported rate coefficient as abstraction from the tertiary carbon exclusively. The pyrolysis of 2-methylpropane and 13% D_2 was studied from 903 – 1070 K using the competitive reactions of abstraction from 2-methylpropane by methyl and from D_2 by methyl radical; the concentrations of methane and CH_3D were measured for a reaction time of 0.04 – 0.08 seconds to determine the branching ratio. Assuming a rate coefficient of $10^{-11.79}$ exp(-12300 cal mol^{-1} / RT) cm^3 molecule^{-1} s^{-1} for abstraction of D_2 by methyl yielded their reported rate coefficient.
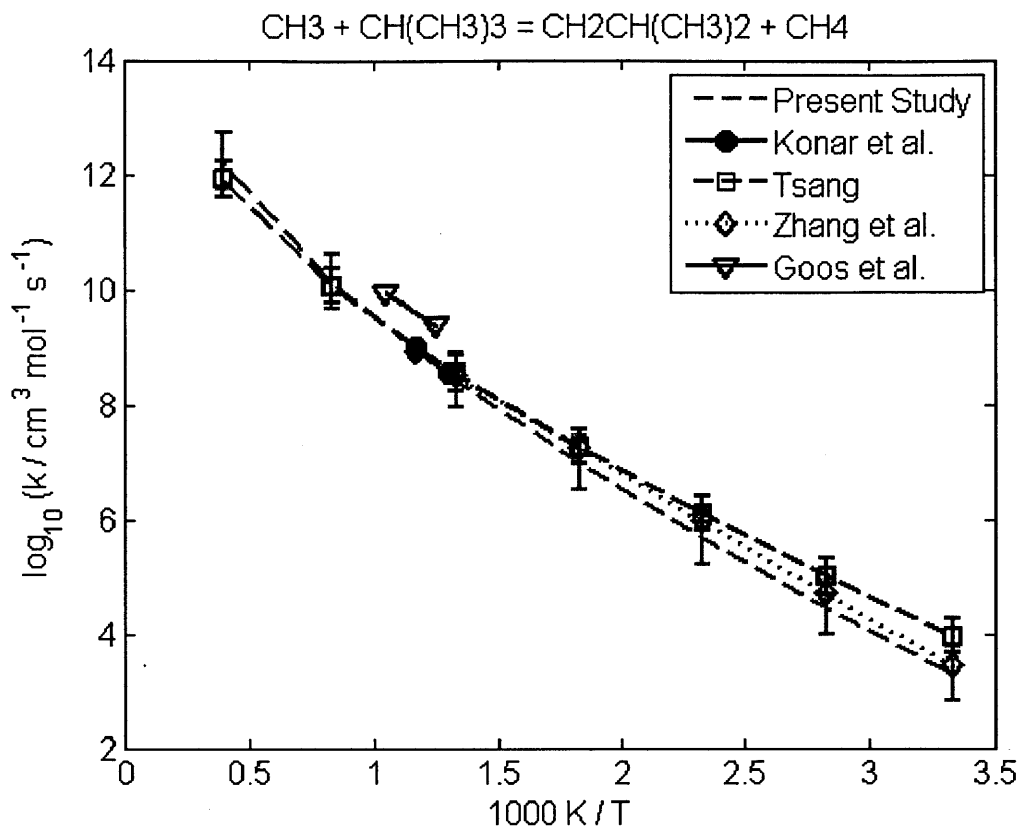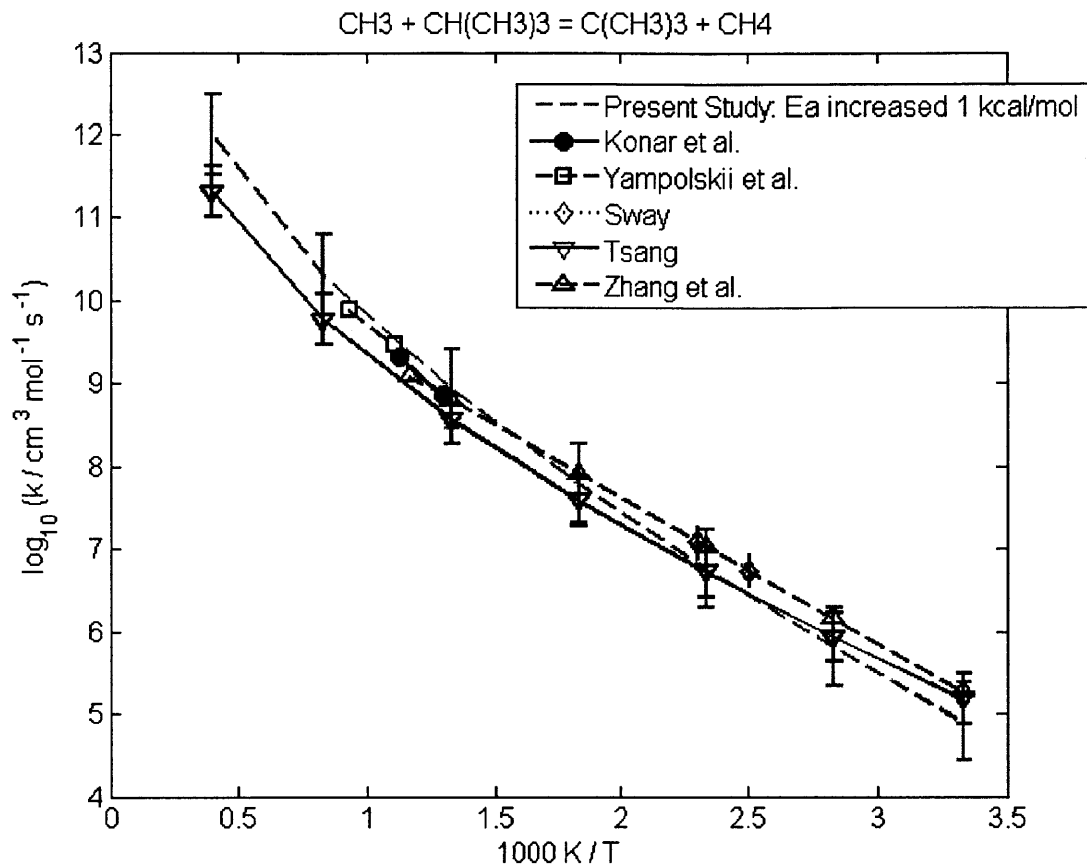
Figure 4-4: Rate coefficient for the abstraction from the tertiary carbon of 2-methylpropane by methyl radical.

Our calculated rate coefficient is in reasonable agreement with the available datasets, being no more than a factor of three larger than any of the non-Tsang recommendations, Figure 4-4; our calculations are no larger than a factor of six of the recommendation of Tsang. Increasing our fitted E_A by 1 kcal mol^{-1} places our calculations in very good agreement with the experiments. Thus, we recommend use of the expression $\log_{10}(k / cm^3 mol^{-1} s^{-1}) = (0.640 \pm 0.477) + 3.498 \log_{10}(T / 1K)$ $- 6.042$ kcal mol^{-1} / 2.3RT.

Comparing our recommended total rate coefficient for H-abstraction of 2-methylpropane by methyl radical, Sections 4.2.3 and 4.2.8, with the recommendations by Zhang and Back [86], Konar et al. [84], Anastasi [96], Marshall and Shahkar [97], Kerr and Parsonage [94], and Yampolskii and

Tsikhlinski [95] show our recommendations to be in very good agreement over the recommendations' respective temperature range.

H + Secondary C-H and H + Tertiary C-H

4.2.9 $CH_3CH_2CH_2CH_2CH_3 + H = H_2 + CH_3CHCH_2CH_2CH_3$

4.2.10 $CH_3CH_2CH_2CH_2CH_3 + H = H_2 + CH_3CH_2CHCH_2CH_3$

4.2.11 $CH_3CH_2CH(CH_3)_2 + H = H_2 + CH_3CHCH(CH_3)_2$

4.2.12 $CH_3CH_2CH(CH_3)_2 + H = H_2 + CH_3CH_2C(CH_3)_2$
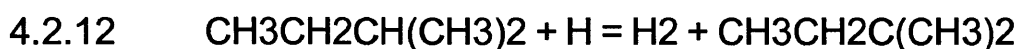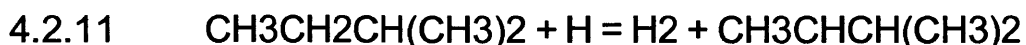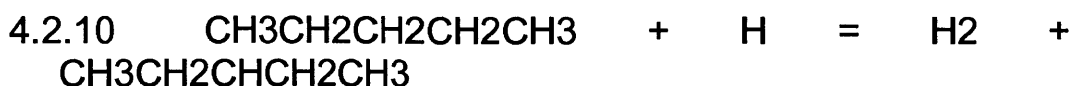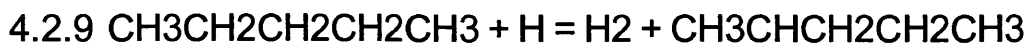
Hydrogen abstraction from the secondary carbons of n-pentane (forming both the 2- and 3-pentyl radical) and 2-methylbutane by H atom are discussed in this section, in addition to the abstraction from the tertiary carbon of 2-methylbutane by H atom. The computed rate coefficients for the secondary C-H are similar across the entire temperature range, differing by no more than a factor of two. The kinetics for abstraction from the tertiary carbon is faster by at least a factor of five at temperatures below 1300 K; the kinetics become comparable to abstraction from secondary carbons at higher temperatures.

Baldwin and Walker have reported Arrhenius parameters for several abstractions from primary, secondary, and tertiary carbons by H atom from 753 – 773 K [98]. We recommend our kinetics calculations for H abstraction from the two distinct secondary carbons from n-pentane by H atom, and from the secondary and tertiary carbons of 2-methylbutane by H atom, which cover a broad temperature range; the uncertainty in the calculations is a factor of three. Our recommendations are in good agreement with the experimental data, Figure 4-5; it is interesting to note that our recommendations for abstraction from secondary carbons are a bit slower than the Baldwin and Walker rules, while our recommendation for abstraction from the tertiary carbon is a bit faster.
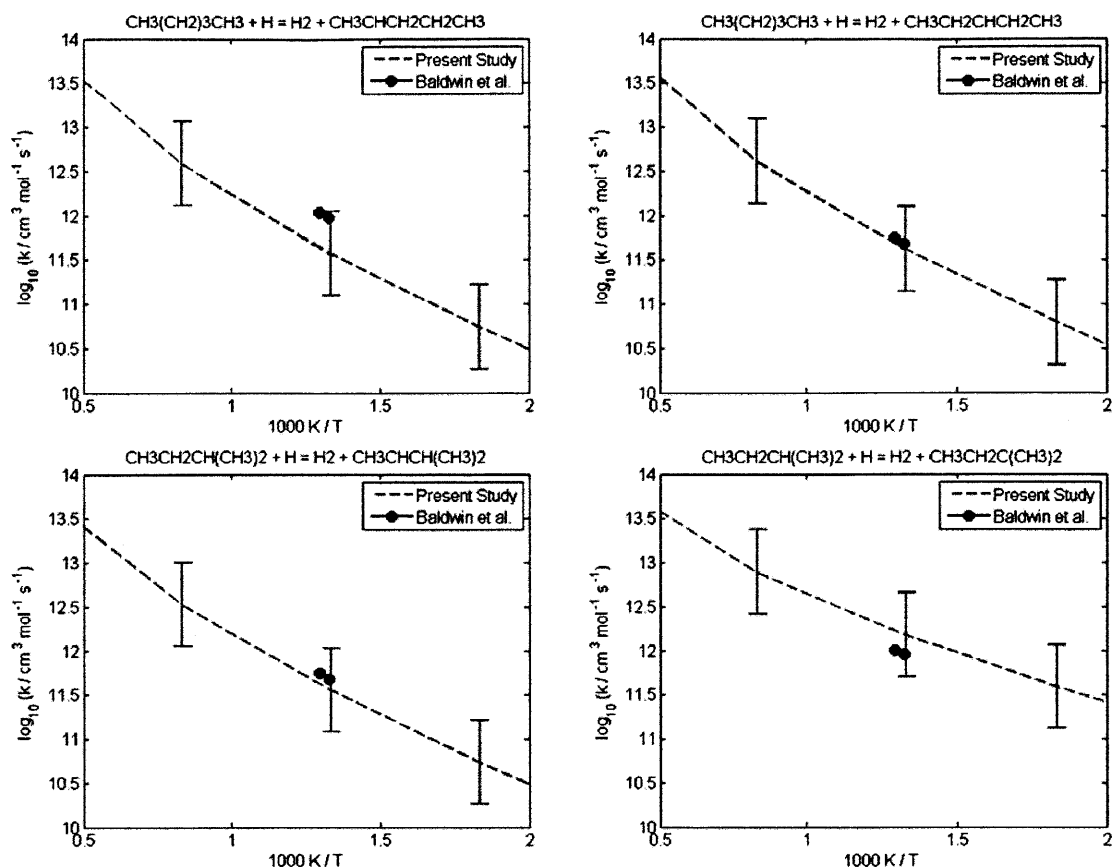
Figure 4-5: Rate coefficient for the abstraction from the secondary carbons of n-pentane forming 2-pentyl (upper-left) and 3-pentyl (upper-right) by H atom, and for the abstraction from the secondary (lower-left) and tertiary (lower-right) carbons of 2-methylbutane by H atom.

H + cyclopropane and H + oxirane

4.2.13 $CYC3H6 + H = H2 + CYC3H5$

4.2.14 $CYCH2CH2O + H = H2 + CYCHCH2O$
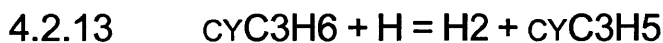
The rate coefficients for these two cyclic species are noticeably smaller than their non-cyclic counterparts, see Sections 4.2.9-4.2.12, by more than an order of magnitude at temperatures below 800 K. The two cyclic rate coefficients are within a factor of two of each other between 500 – 1200 K, with abstraction from cyclopropane predicted by our quantum calculations to be faster than from oxirane at temperatures above 600 K.

Marshall et al. have reported the rate coefficient for the hydrogen abstraction from cyclopropane by H atom over the temperature range 628 – 779 K [99]; the reported

value is $\log_{10}(k / cm^3 mol^{-1} s^{-1}) = 13.6 \pm 1.0 - (48.5 \pm 13.0 kJ mol^{-1} / 2.3RT)$. The experiments were performed in a flow reactor, the H atoms were generated by flowing H_2 through a microwave discharge, and the kinetics were fit to a four reaction kinetic model to match the observed propene to cyclopropane ratio in the outlet. Marshall et al. also report the rate coefficient for this system at lower temperatures, from 358 – 550 K [100]; the reported value is $\log_{10}(k / cm^3 mol^{-1} s^{-1}) = 14.21 \pm 0.13 - (49.0 \pm 1.1 kJ mol^{-1} / 2.3RT)$. These experiments were similar to those performed in Ref. [99], with the difference being the kinetics were fit to an 18 reaction kinetic model to match the measured H atom (with cyclopropane in excess) or methane (with H atom in excess) concentration. The authors note the discrepancy, approximately a factor of three, between their two reported k(T), and place their confidence in the newer measurements. Our computed value, with uncertainty of a factor of three, agrees very well with the higher temperature experimental rate coefficient reported by Marshall et al., and is in reasonable agreement with the lower temperature rate coefficient, Figure 4-6. We recommend use of our k(T), which covers a broad temperature range.

Lifshitz and Ben-Hamou [101] report the rate coefficient for H-abstraction from oxirane by H atom from 830 -1200 K by fitting parameters in a kinetic model to match their experimental measurements of C_2H_6, CH_4, C_2H_4, C_2H_2, C_3H_8, CH_3CHO, and H_2 conducted in a shock tube. The authors note the normalized sensitivity coefficient of the hydrogen atom concentration with respect to the rate coefficient employed is nearly -1. Baldwin et al. report the rate coefficient for temperatures from 297 – 753 K from their studies of oxirane addition to reacting mixtures of H_2 and O_2 [102]; the kinetics, $\log_{10}(k / cm^3 mol^{-1} s^{-1}) = 10.9 \pm 0.2 - (41 \pm 2 kJ mol^{-1} / 2.3RT)$, were obtained by fitting parameters to a kinetic model to match the experimentally-measured oxirane and H_2 concentrations. Our calculated k(T) value is within a factor of two of the value reported by Lifshitz and Ben-Hamou, however it is always at least a factor of five less than the value reported by Baldwin et al., Figure 4-6. We recommend our calculated k(T), with a decrease of 1 kcal mol^{-1} to the fitted activation energy; the uncertainty is a factor of three. This

recommendation is in good agreement with both sets of experiments over their respective valid temperature range.
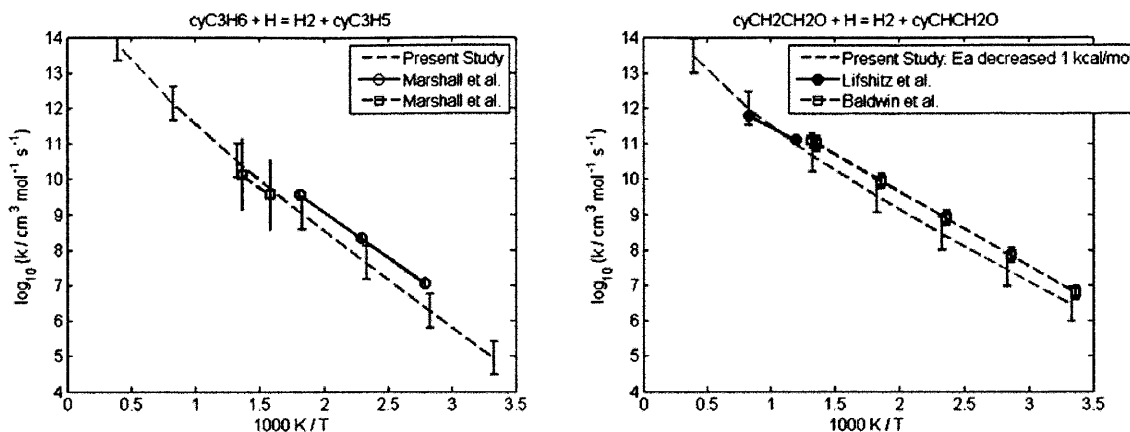
Figure 4-6: Rate coefficient for abstraction of cyclopropane (left) and oxirane (right) by H atom.

CH_2OH + Secondary C-H and CH_2OH + Tertiary C-H

4.2.15 $CH2OH + CH(CH3)3 = C(CH3)3 + CH3OH$

4.2.16 $CH2OH + CH3CH2CH3 = CH3CHCH3 + CH3OH$
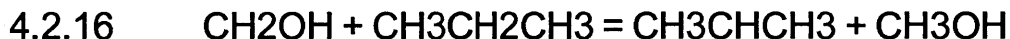
The abstraction from secondary and tertiary carbons by hydroxymethyl radical is discussed in this section. For the reactions explored in this Section, the recommended kinetics are estimated to be within a factor of three of each other over the entire temperature range. There is a cross-over temperature at 900 K at which the kinetics favor the abstraction from secondary carbons over tertiary carbons; at lower temperatures, the weaker C-H bond favors formation of the tertiary radical, however at higher temperatures the reaction path degeneracy of the hydrogens bound to the secondary carbon dominates.

There are no literature measurements of these reactions. Tsang's estimates [78, 85] are based on his estimate of hydroxymethyl radical abstraction from ethane [103]; that estimate is based on Tsang's estimate of methyl abstraction from methanol (through equilibrium). Tsang's estimated A factor for CH_2OH + propane is unexpectedly large.

72
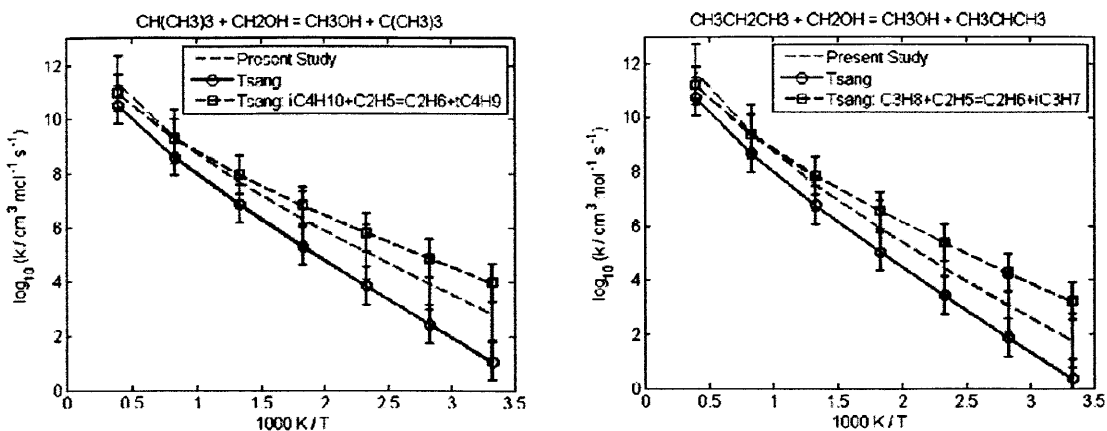
Figure 4-7: Rate coefficient for abstraction from the tertiary carbon of 2-methylpropane (left) and the secondary carbon of propane (right) by hydroxymethyl radical.

Our calculated value, especially at low temperatures, is significantly different from the Tsang estimates, Figure 4-7. This figure also shows Tsang's estimates for H abstraction from the tertiary carbon of 2-methylpropane by ethyl [78] and from the secondary carbon of propane by ethyl [85]. Abstraction by hydroxymethyl and ethyl radical should be similar, with each being a non-linear, two heavy-atom, carbon radical species. For temperatures above 1000 K, our calculations agree very well with these H-atom abstraction estimates by ethyl radical; our calculations are up to an order of magnitude slower at temperatures near 300 K.

In absence of more information, we recommend our calculations which are in general agreement with a chemically-similar system (abstraction by ethyl radical). Since there is no experimental data at all, we suggest an uncertainty of ten.

R• + propene → allyl + R-H

4.2.17   C3H6 + C2H5 = C2H6 + AC3H5

4.2.18   C3H6 + CH3CHCH3 = CH3CH2CH3 + AC3H5

4.2.19   C3H6 + C(CH3)3 = CH(CH3)3 + AC3H5
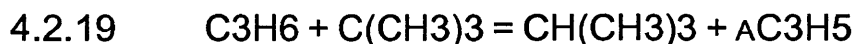
There is very little experimental data on R• + propene → allyl + R-H, but Tsang has provided estimates. Measuring the forward rate is complicated because of the

73

competing pressure-dependent addition reaction. The reverse reactions are endothermic by more than 30 kJ mol^{-1}. Tsang's estimates for all R• + propene → allyl + R-H are based primarily on the experimental data on methyl + propene, measured by Kerr and Parsonage [94] at T = 350 – 600 K.

Tsang assumed ethyl + propene had a 4 kJ mol^{-1} smaller E_A than methyl + propene. Our quantum calculations agree with his estimates within a factor of 2.5, see Figure 4-8. Our quantum chemistry calculations and Tsang's estimates differ by more than an order of magnitude from rate coefficients proposed by Löser et al. using the bond strength-bond length (BSBL) estimation technique [104].

Szirovicza and Márta measured pyrolysis products from a mixture of propene and azoisopropane, and reported the ratio of iso-propyl radical abstracting the allylic hydrogen of propene to iso-propyl radical recombination by fitting the parameters of a reaction mechanism to their dataset [105]. Employing the high-p limit of $10^{12.5}$ cm^3 mol^{-1} s^{-1} reported by Golden et al. [106] for iso-propyl radical recombination yielded their recommended value; the high-pressure limit employed is in good agreement with recent calculations by Klippenstein et al. [107] Szirovicza and Márta's stated uncertainty in $\log_{10}k$ of ± 0.7 corresponds to one standard deviation from the mean. Tsang's estimate for iso-propyl + propene [108] is based on his estimate for ethyl + propene, but adjusted to match Szirovicza and Márta's value. Tsang notes in his recommendation that the experimental data of Szirovicza and Márta are widely scattered about the best-fit line. Our computed k(T) closely agrees with the Tsang estimate at temperatures greater than 400 K, Figure 4-8, but disagrees by more than an order of magnitude at lower temperatures. We believes Tsang's estimate is skewed because he forced his expression to match the data of Szirovicza and Márta. Our estimate is faster than the data of Szirovicza and Márta, however, our uncertainty range overlaps with theirs and the two are therefore not statistically different. Once again, both our calculation and Tsang's estimate is more than an order of magnitude slower than the BSBL estimate of Löser et al. [104] We

recommend use of our expression for k(T), though due to the paucity of experimental data our recommendation could be uncertain by an order of magnitude.

Tsang estimates the kinetics of tert-butyl radical abstracting the allylic hydrogen of propene through equilibrium [108]. The reverse rate coefficient is based on the kinetics of allyl abstracting from the secondary carbon of propane; the temperature-independent pre-exponential factor is divided by two to account for the difference in reaction path degeneracy and the activation energy is decreased by 5 kJ mol^{-1}. At temperatures greater than 500 K, our estimate is in good agreement with Tsang's estimate, Figure 4-8. At lower temperatures, we predict a much higher rate coefficient, since our estimate of E_A is 4 kcal mol^{-1} lower than Tsang's estimate. We believe this discrepancy can be resolved by utilizing Tsang's recommendation for H-abstraction from the tertiary carbon of iso-butane by allyl radical with the thermochemistry from the Third Millennium Thermodynamic Database for Combustion and Air-Pollution Use with updates from Active Thermochemical Tables (ATcT) [109]; the estimated rate coefficient for propene + tert-butyl radical is now $\log_{10}(k / cm^3 \ mol^{-1} \ s^{-1}) = -6.13 + 5.36 \log_{10}(T / K) - 4.93 \ kcal \ mol^{-1} / 2.3RT$, which is in good agreement with our calculation over the entire temperature range, Figure 4-8. Thus, we recommend use of our k(T); in the absence of experimental data, we recommend an uncertainty of a factor of ten.
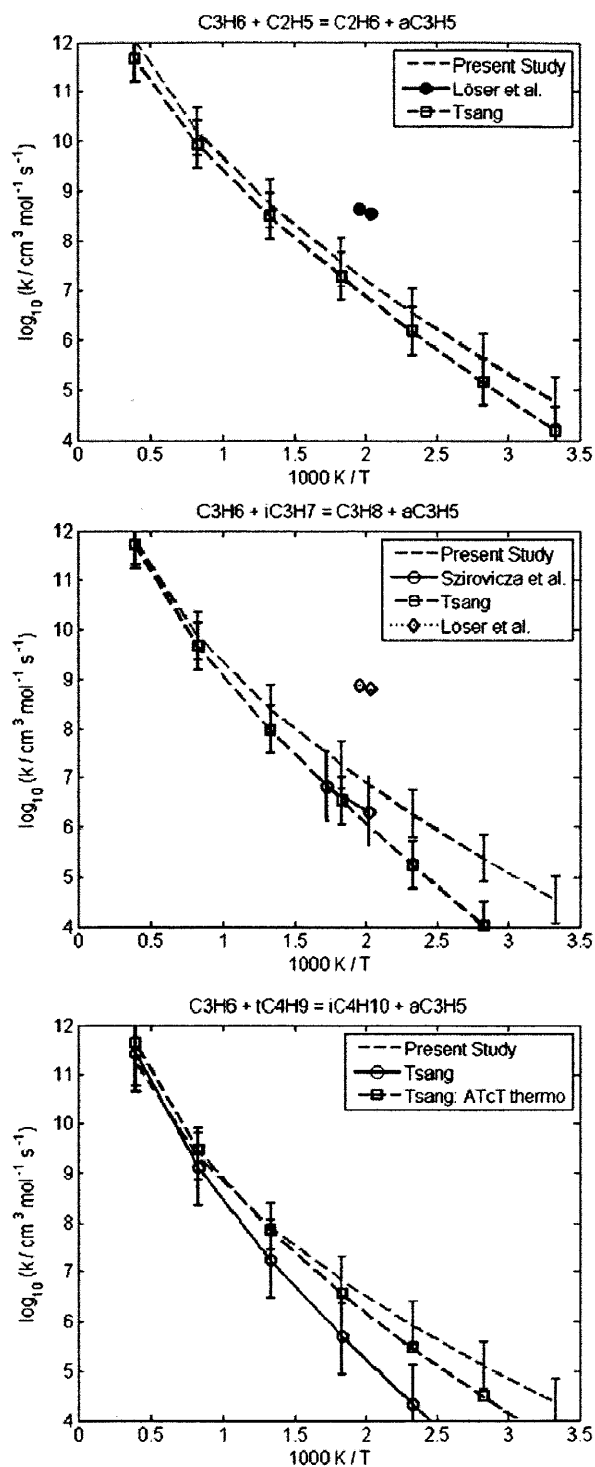
Figure 4-8: Rate coefficient for the abstraction from the allylic carbon of propene by ethyl (top), iso-propyl (middle), and tert-butyl (bottom) radical.

For the reported rate coefficients, the temperature trends are similar, with the order being abstraction by tertiary, secondary, and primary, in ascending order. At

temperatures above 700 K, the abstraction by primary is two and six times faster than abstraction by secondary and tertiary radical, respectively.

One interesting note: the Tsang recommendation for allyl radical abstracting from a tertiary carbon (2-methylpropane) is based on his recommendation for allyl radical abstraction from a secondary carbon (propane), which is based on his recommendation for allyl radical abstraction from a primary carbon (ethane), which itself is based on his recommendation for allyl radical abstraction from methane; even the kinetics of allyl abstracting from methane was not known exactly, introducing more uncertainty in the rate coefficient estimation. This statement is made to show how necessary it is to have kinetics of small molecules for each system explored, e.g. hydrocarbons, alcohols, esters, etc.; if the initial allyl abstracting hydrogen from methane was incorrect, it could propagate to the general rule for allyl radical abstracting from any hydrocarbon.

Vinyl + Primary and Tertiary C-H

4.2.20	$C_2H_3 + C_2H_6 = C_2H_5 + C_2H_4$
4.2.21	$C_2H_3 + CH(CH_3)_3 = CH_2CH(CH_3)_2 + C_2H_4$
4.2.22	$C_2H_3 + CH(CH_3)_3 = C(CH_3)_3 + C_2H_4$
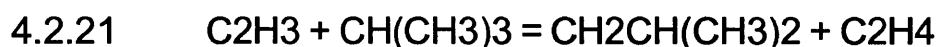
This section discusses the kinetics of H abstraction from primary (ethane and 2-methylpropane) and tertiary (2-methylpropane) carbons by vinyl radical.

Hidaka et al. measured the rate coefficient for H abstraction from ethane by vinyl over the temperature range 1200 – 1700 K by fitting parameters in their proposed reaction mechanism for ethane decomposition to their shock tube experimental data [110]. Tsang and Hampson estimate this rate coefficient through equilibrium [111]; the reverse rate coefficient is based on the expression reported by Halstead and Quinn [112], who fitted the parameters of a kinetic model for ethylene pyrolysis to the experimentally-measured 1-butene and ethane concentrations. Scherzer et al. estimated the kinetics using the BSBL method [113]. Each of these evaluations

yields very different kinetics over the temperature range 300 – 2500 K. We recommend the kinetics calculated in this study, which is in reasonable agreement with the measurements of Hidaka et al. and the calculations of Scherzer et al., Figure 4-9; our estimate is in good agreement with the recommendation of Tsang and Hampson at temperatures above 500 K. We believe the discrepancy between our calculation and the recommendation of Tsang and Hampson at low temperatures can be resolved by utilizing the ATcT thermochemistry [109] with the rate coefficient reported by Halstead and Quinn; the estimated rate coefficient for H-abstraction from ethane by vinyl is now $\log_{10}(k / cm^3 mol^{-1} s^{-1}) = 12.60 + 0.05 \log_{10}(T / K) -$ 9.65 kcal mol^{-1} / 2.3RT. This new estimate is in good agreement with our calculated k(T) over the entire temperature range.

Tsang estimates the kinetics of H abstraction from the primary carbons of 2-methylpropane by vinyl based on the kinetics of H abstraction from the primary carbons of 2-methylpropane by methyl [78], with a decrease in the activation energy of 8.5 kJ mol^{-1}; the uncertainty is a factor of five. The kinetics reported by this study is in good agreement with the recommendation of Tsang, over the entire temperature range, Figure 4-9. Given that this study's two calculations for H abstraction from primary carbons by vinyl are similar, and that our kinetics for H abstraction from ethane by vinyl are in reasonable agreement with previously reported experimental data, we recommend our expression for H abstraction from the primary carbons of 2-methylpropane by vinyl.

Photolysis experiments by Slagle et al. set the upper bound for H abstraction from 2-methylpropane by vinyl at 600 K [114]; vinyl bromide was the source of vinyl radical. Tsang estimates the kinetics of H abstraction from the tertiary carbon of 2-methylpropane by vinyl based on the kinetics of H abstraction from the tertiary carbon of 2-methylpropane by methyl [78], with a decrease in the activation energy of 8.5 kJ mol^{-1}; the uncertainty is a factor five. Our calculation is in good agreement with Tsang's recommendation at temperatures above 1300 K, Figure 4-9; at lower temperatures, our recommendation is significantly faster. Both our computed rate

coefficient and Tsang's estimate at 600 K is below the upper bound set by Slagle et al.
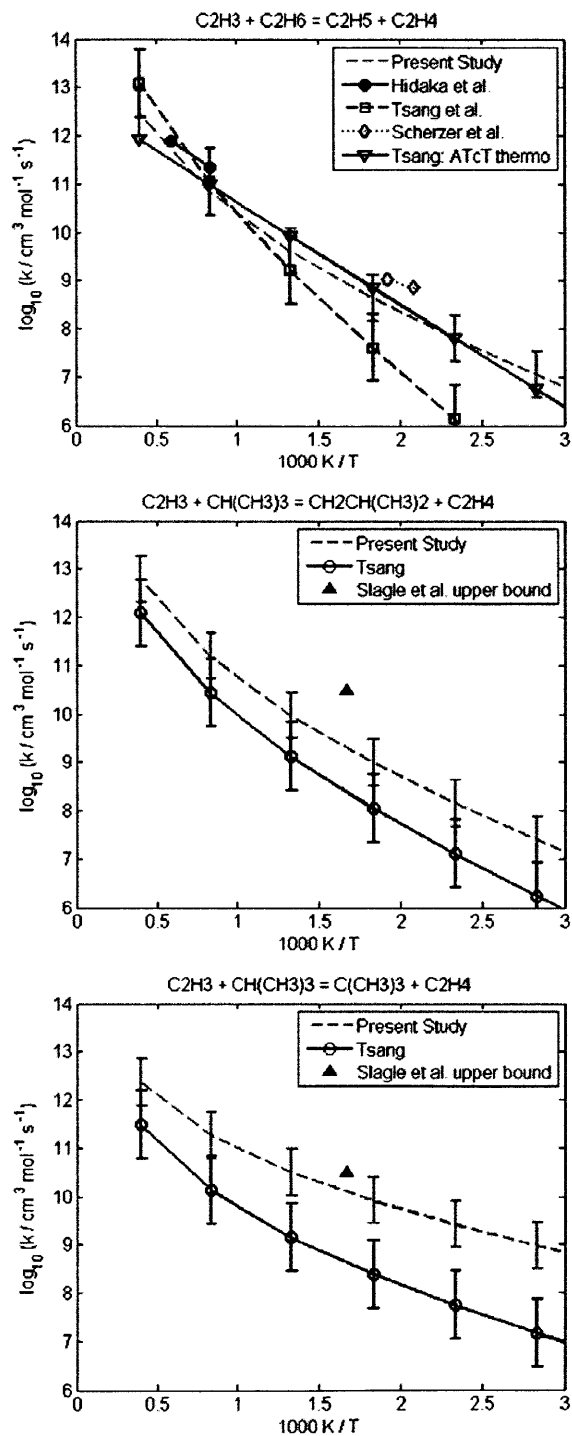
Figure 4-9: Rate coefficient for abstraction from ethane by vinyl radical (top), and for abstraction from 2-methylpropane's primary (middle) and tertiary (bottom) carbons by vinyl radical.

Our computed kinetics for abstraction from the two primary carbons are within a factor of three over the entire temperature range, with the abstraction from 2-methylpropane having faster kinetics (due to the larger reaction path degeneracy). We compute the kinetics for abstraction from the tertiary carbon is faster than from the primary carbons at temperatures below 1400 K, due to the weaker C-H bond.

Iso-Butane + Primary C-H

4.2.23 $CH(CH3)3 + C2H5 = C2H6 + CH2CH(CH3)2$

4.2.24 $CH(CH3)3 + CH2CH2CH3 = CH3CH2CH3 + CH2CH(CH3)2$

4.2.25 $CH(CH3)3 + CH2(CH2)2CH3 = CH3(CH2)2CH3 + CH2CH(CH3)2$
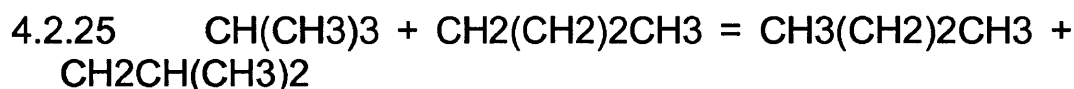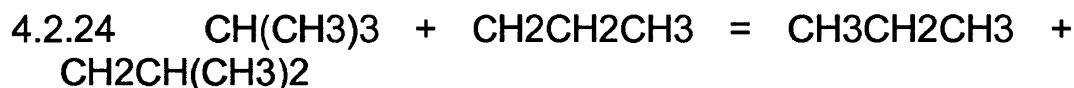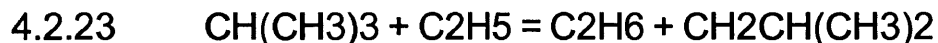
The H abstraction from 2-methylpropane's primary carbons by primary radicals – ethyl, n-propyl, and n-butyl – is discussed in this section. Abstraction by methyl was discussed in Section 4.2.3.

Abstraction from the primary carbons of 2-methylpropane by ethyl radical was estimated by Tsang [78]. The kinetics were based on the abstraction of 2-methylpropane by methyl radical: the pre-exponential factors were assumed to be the same and the activation energy was adjusted to match the results of Boddy and Steacie's experiments [115] for H abstraction from 2,2-dimethylpropane by C_2D_5. Our recommendation agrees very well with the Tsang estimate over the entire temperature range, Figure 4-10; at the lower temperatures, our recommendation is slower by no more than a factor of four.

Abstraction from the primary carbons of 2-methylpropane by n-propyl radical was estimated by Tsang [78] to be equal to abstraction by ethyl radical. Our recommended value agrees very well with Tsang's estimate over the entire temperature range, Figure 4-10, and also with his assumption of abstraction by ethyl being equivalent to abstraction by n-propyl radical.

There is no data available for abstraction from the primary carbon of 2-methylpropane by n-butyl radical. However, given that the kinetics of abstraction by ethyl and n-propyl radical are nearly identical from 300 – 2500 K, and that our calculated kinetics of abstraction by n-butyl are comparable, we have confidence the kinetics would match any future data for this reaction.

The abstraction by ethyl, n-propyl, and n-butyl are similar over the entire temperature range; abstraction by ethyl is faster by no more than a factor of 1.5. Abstraction by methyl is faster by no more than a factor of five at temperatures greater than 800 K. These reactions were marked by the algorithm discussed in Section 4.1 due to the RMG k(T) estimate differing by more than one order of magnitude from the Tsang recommended k(T) at T = 300 K. In the absence of experimental measurements, we recommend an uncertainty of a factor of 5 for reactions 23 – 25.
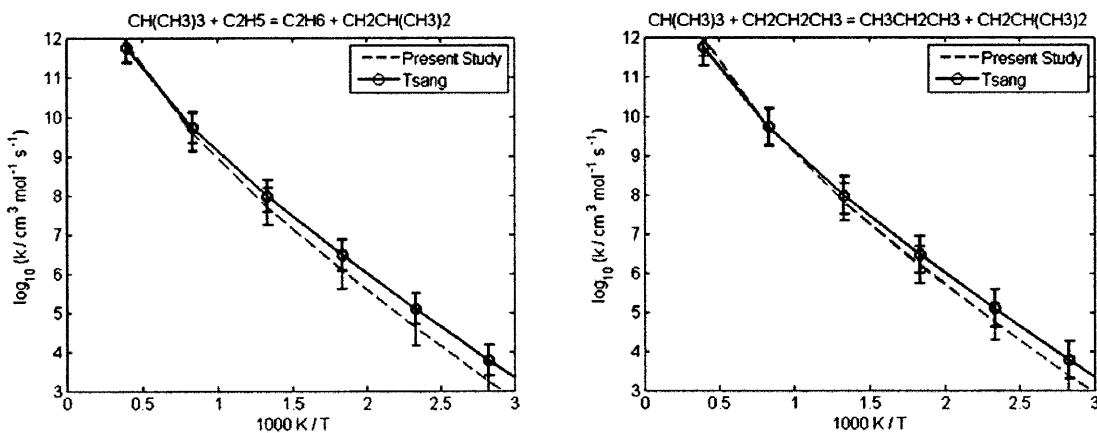
Figure 4-10: Rate coefficient of abstraction from the primary carbons of 2-methylpropane by ethyl (left) and n-propyl (right) radical.

4.2.26 $C6H5OH + H = H2 + C6H5O$

He et al. estimate the kinetics of H atom abstracting the phenol hydrogen based on their experimental shock tube data [116], and knowing the rate coefficient for H abstraction from methane by H atom. A review by Baulch et al. [117] recommends the kinetics of He et al., absent any other experiments. Our calculation is in good agreement with the

81

He et al. expression, Figure 4-11, slower only by a factor of two. We recommend our expression for estimating k(T) over a broad temperature range. We expect our calculation is accurate to within a factor of three at high T, but it is significantly more uncertain at low T where there is no experimental data to check our computed barrier height.

4.2.27   HOC(CH3)3 + H = H2 + HOC(CH2)(CH3)2

Oganesyan and Nalbandyan estimate the kinetics for the titled reaction by measuring the first limit of ignition of H_2/O_2 mixtures with small amounts of tert-butanol in a static reactor over the temperature range 843 – 963 K [118]. Our kinetic expression is in good agreement, Figure 4-11, within a factor of three over this range, but with a noticeably different temperature dependence.

Figure 4-11 also shows the total abstraction rate for abstraction from other primary alkyl positions by H atom: Bryukov et al. calculations for abstraction of ethane by H [119], and Tsang's recommended value for abstraction from the primary carbons of 2-methylpropane by H atom [78]. At temperatures above 500 K, our k(T) calculations for abstraction from tert-butanol are in good agreement with the calculations of Bryukov et al. for abstraction from ethane and with the recommendation of Tsang for abstraction from 2-methylpropane; at lower temperatures where there is no experimental data, our calculations are an order of magnitude slower. Thus, we recommend use of our k(T) expression, with an uncertainty of a factor of three at temperatures above 1000 K and an uncertainty of a factor of ten at lower temperatures.

4.2.28   CH2O + AC3H5 = C3H6 + HCO

These kinetics were estimated by Tsang [108], using microscopic reversibility and analogy to the reaction CH2O + isopropyl = propane + HCO. It should be noted that there is an inconsistency within the reference (2.4 versus 2.1 x 10^{-16} cm^3 molecule^{-1} s^{-1} for the temperature-independent pre-exponential factor), and that the NIST Chemical Kinetic Database has slightly different pre-exponential factors from those

reported in the reference. The reverse kinetics, abstraction of an allylic hydrogen by formyl radical, were assumed by Tsang to be equal to his estimate for the abstraction from the secondary carbons of propane by formyl radical [85]; these kinetics were estimated though equilibrium. The rate coefficient for H abstraction from formaldehyde by iso-propyl was assumed to be equal to twice the kinetics for H abstraction of the aldehydic hydrogen from 2-methylpropanal by iso-propyl [120], for which there are experimental data. These experimental numbers were referenced to the kinetics of iso-propyl radical self-recombination over the range 390 – 627 K.

Our recommendation is within a factor of four of the Tsang estimate over the temperature range 390 – 627 K, Figure 4-11. At temperatures above 700 K, the Tsang estimate is more than an order of magnitude greater than our recommendation. One would not expect iso-propyl to be a very accurate analogy for allyl, so it is surprising that Tsang's estimate agrees at all with the quantum chemistry calculations. Since there are no experimental data we estimate an order of magnitude uncertainty for our computed k(T).

4.2.29   CH2O + CH3OO = CH3OOH + HCO

The rate coefficient at 410 K was estimated by Selby and Waddington [121]. They measured the reactivity difference of di-tert-butyl peroxy decomposition under varying concentrations of formaldehyde, and using a complex mechanism they were able to infer the rate coefficient. Tsang and Hampson estimated the rate coefficient [111] to be equal to that for H abstraction from formaldehyde by HO_2 [122].

Our calculation is in good agreement with the Tsang estimate at temperatures below 1100 K, Figure 4-11. Our recommendation is no more than a factor of five greater than the Tsang estimate above 1100 K, however the temperature dependence of the two estimates are markedly different. Both estimates are in good agreement with the value reported by Selby and Waddington at 410 K. We recommend use of our k(T) expression, with an uncertainty of a factor of three.
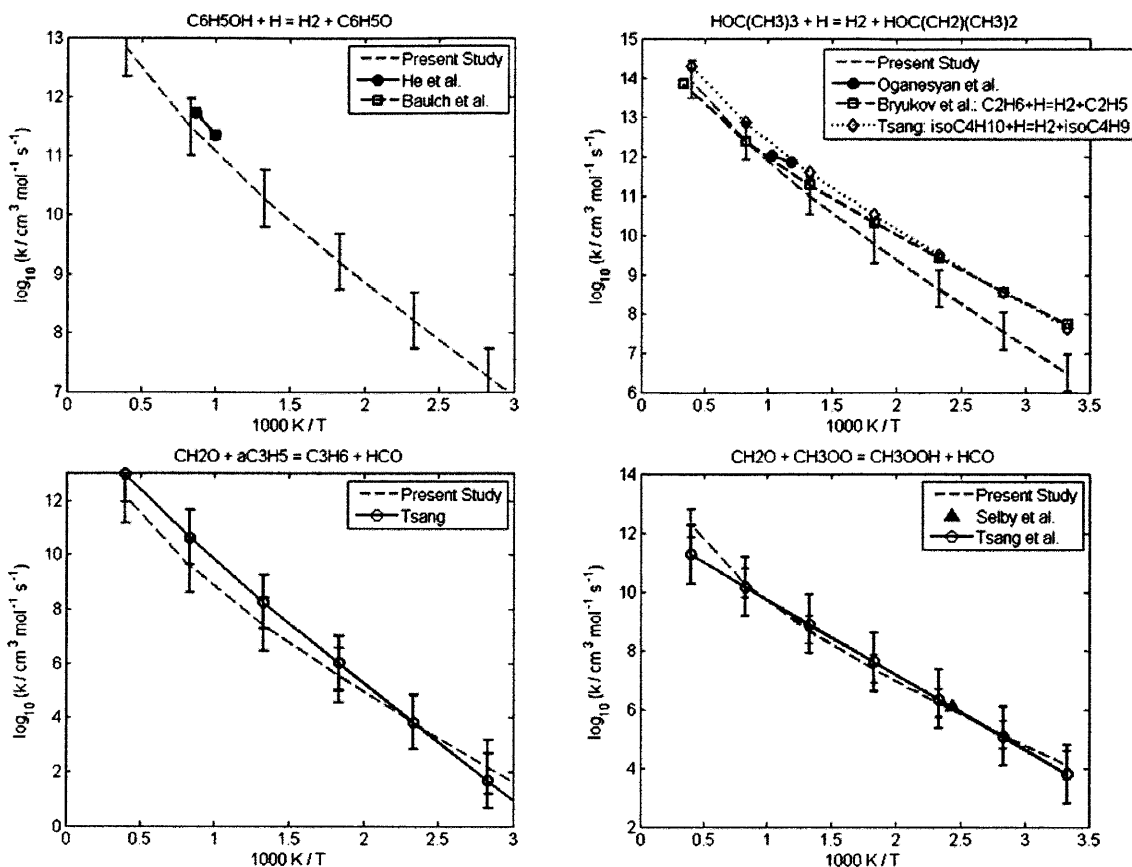
Figure 4-11: Rate coefficient for the abstraction of the hydroxyl hydrogen from phenol by H atom (upper-left), from the primary carbons of tert-butanol by H atom (upper-right), from formaldehyde by allyl radical (lower-left), and from formaldehyde by methylperoxy radical (lower-right). Note: In the upper-right figure, the Bryukov et al. expression is for abstraction from ethane by H atom whereas the Tsang expression is for abstraction from the primary carbons of 2-methylpropane by H atom.

4.2.30 $CH2O + CH2CH2CH3 = C3H8 + HCO$

This rate coefficient was estimated by Knoll et al. between 333 and 363 K [123] by fitting parameters of a kinetic model to their experimental measurements for the pyrolysis of formaldehyde and azo-n-propane (the source of the n-propyl radicals). The pre-exponential factor was assumed to be 1×10^{11} cm^3 mol^{-1} s^{-1} and the activation energy was selected to match their rate coefficient measurements; their reported kinetics was $\log_{10}(k \,/\, cm^3\ mol^{-1}\ s^{-1}) = 11.0 \pm 0.3 - (32.6 \pm 2.1\ kJ\ mol^{-1} \,/\, 2.3RT)$. Tsang estimated the kinetics [85] to be similar to the abstraction from formaldehyde by methyl radical [111]; Tsang assumed the same activation energy

84

but adjusted the pre-exponential factors to match the kinetics reported for n-propyl radical abstracting the aldehydic hydrogen from butanal [124].

Our calculation is no more than a factor of three greater than the estimate of Knoll et al., Figure 4-12, and it is also in reasonable agreement with the estimate of Tsang; the kinetics are always within a factor of five of each other over 300 – 2500 K. We recommend use of our k(T), with an estimated uncertainty of a factor of five. Furthermore, our recommendation is also in good agreement with the rate coefficients for the analogous H abstraction from butanal by n-propyl [125, 126], multiplied by two to account for the reaction path degeneracy. It should be noted that the NIST Chemical Kinetic Database has the incorrect activation energy for Reference [125].

4.2.31 $CH_2O + C_2H_3 = C_2H_4 + HCO$

Tsang and Hampson estimate this rate coefficient based on the kinetics of H abstraction from formaldehyde by methyl [111]; the authors note the uncertainty as a factor of five at temperatures above 1000 K and much higher at lower temperatures. Scherzer et al. estimate the kinetics over 480 – 520 K using the BSBL method [113]. Zhang et al. calculated the kinetics using canonical variational TST with small-curvature tunneling contributions [127]; the geometries were optimized using the MP2/cc-pVDZ method and the energies were further refined at the QCISD(T)/cc-pVTZ level of theory. Xie et al. have calculated the C_3H_5O potential energy surface (PES) at the G3B3 and CBS-QB3 levels [128]; they report the reaction barrier of the H-abstraction reaction to be 4.7 kcal mol^{-1} at the CBS-QB3 level.

Our recommendation is within a factor of three of Tsang and Hampson's estimate at temperatures above 1000 K, Figure 4-12, but our recommendation is significantly faster than their estimate at lower temperatures. Our recommendation is a factor of five faster than the estimates of Scherzer et al. Our recommendation is within a factor of three of the Zhang et al. calculations at temperatures above 700 K; at lower temperatures, our recommendation is faster by up to an order of magnitude.

Although the Zhang calculations use a more advanced TST calculation and larger basis sets, we recommend our value at temperatures below 700 K, due to our calculations treating the low-frequency internal mode of the transition state with our hindered rotor corrections; when we compute the rate coefficient treating this mode with the harmonic oscillator approximation used by Zheng et al., our calculations are within a factor of two of the Zhang et al. calculations. Our CBS-QB3 calculations yield a zero-point reaction barrier of 3.5 kcal mol^{-1} for the H-abstraction reaction at the CBS-QB3 level, similar to the value reported by Xie et al. Since there are no experimental data we recommend use of our calculation with an uncertainty estimate of one order of magnitude.

4.2.32   CH2O + OC(CH3)3 = HOC(CH3)3 + HCO

Al Akeel et al. measured the ratio of the concentration of *tert*-butanol to the concentrations of formaldehyde and acetone in a static system of di-*tert*-butyl peroxide and formaldehyde from 399 – 434 K and 20 – 200 torr [129]. The rate coefficient was then estimated using these measurements and the rate coefficient for the β-scission of the 1,1-dimethylethoxy radical forming acetone and methyl radical; this expression was derived from their proposed mechanism. Al Akeel et al. utilized two different high-pressure limit rate coefficients for the β-scission: the first was $\log_{10}(k / s^{-1}) = 14.5 - 71.6$ kJ mol^{-1} / 2.3RT, leading to a rate coefficient of $\log_{10}(k / cm^3 mol^{-1} s^{-1}) = 12.85 \pm 0.24 - (19.3 \pm 2.3$ kJ mol^{-1} / 2.3RT); the second was $\log_{10}(k / s^{-1}) = 15.5 - 71.6$ kJ mol^{-1} / 2.3RT, leading to a rate coefficient of $\log_{10}(k / cm^3 mol^{-1} s^{-1}) = 13.15 \pm 0.20 - (16.5 \pm 2.2$ kJ mol^{-1} / 2.3RT).

The recent calculations of Buback et al. [130], and the review by Curran [131], suggest the latter set of kinetics reported by Al Akeel et al. to be more accurate, Figure 4-12d. We thus consider the rate coefficient reported by Al Akeel et al. employing $\log_{10}(k / s^{-1}) = 15.5 - 71.6$ kJ mol^{-1} / 2.3RT to be correct. Our calculations are slower than this measured rate coefficient by a factor of three. Decreasing our computed E_A by 1 kcal mol^{-1} places our calculations in good agreement with the experiment; note the scale of Figure 4-12c is expanded

compared to the other figures. We estimate the uncertainty of our recommendation to be a factor of ten.
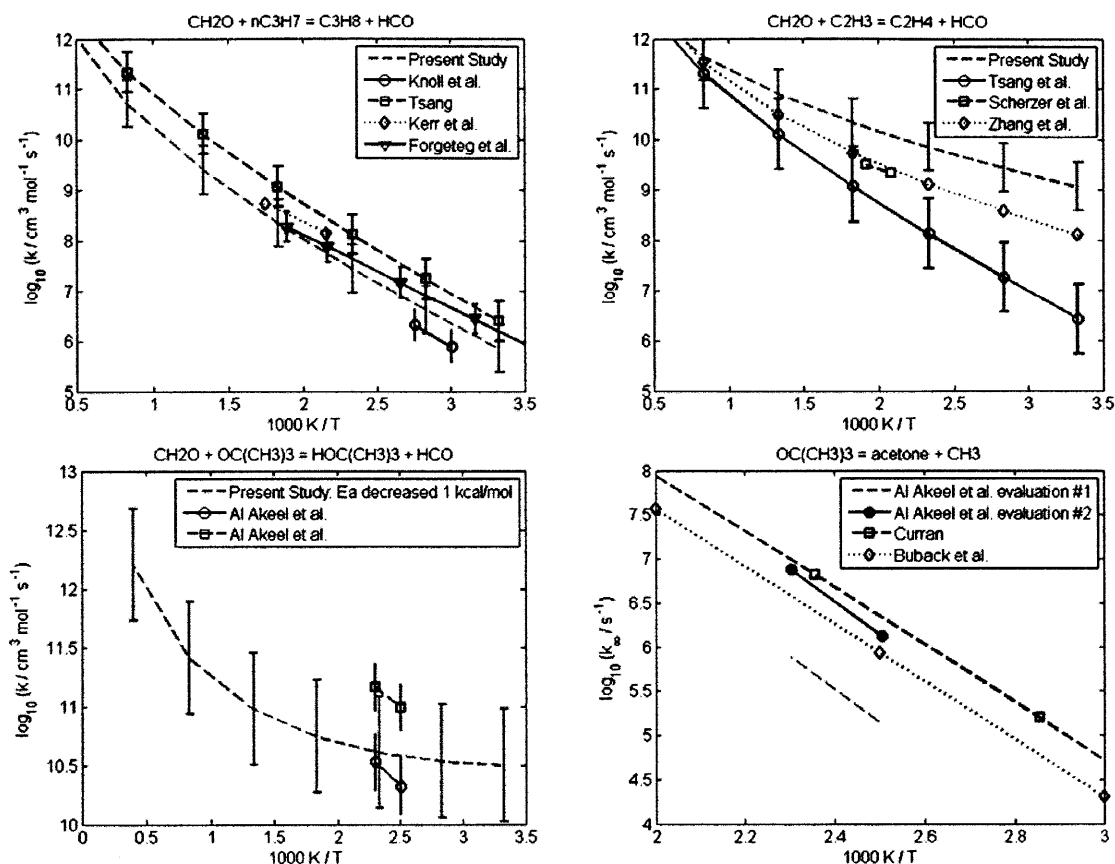
Figure 4-12: Rate coefficients for abstraction from formaldehyde: by n-propyl (upper-left), by vinyl (upper-right), and by 1,1-dimethylethoxy radical (lower-left); the lower-right figure is the rate coefficient for the β-scission of 1,1-dimethylethoxy to acetone and methyl radical. The Kerr et al. and Forgeteg et al. expressions (upper-left) are for abstraction from butanal by n-propyl radical.

4.2.33   C2H5OC2H5 + C2H5OCH2CH2 = C2H5OC2H5 + C2H5OCHCH3

Foucaut and Martin studied the pyrolysis of di-ethyl ether at low conversions in a static reactor [132]. By fitting their measured concentrations of methane and acetaldehyde to their 11-step mechanism – and by assuming all methyl radicals came from the β-scission of ethoxy radical which itself came exclusively from the β-scission of $CH_3CH_2OCH_2CH_2$, and by assuming acetaldehyde came exclusively from the β-scission of $CH_3CH_2OCHCH_3$ – the authors estimated the kinetics of the

titled reaction from 763 – 798 K. Our calculation is in good agreement with this reported value, Figure 4-13, being no faster than a factor of three over the valid temperature range. We recommend use of our k(T) with a broad temperature range; the uncertainty is a factor of three.

4.2.34   C2H5OC2H5 + H = H2 + C2H5OCHCH3

4.2.35   C2H5OC2H5 + H = H2 + C2H5OCH2CH2
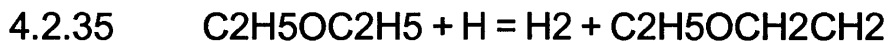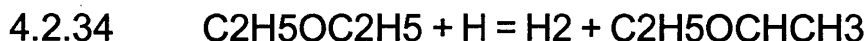
Faubel et al. measured the total hydrogen abstraction from di-ethyl ether by hydrogen atom between 250 and 620 K in a flow reactor [133]; the reported rate coefficient is $k = (1.9 \pm 0.9) \times 10^{13} \exp(- (2600 \pm 100 \text{ K}) / \text{T})$ cm^3 mol^{-1} s^{-1}. It should be noted that the NIST Chemical Kinetic Database reports these total kinetics as abstraction from the secondary carbons (and no value is reported for abstraction from the primary carbon). Our calculations suggest that over the temperature range 250 – 620 K, the abstraction rate coefficient from the secondary sites is indeed essentially equal to the total abstraction rate coefficient.

Our calculation is in reasonable agreement with the data, Figure 4-13; our rate coefficient for abstraction from the secondary carbon is predicted to be between 10 – 60% of the total abstraction rate coefficient as reported by Faubel et al. If we decrease our computed Arrhenius activation energy by 1 kcal mol^{-1}, our calculations are in very good agreement with the experimental data. We therefore recommend $\log_{10} (k / \text{cm}^3 \text{ mol}^{-1} \text{ s}^{-1}) = (6.049 \pm 0.477) + 2.341 \log_{10}(\text{T} / \text{K}) - (2.101 \text{ kcal mol}^{-1} / 2.3\text{RT})$.
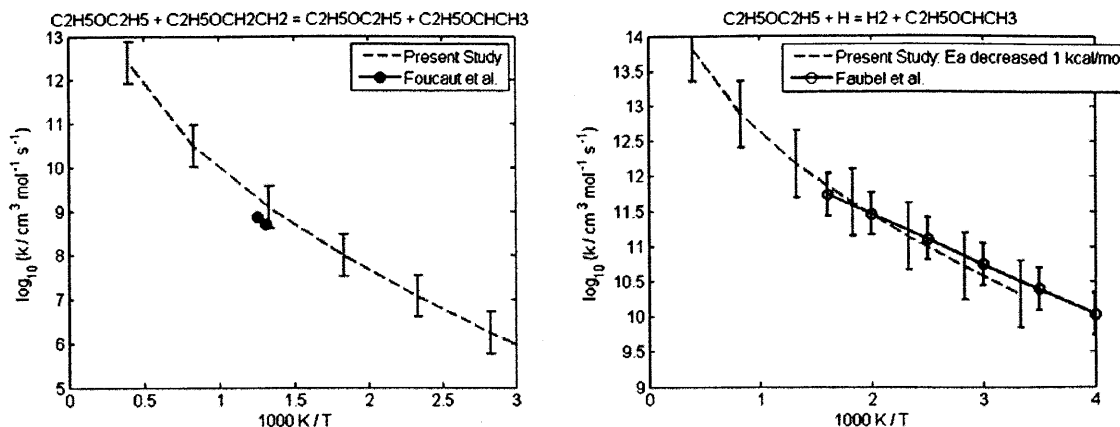
Figure 4-13: Rate coefficient for abstraction from the secondary carbons of diethyl ether by 2-ethoxyethyl (left) and H atom (right).

4.2.36 $C2H5OH + CH3 = CH4 + CH3CHOH$

Bansal and Freeman studied the radiolysis of ethanol and ethanol – propene

mixtures at 423 K [134]. They attributed the decrease in measured methane

concentration between the pure ethanol and ethanol – propene mixture to the

competing reaction of methyl radical adding to propene. Measuring the ratio of

ethanol to propene and the rate of formation of methane, in addition to employing a

total rate coefficient for methyl addition to propene of 5.3×10^7 cm^3 mol^{-1} s^{-1} as

measured by Cvetanov and Irwin [135], yields their reported rate coefficient. The

total rate coefficient for methyl adding to propene employed is in good agreement

with a recent evaluation by Curran [131]. Gray and Herod have estimated the

kinetics from 403 – 523 K by utilizing the kinetic isotope effect with ethanol,

CH_3CD_2OH, and C_2H_5OD [136]; acetone photolysis was the source of the methyl

radicals and the relative concentration of CH_4, CH_3D, CHD_3, and CD_4 were

measured. Their reported rate coefficient is $\log_{10}(k / cm^3 \text{ mol}^{-1} s^{-1}) = (11.60 \pm 0.15)$

$- (9690 \pm 300 \text{ cal mol}^{-1})/2.3RT$. Xu et al. have calculated the kinetics using

canonical variational TST with small-curvature tunneling corrections [137]; it

should be noted that the NIST Chemical Kinetics Database has the incorrect sign for

the activation energy for each of the reported kinetic expressions of Xu et al., in

addition to reporting the per molecule temperature-independent pre-exponential

factor as having units of per mole.

Our calculation is in good agreement with all previously published values at temperatures above 400 K, Figure 4-14: a factor of four greater than the Bansal and Freeman rate coefficient, within a factor of three of the Xu et al. calculations, and within a factor of two of the Gray and Herod values. As our calculations treat the low-frequency internal modes with hindered rotor approximations, rather than the RRHO approximation used by Xu et al., we recommend our expression at temperatures above 400 K, with an uncertainty of a factor of three. Below 400 K there are no experimental data, and the two calculations significantly disagree; a direct measurement at room temperature would be helpful in resolving this discrepancy.

4.2.37   C2H5OH + H = H2 + CH3CHOH

Bansal and Freeman studied the radiolysis of ethanol and ethanol – propene mixtures at 423 K [134]. The authors attributed the decrease in measured hydrogen concentration between the pure ethanol and ethanol – propene mixture to the competing reaction of H atom adding to propene. Measuring the ratio of ethanol to propene and the rate of formation of hydrogen, in addition to employing a total rate coefficient for H atom addition to propene of 1×10^{12} cm^3 mol^{-1} s^{-1} as reported by Trotman-Dickenson [138], yields their reported rate coefficient. The total rate coefficient for H atom adding to propene employed is $\sim 40\%$ of the recent evaluation by Curran for the total rate coefficient for H atom adding to propene [131]. Aders and Wagner estimate the kinetics by referencing the reaction to the reaction ethanol and hydrogen atom forming water and ethyl radical [139]. Park et al. have calculated the kinetics using canonical variational TST with small-curvature tunneling correction; it appears Park et al. assumed RRHO for all frequencies in the evaluation of the vibrational partition function [140].

Our calculations are in good agreement with all previously published values, Figure 4-14: 40% greater than the Bansal and Freeman rate coefficient (which would increase by a factor of ~2 if employing more recent evaluations of H atom adding to

90

propene), within a factor of two of the Aders and Wagner expression, and within a factor of 1.5 of the Park et al. expression. As our calculations treat the low-frequency modes with hindered rotors corrections, we recommend our value, though all data lie within each kinetics' respective uncertainty region. We estimate an uncertainty of a factor of three.
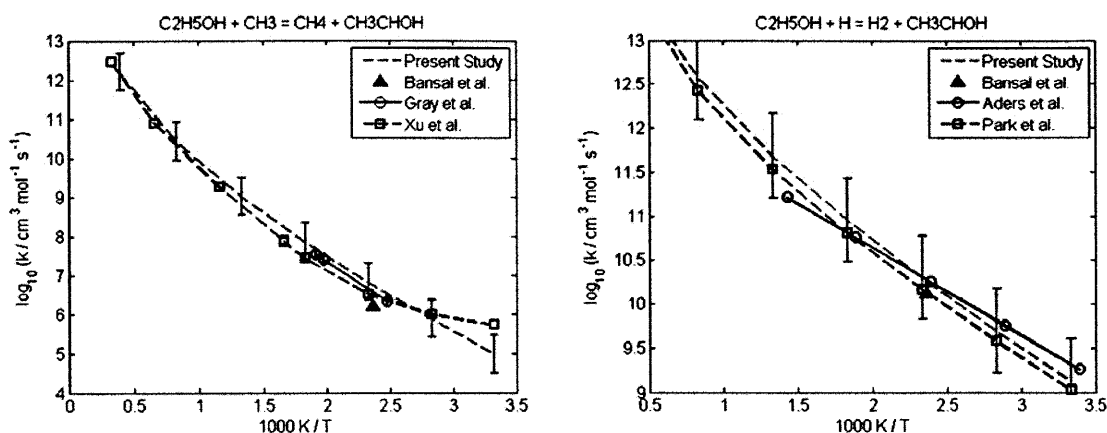
Figure 4-14: Rate coefficient for abstraction from the secondary carbon of ethanol by methyl radical (left) and by H atom (right).

4.2.38   CH(CH3)3 + OC(CH3)3 = TBUOH + CH2CH(CH3)2

Brokenshire et al. studied this reaction experimentally through the chlorination of 2-methylpropane by tert-butyl hypochlorite, estimating its kinetics from 283 – 343 K in reference to the kinetics of the β-scission of 1,1-dimethylethoxy radical forming acetone and methyl radical [141].

Our calculation is at least two orders of magnitude faster than the values reported by Brokenshire et al., see Figure 4-15. Sway and Waddington have measured the rate coefficient from 399 – 434 K of 1,1-dimethylethoxy abstracting from 2,2-dimethylpropane [142]. One would expect the abstraction from 2-methylpropane to be faster since it has an abstractable tertiary C-H. Our recommended kinetics are consistent with Sway and Waddington's value. Furthermore, the data analysis of the Brokenshire et al. paper is confusing. The authors quote the ratio of the hydrogen abstraction rate coefficient to the β-scission rate coefficient as unitless. Although

the excess concentration of 2-methylpropane could have been lumped into the hydrogen abstraction rate coefficient, this assumption was not made obvious by the authors; furthermore, it is not clear if the authors also varied the initial concentration of 2-methylpropane in estimating the kinetics. The study reports the E_A for abstraction from the tertiary carbon to be 20 kJ mol^{-1}, 7 kJ mol^{-1} less than abstraction from the primary carbons. We recommend our k(T) expression for this reaction, with an uncertainty of a factor of three.
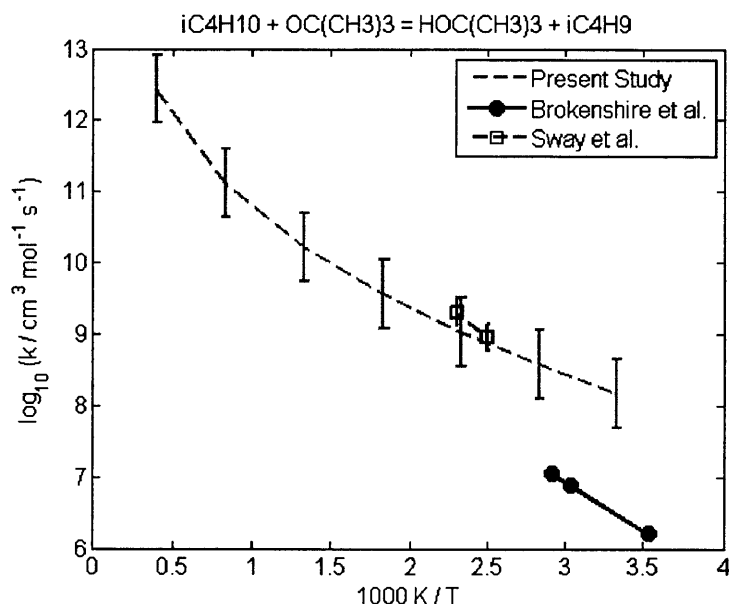
Figure 4-15: Rate coefficient for the abstraction from the primary carbons of 2-methylpropane by 1,1-dimethylethoxy radical. The Sway et al. kinetics are for the abstraction from the primary carbons of 2,2-dimethylpropane by 1,1-dimethylethoxy radical.

4.2.39   HOOC(CH3)3 + CH3O = CH3OH + OOC(CH3)3

Kirsch and Parkes studied the photolysis of azo-tert-butane – oxygen mixtures from 298 – 373 K [143]. The experiments at 373 K showed increased methanol formation compared to experiments at lower temperatures, and the authors attributed this to the titled reaction; H abstraction from the carbons of tert-butyl hydroperoxide was not considered. Methoxy radical disappearance was attributed to the titled reaction, and reaction with O_2 forming HO_2 and formaldehyde; the ratio of these two reaction's rate coefficients was measured to be < 0.4 at 373K. The derivation of this expression is not obvious.

Our calculations are in good agreement with the available experimental data, Figure 4-16; our rate coefficient is a factor of two less than the Kirsch and Parkes lower bound at 373 K. We recommend use of our k(T) expression which covers a broad temperature range and explicitly considers H abstraction from the hydroperoxy group. The uncertainty is a factor of three.

4.2.40   HOOC(CH3)3 + CH3 = CH4 + OOC(CH3)3

Mulder and Louw studied the pyrolysis of *tert*-butyl hydroperoxide, in the presence and absence of toluene, over 501 – 528 K [144]. The measured concentration of ethane and a methyl recombination rate coefficient of $log_{10}(k / cm^3 \, mol^{-1} \, s^{-1}) = 13.3$ yielded the concentration of methyl radical; the rate coefficient employed is in good agreement with recent calculations by Klippenstein et al. [107]. Knowing the concentration of methyl, and assuming the measured methane came from the titled reaction, yielded estimates for the rate coefficient of the titled reaction at different temperatures: $k = 2.5 \times 10^9$ and $6.0 \times 10^9 \, cm^3 \, mol^{-1} \, s^{-1}$ at T = 501 and 528 K, respectively. Mulder and Louw did not consider H abstraction from the carbons, so their reported rate coefficients may be treated as upper bounds.

Our calculations are no more than a factor of 2.5 times slower than the values reported by Mulder and Louw, Figure 4-16. We recommend use of our k(T) expression which covers a broad temperature range, and explicitly considers H abstraction from the hydroperoxy group; the uncertainty is a factor of three.
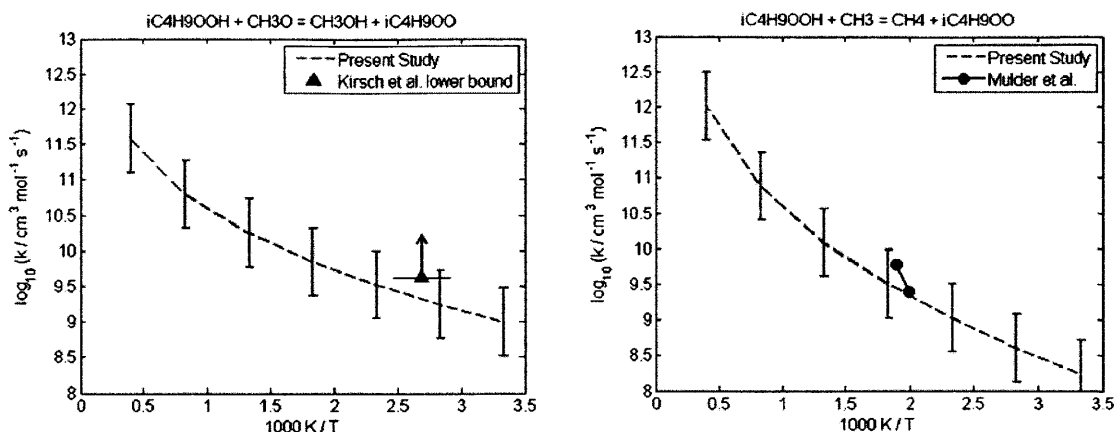
Figure 4-16: Rate coefficient for the abstraction from tert-butyl hydroperoxide by methoxy (left) and methyl (right) radical.

The recommended kinetics for abstraction by methyl radical follow a similar trend to our recommended value for abstraction by methoxy radical; at lower temperatures, abstraction by methyl is approximately an order of magnitude slower than by methoxy radical, while the values converge at high temperatures.

4.2.41   CH3C(=O)OCH3 + CH3 = CH4 + CH3C(=O)OCH2

4.2.42   CH3C(=O)OCH3 + CH3 = CH4 + CH2C(=O)OCH3
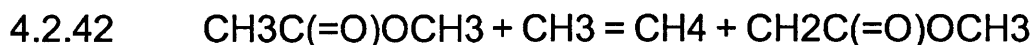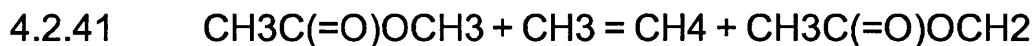
Ferguson and Pearson measured the rate coefficients of the titled reactions through studies of the photolysis of methylacetate – acetone, $CH_3C(=O)OCD_3$ – acetone, and $CD_3C(=O)OCH_3$ – acetone mixtures over the temperature range 393 – 553 K [145]. Arthur and Newitt measured the total abstraction of methyl acetate by methyl radical, using the photolysis of acetone as the source of methyl radicals [146]. The branching ratio between the methoxy and acetyl sites were then computed by running experiments with two deuterated methyl acetates, $CD_3C(=O)OCH_3$ and $CH_3C(=O)OCD_3$ [147].

Our computed values agree very well with all sets of experimental data, Figure 4-17; our values are within a factor of three of both Arthur and Newitt experiments and the Ferguson and Pearson experiments. We recommend use of our computed k(T) with an uncertainty of a factor of three.

94
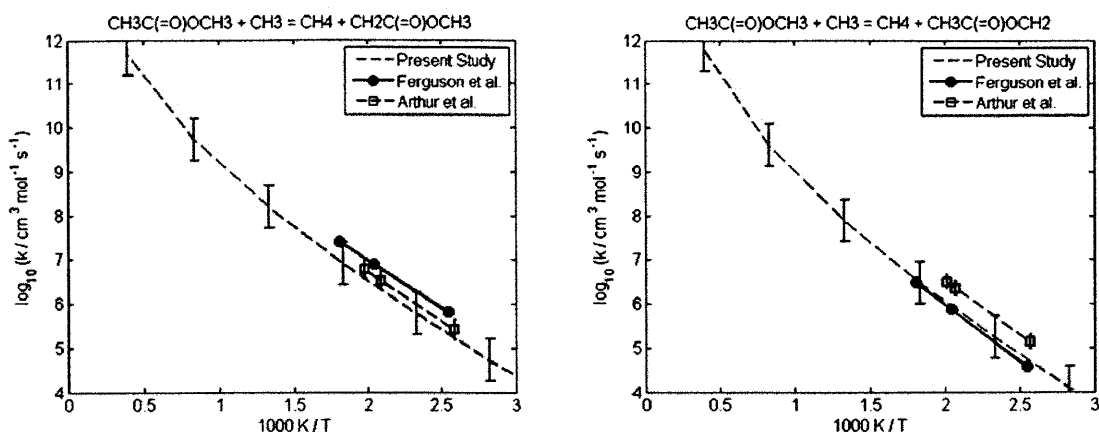
Figure 4-17: Rate coefficient for the abstraction from methyl acetate by methyl radical at the acetyl (left) and methoxy (right) site.

4.2.43   C6H5CH2CH3 + HO2 = H2O2 + C6H5CHCH3

Baulch et al. estimated the kinetics of this reaction based on the total abstraction rate coefficient of H abstraction from ethylbenzene by H atom at 773 K [148]; the abstraction from the primary carbon was assumed to equal half the rate coefficient of H abstraction from ethane by HO_2. Scott and Walker have measured the total rate coefficient of this reaction at 773 K by adding small amounts of ethylbenzene to a mixture of H_2 and O_2 [149].

Our calculations are in good agreement with both sets of data, Figure 4-18. We recommend use of our k(T) which covers a broad temperature range; the uncertainty is a factor of three. Our recommendation yields a rate coefficient that is equal to ~55% of the total rate coefficient reported by Scott and Walker.
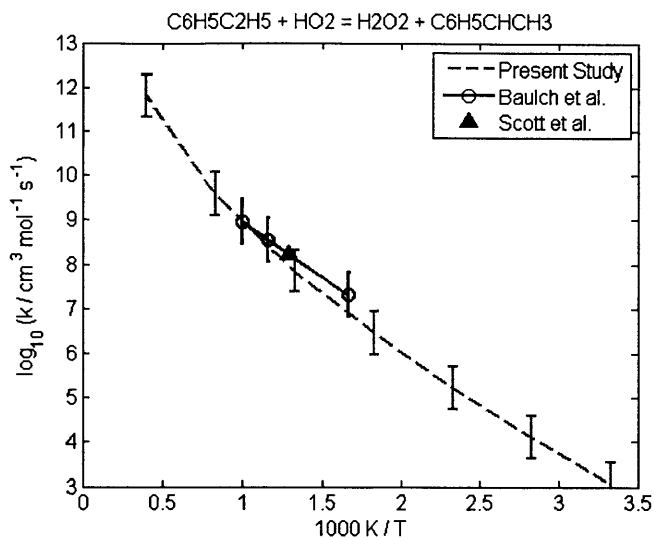
Figure 4-18: Rate coefficient of the abstraction from the benzylic carbon of ethylbenzene by hydroperoxy radical.

4.2.44   C6H5CH2CH3 + H = H2 + C6H5CHCH3

4.2.45   C6H5CH2CH3 + H = H2 + C6H5CH2CH2
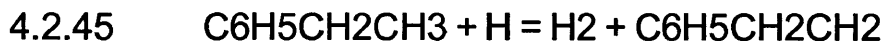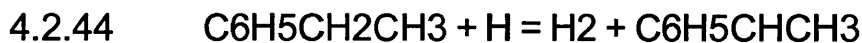
Ebert et al. estimated the kinetics of these reaction from 773 – 1020 K by fitting parameters for their ethylbenzene reaction mechanism to their pyrolysis data [150]; those authors only consider abstraction from the benzylic carbon. Müller-Markgraf and Troe estimated the kinetics of these reaction at higher temperatures, fitting parameters for their ethylbenzene reaction mechanism to their pyrolysis data obtained in a shock tube [151], again only considering abstraction from the benzylic carbon. Baulch et al. estimate the total rate coefficient for hydrogen abstraction at 773 K [117]; there is no discussion on the choice in value. Ellis et al. have measured the total rate coefficient from ethylbenzene abstraction by hydrogen atom at 773 K by adding small amounts of ethylbenzene to a mixture of H_2 and O_2 [152]; by assuming abstraction from the primary carbon to be half that of abstraction from ethane by H atom, the authors make predictions on abstraction from both the primary and benzylic carbon over a broad temperature range, 500 – 1500 K. Their estimated branching ratio between abstraction from the benzylic carbon to abstraction from the primary carbon is < 5 at 773 K.
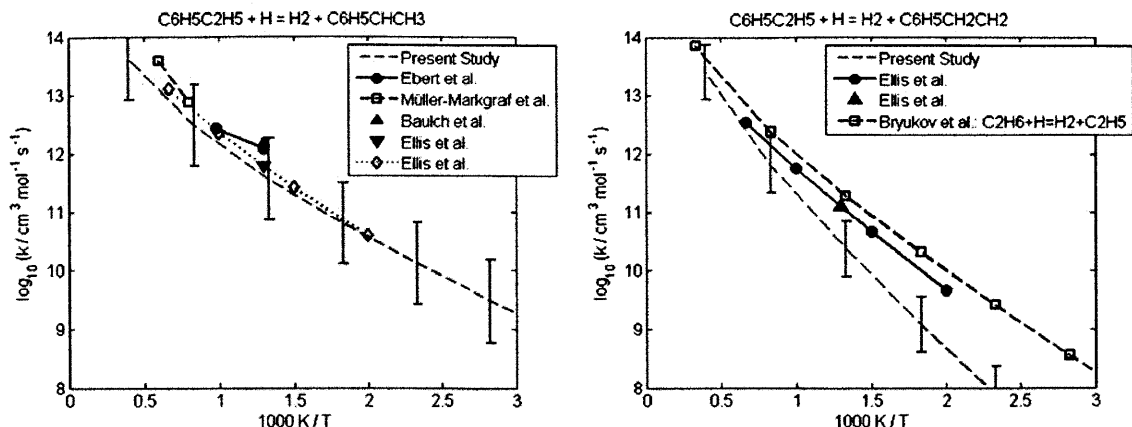
Figure 4-19: Rate coefficient of abstraction from the primary (left) and benzylic (right) carbons of ethylbenzene by H atom.

Our calculations are in good agreement with the experimental data for abstraction from the benzylic carbon of ethylbenzene, Figure 4-19, particularly since most of the experimental data should be treated as an upper bound. We thus recommend use of our calculated k(T) which covers a broad temperature range.

However, our calculations for abstraction from the primary carbon of ethylbenzene by H atom do not agree with the estimate of Ellis et al. at temperatures below 1000 K, Figure 4-19; although the evaluated k(T) agree within a factor of three at higher temperatures, the temperature dependence of the two expressions is different. The Ellis et al. estimate is based on the assumption that abstraction from the primary carbon of ethylbenzene is similar to abstraction from the primary carbons of ethane. In Figure 4-19, we compare our calculation for abstraction from the primary carbon of ethylbenzene by H atom with Bryukov et al.'s calculation for abstraction from the primary carbons of ethane by H atom [119]. Recall that in Section 4.2.27, we concluded that our calculation for the abstraction from the primary carbons of tert-butanol by H atom were in agreement with these Bryukov et al. calculations at temperatures above 500 K; that is not the case for our calculation for abstraction from the primary carbon of ethylbenzene by H atom. Thus, we conclude the Ellis et al. assumption that abstraction from the primary carbon of ethylbenzene by H atom is similar to the abstraction from ethane by H atom not to be valid and thereby recommend our calculations for this reaction. Our calculated branching ratio of

abstraction from the benzylic carbon to abstraction from the primary carbon is ~14 at 773 K.

4.2.46   C6H5OCH3 + CH3 = CH4 + C6H5OCH2

Mulcahy et al. estimated the kinetics for this reaction based on fitting the parameters of their methoxybenzene reaction mechanism to stirred-reactor data [153]; the methoxybenzene was in excess and the source of the methyl radicals came from the pyrolysis of di-tert-butyl peroxide. The rate coefficient was referenced to the rate coefficient of methyl self-recombination; the value employed was a temperature-independent 2.2×10^{13} cm^3 mol^{-1} s^{-1}, in good agreement with recent calculations by Klippenstein et al. [107].

Our calculation is in good agreement with the available data, Figure 4-20; our rate coefficient estimate is no more than a factor of three slower than the estimate of Mulcahy et al. If we decrease our computed Arrhenius activation energy by 1 kcal mol^{-1}, our calculations are in very good agreement with the data. We thus recommend use of $\log_{10}(k / cm^3 \, mol^{-1} \, s^{-1}) = -2.050 \pm 0.477 + 4.251 \log_{10}(T / K) - (5.253 \, kcal \, mol^{-1} / 2.3RT)$.

4.2.47   P-CH3C6H4CH3 + H = H2 + P-CH2C6H4CH3

Hippler et al. measured this rate coefficient from p-xylene pyrolysis experiments performed in a shock tube [154]. The rate coefficient was derived from a reaction mechanism for p-xylene decomposition and was referenced to the recombination of hydrogen atom and 4-methylbenzyl radical; the assumed rate coefficient for the recombination was a temperature-independent 2×10^{14} cm^3 mol^{-1} s^{-1}.

Our calculation is in reasonable agreement with the available experimental data, Figure 4-20; our estimate is no more than an order of magnitude slower than the estimate of Hippler et al. This discrepancy can be explained by recognizing the recombination of hydrogen atom and 4-methylbenzyl radical is probably in the fall-

off regime at temperatures between 1000 and 1800 K and total concentrations of 10^{-6} and 10^{-5} mol cm^{-3}.

4.2.48   C6H5CH3 + AC3H5 = C3H6 + C6H5CH2

Akers and Throssell have estimated the rate coefficient of allyl radical abstracting hydrogen from the methyl group of toluene from 850 to 950 K by fitting parameters from their reaction mechanism to their stirred-reactor data [155]; the decomposition of 4-phenyl-1-butene was the source of allyl radical. The abstraction rate coefficient was obtained in reference to the rate coefficient of the recombination of methyl and allyl radical; the concentration of methyl was determined from the flow rate of methane – the authors assumed methane formed exclusively by H abstraction from toluene by methyl – and the concentration of allyl was determined from the flow rates of 1-butene. Throssell revised this estimate [156] in a later paper, using a recently published (at the time) high-pressure rate coefficient for 1-butene decomposition [157]; this revised estimate yields rate coefficients approximately an order of magnitude faster than the original estimate of Akers and Throssell. It should be noted that the NIST Chemical Kinetics Database has the incorrect activation energy listed for the Throssell kinetics; the activation energy was reported in $\log_{10}$ space, not $\log_e$ space. Louw also estimated the kinetics of this reaction by fitting the parameters of a reaction mechanism to match experiments [158]; the rate coefficient was determined in reference to the kinetics of the self-recombination of allyl radical. Diallyl oxalate was the source of allyl radicals.

Our calculated rate coefficients are in reasonable agreement with the original Akers and Throssell value and with the Louw data, Figure 4-20, a factor of three-to-six less than the two estimates. Our calculation does not agree with the Throssell revision; the discrepancy is more than an order of magnitude. Although this revision utilizes the improved high-pressure limit rate coefficient of Trenwith [157], Akers and Throssell never state what pressure or total concentration they are operating at; thus, it is difficult to check whether Throssell's use of the high-pressure limit rate coefficient is correct.

If we decrease the fitted E_A of our calculations by 2 kcal mol^{-1}, our calculations are in excellent agreement with the Akers and Throssell and the Louw estimate. We thus recommend use of log$_{10}$(k / cm^3 mol^{-1} s^{-1}) = -4.948 ± 0.477 + 5.019 log$_{10}$(T / K) − (10.952 kcal mol^{-1} / 2.3RT).

4.2.49   C6H5OH + cYC5H5 = cYC5H6 + C6H5O

Lovell et al. estimate the kinetics for this reaction by fitting the kinetic parameters in their phenol pyrolysis reaction mechanism to match their flow reactor speciation data [159]. In their mechanism, cyclopentadienyl radical is formed by the decomposition of phenoxy radical and is depleted by either abstracting an H from phenol or by recombination with phenoxy radical.

Our computed value is an order of magnitude slower than the Lovell et al. expression, Figure 4-20. We believe the value obtained by Lovell et al. should be treated as an upper bound for the hydrogen abstraction rate coefficient, due to the limited number of cyclopentadienyl decomposition pathways included in their kinetic model. For example, Lovell et al.'s mechanism does not contain the recombination with hydrogen to form cyclopentadiene, nor the self-recombination, nor any reaction with cyclopentadiene, e.g. to form the experimentally-observed naphthalene and indene. We thus recommend use of our k(T), with an uncertainty of a factor of five.
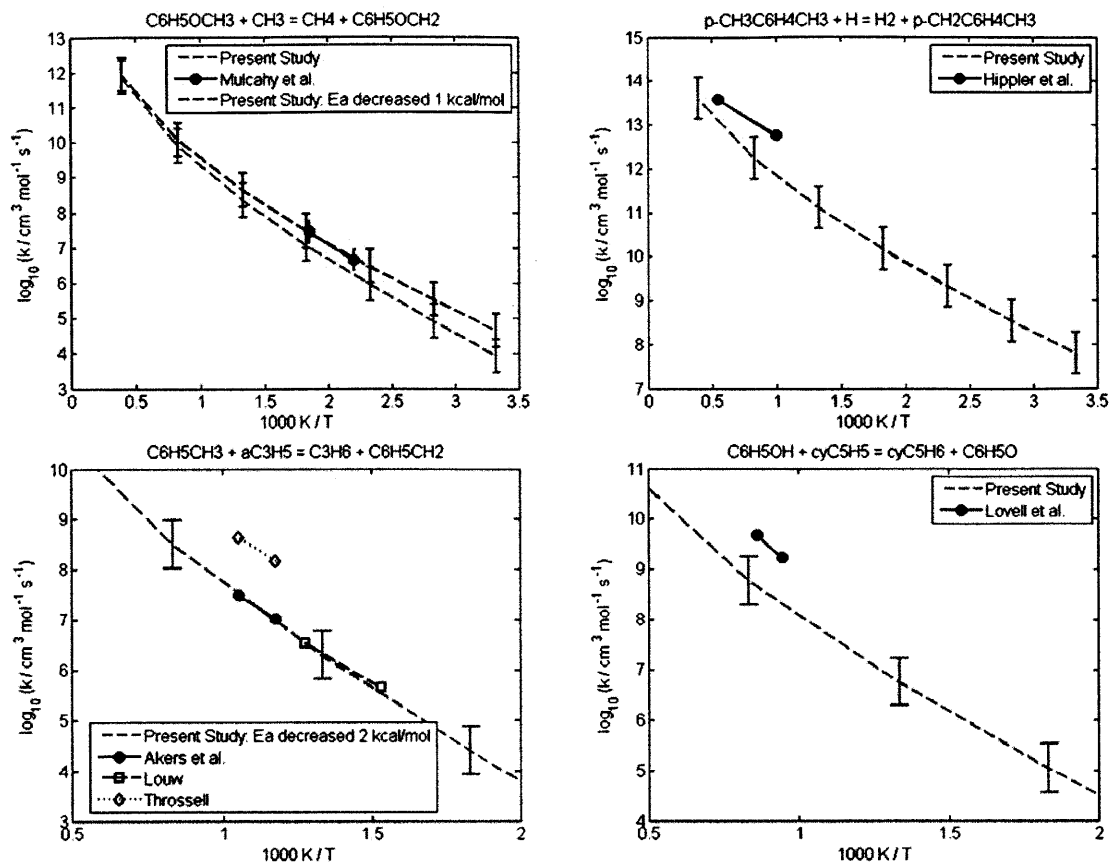
Figure 4-20: Rate coefficient for abstraction from the primary carbon of methoxybenzene by methyl radical (upper-left), the primary carbons of *p*-xylene by H atom (upper-right), the primary carbon of toluene by allyl radical (lower-left), and the hydroxyl hydrogen of phenol by cyclopentadienyl radical (lower-right).

4.2.50 $C_2H_5OCHO + C_2H_5 = C_2H_6 + C_2H_5OCO$

4.2.51 $C_2H_5OCHO + CH_3 = CH_4 + C_2H_5OCO$
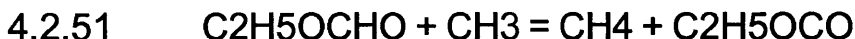
Thynne estimates the kinetics for both reactions by fitting the parameters in a proposed ethyl formate reaction mechanism to experimental data [160]. In Thynne's experiments, the radical pool comes from thermal decomposition of acetone to methyl and acetyl radical; methyl abstracts the aldehydic hydrogen from ethyl formate, and the resulting radical forms CO_2 and ethyl radical through β-scission. In Thynne's fits, the rate coefficients of methyl self-recombination, ethyl self-recombination, and the recombination of methyl and ethyl were fixed to literature estimates.

101

The rate coefficient of abstraction from ethyl formate by methyl radical reported by Thynne is in good agreement with previous measurements of abstraction from methyl formate by methyl radical [160-162]. Our calculations also agree with Thynne's value for H abstraction from ethyl formate by methyl, Figure 4-21. Our computed values are significantly faster than the *ab initio* calculations of Good et al. at lower temperatures. In their study, Good et al. assumed a Wigner tunneling correction and the RRHO approximation for all frequencies when computing the vibration partition functions; using the same assumptions as Good et al., our TST calculations are in good agreement with their computed value, within a factor of three, over the entire temperature range.

However, our computed rate for abstraction from ethyl formate by ethyl radical is significantly slower than the estimate of Thynne, Figure 4-21. According to Thynne, abstraction by methyl is predicted to be a factor of four-to-five slower than the abstraction by ethyl radical, a trend that is not normally observed in abstractions by alkyl radicals. We believe Thynne's rate coefficient for ethyl formate abstraction by ethyl radical is too fast and recommend our expression, with an uncertainty of a factor of three, instead.
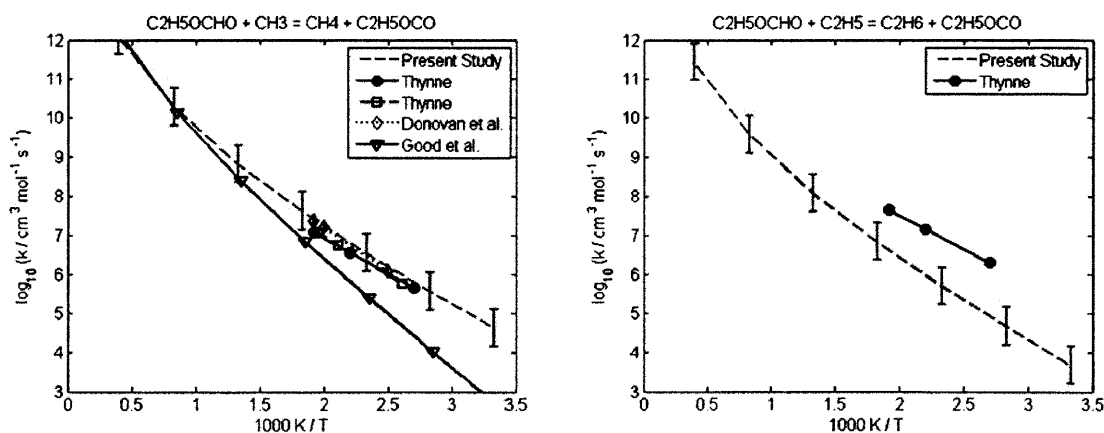
Figure 4-21: Rate coefficient for the abstraction of the aldehydic hydrogen from ethyl formate by methyl (left) and ethyl (right) radical. For abstraction by methyl radical (the left figure), the Donovan et al., Good et al., and second Thynne kinetic expressions are for abstraction from methyl formate by methyl radical.

4.2.52 cYC6H12 + CH3 = CH4 + cYC6H11

Al-Niami et al. estimated the kinetics over 373 – 473 K by fitting parameters to a proposed cyclohexane decomposition mechanism in the presence of acetone, based on the measured flow rates of methane and ethane [163]; the photolysis of acetone was the source of methyl radicals. The rate coefficient was in reference to the self-recombination kinetics of methyl radical. Sway also estimated the kinetics between 399 and 434 K by fitting parameters to a proposed cyclohexane decomposition mechanism [93]; di-tert-butyl ether was the source of methyl radicals, and the rate coefficient was also in reference to the kinetics of methyl recombination.

Our calculation is in good agreement with the available experimental data, Figure 4-22; our estimate is within a factor four of the Al-Niami et al. estimate and within a factor three of the Sway estimate. Decreasing our fitted E_A by 1 kcal mol^{-1} places our calculations in excellent agreement with the data; we thus recommend use of $\log_{10}(k / cm^3 \; mol^{-1} \; s^{-1}) = -4.477 \pm 0.477 + 3.977 \log_{10}(T / K) - (5.150 \; kcal \; mol^{-1} / 2.3RT)$.

4.2.53 cYC6H10 + C2H5 = C2H6 +

James and Steacie estimate the kinetics of this reaction from 298 to 500 K by fitting the parameters of their proposed reaction mechanism to their speciation data [164]; the pyrolysis of 3-pentanone provided the ethyl radicals. The rate coefficient was referenced to the self-recombination kinetics of ethyl radical; the k(T) implemented by those authors is larger than recent calculations by Klippenstein et al. [107] by as much as a factor of four over the experiment's temperature range, meaning their reported k(T) may be overestimated by as much as a factor of two. Furthermore, the authors assumed the only significant reaction between ethyl and cyclohexene is abstraction from the allylic position.

It should be noted that the expressions reported by the NIST Chemical Kinetics Database for James and Steacie's rate coefficients for H abstraction from n-heptane, 1-heptene, 1-octene, cyclohexene, trans-4-octene, 1-heptyne, and diethyl ketone by

ethyl radical are incorrect. In Table 2 of James and Steacie's article, the reported Arrhenius A factors are on the order of 10^{-13} with units of cm^3 moleclule^{-1} s^{-1}, not on the order of 10^{13} with units of cm^3 mol^{-1} s^{-1}.

Our calculations are in reasonable agreement with the experimental data; if we increase our computed E_A by 1 kcal mol^{-1}, our calculations are in very good agreement, Figure 4-22. We thus recommend the rate coefficient $\log_{10}$(k / cm^3 mol^{-1} s^{-1}) = -0.559 ± 0.477 + 3.843 $\log_{10}$(T / K) – 4.559 kcal mol^{-1} / 2.3RT, which covers a broad temperature range.

4.2.54   C3H6 + CH3O = CH3OH + AC3H5

Tsang states that he estimates the kinetics of this reaction to be 1.5 times that of H abstraction from the secondary carbon of propane by methoxy [108]. The CH_3O + C_3H_8 value is based on experiments by Shaw and Trotman-Dickenson [79] on the total H-abstraction from propane by methoxy radical from 473 – 673 K; the source of methoxy radical was the pyrolysis of methyl nitrite and dimethyl peroxide, and the rate coefficient was calculated from the measured disappearance of propane in a flow reactor. However, what was actually reported by Tsang is 1.5 times the rate coefficient of hydroxymethyl (CH_2OH) abstracting from the secondary carbon of propane, a much smaller number. The NIST Chemical Kinetic Database currently stores the reported value of Tsang, not the intended value.

Our recommended value is significantly faster than the intended kinetic expression of Tsang, Figure 4-22c. This is not surprising, since abstractions forming allylic radicals are usually faster than those forming alkyl radicals. Our estimate is an order of magnitude faster at 300 K and increases to almost two orders at 2000 K.
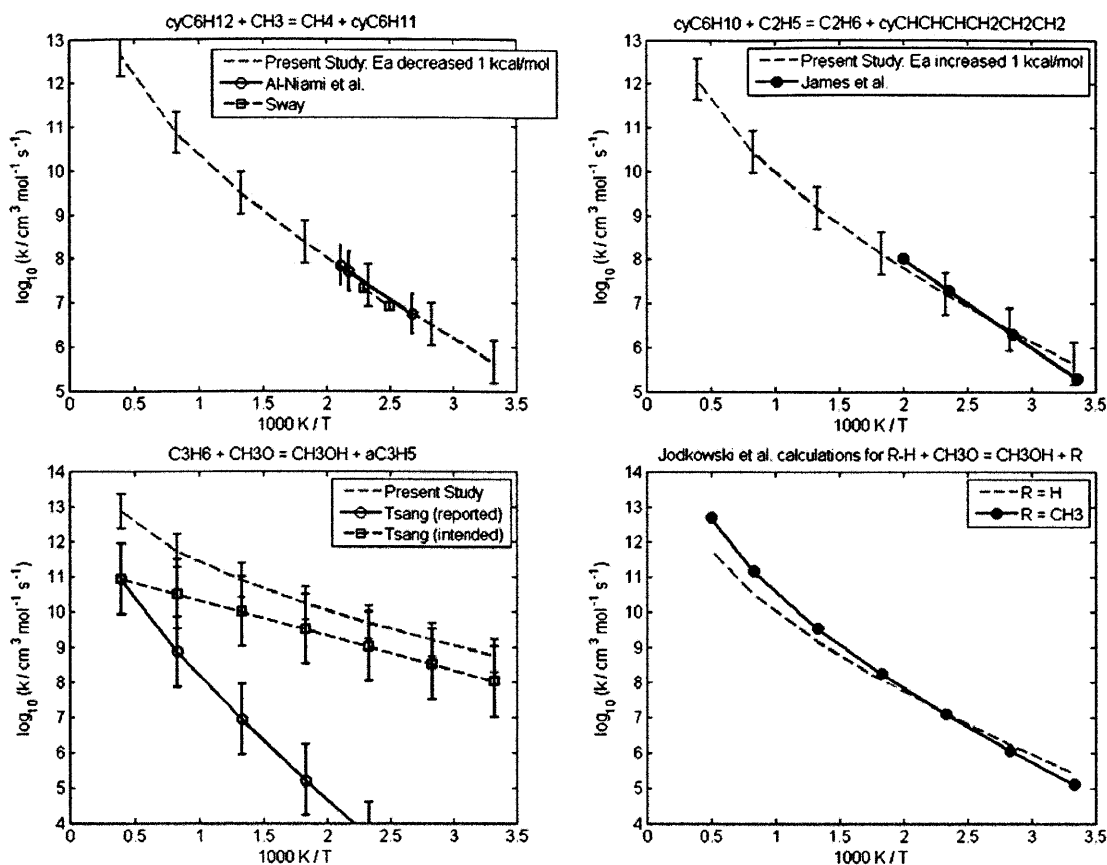
Figure 4-22: Rate coefficient for the abstraction from cyclohexane by methyl radical (upper-left), cyclohexene by ethyl radical (upper-right), and the allylic carbons of propene by methoxy radical (bottom-left). For the bottom-right figure, the Jodkowski et al. references are for abstraction from hydrogen and methane by methoxy radical, respectively.

Jodkowski et al. have calculated the rate coefficient for H abstraction from H_2 and methane by methoxy using conventional TST [165]; the geometries were computed using DFT and the energies were refined using the G2 method. Based on the bond energy, one would think the order of abstraction would be hydrogen, methane, then the secondary carbon of propane, and then the allylic carbon of propene, in ascending order of rate coefficients. Our computations and the calculations of Jodkowski et al. are consistent with this expected trend, Figure 4-22d; the Tsang estimate for H abstraction from propane by methoxy does not follow the trend. In the absence of experiments, we recommend use of our k(T) with an uncertainty of ten.

4.3   CONCLUSION

54 evaluated rate coefficients have been reported for hydrogen abstraction reactions involving hydrocarbon and oxygenated hydrocarbons. Trends within the evaluated rate coefficients, e.g. the abstraction from primary, secondary, and tertiary carbons by methyl radical, were discussed. These results should be useful in quickly estimating a hydrogen abstraction reaction's kinetics, whether by automation or by hand.

CHAPTER 5
1-BUTANOL PYROLYSIS AND COMBUSTION

Note: Some of the results reported here have been recently presented in References [166-168].

5.1   INTRODUCTION

Biofuels have generated much interest over the past few years as the world looks to move to a renewable fuel source. n-butanol is considered an attractive alternative and additive to gasoline, to an even greater extent than ethanol. Compared to ethanol, n-butanol has many superior properties as an alternative fuel [169]. These include:

- Higher energy content. Whereas ethanol has approximately two-thirds the energy density of gasoline (21.2 vs. 32.5 MJ/L), n-butanol has approximately 90 percent (29.2 MJ/L).

- Less volatile. n-butanol is six times less volatile than ethanol, whose evaporative emissions cause smog.

- Less corrosive. n-butanol is not as corrosive, so there are fewer issues with corroding aluminum or polymer components in fuel and dispensing systems.

- More hydrophobic. n-butanol is more hydrophobic and can be shipped in existing fuel pipelines whereas ethanol must be transported via rail, barge, or truck.

- n-butanol can be used as a replacement for gasoline liter-for-liter; 100% ethanol fuel (E100) is used in Brazil, but only after significant engine modifications.

Until recently, there were few published studies on the pyrolysis or oxidation of n-butanol. One of the first published n-butanol studies was the pyrolysis experiments of Barnard [170]. From observing formaldehyde in the product stream, but no other aldehydes or alcohols, Barnard proposed a decomposition mechanism to be the fission of the $CH_3CH_2CH_2-CH_2OH$ bond, followed by β-scission reactions of n-propyl radical (to form ethene and methyl radical) and of hydroxymethyl radical (to form formaldehyde and hydrogen atom). Smith $et\ al.$ studied diffusion flames of the four butanol isomers [171]. In their work on n-butanol, they proposed a mechanism where the chain initiation steps were molecular oxygen abstracting a hydrogen atom from n-butanol, followed by a series

107

of β-scissions to form products such as ethene, propene, and 1-butene. More recently, McEnally and Pfefferle doped a methane diffusion flame with one of the four butanol isomers [172], in order to study an oxygenated fuels' effect on particulate formation. One of their conclusions was that the dominant decomposition pathway for all four butanol isomers, in the non-premixed flame, was unimolecular dissociation, either through four-centered eliminations or C-C bond fissions. Yang *et al.* identified combustion intermediates in fuel-rich, premixed butanol flames at low pressure [173]. By comparing measured photoionization efficiency spectra against known ionization energies, the authors determined the relative ratios of intermediate species with equal molecular weight (*e.g.* ethanal and ethenol), further supporting that enols are important combustion intermediates [174]. No mechanisms were proposed, but a product study for all four butanol flames agreed well with previously published results on the relative importance of simple fission, complex fission, and hydrogen abstraction reactions in butanol decomposition. A recent study by Gu *et al.* investigated the effects of pressure, temperature, and equivalence ratio on flame stability by measuring the laminar flame speed and Markstein length of premixed n-butanol/air mixtures [175].

Detailed chemical mechanisms for the oxidation of n-butanol have been proposed within the last year. Dagaut and Togbé constructed a mechanism for the oxidation of a butanol/gasoline surrogate mixture (85/15 volume %) that demonstrated good agreement with data obtained in a jet-stirred reactor [176]. The experiments were conducted at a pressure of 10 atm, over a temperature range 770-1220 K, with an initial fuel concentration of 0.1 mole%. More recently, Dagaut and Togbé constructed a mechanism for the oxidation of a butanol/n-heptane mixture that was also validated against jet-stirred reactor data obtained at 10 atm [177]. Dagaut *et al.* also constructed a mechanism for the high-pressure oxidation of n-butanol in a jet-stirred reactor [178]. The experiments were conducted at a pressure of 10 atm, over a temperature range 800-1150 K, with an initial fuel concentration of 0.1 mole%. Their study concluded that n-butanol consumption was dominated by hydrogen-abstraction reactions from the alpha, beta, and gamma carbons of n-butanol. This mechanism was refined in a recent paper by Sarathy *et al.* [179] and agreed well with data obtained in a jet-stirred reactor at 1 atm, in an opposed-flow diffusion flame, and against laminar flame speeds, in addition to the aforementioned 10

108

atm jet-stirred reactor experiments. The revised n-butanol mechanism contained 117 species and 884 reactions. Moss *et al.* constructed a mechanism for the oxidation of the four isomers of butanol, comprised of 161 species and 1256 reactions, and compared their mechanism's predictions to ignition delay times measured in shock tube experiments [180]. The reflected shock temperature and pressure ranges measured were 1200-1800 K and 1-4 bar, respectively, with an initial fuel composition of 0.5 or 1.0 mole%. Their study concluded that n-butanol was consumed primarily by hydrogen-abstraction reactions. Recently, Black *et al.* [181] studied the autoignition delay time for n-butanol at equivalence ratios of 0.5, 1 and 2, at reflected shock pressures of 1, 2.6 and 8 atm, and temperatures from 1100 to 1800 K. The authors also computed the bond dissociation energies of n-butanol, using quantum chemistry. With this knowledge, a detailed chemical kinetic model composed of 243 species and 1446 reactions was constructed and tested against their ignition delay times and also against the 10 atm jet-stirred reactor data of Dagaut *et al.* [178].

The aforementioned reaction mechanisms have contributed to a large wealth of knowledge in a small period of time; within the last year, the community went from no published mechanisms on n-butanol decomposition to multiple mechanisms, validated with differing reactor models, over a large temperature range. However, for all mechanisms mentioned in the previous paragraph, the experiments were fuel dilute (in inert gas). In particular, this detail may limit the mechanism's ability to predict soot formation. To the authors' knowledge, there has been no n-butanol mechanism published that was validated against experiments with non-dilute fuel conditions. Furthermore, of the mechanisms mentioned in the previous paragraph, only the Black *et al.* [181] mechanism contains enol chemistry, which is known to be significant in combustion processes [174].

Herein we present a reaction mechanism for n-butanol to address these gaps. In addition to the data sets mentioned above, the mechanism is tested against two sets of data which were not modeled previously: new experimental pyrolysis data obtained at the Laboratory for Chemical Technology (LCT) of Ghent University and a butanol-doped methane diffusion flame previously reported by McEnally and Pfefferle [172]. Furthermore, we test our mechanism against the recent study on the autoignition delay time of butanal

[182]. Section 2 describes the experimental apparatus and techniques used in the pyrolysis experiments. Section 3 describes how the n-butanol reaction mechanism was constructed, by using an automated reaction mechanism generation software package, and how each of the reactors was modeled. Section 4 presents our mechanism's predictions against all the experimental data. Section 5 summarizes our findings and discusses the next steps in generating a robust reaction mechanism for n-butanol.

5.2   EXPERIMENTAL

5.2.1 PYROLYSIS

Experiments involving the pyrolysis of n-butanol were performed by our collaborators – Prof. Kevin M. Van Geem, Steven P. Pyl, and Prof. Guy B. Marin – at Gent University, Belgium. Details on the experimental apparatus and analytical techniques may be found in the manuscript mentioned at the beginning of this Chapter.

5.2.2 COMBUSTION

Experiments involving the combustion of n-butanol were not performed by the authors. Rather, we compare our mechanism to the results obtained by Dagaut *et al.* [178], Sarathy *et al.* [179], Moss *et al.* [180], Black *et al.* [181], and McEnally and Pfefferle [172].

5.3   COMPUTATIONAL METHODS

5.3.1 GENERATING THE REACTION MECHANISM

A reaction mechanism for n-butanol was constructed using the software package Reaction Mechanism Generator, or RMG, originally developed by Jing Song *et al.* [49, 183]. The RMG software is an automated, rate-based reaction mechanism generator that formulates pressure-dependent reaction mechanisms for isothermal, isobaric batch systems. The user must input the following information: system temperature and pressure; initial species concentrations and structures, in the form of a graph; termination goal, either conversion or time of reaction; and an error tolerance. If the user supplies no thermochemical information, the RMG software will estimate a species' thermochemistry using Benson's group-additivity method [58]; a reaction's high-pressure limit rate coefficient is estimated using RMG-defined reaction family templates, and fall-off effects

and chemical activation may be estimated using either the steady-state master equation method (hereafter referred to as the "Reservoir State" method) of Green and Bhatti [184] or the "Modified Strong Collision" approach of Chang et al. [185]. If the kinetics of a pressure-dependent network becomes too stiff, i.e. the difference in magnitude between the slowest and fastest rate is very large, the Reservoir State method may fail; if this occurs, RMG then attempts to solve the pressure-dependent network using the Modified Strong Collision approach. For this study, all pressure-dependent rates generated by RMG are reported in the Chebyshev polynomial format [186].

Table 5-1: The number of significant (and considered) species and reactions generated in a RMG simulation for the pyrolysis of n-butanol at 1000 K and 1 bar, as a function of the user-specified error tolerance and user-specified mode for handling pressure-dependence (see text for details and references regarding the pressure-dependence mode options). A considered species is any species generated during a single RMG simulation; a significant species is one whose flux exceeds some characteristic flux (which depends on the specified error tolerance).

	Significant species / reactions		
Error tolerance	High-Pressure Limit	Modified Strong Collision	Reservoir State
0.5	48 spcs / 265 rxns	18 spcs / 85 rxns	18 spcs / 85 rxns
0.1	72 spcs / 711 rxns	37 spcs / 616 rxns	34 spcs / 499 rxns
0.05	107 spcs / 1730 rxns	41 spcs / 807 rxns	43 spcs / 1043 rxns
0.01	(>125 spcs / 2208 rxns)	76 spcs / 2834 rxns	**71 spcs / 2980 rxns**

	Considered species / reactions		
Error tolerance	High-Pressure Limit	Modified Strong Collision	Reservoir State
0.5	4712 spcs / 17796 rxns	204 spcs / 420 rxns	204 spcs / 420 rxns
0.1	9981 spcs / 36001 rxns	1699 spcs / 4343 rxns	1033 spcs / 2780 rxns
0.05	36971 spcs / 126106 rxns	2169 spcs / 5729 rxns	2152 spcs / 6115 rxns
0.01	(>47250 spcs / 173954 rxns)	12571 spcs / 35936 rxns	**9165 spcs / 28326 rxns**

The RMG software enlarges the reaction mechanism using the rate-based algorithm [57]. One example of how the user-specified error tolerance and mode of handling pressure-dependence influences the size of a reaction mechanism reported by RMG is shown in Table 5-1. In the example of butanol pyrolysis at 1000 K and 1 bar with no pressure-dependence, the number of significant species increases three-fold and the number of

reactions increases nine-fold when tightening the error tolerance from 0.5 to 0.01. For the n-butanol system studied here, an error tolerance tighter than 0.01 caused the RMG simulation to run into memory limitations.

The output files of a RMG simulation include a reaction mechanism valid for the pressure and temperature simulated (in the form of a CHEMKIN file), species concentration profiles, and reaction flux profiles. The models constructed by the RMG software have been shown to be in good agreement with experimental data for the pyrolysis and combustion of hydrocarbons [187-190].

Although a mechanism generated by a RMG execution is only certain to be valid for a single condition (*i.e.* temperature, pressure, equivalence ratio, etc.), a more robust model can be generated using the Seed Mechanism feature. In RMG, a Seed Mechanism is a list of species and reactions the user can supply which must be included in the mechanism; RMG then adds additional species and reactions to the model by the rate-based method. Initially, the n-butanol reaction mechanism was constructed to match the experimental conditions of the doped methane diffusion flame of McEnally and Pfefferle [172]; this was accomplished by segmenting the flame into 38 regions, corresponding to the 38 experimentally-measured data points along the centerline of the flame. The simulation conditions of the first RMG execution matched those at the burner outlet, as described in Ref. [172]: temperature of 298 K, atmospheric pressure, and initial mole fractions of 0.4964 CH_4, 0.4857 N_2, 8400ppm Ar, 3500ppm n-butanol, and 6000ppm O_2. [Note: Although no O_2 leaves the burner, a non-zero concentration of oxygen is measured near the burner exit, due to entrainment; thus, the RMG simulation was supplied with the experimentally measured concentration of O_2, extrapolated from an axial distance from the burner of 10 mm to 0 mm; the N_2 mole fraction was adjusted to ensure the mole fractions summed to one.] Finally, the GRI-Mech 3.0 mechanism [191], omitting nitrogen chemistry, and Marinov ethanol oxidation mechanism [192] were both supplied as a Seed Mechanism. Thus the mechanism output from this simulation included the GRI-Mech 3.0 and Marinov ethanol oxidation mechanisms, in addition to the species and reactions RMG added using the rate-based methodology.

The next region of the flame, spanning axial positions between 2 and 4 mm from the burner, was modeled with the following conditions: atmospheric pressure, the

experimentally-measured centerline temperature at $z = 2$ mm, and initial mole fractions equal to the outlet mole fractions from the previous simulation. Furthermore, the mechanism generated from the previous simulation was supplied as the Seed Mechanism. This process was continued for the remaining 36 regions, which yielded a mechanism valid at atmospheric pressure under rich conditions, spanning temperatures from 300-1900 K.

The mechanism was further expanded, using similar Seed Mechanism approaches, to include:

- Infinitely-rich, *i.e.* pyrolysis, chemistry using the experimental conditions described in Section 5.2.1. The simulations were performed at 1.5 atm with an initial n-butanol mole fraction of 1.0, over a temperature range of 900-1200 K.

- Lean chemistry using the most oxygen-rich experimental conditions described in Ref. [179]. The simulations were performed at 1.0 atm with mole fractions of 0.1% n-butanol, 2.4% O_2, 0.01% H_2O, and 97.49% N_2 over a temperature range of 800-1260 K.

Finally, flux and sensitivity analysis from the different reactor models, described in the next section, identified important reactions where more accurate rate estimates were required. These numbers were either obtained from the literature or calculated using quantum chemistry, see Section □. The final n-butanol reaction mechanism, the topic of this study, contains 263 species and 3381 reactions.

5.3.2 REACTOR MODELS FOR THE EXPERIMENTS

Most of the experiments were modeled using the CHEMKIN-Pro software package [193]; the doped methane diffusion flame was modeled using an in-house code constructed by Sharma *et al.* [190].

5.3.2.1 PYROLYSIS EXPERIMENTS

For simulating the pyrolysis experiments in the bench scale set-up, the reaction network was implemented in CHEMKIN-Pro. The laminar flow reactor was simulated first using CHEMKIN's cylindrical shear flow option to investigate the importance of radial temperature and concentration gradients for this set-up. The results of these simulations can be found in the Supplemental Information. Only very small radial concentration and

temperature gradients are computed, indicating that the assumption of using a plug flow reactor model for this reactor is indeed valid, as assumed by Chen and Froment [194]. Extensive analytical studies on laminar flow reactors have been performed previously; see, for example, the review of Varma and Aris [195] and the work of Lee et al. [196]. Cutler et al. [197] have summarized different optimization criteria used by various researchers in extracting kinetic information. Based on the characteristic times and dimensionless numbers pertinent to our tubular flow reactor, the use of plug flow treatment for the tubular reactor data is valid; these calculations are reported in the Supplemental Information.

Hence, we have employed the CHEMKIN-Pro plug flow reactor (PFR) module for modeling the tubular reactor. The PFR module was supplied with the measured temperature and pressure profile, and the reactor dimensions used were those discussed in Section 5.2.1. The mass flow rate for all experiments was 6.7463×10^{-2} grams of n-butanol per second. The default absolute and relative tolerances were sufficient for convergence.

To gain further insight in the reaction mechanism and the role of certain kinetic parameters, a rate of production and sensitivity analysis is carried out for the pyrolysis experiments. The normalized sensitivity coefficients are calculated as follows:

$$\tilde{S}_{ij} = \frac{A_j}{X_i} \frac{\partial X_i}{\partial A_j} = \frac{\partial(\ln X_i)}{\partial(\ln A_j)} \tag{3.1}$$

In which the effect of the change on the pre-exponential factor A_j of reaction j on the mole fraction X_i of component i is evaluated. Note that the reactions are defined as reversible reactions. The consequence of this is that the equilibrium coefficients are kept fixed while changing the rate coefficients, i.e. forward and reverse rates are changed in concert.

5.3.2.2 DOPED METHANE FLAME

The reactor model used to simulate the doped methane flame is the same reactor model constructed and utilized by Sharma et al. [190] in their work on constructing a reaction mechanism for three of the hexadiene isomers. A brief description of the reactor model follows; please see the reference for a more detailed explanation.
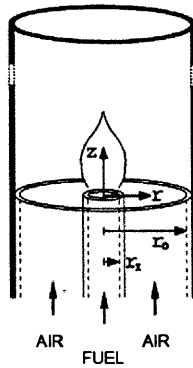
Figure 5-1: Geometry of the doped methane flame studied by McEnally and Pfefferle [172]. Values of r_I and r_o are 5.5 mm and 54 mm, respectively. Picture from Ref. [198].

The doped methane flame (Figure 5-1) was modeled as a steady-state system, using an axisymmetric geometry. In general, solving this problem requires solving for the temperature, axial and radial velocities, and species concentration profiles as a function of r and z. Bennett et al. [198] solved this problem for an undoped methane diffusion flame, comparing their computational results to experimental results obtained using the same apparatus as described in Ref. [172]. The McEnally and Pfefferle studies on doped methane flames, Refs. [172, 199, 200] among others, have demonstrated that for the small amount of dopant used, the centerline temperature profile exhibits no significant change between the undoped- and doped-flame (Figure 5-2). Hence, we used the temperature profile obtained in the numerical solution of the undoped methane flame as the temperature profile for the doped methane flame. Furthermore, since the temperature profile was not greatly affected (< 1% difference), we assumed the velocity profiles would not be affected significantly either. With the temperature and velocity profiles known, the Sharma et al. reactor model only needs to solve for the species concentration profiles in the doped methane flame.

115
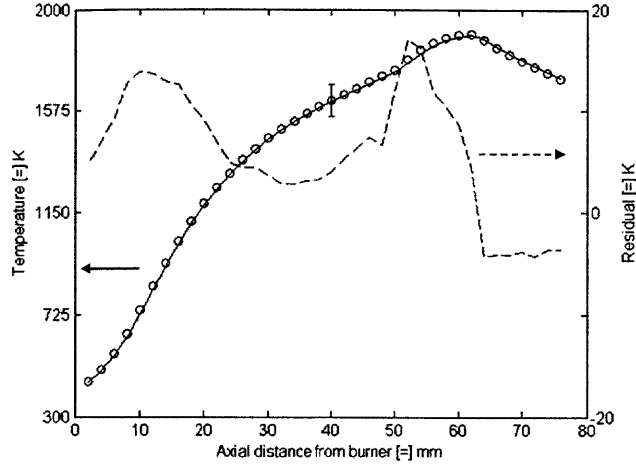
Figure 5-2: Experimental centerline temperature profile for the doped and undoped methane flame, as measured in Ref. [172]. Solid line is the undoped flame, circles are the doped flame, and the dashed line is the residual (doped - undoped).

The form of the species conservation equation is given in Equation (3.2).

$$\rho v_z \frac{\partial Y_i}{\partial z} + \rho v_r \frac{\partial Y_i}{\partial r} = \gamma_i MW_i - \frac{1}{r}\frac{\partial}{\partial r}(r\rho v_{r,i}Y_i) - \frac{\partial}{\partial z}(\rho v_{z,i}Y_i) \tag{3.2}$$

ρ is the total density, v_z is the axial velocity, Y_i is the mass fraction of species i, v_r is the radial velocity, γ_i is the molar rate of production of species i, MW_i is the molecular weight of species i, and the radial and axial diffusive flux terms are given in Equations (3.3) and (3.4), respectively. D_i is the multi-component diffusivity coefficient for species i.

$$v_{r,i}Y_i = -D_i(\underline{Y})\frac{\partial Y_i}{\partial r} \tag{3.3}$$

$$v_{z,i}Y_i = -D_i(\underline{Y})\frac{\partial Y_i}{\partial z} \tag{3.4}$$

The Soret and Dufour effects are neglected. If the axial diffusive term, the last term on the right-hand side of Equation (3.2), is neglected for all species, the species conservation equation can be solved numerically using the Method Of Lines [201]; this approximation is reasonable considering that the Peclet number on the centerline exceeds 70, and because in this flame geometry the important diffusion effects are perpendicular to the convective flow. Moving the radial convective term from the left-hand side of Equation (3.2) to the right-hand side isolates all r-dependent terms to the right-hand side of the equation, resulting in Equation (3.5).

116

$$\rho v_z \frac{\partial Y_i}{\partial z} = \gamma_i MW - \rho v_r \frac{\partial Y_i}{\partial r} - \frac{1}{r} \frac{\partial}{\partial r}(r \rho v_{r,i} Y_i) \qquad (3.5)$$

Using centered finite differences to approximate all derivatives on the right-hand side of Equation (3.5) reduces the overall problem from a partial differential equation to a first-order ordinary differential equation initial value problem (ODE-IVP). This problem can now be solved using a commercially available ODE solver software package, such as DASPK 3.1 [202], if the temperature and velocity fields are supplied. This formulation has > 18,000 ($N_{species}$ * $N_{radial\ mesh\ points}$) state variables, and the ODE system is stiff, so this computation is still pretty demanding. To accelerate the solution, the Jacobian was computed analytically using parallel computers; see Ref. [190] for details.

The boundary conditions for the doped methane flame were handled in the following way. Ignoring the axial diffusion term leaves one boundary condition to satisfy in the z-direction for each species. This boundary condition materializes as the initial condition in the ODE-IVP system and is known for all species in the system: all species mole fractions are zero except for the species CH_4, N_2, O_2, Ar, and n-butanol. There are two boundary conditions in the r-direction for each species. Since the geometry of the problem is assumed to be axisymmetric, $dY_i/dr = 0$ at $r = 0$ for all species. The other boundary condition we impose in the r-direction is $dY_i/dr = 0$ at the edge of the reactor model, 54 mm from the center of the burner; the burner has an outer diameter of 6.35 mm.

5.3.2.3 JET-STIRRED REACTORS

The new mechanism was tested against the jet-stirred reactor (JSR) data of Dagaut et al. [178] and Sarathy et al. [179]. Each of these reactors was simulated using the Perfectly-Stirred Reactor (PSR) module in CHEMKIN-Pro. The isothermal reactor was solved using the default steady-state solver for a reactor volume of 30.5 cm^3. The temperature range simulated was 800-1160 K and 800-1260 K for the 10 atm and 1 atm JSR, respectively; the surface temperature for each simulation was equal to the reactor temperature. For the 10 atm JSR: the initial mole fraction of n-butanol was 0.1%, the equivalence ratios simulated were 0.5, 1.0, and 2.0 with N_2 as the bath gas, and the residence time simulated was 0.7 seconds. For the 1 atm JSR: the initial mole fractions of n-butanol and H_2O were 0.1% and 0.01%, respectively, the equivalence ratios simulated were 0.25, 0.5, 1.0, and 2.0 with N_2 as the bath gas, and the residence time

simulated was 0.07 seconds. The absolute and relative tolerance was set to 1×10^{-16} and 1×10^{-8}, respectively; the absolute and relative tolerance for pseudo time stepping was also set to 1×10^{-16} and 1×10^{-8}, respectively.

5.3.2.4 OPPOSED-FLOW DIFFUSION FLAME

The mechanism was also tested against the opposed-flow diffusion flame data of Sarathy *et al.* [179] using the Diffusion or Premixed Opposed-flow Flame module in CHEMKIN-MFC[203]. The energy equation was solved at atmospheric pressure using the experimentally-measured temperature profile as an initial guess; cylindrical coordinates, a windward differencing scheme, thermal diffusion, and a mixture-averaged transport model were employed. The simulated conditions for one of the inlet streams: a mass flow rate of 1.31×10^{-2} g cm^{-2} s^{-1} and an inlet temperature of 83.0°C, with mole fractions of 0.0589 and 0.9411 for n-butanol and N_2, respectively. The simulated conditions for the other inlet stream, located 20 mm from the first: a mass flow rate of 1.26×10^{-2} g cm^{-2} s^{-1} and an inlet temperature of 150.0°C, with mole fractions of 0.4225 and 0.5775 for O_2 and N_2, respectively. The values for the gas flow rates come from [204]. The initial grid had 100 uniform points and the maximum number of grid points was set to 750. The absolute and relative tolerances were 1×10^{-9} and 1×10^{-4}, respectively; the absolute and relative tolerances for pseudo time stepping were 1×10^{-9} and 1×10^{-4}, respectively. The adaptive grid control based on solution gradient and curvature were both set to 0.13.

5.3.2.5 SHOCK TUBE

The new mechanism was further tested against the n-butanol ignition delay data of Moss *et al.* [180] and Black *et al.* [181] and the butanal ignition delay time data of Davidson *et al.* [182]. Each of these shock tube experiments were simulated using the Closed Homogenous Batch Reactor module in CHEMKIN-Pro. The energy equation was solved, constraining the volume of the reactor. The initial temperatures, pressures, and mole fractions simulated are summarized in Table S4 of the Supplementary Information. The Legacy Solution Technique was employed, using the default absolute and relative tolerances. The ignition delay time was computed in multiple ways, including: the time that maximized [C_2H]*[O] and the time to reach half the maximum [OH]; all computed values differed by less than 10%.

5.3.3 Estimating species transport properties

In addition to requiring species thermochemistry and reaction rate coefficients, some of the aforementioned reactor models require transport properties for every species in the mechanism. The CHEMKIN-II [205] and Transport [206] subroutine libraries were used to estimate species transport properties. The transport properties for the species present in the GRI-Mech 3.0 mechanism were accepted as is; for species present in the Marinov ethanol oxidation mechanism but not in GRI-Mech 3.0, the transport properties reported by Marinov were employed. For all remaining species, we estimated the Lennard-Jones parameters using an empirical relationship that depends on a species' critical temperature and pressure [207], Equations (3.6) and (3.7). In these equations, k_B is the Boltzmann constant.

$$\sigma = 2.44 \left(\frac{T_c}{P_c} \right)^{1/3} \tag{3.6}$$

$$\varepsilon_A / k_B = 0.77 T_c \tag{3.7}$$

The critical temperature and pressure for each molecule were estimated using a group-additivity approach devised by Joback [208], Equations (3.8)–(3.10). $v_i^{(j)}$ is the number of groups of type j in compound i, n_a is the total number of atoms in the molecule, and T_b is the normal boiling point.

$$T_c = \frac{T_b}{0.584 + 0.965 \sum_j v_j^{(i)} \Delta_{T_{cj}} - \left(\sum_j v_j^{(i)} \Delta_{T_{cj}} \right)^2} \quad \text{(in K)} \tag{3.8}$$

$$P_c = \frac{1}{\left[0.113 + 0.0032 n_a - \sum_j v_j^{(i)} \Delta_{P_{cj}} \right]^2} \quad \text{(in bar)} \tag{3.9}$$

$$T_b = 198 + \sum_j v_j^{(i)} \Delta_{T_{bj}} \quad \text{(in K)} \tag{3.10}$$

Note that this estimate of transport properties does not account for intermolecular interactions due to the charge distributions on the molecules. It was assumed that rotational relaxation to the bath gas temperature was fast (single collision). The indicator regarding the geometrical configuration of the molecule was determined from the molecule's structure. For radical species R•, the transport properties of the stable parent

molecule R-H were used. As discussed in Section 5.4.2.5, the doped flame simulations are not sensitive to most of these numerical values so this approximate treatment is adequate.

5.3.4 REFINING THE REACTION MECHANISM

The following changes have been made to the GRI-Mech 3.0 mechanism:

- Removed all nitrogen-based chemistry (17 species, 106 reactions).

- Removed all C_3H_7 chemistry (1 species, 13 reactions): The GRI-Mech 3.0 C_3H_7 species is a convolution of the 1- and 2-propyl radical, which are treated as two distinct species by RMG.

Furthermore, the following reactions' rate coefficients were updated with the values reported in the noted reference:

- C2H2 + H (+m) = C2H3 (+m) [192]

- H + O2 = O + OH [209]

- H + CH2O = HCO + H2 [111]

- HO2 + CH3 = O2 + CH4 [111]

- H + C2H4 = C2H3 + H2 [117]

- OH + C2H6 = C2H5 + H2O [117]

- C2H3 + O2 = HCO + CH2O [117]

- H + CH2CO = CH3 + CO [210]

- OH + CH4 = CH3 + H2O [211]

- HO2 + CH3 = OH + CH3O [212]

- HO2 + CH2O = HCO + H2O2 [213]

- CH3 + CH3 (+m) = C2H6 (+m) [107]

- CH2OH + O2 = HO2 + CH2O [103]

- C2H3 + O2 = CH2CHO + O [214]

5.3.5 QUANTUM CHEMICAL CALCULATIONS

For some important reactions in the mechanism, the high pressure rate coefficient was calculated with canonical transition state theory using the rigid rotor harmonic oscillator (RRHO) approximation, Equation (3.11), with hindered rotor corrections.

120

$$k = \kappa(T)\frac{k_B T}{hC^0}\exp\left(-\left(G^{TS} - \sum_{\text{Reactant}} G^i\right)/RT\right)$$ (3.11)

k is the reaction rate coefficient, $\kappa(T)$ is the tunneling correction, k_B is the Boltzmann constant, T is the temperature, h is the Planck constant, C^0 is the standard-state concentration, R is the universal gas constant, and G^i is the gas-phase Gibbs free energy of species i at concentration C^0.

An asymmetric Eckart tunneling correction [71] was applied for the transition states, using the formalism described by Johnston and Heicklen[215]; Johnston and Heicklen's Equation (15) was corrected, as noted in the references of Garrett and Truhlar[73]. The Gibbs free energy of the reactants and transition states were computed through quantum calculations. The CBS-QB3 calculations [68, 216, 217] were performed using the Gaussian03 software suite [69] to calculate the electronic energies, vibrational frequencies, and moments of inertia. The frequencies given by the CBS-QB3 calculations were calculated using the B3LYP/CBSB7 method and are scaled by a factor of 0.99 [70]. The RRHO approximation with hindered rotor corrections was used to calculate the thermal correction, entropy, and heat capacity of each species. For each hindered rotor, a scan at dihedral increments of 12° was performed using the B3LYP/6-31G(d) method, re-optimizing the geometry at each step, and the resulting energies were fit to a Fourier series, Equation (3.12). The reduced moment of inertia $I^{(2,3)}$ of the equilibrium geometry was computed [75] and the resulting one-dimensional Schrodinger equation was solved. For the heats of formation, Bond Additivity Corrections (BAC) and spin orbital corrections were applied, as suggested by Petersson et al. [218]. These calculations were performed using an in-house software package, CanTherm [74].

$$V(\phi) = \sum_{m=0}^{5}\left(A_m \cos(m\phi) + B_m \sin(m\phi)\right)$$ (3.12)

5.3.6 PRESSURE-DEPENDENT NETWORKS

The reported mechanism contains reaction rates for 147 different pressure-dependent networks. More detailed information for some of the networks is discussed in the following sections, including the identity of each well, the value and reference for the high-pressure-limit rate coefficients, and the numerical method employed.

121

5.3.6.1 C4H10O NETWORK

The C4H10O pressure-dependent network was solved in RMG using the Reservoir State method. The high-pressure-limit rate for each of the bond fission reactions (3 carbon-carbon, 1 carbon-oxygen, 4 unique carbon-hydrogen, and 1 oxygen-hydrogen) was computed using microscopic reversibility: the recombination rate of a hydrogen atom and heavy-atom radical was assumed to be a temperature-independent 2×10^{14} cm^3 mol^{-1} s^{-1} and the recombination rate of two heavy atom radicals was assumed to be a temperature-independent 1×10^{13} cm^3 mol^{-1} s^{-1}. The thermochemistry of H atom, methyl, ethyl, 2-hydroxyethyl, n-propyl, hydroxymethyl, n-butyl, and hydroxyl radical came from the Active Thermochemical Tables (ATcT) [109]; the thermochemistry of n-butanol, 4-hydroxybutyl, 3-hydroxy-1-methylpropyl, 1-(hydroxymethyl)propyl, 1-hydroxybutyl, n-butoxy, and 3-hydroxypropyl radical came from this study, using quantum chemistry as described in Section 5.3.5.

The water elimination's kinetics was also computed using quantum chemistry as described in Section 5.3.5; the rate was calculated as 3.20×10^4 T$^{2.53}$ exp(-62.94 kcal/mol / RT) s^{-1}. We compute the barrier enthalpy at 0 K, E_0(0 K), for the four-centered elimination of water from n-butanol to be 67.69 kcal/mol at the CBS-QB3 level, in excellent agreement with the value of 67.88 kcal/mol computed by Moc et al. [219].

5.3.6.2 C4H9O NETWORK

The C4H9O pressure-dependent network was solved in RMG using the Modified Strong Collision approximation. The network contained: 4-hydroxybuyl radical and its 2 sets of β-scission products, 3-hydroxy-1-methylpropyl radical and its 3 sets of β-scission products, 1-(hydroxymethyl)propyl radical and its 4 sets of β-scission products, 1-hydroxybutyl radical and its 3 sets of β-scission products, n-butoxy radical and its 2 sets of β-scission products, and the 10 isomerizations between each of the C4H9O radicals. All high-pressure-limit rates were estimated by RMG. All species thermochemistry were also estimated by RMG, with the following exceptions: the thermochemistry for H atom, methyl, ethyl, n-propyl, hydroxymethyl, and 2-hydroxyethyl radical came from the ATcT; and the thermochemistry for the C4H9O radicals were computed in this study.

5.3.6.3 C4H9 NETWORK

The C4H9 pressure-dependent network was solved in RMG using the Reservoir State method. The network contained 1-butyl radical, its isomerization to 2-butyl radical (via the three- and four-member ring transition states), the two β-scission reactions of 1-butyl radical (forming H atom + 1-butene and ethane + ethyl radical), and the three β-scission reactions of 2-butyl radical (forming H atom + 1-butene, H atom + 2-butene, and propene + methyl radical). All high-pressure-limit rates were estimated by RMG. The thermochemistry employed for H atom, 1-butyl, ethyl, and methyl radical are from the ATcT; the thermochemistry for 1-butene, 2-butene, propene, ethene, and 2-butyl radical were estimated by RMG.

5.3.6.4 C4H8 NETWORK

The C4H8 pressure-dependent network was solved in RMG using the Reservoir State method. The network contained 1-butene; the products of the six bond fissions of 1-butene; 2-butene; and the products of the three bond fissions of 2-butene (one of which is equivalent to one of the bond fission products of 1-butene). The high-pressure-limit rate for each of the bond fission reactions was estimated using microscopic reversibility; all recombination rates were estimated by RMG. The thermochemistry employed for H atom, methyl, and ethyl radical are from the ATcT; all remaining species thermochemistry were estimated by RMG: 1-butene, 2-butene, allyl, vinyl, 1-buten-1-yl, 1-methylenepropyl, 1-methyl-2-propenyl (treated as equivalent to 2-buten-1-yl within RMG), 3-buten-1-yl, 1-methyl-1-propen-1-yl, and 1-propenyl radical.

5.4   RESULTS

Our n-butanol reaction mechanism was employed in all reactor models mentioned previously. Here, and in the Supplemental Information, the model predictions are compared with all experimental data. Also, results obtained with the reaction mechanisms of Sarathy et al. [179], Moss et al. [180], and Black et al. [181] are presented and discussed.

5.4.1 PYROLYSIS EXPERIMENTS

The measured and predicted n-butanol conversions as a function of the maximum temperature are plotted in Figure 5-3. Our mechanism matches the data well, within 10% over the entire temperature range. The Sarathy *et al.* mechanism produces the correct shape of the temperature dependence, but overestimates the conversion for all experiments. The Moss *et al.* mechanism does not capture this data set well: the conversion is too low at low temperature, while at higher temperatures the conversion is overestimated. The predicted conversion with the mechanism of Black *et al.* agrees well with the experimentally measured conversion.
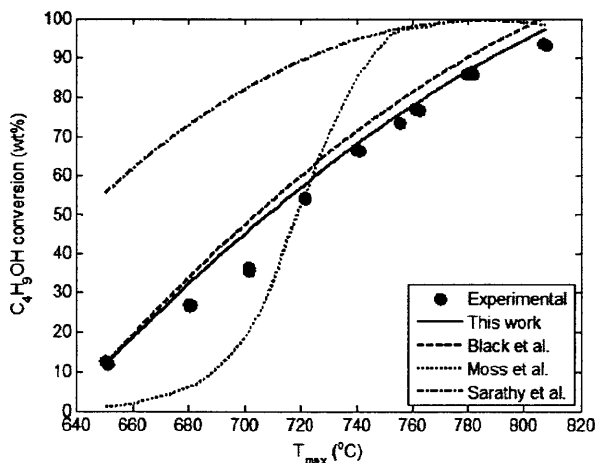
Figure 5-3: Comparison between measured and predicted conversion of n-butanol in the pyrolysis reactor.

Looking more closely at the results presented in Table 5-2 it can be seen that our mechanism agrees well for all product yields, except CO and formaldehyde are underestimated. The results for the other mechanisms for these 2 components have even larger discrepancies. In our mechanism, most of the formaldehyde is formed via a C-H scission reaction of the hydroxymethyl radical. Another significant pathway in our model is the route from the n-butoxy radical to formaldehyde and n-propyl radical. For the Black et al. mechanism, these are also the dominant pathways. In the mechanism of Sarathy et al., the n-butoxy pathway is not significant, while in the mechanism of Moss et al. the hydroxymethyl radical C-H scission is very slow. Most likely the reactions involving the n-butoxy radical are not fully understood yet.

For the other products, the mechanism of Black *et al.* agrees reasonably well with data found in Table 3, although important C5 and aromatic chemistry is clearly missing. The mechanism of Moss *et al.* is not able to capture most the data well, although for products such as ethene, ethane, and methane, a reasonable agreement is obtained. Some products are missing or the yield is very small such as propene, 1,3-butadiene, benzene, and propyne; the predicted butanal yield is significantly overestimated. The Sarathy *et al.* mechanism is able to capture the trends of the major product yields, but some pathways to C5 and aromatic species are incomplete.

Table 5-2: Comparison between predicted product yields (wt%) from different mechanisms and experimental data for n-butanol pyrolysis.

Conditions: $T_{inl} = 463°C$, $T_{max} = 781°C$, $P = 1.72 \times 10^5$ Pa, $F = 6.75 \times 10^{-2}$ g s^{-1}

	Black et al.	Sarathy et al.	Moss et al.	Present Model	Expt.
H2	0.98	1.15	1.93	1.12	1.18
H2O	7.60	6.73	2.37	7.83	7.61
CO	10.43	23.21	28.75	15.62	15.08
CH4	9.03	18.10	16.60	11.48	11.25
CH2O	0.49	0.03	0.00	0.77	1.55
CH3OH	4.01	0.59	0.18	0.71	1.01
C2H5OH	0.04	0.00	0.00	0.32	0.06
C2H2	0.79	0.12	0.16	0.69	0.12
C2H4	22.06	18.99	24.18	18.56	17.22
C2H6	3.19	5.13	8.66	5.97	5.02
CH3CHO	7.15	3.60	3.13	4.66	5.85
1-C3H4	0.14	0.10	0.00	0.27	0.08
1,2-C3H4	0.10	0.03	0.00	0.14	0.05
C3H6	9.37	9.59	1.23	9.32	10.80
C3H8	0.94	1.36	0.00	0.23	0.48
1,3-C4H6	3.16	5.77	0.00	2.40	1.52
1-C4H8	3.75	0.40	0.27	2.00	2.00
2-C4H8	0.25	1.41	0.00	1.23	0.63

C4H8O	0.06	1.03	6.57	0.32	0.31
1-C5H10	0.00	0.00	0.21	0.54	0.37
1,3-C5H6	0.00	0.06	0.00	0.09	0.39
C6H6	0.00	0.24	0.00	0.97	0.89
C7H8	0.00	0.00	0.00	0.03	0.14
$X_{nC4H9OH}$	91.68	98.55	99.80	89.69	85.95

Looking at the trends of the products ethene, butanal + 1-buten-1-ol, and benzene shown in Figure 5-4a-c respectively, our mechanism matches the data well. In particular, the local maximum in the butanal curve is located at the appropriate temperature. However, the presented mechanism slightly overestimates the benzene yield. More accurate values for the kinetics of the dominant reaction paths to aromatics would improve the quality of the presented mechanism.

The Sarathy *et al.* mechanism finds a local maximum for butanal, but the maximum is not at the correct temperature. The discrepancy in their model is caused by the fast rates of methyl and ethyl radical abstracting hydrogen atoms from n-butanol. Hence, the predicted yields of methane and ethane are overestimated; the discrepancy is particularly large at low temperatures. Their overestimation of the butanal yield is due to their β-scission rate of the n-butoxy radical, forming formaldehyde and n-propyl radical, being very slow compared to their β-scission rate of n-butoxy yielding butanal and H atom. The predicted benzene yields using the Sarathy *et al.* mechanism are low compared to the measured experimental data. The mechanism of Black *et al.* does a good job for ethene and butanal, but does not include any reactions forming benzene. The Moss *et al.* mechanism does not predict the correct trend for ethene or butanal, and it also does not include pathways to benzene.
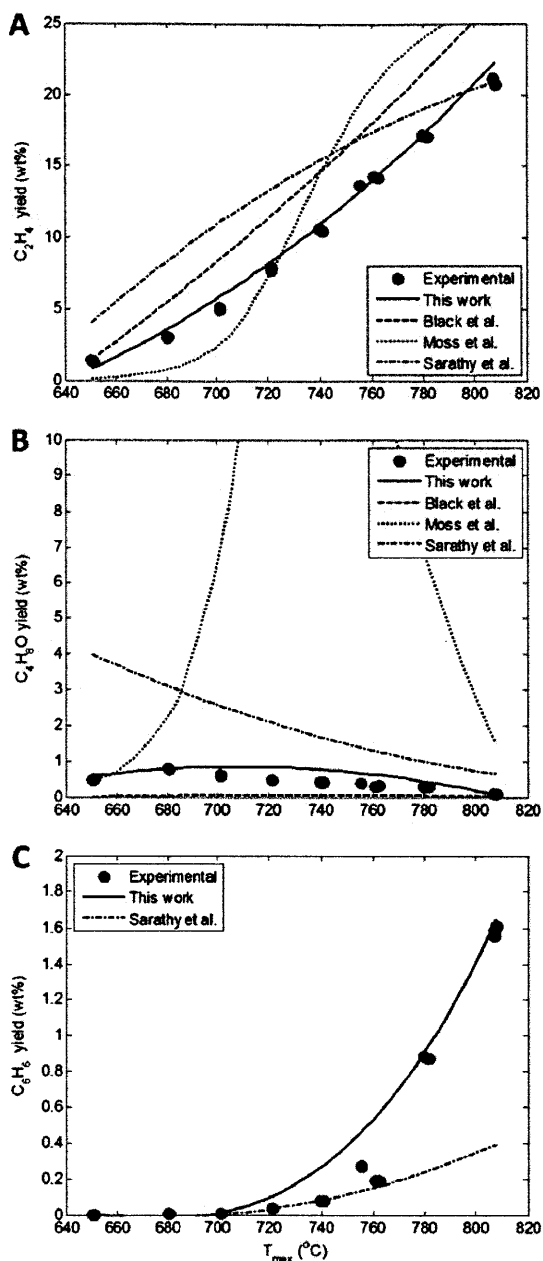
Figure 5-4: Measured and predicted yields for [a] ethene [b] butanal + 1-buten-1-ol and [c] benzene as a function of temperature in the pyrolysis reactor.

The reaction path analysis diagram for the decomposition of butanol, based on the new mechanism, is shown in Figure 5-5. The paths towards the main products all start from hydrogen abstractions by hydrogen atom and methyl radical, giving the different C4H9O radicals; the five H-abstraction reactions from n-butanol by H atom and methyl radical were computed in this study. The C4H9O radicals decompose and form ethene, propene, formaldehyde, butanal, ethenol, etc. The keto-enol isomerization reactions, which

convert enols into the corresponding aldehydes, are clearly important, although the chemistry of enols is still not completely understood. The reaction rate expression used in this study for all tautomerization reactions is $k = 8.59 \times 10^{11} \, T^{0.318} \exp(-55900 \text{ cal/mol} / RT) \, s^{-1}$, as recommended by da Silva *et al.* [220]. The activation energy is in good agreement with studies by Yamada *et al.* [221] and Teixeira-Dias *et al.* [222]. Since the work of Taatjes *et al.* [174] significant steps have been made, but the current level of knowledge of enol chemistry is far from complete.
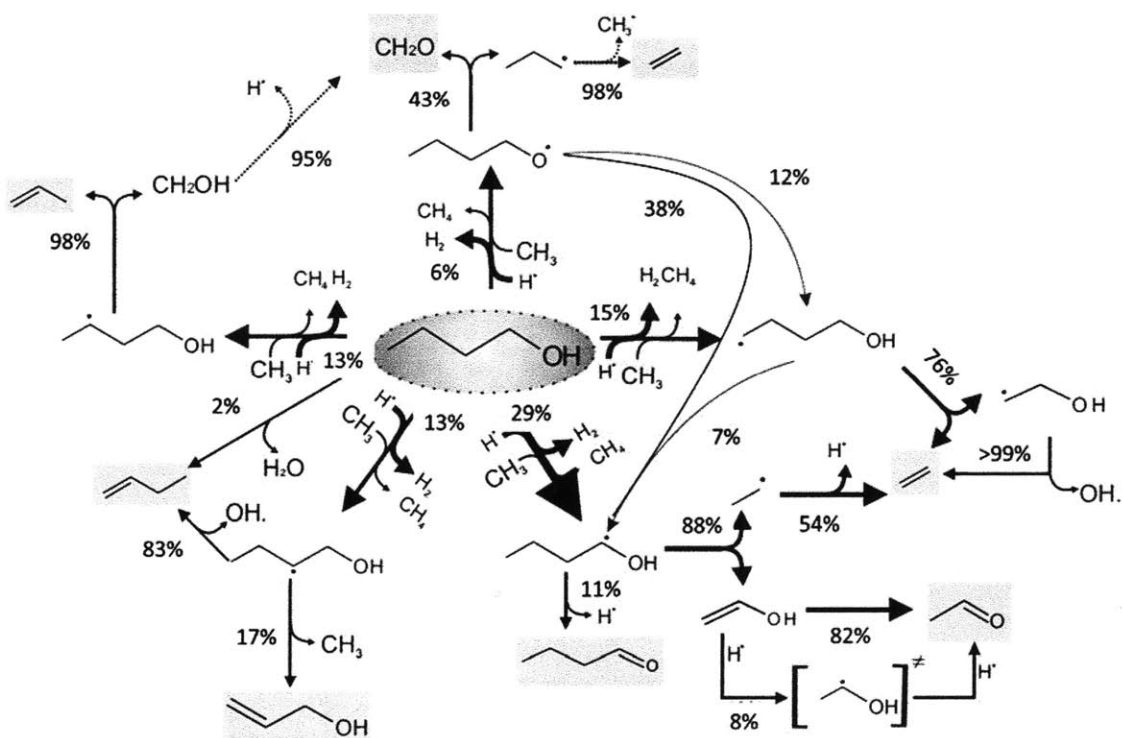
Figure 5-5: Reaction pathway analysis for n-butanol pyrolysis towards the main products performed at the maximum temperature along the reactor coil. The arrow thickness and percentages represent the reaction rate of decomposition for that species. $T_{inl} = 473°C$, $T_{max} = 807°C$, $P = 1.72 \times 10^5$ Pa, $F = 6.75 \times 10^{-2}$ g s^{-1}

The results of the sensitivity analysis are shown in Table 5-3. It is obvious that the C-C scission reactions are dominating at the entrance of the reactor where the initial n-butanol is converted. Not surprising is the dominance of one particular C-C scission, *i.e.* the one giving n-propyl and hydroxymethyl radical. The latter is in agreement with the bond dissociation energies calculated by Black *et al.* [181]. Near the end of the reacting zone, the species concentrations are still sensitive to this reaction but to a lesser extent.

Table 5-3: Reactions with the highest sensitivity coefficients affecting major species from n-butanol pyrolysis at operating conditions:
$T_{inl} = 463°C$, $T_{max} = 781°C$, $P = 1.72\text{x}10^5$ Pa, $F = 6.75\text{x}10^{-2}$ g s^{-1}.

Reaction equations	Normalized sensitivity coefficient (x 10^2)											
	Reactor inlet						Reactor outlet					
	CO	C2H4	C2H6	benzene	CH3CHO	nC4H10O	CO	C2H4	C2H6	benzene	CH3CHO	nC4H10O
C4H9OH = CH3 + CH2CH2CH2OH	90	45	45	463	42	0	2	0	-3	14	-4	-17
C4H9OH C2H5 + CH2CH2OH	26	13	14	130	22	0	0	2	1	6	-4	-9
C4H9OH = n-C3H7 + CH2OH	167	82	84	836	77	0	6	3	-5	14	-21	-36
C2H5 = C2H4 + H	0	4	-1	8	0	0	-1	7	-18	7	-5	-6
C4H9OH + H = H2 + CH2CH2CH2CH2OH	0	3	0	0	0	0	0	4	0	0	0	-9
C4H9OH + H = H2 + CH3CHCH2CH2OH	0	0	0	0	0	0	0	0	0	0	0	-7
C4H9OH + H = H2 + CH3CH2CHCH2OH	0	0	0	0	0	0	0	0	-5	0	0	-7
C4H9OH + H = H2 + CH3CH2CH2CHOH	-1	-1	3	-36	-4	0	3	-2	11	-15	22	-19
C4H9OH + H = H2 + CH3CH2CH2CH2O	0	0	0	0	0	0	0	0	0	0	0	0
C4H9OH + CH3 = CH4 + CH3CH2CH2CHOH	0	0	4	-75	0	0	0	0	5	-7	0	-9

Hydrogen abstraction from butanol by hydrogen atom and methyl radical giving the 1-hydroxybutyl radical soon becomes equally or even more important. The sensitivity to the other hydrogen abstractions is significantly less. The β-scission of the ethyl radical is also important as it provides the H atoms which drive the free radical chemistry; it also plays a crucial role in determining the yields of ethane and ethene.

5.4.2 DOPED METHANE FLAME

The model's comparison with the centerline concentration profiles measured in the n-butanol doped methane flame is presented herein. As a reminder, only the concentration profiles were solved for in this study. The axial and radial velocities were those from the numerical solution to an undoped methane diffusion flame [198]; the temperature profile was also taken from the numerical solution, which assumed the temperature boundary condition at the burner to be 300 K. A direct comparison between this employed temperature profile and the experimentally-measured profile is shown in Figure 5-6: Centerline temperature profile in the 2-d methane diffusion flame: Experimental [172] (open circles) and the profile employed in this study (solid line + filled circles), as computed in [198].. The figure shows that the experimental temperature at the burner is ~450 K, not the nominal 300 K value assumed as a boundary condition by Bennett *et al.*; this discrepancy permeates down the length of the flame, including the region from 1 to 6 cm from the burner, where a majority of the fuel chemistry occurs. Thus, the question of what temperature profile to employ requires resolution.
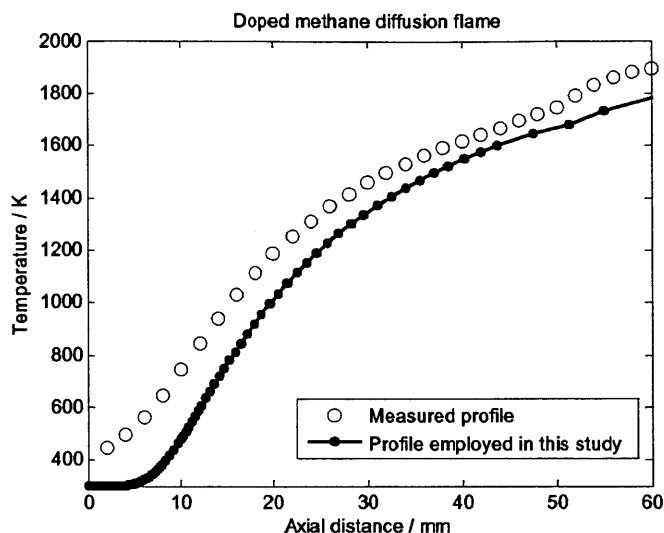
Figure 5-6: Centerline temperature profile in the 2-d methane diffusion flame: Experimental [172] (open circles) and the profile employed in this study (solid line + filled circles), as computed in [198].

5.4.2.1 SENSITIVITY ANALYSIS: ASSUMED TEMPERATURE PROFILE

In addition to running the doped flame simulator with the temperature field solved for by Bennett et al., two other profiles were tested: one which increased the entire Bennett temperature profile by 50 K and another which increased the profile by 100 K. The results, presented in Figure 5-7a-c, show the predicted concentration profiles' peak concentrations are not very sensitive to the assumed temperature profile; however the axial location of the peak concentration is sensitive to the temperature profile. For butanol, the axial position at which the concentration drops toward zero shifts from 33 mm from the burner for the base-case temperature profile to 28 mm from the burner for the base-case + 100K profile; the experimental spatial resolution for the concentration measurements is 1 mm. For the concentration profiles of 1-butene and formaldehyde, in addition to the curves shifting towards the burner by approximately 5 mm, the maximum concentrations also decrease by 10-20%. In general, all species mole fraction profiles generated with the base-case + 100K profile shift toward the burner by ~5mm when compared to the base-case profile. Moreover, essentially all butanol-derived species' profiles experience a decrease in their peak concentration; one counterexample is ethanal. Overall, the major effect of the temperature field, assuming the same radial and axial velocity fields, is a shift in the predicted concentration profiles ~5 mm towards the fuel

131

port. This study employs the base-case temperature profile, as the assumed axial and radical velocities were solved in concert with this temperature profile. However, due to the uncertainty in the temperature boundary condition, an offset of ~5 mm (towards the burner) in the axial position is assumed for the predicted concentration profiles.
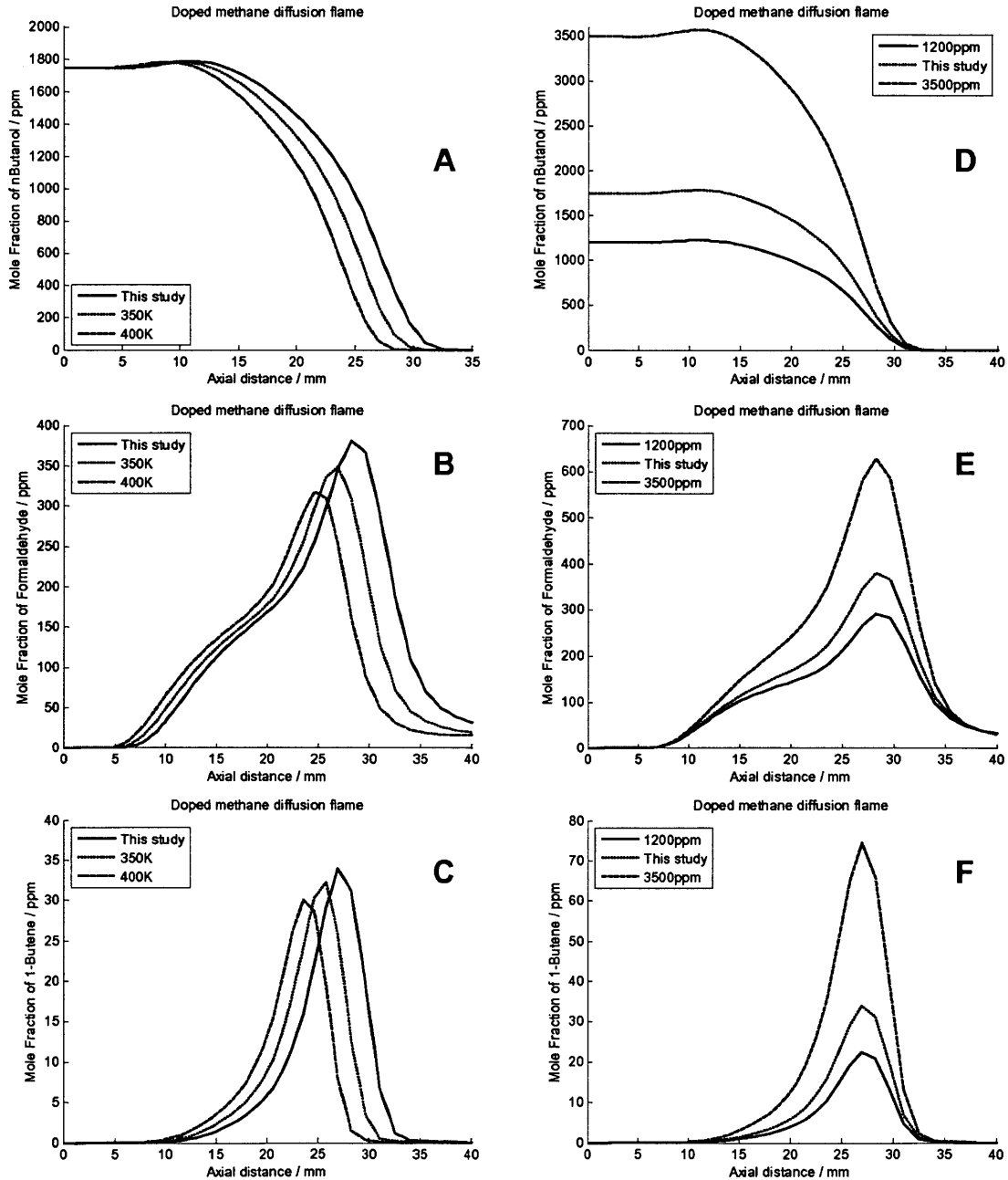
Figure 5-7: Centerline concentration profiles of n-butanol, formaldehyde, and 1-butene for different assumed temperature profiles (A, B, and C, respectively) and initial n-butanol concentrations (D, E, and F, respectively).

5.4.2.2 SENSITIVITY ANALYSIS: ASSUMED INITIAL CONCENTRATION

The centerline mole fraction profile of n-butanol is presented in Figure 5-8. In modeling the doped methane flame, the question of what initial n-butanol concentration should be used also required resolution. McEnally and Pfefferle stated the initial n-butanol concentration in their experiments is 3500ppm; however, their data suggest the initial concentration might actually be as low as 1200ppm; the origin of this discrepancy is unknown.
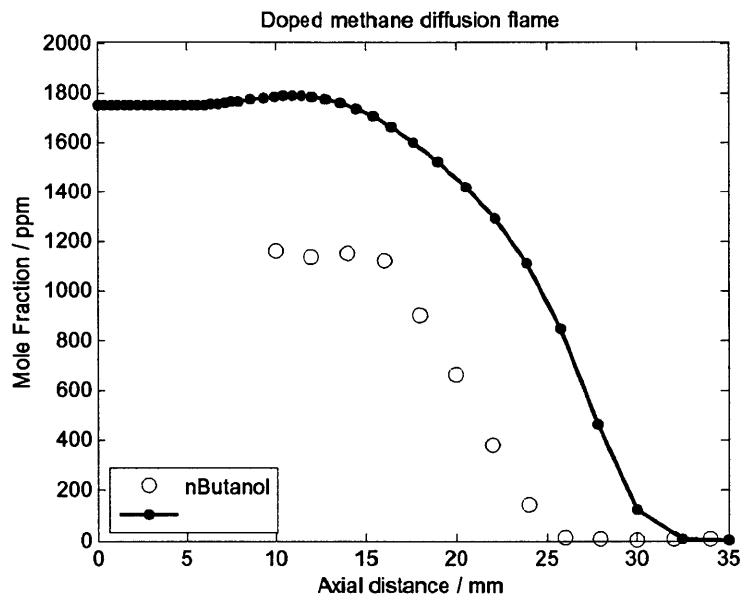
Figure 5-8: Centerline n-butanol mole fraction profile in the doped methane diffusion flame:
Experiment [172] (open circles) and predicted (solid line + filled circles)

Running the reactor model at these extreme values produces the plots in Figure 5-7d-f. The n-butanol curve drops toward zero concentration at approximately 33 mm from the burner, regardless of the initial concentration. However, the sensitivity of the model to the initial concentration is more clearly observed when viewing the profiles of 1-butene or formaldehyde. The predicted maximum centerline 1-butene concentration can vary from ~25ppm to ~75ppm, while the predicted maximum centerline formaldehyde concentration can vary from ~300ppm to ~625ppm; the absolute uncertainty in the experimental concentration measurements are up to a factor of 2. The axial position corresponding to the species' maximum concentration remains unchanged for all initial n-butanol concentrations tested.

133

Moreover, regardless of the initial concentration value employed, the predicted centerline mole fraction did not fall below 99% of its initial value until reaching an axial length of 1.17 cm. A line was fit, using least-squares regression, to the experimental data from 1.6 cm to 2.4 cm from the burner – using three, four, or all five data points – and the hypothetical concentration of n-butanol was computed at 1.17 cm from the burner for each line; the concentrations obtained ranged from 1615 to 1750 ppm. All results presented here assume an n-butanol concentration of 1750 ppm at z = 0.0 cm.
Given the uncertainty in the initial butanol concentration, assumed temperature profile, and uncertainties in our butanol model, we assume a relative uncertainty of two for the predicted concentrations profiles.

5.4.2.3 FLUX AND SENSITIVITY ANALYSIS: N-BUTANOL

Our model captures the centerline n-butanol concentration profile reasonably well: the predicted concentration is within a factor of two of the experimental measurements and the position where the predicted concentration drops toward zero (33 +0/-5 mm) matches well with the experimental observation (~27 mm). The rate of production for n-butanol reactions – unimolecular, H-abstraction by H atom, and H-abstraction by methyl radical – along the centerline of the doped methane flame are presented in Figure 5-9a-c, respectively. The dominant decomposition route is through the C-C bond fission forming n-propyl and hydroxymethyl radical. Minor decomposition routes include: the C-C bond fission forming ethyl and 2-hydroxyethyl radical, the bond fission forming methyl and 3-hydroxypropyl radical, and the four-center water elimination reaction forming 1-butene and water; the ratios of the maximum flux through these reactions, normalized to the maximum flux through the dominant n-propyl and hydroxymethyl radical pathway, are 0.27, 0.08, and 0.15, respectively. The pressure-dependent rates for each of these reactions was computed by RMG, see Section 5.3.6.1.

134
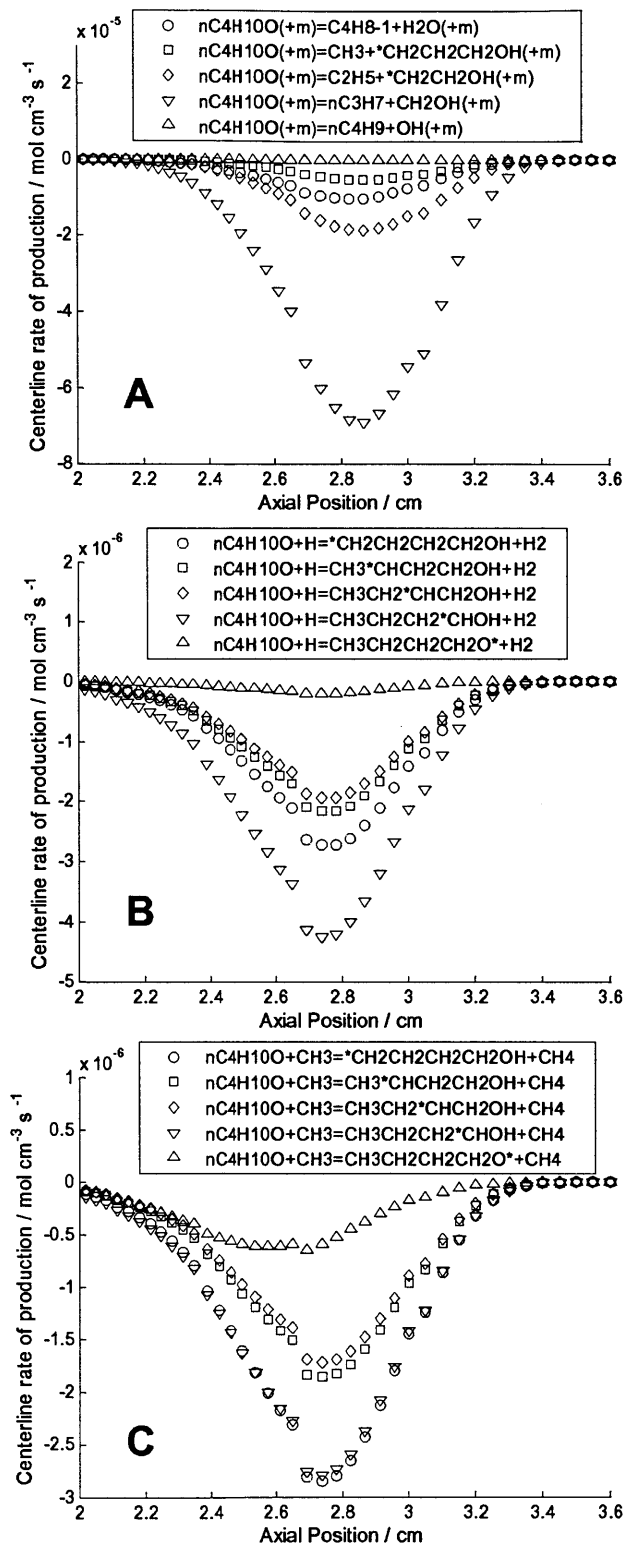
Figure 5-9: Predicted centerline rate of production of n-butanol in the doped methane diffusion flame. Note: All other reactions involving n-butanol have |ROP| < 1.8x10⁻⁶ mol cm⁻³ s⁻¹.

For H-abstraction reactions by H atom and methyl radical, the dominant decomposition products are calculated to be 1-hydroxybutyl and 4-hydroxybutyl radicals; the 3-hydroxy-1-methylpropyl and 1-(hydroxymethyl)propyl radicals are comparable to one another and about a factor of 2 less important. The formation of n-butoxy radical via H-abstraction is predicted to be very minor at these pyrolysis conditions. Although the concentration of n-butanol is relatively insensitive to the H-abstraction rates in this flame, the product distribution is very sensitive to these rates, as discussed in the next section.

The normalized sensitivity coefficients for the unimolecular reactions, computed using centered finite differencing, Equation (3.13), are shown in Figure 5-10a; for these pressure-dependent rate coefficients, the sensitivity coefficients were calculated by changing a_{11}, the coefficient multiplying the constant (temperature- and pressure-independent) Chebyshev polynomial term.

$$\tilde{s}_{ij} \equiv \frac{d\ln c_i}{d\ln k_j} = \frac{k_j}{c_i}\frac{dc_i}{dk_j} \approx \frac{k_j(a_{11})}{c_i[k_j(a_{11})]}\frac{c_i[k_j(a_{11}+\Delta a_{11})]-c_i[k_j(a_{11}-\Delta a_{11})]}{k_j(a_{11}+\Delta a_{11})-k_j(a_{11}-\Delta a_{11})} \quad (3.13)$$
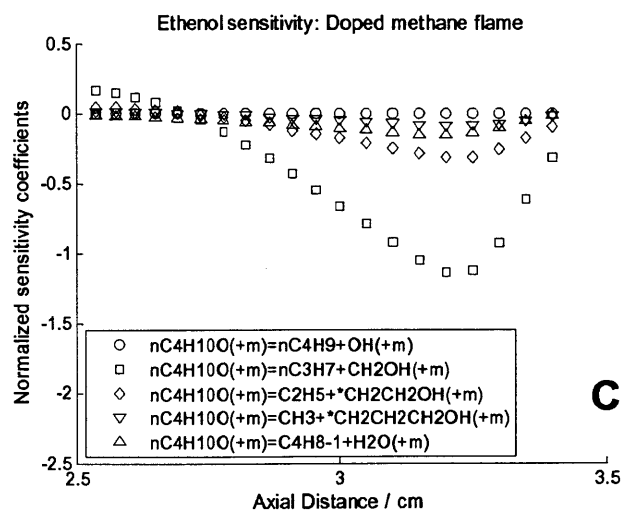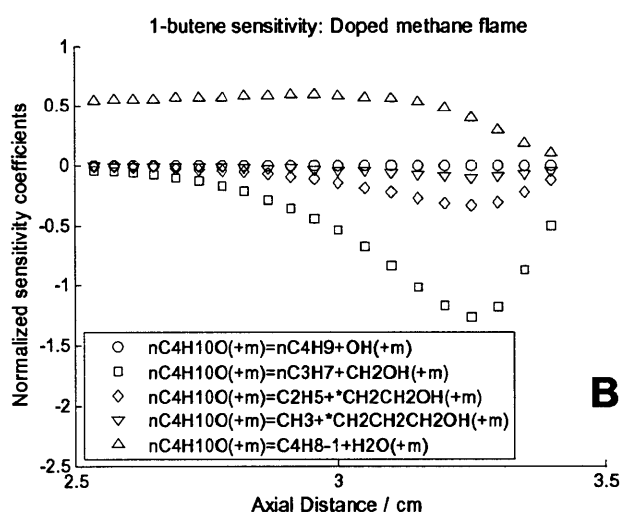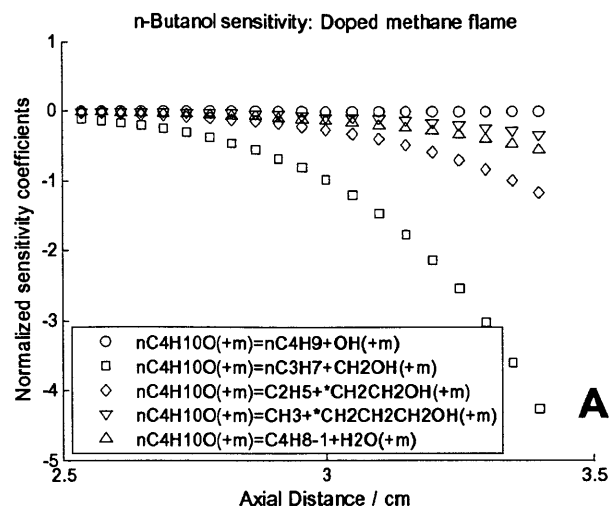
Figure 5-10: Normalized sensitivity coefficients for the centerline concentrations of a) n-butanol, b) 1-butene, and c) ethenol in the doped methane flame, with respect to the n-butanol unimolecular decomposition reactions.

The n-butanol centerline concentration profile is extremely sensitive to the C-C bond fission producing n-propyl and hydroxymethyl radical, with the normalized sensitivity coefficient reaching a value of -1 at 3 cm from the burner; the centerline butanol concentration is not particularly sensitive to the remaining unimolecular reactions. The normalized sensitivity of n-butanol towards each of the unimolecular reactions sharply increases along the length of the flame, peaking when the n-butanol concentration drops toward zero; as the concentration of n-butanol appears in the denominator of Equation (3.13), the values of the normalized sensitivity coefficients at axial positions >3.3 cm from the burner are irrelevant.

5.4.2.4 FLUX AND SENSITIVITY ANALYSIS: PRODUCTS

In general, our mechanism captures the dataset well. The doped centerline concentration profiles for some typical examples – species with MW=56 (1-butene, 2-butene, 2-propenal, and methylketene), species with MW=44 (ethanal and ethenol), and formaldehyde – are presented in Figure 5-11a; the rate of production analysis for each of these species is presented in Figure 5-12.
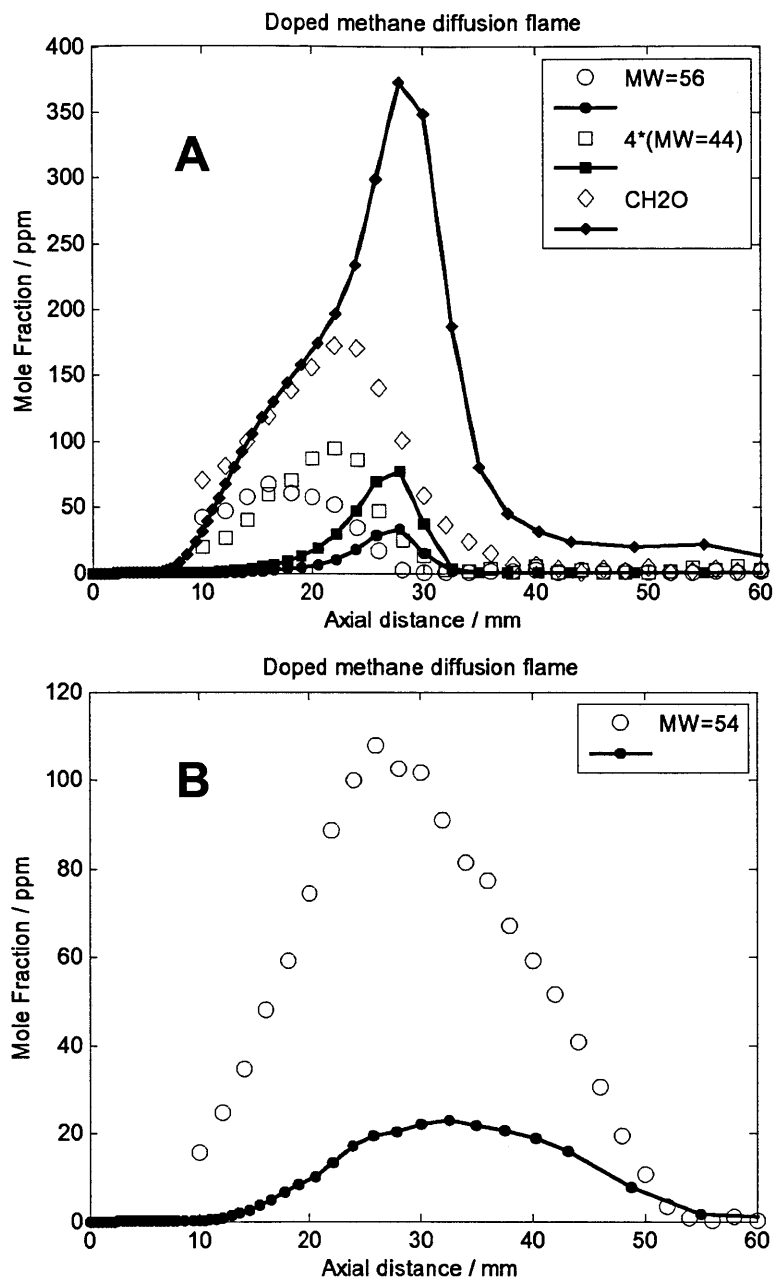
Figure 5-11: Experimental [172] (open shapes) and predicted (lines with filled shapes) centerline mole fraction profiles for the doped methane diffusion flame. The MW=56 curve is the summation of 1-butene, 2-butene, 2-propenal, and methylketene; the MW=44 curve is the summation of ethanal and ethenol; and the MW=54 curve is the summation of 1,2-butadiene, 1,3-butadiene, 1-butyne, 2-butyne, and propadienal. The absolute uncertainty for both the experimental data and the predicted curve is +100/-50%.

The main routes to 1-butene are the water elimination reaction of n-butanol and the β-scission reaction of the 1-(hydroxymethyl)propyl radical to 1-butene and hydroxyl radical; the 1-(hydroxymethyl)propyl radical is formed via H-abstraction from n-butanol

by H atom and methyl radical. The major decomposition route from 1-butene is the bond fission forming methyl and allyl radical; the pressure-dependent rate was estimated by RMG, see Section 5.3.6.4. One minor route consuming 1-butene is the chemically-activated pathway 1-butene+H(+M)=propene+CH3(+M); this rate was also estimated by RMG, see Section 5.3.6.3. Sensitivity analysis, Figure 5-10b, reveals the centerline 1-butene concentration to be sensitive to the n-butanol dehydration reaction and the C-C bond fission forming n-propyl and hydroxymethyl radical.

The dominant route to ethanal is through the tautomerization of ethenol; the major decomposition pathway is the bond fission forming methyl and formyl radical. The kinetics for these reactions come from studies by da Silva et al. [220] and Tsang and Hampson [111], respectively. Ethenol is derived from the β-scission of 1-hydroxybutyl radical, which is primarily formed by H-abstraction from n-butanol. Sensitivity analysis, Figure 5-10c, reveals the centerline ethenol concentration is sensitive to the C-C bond fission forming n-propyl and hydroxymethyl radical. Interestingly, the normalized sensitivity coefficient changes sign at ~2.7 cm from the burner: from positive to negative. At axial distances within 2.7 cm of the burner exit, increasing the bond fission rate will increase the radical pool concentration, thus increasing the 1-hydroxybutyl concentration (via H-abstraction from n-butanol by a radical), resulting in an increased concentration of ethenol. However, further downstream, increasing the bond fission rate will lead to a decrease in ethenol concentration: although the radical pool increases, the amount of butanol remaining also decreases; since ethenol comes directly from n-butanol, the decrease in n-butanol concentration results in a decrease in the ethenol concentration. Two of the main routes to formaldehyde formation are through the hydroxymethyl radical, one of the products of the dominant n-butanol decomposition pathway, via the pressure-dependent reaction CH2OH(+M)=CH2O+H(+M) and the assisted elimination reaction CH2OH+O2=HO2+CH2O; the rate coefficients come from the GRI-Mech 3.0 mechanism [191] and Tsang [103], respectively. The major decomposition pathways of formaldehyde are through H-abstraction by H atom, methyl and propargyl radical. The rate coefficients for H-abstraction by H atom and methyl come from Tsang et al. [111]; the rate for abstraction by propargyl comes from RMG [183]. The computed

140

formaldehyde concentration is sensitive to the n-butanol C-C bond fission forming n-propyl and hydroxymethyl radical.
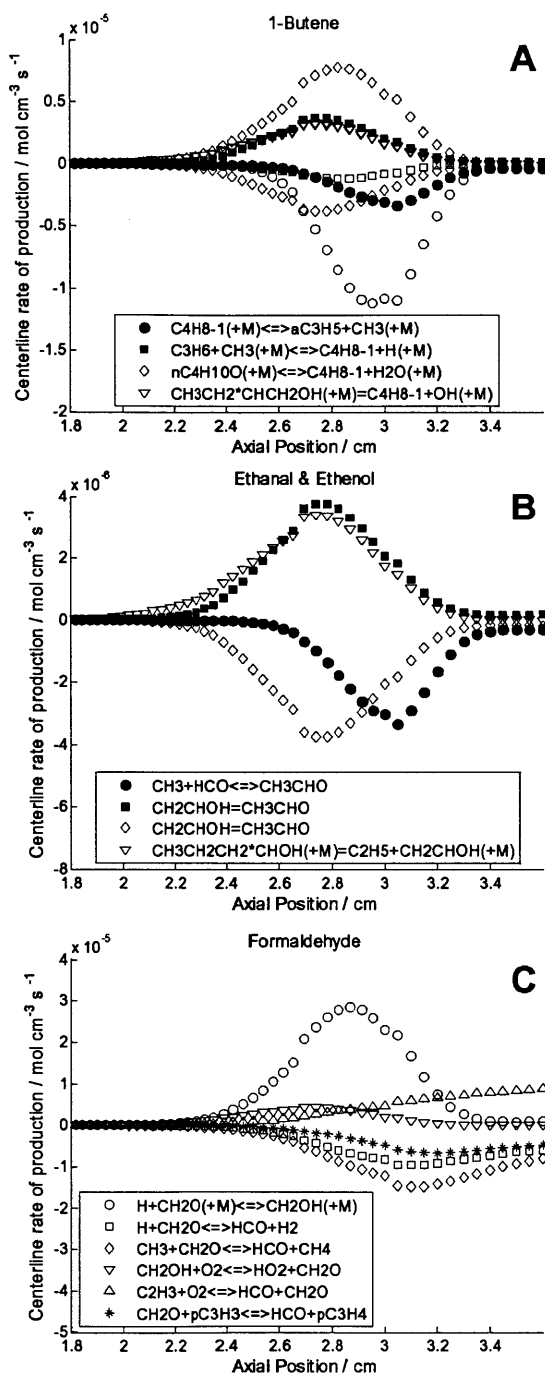
Figure 5-12: Predicted centerline rate of production for (a) 1-butene, (b) ethanal and ethenol, and (c) formaldehyde in the doped methane diffusion flame. Note: All other reactions involving 1-butene, ethanal, ethenol, and formaldehyde have $|ROP| < 1 \times 10^{-6}$, 3×10^{-7}, 7×10^{-8}, and 4×10^{-6} mol cm^{-3} s^{-1}, respectively.

One species profile our model does not predict accurately is the MW=54 profile, Figure 5-11b, which for our model consists of the species 1,3-butadiene, 1,2-butadiene, 1-butyne, 2-butyne, and propadienal. In our model, the MW=54 curve is predicted to be primarily 1,3-butadiene. The thermochemistry for this species is taken from the ATcT. We computed the thermochemistry of 1,3-butadiene using CBS-QB3, G3, and CCSD(T)/CBS calculations to test the model's sensitivity to the butadiene thermochemistry; the model was insensitive regardless which value was used. Additional sensitivity analysis was performed for the dominant reaction pathways, including H-abstraction from 1,3-butadiene by H atom, methyl and hydroxyl radical; the model was also insensitive to the reaction rates tested. We suspect our model is missing an important pathway for butadiene and/or butyne formation; future work is needed to resolve this discrepancy.

5.4.2.5 SENSITIVITY ANALYSIS: LENNARD-JONES PARAMETERS

Normalized sensitivity coefficients were also computed with respect to some of the Lennard-Jones sigma and epsilon parameters supplied in the transport properties file, Figure 5-13.
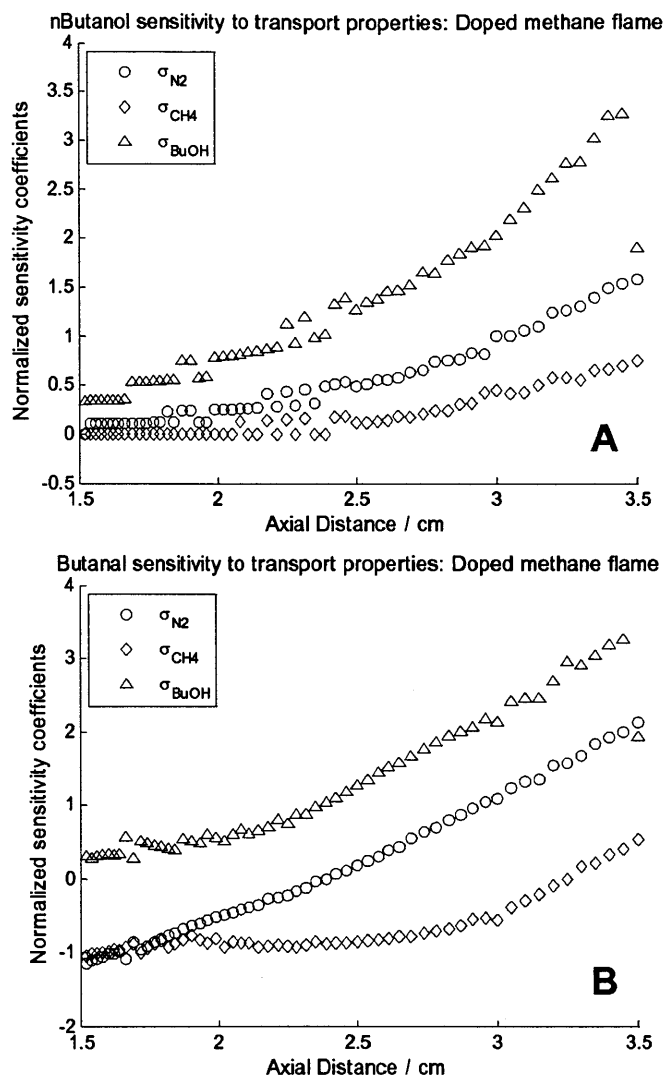
Figure 5-13: Normalized sensitivity coefficients for the centerline (a) n-butanol and (b) butanal concentrations in the doped methane diffusion flame, with respect to the Lennard-Jones collision diameters (sigma parameters) for nitrogen, methane, and n-butanol.

Although the normalized sensitivity coefficients carry the same meaning as those derived using the pre-exponential factor, the uncertainty in the sigma-epsilon parameters is inherently much smaller; whereas a value of 10 is a typical multiplicative uncertainty in the pre-exponential factor, a value of 1.25 is more typical for sigma-epsilon parameters. As an example: a normalized sensitivity coefficient of 0.3 for a reaction rate, coupled with a multiplicative uncertainty of 10 in the pre-exponential factor, results in a multiplicative uncertainty of 2 in the concentration, Equation (3.14). In comparison, the normalized sensitivity coefficients, with respect to the Lennard-Jones parameter, would

need to be 3.11 to produce the same multiplicative uncertainty in the concentration, Equation (3.15).

$$\Delta\left(\ln c_i\right) \approx \tilde{s}_{ij}\Delta\left(\ln A_j\right) \approx 2.30\tilde{s}_{ij} \quad \Delta\left(\ln c_i\right) = 0.693 \Rightarrow \tilde{s}_{ij} = 0.3 \qquad (3.14)$$

$$\Delta\left(\ln c_i\right) \approx \tilde{s}_{ik}\Delta\left(\ln \sigma_k\right) \approx 0.22\tilde{s}_{ik} \quad \Delta\left(\ln c_i\right) = 0.693 \Rightarrow \tilde{s}_{ik} = 3.11 \qquad (3.15)$$

In general, most centerline concentration profiles are sensitive to the collision diameters (sigma parameters) of N_2 and CH_4 since these species have high mole fractions. The values of these parameters were obtained from the GRI-Mech 3.0 mechanism. Most profiles are also sensitive to the collision diameter of n-butanol. The binary diffusion coefficient depends on the inverse square of the reduced collision diameter; thus, if the diffusion coefficient of n-butanol is decreased, thereby reducing its radial diffusion, the centerline concentration of n-butanol, as well as all n-butanol derived species, will increase. The value of the n-butanol sigma parameter reported in this study, 5.676 Å, was computed using the Group Additivity scheme mentioned in Section 5.3.3; this value is within 10% of those reported in the literature [223].

5.4.3 JET-STIRRED REACTOR

The new mechanism was also tested against the jet-stirred reactor (JSR) data of Dagaut *et al.* [178] and Sarathy *et al.* [179]. In all plots presented in this Section, the "C4H8O" curve is the summation of butanal and its tautomer, 1-buten-1-ol, as any enol leaving the reactor will likely tautomerize to the aldehyde before reaching the analytical equipment; the "CH3CHO" curve is the summation of ethanal and its tautomer, ethenol.

5.4.3.1 COMPARISON WITH JSR DATA: 1 ATM

A comparative study between our model and the models of Sarathy et al. [179], Moss et al. [180], and Black et al. [181] has been performed for all jet-stirred reactor datasets at 1 atm. Some of the results are presented in Figure 5-14 and Figure 5-15; the remaining results are supplied in the Supplementary Information.
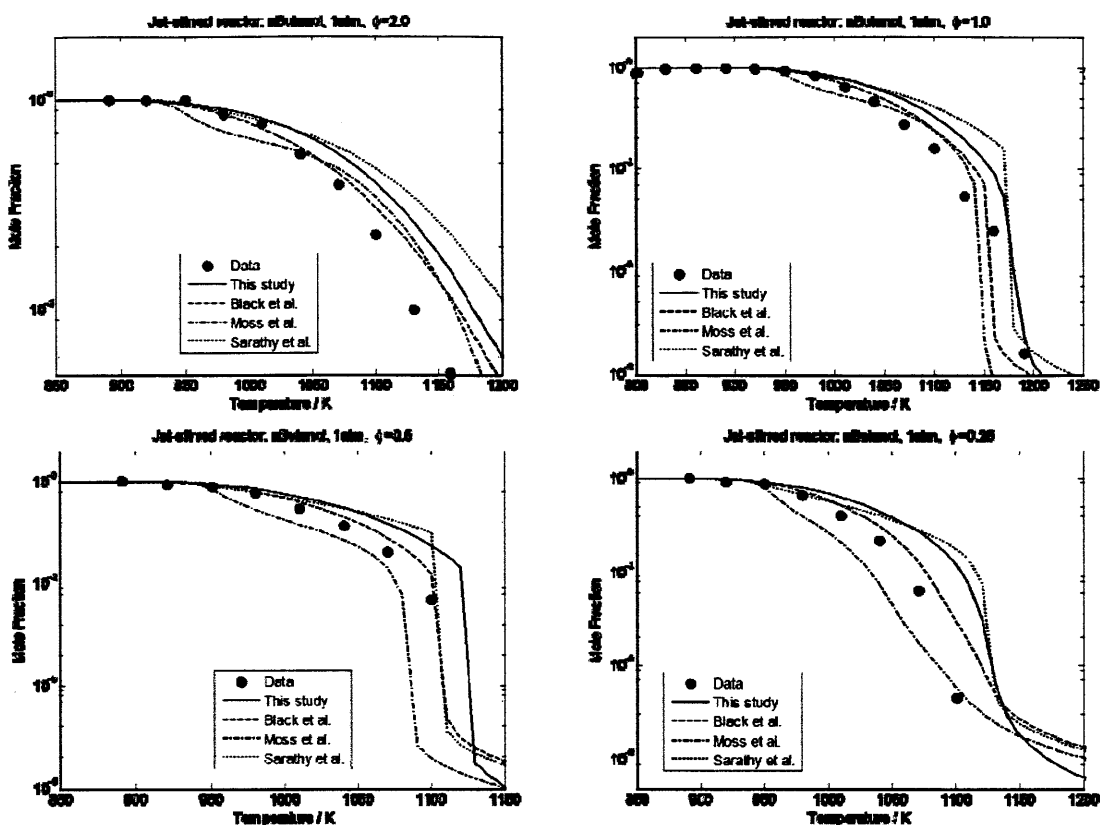
Figure 5-14: The predicted n-butanol concentration in the jet-stirred reactor at 1 atm, as a function of temperature and equivalence ratio. The filled circles are the dataset from Sarathy et al. [179].

Figure 5-14 contains each mechanism's prediction for the n-butanol concentration as a function of temperature, for each equivalence ratio studied. Our mechanism predicts the dataset well up to temperatures of 1100K for the ϕ=2.0 and 1.0 experiments, and up to 1050K for the ϕ=0.5 and 0.25 experiments. At higher temperatures, our model underestimates the n-butanol reactivity. Overall, the Black et al. mechanism does very well at capturing the complete n-butanol dataset. The Sarathy et al. mechanism behaves similarly to our mechanism and the Moss et al. mechanism's predictions lie between ours and the Black et al. model.

The Moss model's rate-of-production plateaus at a temperature of 1050K before falling off at 1080K; the Black model plateaus at 1100K before falling off at 1120K. The rate-of-production for the Sarathy model and our model peak at 1120K, but then quickly falls off at greater temperatures. In the Black et al. mechanism, the four fastest decomposition pathways at temperatures < 1130 K are through H-abstraction from n-butanol by hydroxyl radical, with the fastest route across all temperatures being the abstraction of n-

145

butanol forming 3-hydroxy-1-methylpropyl radical. The four fastest decomposition routes in the Sarathy mechanism, across all temperatures, are abstraction by hydroxyl radical; the two equally fastest reactions form 1-(hydroxymethyl)propyl and 3-hydroxy-1-methylpropyl radicals. The dominant route (accounting for 50% of the total rate of production) in the Moss mechanism at temperatures < 1130 K is H-abstraction from n-butanol by H atom, forming 1-hydroxybutyl radical. The fastest routes in the present mechanism at temperatures < 1130 K are abstraction by hydroxyl radical forming 1-hydroxybutyl and 1-(hydroxymethyl)propyl radical; at temperatures > 1130 K, H-abstraction by atomic oxygen, forming 1-hydroxybutyl radical, is the predominant reaction (accounting for 50% of the total rate of production).
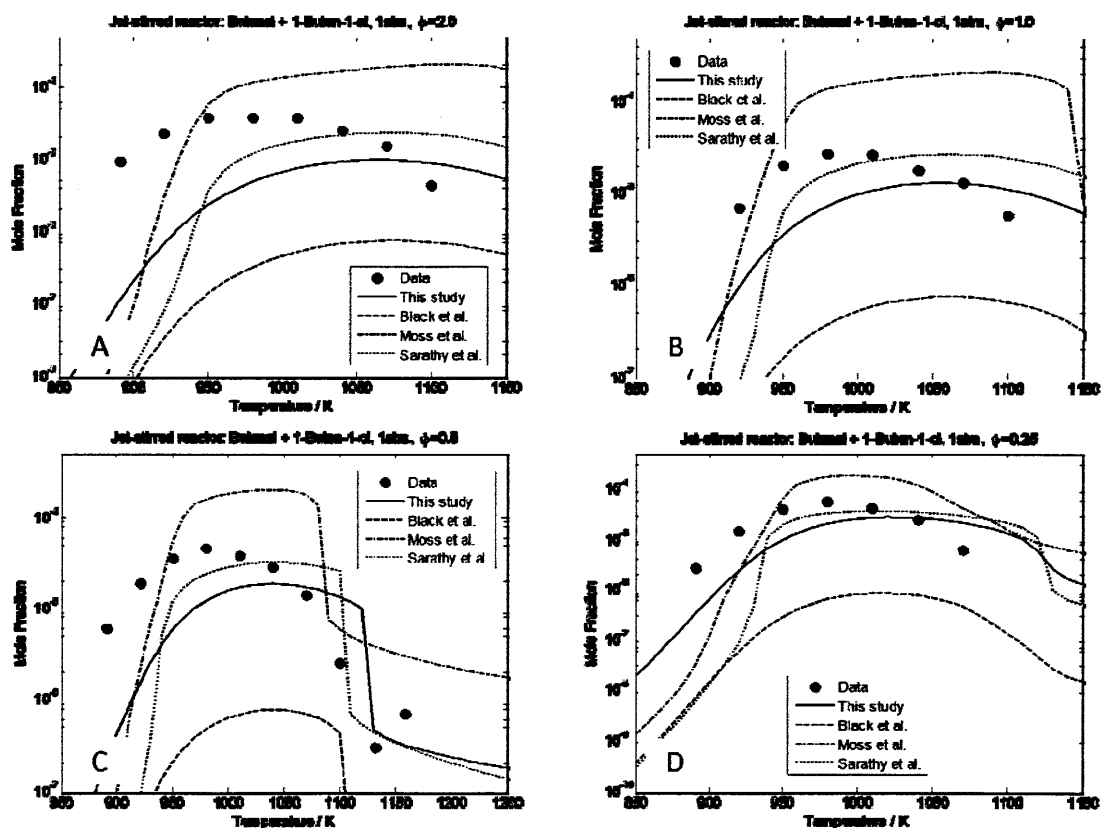
Figure 5-15: The predicted butanal + 1-buten-1-ol concentration in the jet-stirred reactor at 1 atm, as a function of temperature and equivalence ratio. The filled circles are the dataset from Sarathy et al. [179].

One particularly interesting species in the 1 atm jet-stirred reactor dataset is butanal; the predictions of the four mechanisms vary greatly over the temperatures and equivalence ratios tested. The predicted concentration profile of butanal for each mechanism is

presented in Figure 5-15. The Sarathy model and our model predict the C4H8O concentration well across all temperatures and equivalence ratios tested; the maximum rate of production for butanal for both models is $\sim 5 \times 10^{-9}$ mol cm^{-3} s^{-1}. The Moss model overestimates the concentration for all conditions, whereas the Black model underestimates the concentration for all conditions. The maximum rate of production for butanal in the Moss model is $\sim 3.25 \times 10^{-8}$ mol cm^{-3} s^{-1}; for the Black model, the value is $<$ 1×10^{-10} mol cm^{-3} s^{-1}. For the Black et al. mechanism, the exclusive route to butanal is the β-scission of 1-hydroxybutyl radical to H atom and butanal; 1-hydroxybutyl radical is generated by H-abstraction reactions from n-butanol by hydroxyl, H atom, hydroperoxy, and methyl radical. The Moss et al. mechanism also predicts the only significant route to butanal being the β-scission reaction of 1-hydroxybutyl radical, which comes from H-abstraction from n-butanol by H atom, hydroperoxy and hydroxyl radical. The Sarathy et al. mechanism predicts the β-scission of n-butoxy radical as the exclusive route to butanal; n-butoxy radical comes exclusively from H-abstraction from n-butanol by hydroxyl radical. For our mechanism, the dominant route to butanal is the assisted elimination reaction of 1-hydroxybutyl radical by molecular oxygen to form butanal and hydroperoxy radical; three minor pathways are: the tautomerization of 1-buten-1-ol; the β-scission of 1-hydroxybutyl; and the assisted elimination of n-butoxy by molecular oxygen, forming butanal and hydroperoxy radical. The 1-hydroxybutyl radical is generated by H-abstraction from n-butanol by hydroxyl, H atom, and hydroperoxy radical. Overall, the Black model captures this dataset very well, with the exception of the C4H8O curve and the acetylene curve (which it overestimates for most conditions). The Sarathy model also captures most of the dataset well, with the exception of the CO and acetylene curves, both of which are underestimated for most conditions. The Moss model does not capture this dataset well; some concentration profiles that are reasonably predicted across all temperatures and equivalence ratios are methane, ethane, ethene, and formaldehyde.

A summary of our model's predictions against all of the 1 atm jet-stirred reactor dataset is presented in Table 5-4. In general, our model predicts the concentration profiles of all species within a factor of 2, across all temperatures and equivalence ratios tested. We capture the propene, 1-butene, 1,3-butadiene, and "C4H8O" curves well for all conditions,

with the exceptions of: 1,3-butadiene and C4H8O at the ϕ=2.0 conditions, in which we underestimate the concentration by a factor of 3; and propene at the ϕ=0.25 conditions, which we underestimate by a factor of 2.4. The model predicts the concentrations of CO and methane well for all conditions. The model does well at capturing the CO_2 data above 1050 K for all tested equivalence ratios. Below 1050 K, the model underestimates the CO_2 concentration, including missing a local maxima at 1000 K for the ϕ=2.0 experiment; this fact is true of all four models. The model also captures the acetylene, ethene, and "C2H4O" curves well for all tested conditions, with the exception of our overestimating the acetylene concentration by a factor of 2.3 for the ϕ=0.25 experiments. The ethane concentration is well predicted above 950 K; below 950 K, the model underestimates the concentration, which is true of all four models. Lastly, the model captures the formaldehyde and water concentration profiles for all temperatures and equivalence ratios; the model underestimates the concentration of hydrogen by as much as a factor of three.

Table 5-4: Comparison of peak measured and predicted product concentration in the jet-stirred reactor of [179]. Italicized numbers represent measured values, bold numbers are the predicted values using the new mechanism, and underlined numbers are the ratio of measured to predicted.

	$\phi = 2.0$	$\phi = 1.0$	$\phi = 0.5$	$\phi = 0.25$
Butanal + 1-buten-1-ol	*38*	*27*	*47*	*57*
	10	**13**	**19**	**28**
Propene	*132*	*118*	*116*	*121*
	78	**76**	**70**	**63**
1-Butene	*44*	*46*	*46*	*49*
	37	**44**	**53**	**59**
Methane	*353*	*264*	*203*	*147*
	196	**161**	**134**	**112**
CO	*2223*	*2533*	*1499*	*2814*
	2325	**2262**	**1231**	**1908**
CO2	*279*	*1970*	*3833*	*3126*
	351	**3249**	**3560**	**3550**
Acetylene	*349*	*84*	*23*	*12*
	290	**70**	**35**	**23**
Ethene	*884*	*750*	*684*	*531*
	562	**477**	**386**	**316**
Ethane	*90*	*75*	*50*	*27*
	81	**62**	**42**	**25**

Ethanal + Ethenol	74	84	75	55
	117	132	150	161
Water	1796	4794	5363	5397
	2173	4754	4949	4973
Formaldehyde	163	184	206	223
	116	129	139	142
Hydrogen	2271	1498	780	492
	1713	921	433	259
1,3-butadiene	18	16	15	14
	3	3	5	7

5.4.3.2 COMPARISON WITH JSR DATA: 10 ATM

The experimental and modeling results obtained at φ=0.5 in the 10 atm jet-stirred reactor are presented in Figure 5-16; the comparisons for the ϕ=1.0 and 2.0 experiments are supplied in the Supplementary Information.
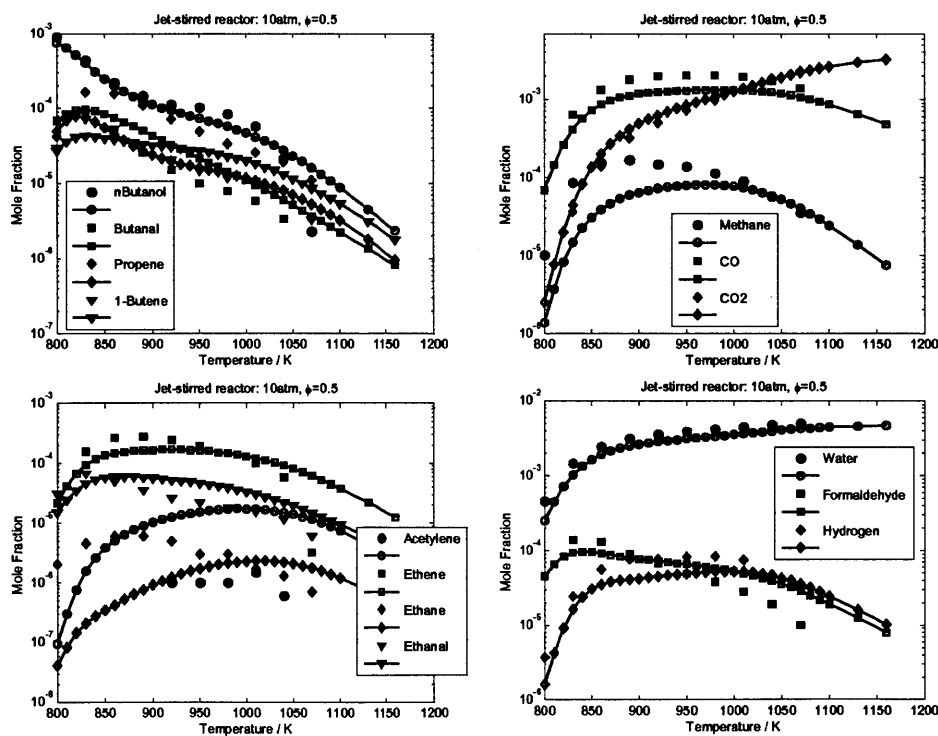
Figure 5-16: Model comparison with the jet-stirred reactor data [178] at φ=0.5, P=10atm, τ=0.7s. Note: The Butanal curve is the summation of butanal and 1-buten-1-ol and the Ethanal curve is the summation of ethanal and ethenol.

A summary of the model's predictions against the entire dataset may be found in Table 5-5.

Table 5-5: Comparison of peak measured and predicted product concentrations in the jet-stirred reactor of [178] Italicized numbers represent measured values, bold numbers are the predicted values using the new mechanism, and underlined numbers are the ratio of measured to predicted.

	$\phi = 2.0$	$\phi = 1.0$	$\phi = 0.5$
Butanal + 1-buten-1-ol	*92*	*94*	*94*
	39	**61**	**88**
Propene	*220*	*193*	*164*
	85	**87**	**89**
1-Butene	*80*	*86*	*72*
	43	**38**	**28**
Methane	*664*	*257*	*165*
	381	**183**	**90**
CO	*2000*	*2040*	*2050*
	2052	**1561**	**1424**
CO2	*387*	*1360*	*2330*
	819	**2523**	**3336**
Acetylene	*13*	*3*	*2*
	69	**17**	**16**
Ethene	*448*	*356*	*276*
	379	**242**	**134**
Ethane	*31*	*15*	*6*
	28	**14**	**5**
Ethanal + Ethenol	*80*	*59*	*67*
	128	**112**	**89**
Water	*2370*	*6170*	*5020*
	2293	**4432**	**4826**
Formaldehyde	*156*	*148*	*140*
	138	**118**	**99**
Hydrogen	*949*	*404*	*84*
	1259	**277**	**61**

The model's predicted n-butanol concentration profiles agree very well with the data across all temperatures and equivalence ratios. A flux analysis of n-butanol for each of these experiments is shown in Figure 5-17.
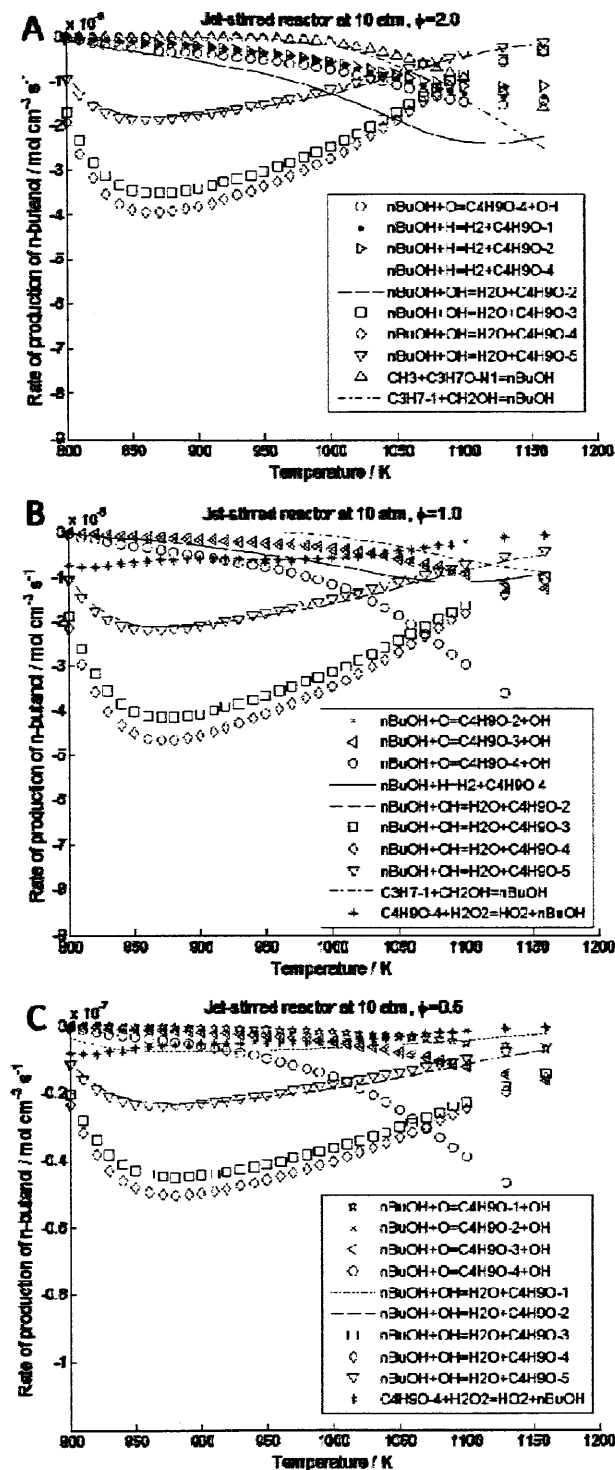
Figure 5-17: The ten largest rates of production for n-butanol in the 10 atm jet-stirred reactor simulations for equivalence ratios of A) 2.0, B) 1.0, and C) 0.5.

For all three equivalence ratios, the two most dominant decomposition reactions at temperatures < 1050 K are H-abstractions from n-butanol by hydroxyl radical, forming

151

the 1-hydroxybutyl and 1-(hydroxymethyl)propyl radical; the maximum flux through these reactions occurs at ~890 K. The rate coefficients for these reactions come from RMG [183] and Cohen [224], respectively. Two other significant pathways are H-abstractions from n-butanol by hydroxyl radical forming n-butoxy and 3-hydroxy-1-methylpropyl radical; the rates for these reactions are also estimates from RMG. For the lean and stoichiometric experiments, the dominant pathway at temperatures > 1050 K is H-abstraction from n-butanol by O atom forming 1-hydroxybutyl radical; for the rich experiments, the dominant pathway at high temperatures is H-abstraction from n-butanol by H atom forming 1-hydroxybutyl radical. The former rate was estimated by RMG whereas the latter was computed by this study, using quantum chemistry as discussed in Section 5.3.5.

The model's predictions for the concentrations of 1-butene, butanal + 1-buten-1-ol, CO, ethene, ethanal + ethenol, water, formaldehyde, and hydrogen are within a factor of two of the experimental data across the entire temperature range for all equivalence ratios tested. The model predicts the concentrations of methane and ethane well for the rich and stoichiometric experiments; the model underestimates their concentrations by as much as a factor of 2.6 for the lean conditions. The model predicts the concentration of CO_2 well for the lean and stoichiometric conditions; the model overestimates the concentration by a factor of 2.1 for the rich experiments.

The predicted propene concentration is consistently less than the experimental data, and is underestimated by as much as a factor of three. Our model predicts propene is formed exclusively by the β-scission of 3-hydroxy-1-methylpropyl radical at temperatures < 930 K; at higher temperatures, the chemically-activated pathway from 1-butene + H atom also contributes to the formation of propene (and methyl radical). Both of these pressure-dependent rates were estimated by RMG, see Sections 5.3.6.2 and 5.3.6.3, respectively. The main decomposition pathway of propene at temperatures < 1010K is H-abstraction from propene by hydroxyl radical forming water and allyl radical; this rate expression comes from a literature review on propene combustion chemistry by Tsang [108].

The model also does not estimate the concentration of acetylene well; for all temperatures and equivalence ratios, the concentration is overestimated, especially for the lean experiments. A flux analysis of acetylene for the three equivalence ratios is located in Figure 5-18. For all experiments, four pathways contribute to the production of acetylene: the β-scission of 2-hydroxyethenyl, the chemically-activated pathway propyne + H atom to methyl radical + acetylene, the assisted elimination reaction of vinyl radical by molecular oxygen forming hydroperoxy radical and acetylene, and the β-scission of 1,3-butadien-1-yl; the rate expressions come from Baulch et al. [117], Sharma et al. [190], Mebel et al. [225], and Weissman et al. [226], For the rich and stoichiometric experiments, H atom addition to acetylene forming vinyl radical is the predominant acetylene decomposition pathway at temperature < 1070 K; above this temperature, the chemically-activated reactions of acetylene and oxygen atom – forming H + HCCO or methylene + CO – are the dominant decomposition routes. For the lean experiments, the same dynamic exists for acetylene formation and destruction, except the temperature threshold is 1010 K. All of the mentioned acetylene decomposition reaction rates are from the GRI-Mech 3.0 mechanism.
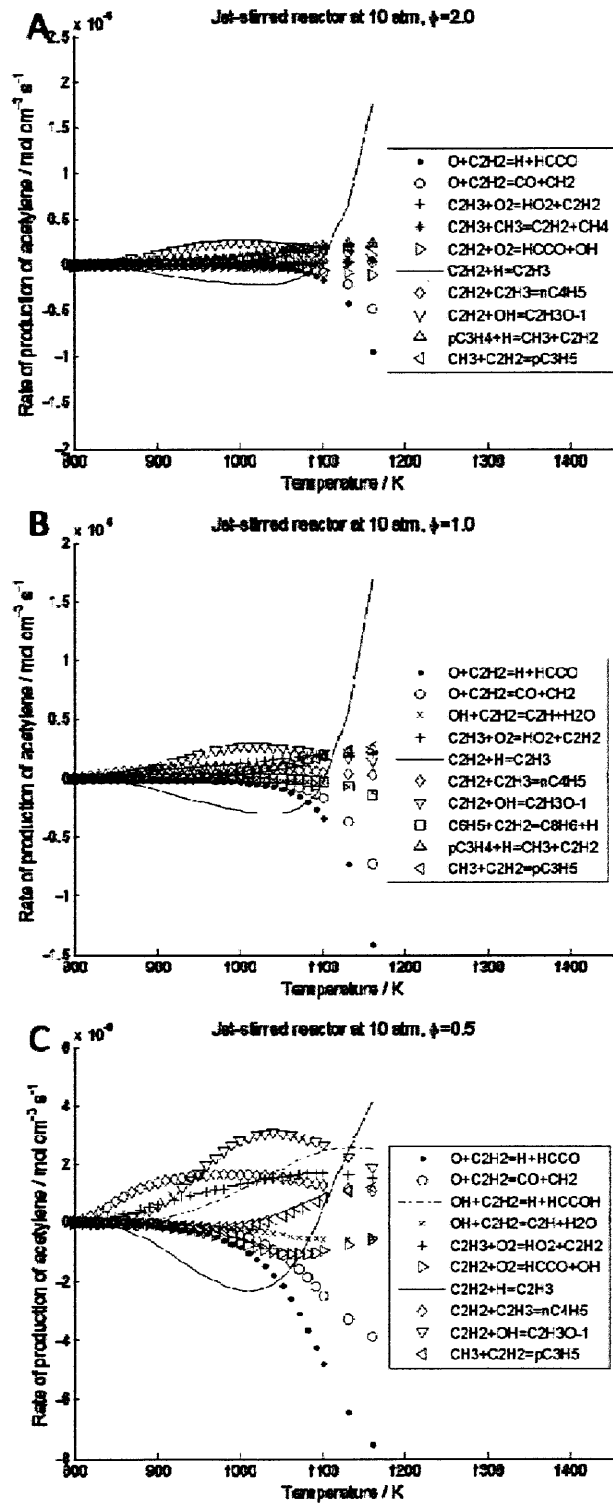
Figure 5-18: The ten largest rates of production for acetylene in the 10 atm jet-stirred reactor simulations for equivalence ratios of A) 2.0, B) 1.0, and C) 0.5.

5.4.4 OPPOSED FLOW DIFFUSION FLAME

Our mechanism was also tested against the opposed-flow diffusion flame data measured by Sarathy *et al.* [179], using the Opposed-Flow Flame module (OPPDIFF) in CHEMKIN-MFC. The experimental and modeling results are presented in Figure 5-19. Once again, the "C4H8O" curve is the summation of butanal and 1-buten-1-ol, and the "C2H4O" curve is the summation of ethanal and ethenol.
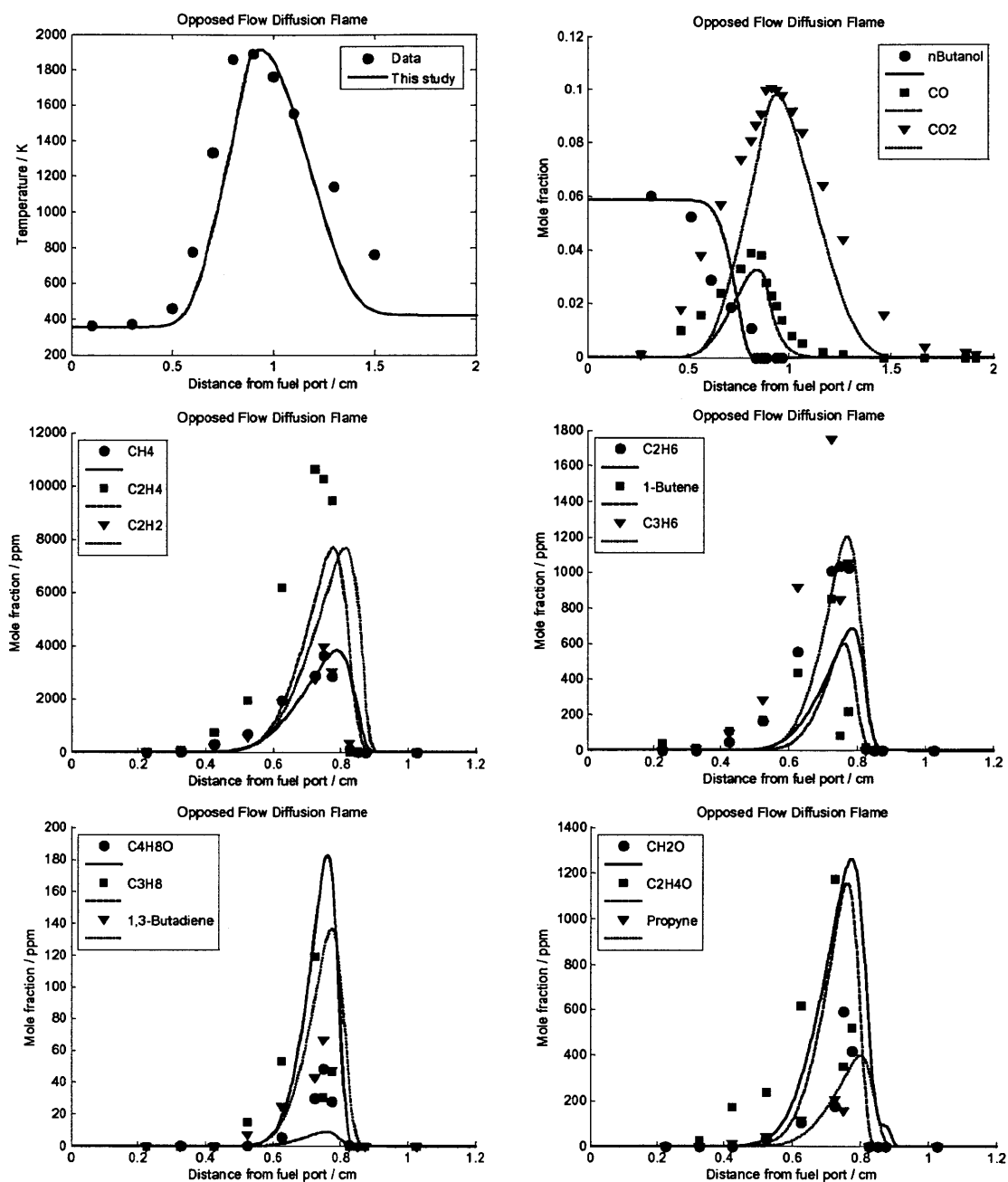
Figure 5-19: Model comparison with the opposed-flow diffusion flame reported in Ref. [179]. Note: The C4H8O curve is the summation of butanal and 1-buten-1-ol and the C2H4O curve is the summation of ethanal and ethenol.

A summary of our results is presented in Table 5-6. The Black et al. and Moss et al. mechanisms do not report species transport properties, so those mechanisms could not be tested against the opposed-flow diffusion flame.

Table 5-6: Comparison of peak measured and predicted product concentrations (rounded to the nearest ppm) in the opposed-flow diffusion flame of [179].

	Measured	Predicted	Ratio
CO	39000	32714	1.19
CO2	101000	98290	1.03
Methane	3622	3828	0.95
Ethene	10612	7684	1.38
Acetylene	3964	7676	0.52
Ethane	1035	686	1.51
1-Butene	852	600	1.42
Propene	1751	1205	1.45
Butanal + 1-buten-1-ol	49	182	0.27
Propane	119	9	13.19
Propyne	207	399	0.52
1,3-butadiene	67	137	0.49
Formaldehyde	592	1263	0.47
Ethanal + Ethenol	1173	1156	1.01

Our model's predicted temperature profile captures the experimental curve reasonably well: the maximum temperature is predicted to within 1.2% and the predicted axial position corresponding to the peak is 0.4 mm further from the fuel port than the experimental value. However, the predicted temperature profile has a narrower reaction zone than the experiment, and the predicted curve lags the experimental curve by ~0.7 mm; the Sarathy model captures the temperature profile equally well.

Our mechanism captures the concentration profiles of CO, CO_2, and n-butanol well; the predicted CO and CO_2 maximum concentrations are within 17% and 2% of the experimental maxima, respectively. The n-butanol profile drops toward zero concentration ~8.4 mm from the fuel port, in good agreement with the experiment. The Sarathy model also captures each of the CO, CO_2, and n-butanol concentration profiles well.

A flux analysis for n-butanol in the opposed-flow diffusion flame, as predicted using our model, is presented in Figure 5-20. Our model's predictions suggest the n-butanol chemistry occurs in the range 7.1 − 8.6 mm from the fuel port. From 7.1 − 7.5 mm from

157

the fuel port, the main decomposition routes are through H-abstraction from n-butanol by H atom and hydroxyl radical; after this distance, the abstraction by hydroxyl radical becomes less important, having its maximum flux occur at 7.8 mm from the fuel port, while the bond fission of n-butanol forming n-propyl and hydroxymethyl radical becomes significant. This bond fission becomes the dominant decomposition pathway at a distance of 7.8 mm from the fuel port; H-abstractions by H atom peak at a distance of 7.95 mm from the fuel port. The bond fission reaction peaks at a distance of 8.1 mm from the fuel port and its maximum rate is nearly double that of the next dominant channel (H-abstraction by H atom forming 1-hydroxybutyl radical).
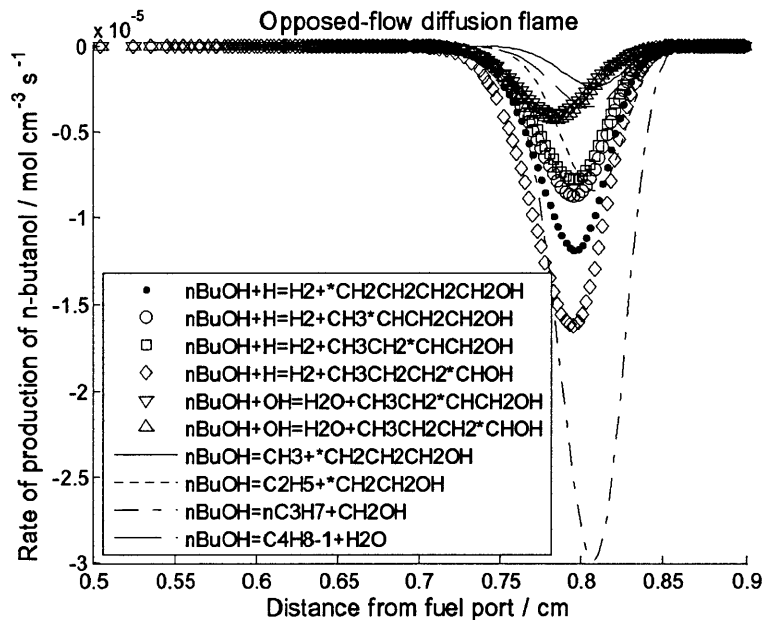
Figure 5-20: The ten largest rates of production for n-butanol in the opposed-flow diffusion flame simulation.

Our mechanism captures most of the minor products' concentration profiles very well, including the axial position corresponding to the maximum concentration. For all minor products, the predicted position of the species maximum concentration is further from the fuel port than the experimental values; however, the only concentrations that are shifted more than 0.5 mm are those for ethene, acetylene, and propyne and these are no worse than 0.76 mm. The source of the shift can be explained by comparing the predicted and experimentally-measured temperature profiles: the predicted curve is shifted from the experimental curve by ~0.7 mm. For the Sarathy model, the predicted positions of all

minor species' maximum concentrations are also further from the fuel port than the experimental values.

Both the Sarathy mechanism and our mechanism model the concentrations of methane, ethene, ethane, 1-butene, and ethanal + ethenol very well, predicting the maximum concentration of each within a factor of 1.5; our mechanism also captures propene very well, whereas the Sarathy mechanism captures acetylene very well. Our mechanism captures the acetylene, propyne, 1,3-butadiene, and formaldehyde profiles reasonably well, predicting the maximum concentration of each within a factor of 2 of the experimental value; the Sarathy mechanism captures the propyne concentration profile reasonably well, but does not predict the other species concentration profiles within a factor of 2: formaldehyde and propene are overestimated by a factor of 2.3, whereas 1,3-butadiene is overestimated by a factor of 3.5.

Two species that neither model captures well are the butanal + 1-buten-1-ol and the propane profiles. Our model overestimates the maximum C_4H_8O concentration by a factor of 3.8; the Sarathy model overestimates the curve by a factor of 4.3. In our model, the butanal + 1-buten-1-ol curve is predominantly (> 85%) butanal; the Sarathy model only contains butanal. In our model, the dominant route to butanal is the β-scission of the 1-hydroxybutyl radical; this β-scission comprises ~15% of the total 1-hydroxybutyl radical decomposition with the remaining ~85% directed towards the β-scission forming ethenol and ethyl radical. Other significant pathways to butanal are the tautomerization reaction from 1-buten-1-ol and the assisted elimination reaction of 1-hydroxybutyl radical by molecular oxygen forming hydroperoxy radical and butanal. The main decomposition pathways are through C-C bond fissions and H-abstractions by H atom. Sensitivity analysis reveals three reactions which the butanal concentration is sensitive to: the chain branching reaction $H+O_2=O+OH$, the C-C bond fission of butanal forming methyl and 3-oxopropyl radical, and the C-C bond fission of n-butanol forming n-propyl and hydroxymethyl radical. For all three reactions, the sensitivity coefficients are negative. Our model underestimates the maximum propane concentration by an order of magnitude; the Sarathy model underestimates the maximum by a factor of 5.5. The predominant propane formation pathway in our model is the recombination of methyl and ethyl radical; H-abstraction from formaldehyde by n-propyl radical, forming propane and

159

formyl radical, also contributes to propane formation. The reaction rate coefficients come from the GRI-Mech 3.0 mechanism [191] and Tsang and Hampson [111], respectively. H-abstraction from n-butanol by n-propyl radical is not predicted to be significant in the opposed-flow diffusion flame. The major decomposition routes from propane are H-abstraction reactions by H atom forming n- and iso-propyl radical; both of these rate expressions come from a literature review by Tsang [85]. Sensitivity analysis reveals only one reaction whose absolute normalized sensitivity coefficient exceeds 0.25 at any point in the flame: H-abstraction from propane by H atom forming n-propyl radical.

5.4.5 IGNITION DELAY TIME

Our model was further tested against autoignition delay times measured in shock tube experiments [180, 181, 227-229] and a rapid compression machine [230] for n-butanol, and ignition delay measurements in shock tube experiments for butanal [182]. All sets of experiments were modeled using the Closed Homogeneous Batch Reactor module in CHEMKIN-Pro. The reported ignition delay times correspond to the time which maximized the $[C_2H]^*[O]$ curve; these times corresponded very well with the time to reach maximum $[^3CH_2]$ and the time to reach half the maximum of [OH].

5.4.5.1 N-BUTANOL: EXPERIMENTS CONDUCTED BY BLACK ET AL.

Autoignition delay times of n-butanol were measured by Black $et\ al.$ at reflected shock pressures of 1, 2.6, and 8 atm, at temperatures from 1100–1800 K, for equivalence ratios of 0.5, 1, and 2. Our model's comparison against some of the data sets, including the three previously published n-butanol models' predictions, is presented in Figure 5-21; the remaining comparisons are located in the Supplementary Information.
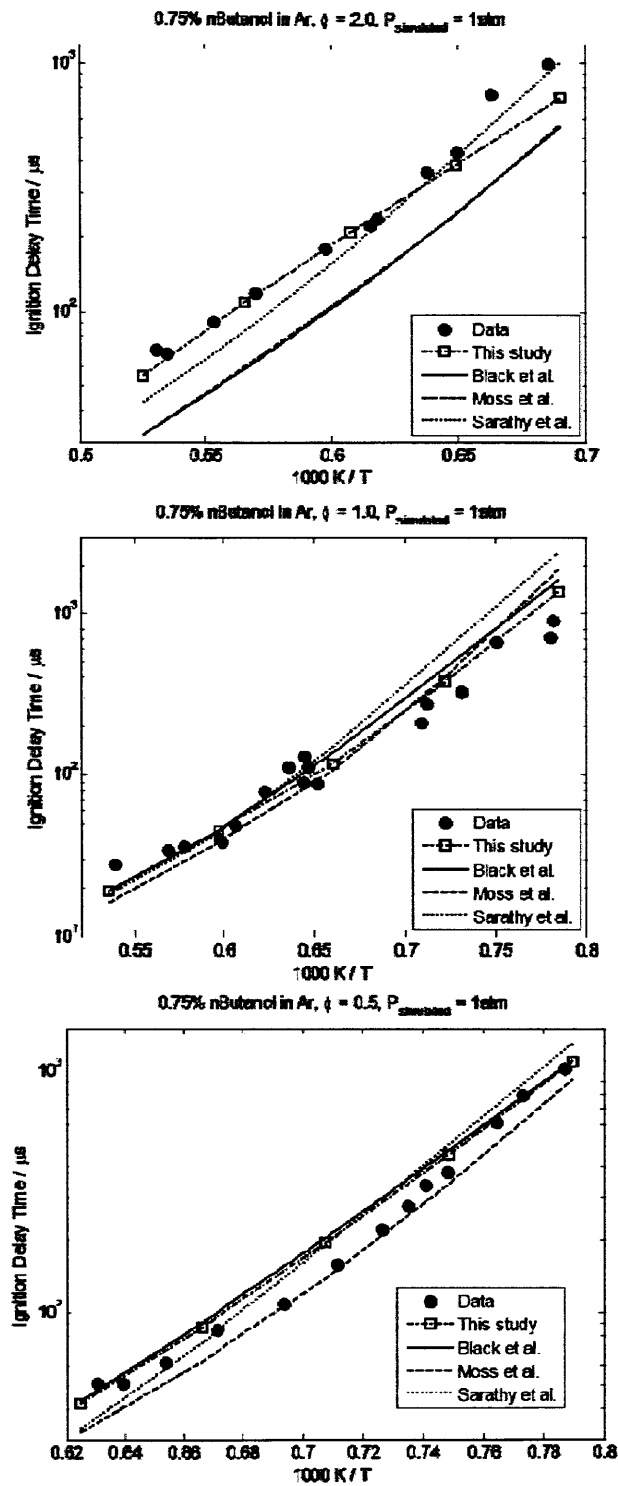
Figure 5-21: The four butanol models' predictions for the ignition delay time of n-butanol at a reflected shock pressure of 1 atm. The data and Black et al. predictions are from [181], the Moss et al. predictions are from [180], and the Sarathy et al. predictions are from [179].

161

For the rich experiments at a reflected pressure of 1atm, both the Sarathy model and our model capture the entire dataset well; the Black and Moss models exhibit the correct power law relationship, but underestimate the ignition delay by a factor of ~2 across most of the temperature range. All four models capture the stoichiometric experiments equally well. For the lean experiments, all four models again capture the dataset well, although the Moss model is the only mechanism that captures the curvature of the ignition delay at high temperatures reasonably well.

For the experiments conducted at a reflected pressure of 2.6 atm: all models capture the 0.6% initial n-butanol concentration experiments well at higher temperatures (>1380 K). At lower temperatures, both the Black model and our model capture the dataset well; the Moss and Sarathy models overestimate the ignition delay at lower temperatures. All four models capture the 3.6% initial n-butanol concentration experiments equally well.

For the experiments conducted at a reflected pressure of 8 atm: the Black model captures the rich dataset well across the entire temperature range. The Moss model captures the dataset at high temperatures (>1430 K) but overestimates the ignition delay at lower temperatures; conversely, our model captures the dataset well for low temperatures (<1490 K) but underestimates the ignition delay at higher temperatures. The Sarathy model overestimates the ignition delay across the entire temperature range. For the stoichiometric experiments, the Black model and our model capture the dataset well for temperatures above 1176 K; both models overestimate the ignition delay at lower temperatures. The Moss model captures the dataset well above 1282 K, but overestimates the ignition delay at lower temperatures. The Sarathy model overestimates the ignition delay for much of the temperature range tested. Lastly, the four models capture the lean condition experiments equally well: the ignition delay is well predicted at temperatures above 1220 K but is overestimated at lower temperatures.

In summary, the Black model and our model predict the ignition delay well across most of the temperature range, but may overestimate the ignition delay at lower temperatures. The Moss model does well at capturing the stoichiometric and lean condition experiments. The Sarathy model does well for the experiments conducted at reflected pressures of 1 atm, but overestimates the ignition delay for most other conditions.

5.4.5.2 N-BUTANOL: EXPERIMENTS CONDUCTED BY MOSS ET AL.

Ignition delay times of n-butanol were also measured by Moss *et al.* for equivalence ratios of ϕ=0.25, ϕ=0.5, and ϕ=1.0, for initial n-butanol mole fractions of 0.25%, 0.5%, and 1%. The reflected shock temperatures and pressures spanned 1200-1700 K and 1-4 bar, respectively. Our model's predictions, in addition to the Black, Moss, and Sarathy n-butanol models' predictions, for the ignition delay of 1% n-butanol are presented in Figure 5-22; the four models' predictions for the ignition delay of 0.5% and 0.25% n-butanol are presented in the Supplemental Information.
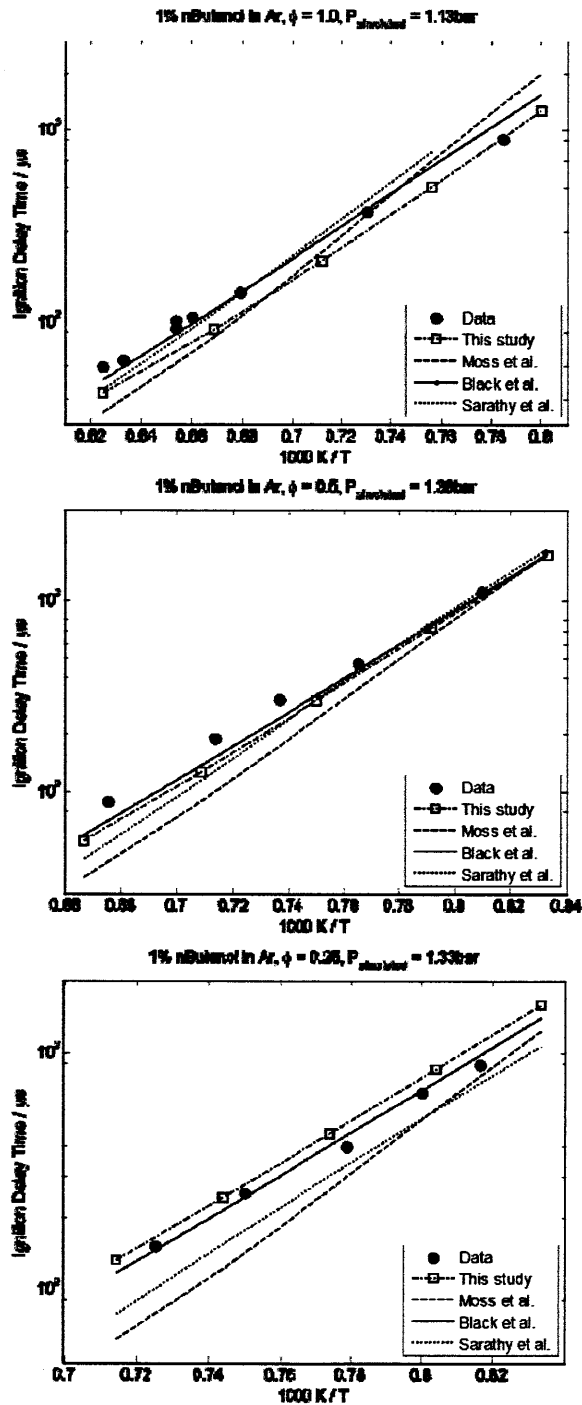
Figure 5-22: The four butanol models' predictions for the ignition delay time of 1% n-butanol at a reflected shock pressure of 1 atm. The Black et al. predictions are from [181], the data and Moss et al. predictions are from [180], and the Sarathy et al. predictions are from [179].

For the 1% initial n-butanol concentration experiments: All models capture the stoichiometric experiments across the entire temperature range equally well. All models also capture the lean experiments (ϕ = 0.5) well at temperatures below 1429 K; while the

164

Black model and our model predict the data well at higher temperatures, the Moss and Sarathy models underestimate the ignition delay. For the very lean ($\phi = 0.25$) experiments, the Black model, Sarathy model, and our model capture the dataset well across the entire temperature range. The Moss model captures the dataset well for temperatures < 1315 K, but underestimates the ignition delay at higher temperatures. For the 0.5% initial n-butanol concentration experiments: The Black model, Sarathy model, and our model predict the ignition delay well across the entire temperature range; the Moss model does well at temperatures < 1613 K but underestimates the ignition delay at higher temperatures. The same analysis is true for the lean experiments, with the temperature cutoff for the Moss model occurring at 1471 K. For the very lean experiments, the Black and Sarathy models do well across the entire temperature range; our model does well at temperatures > 1250 K, and overestimates the ignition delay at lower temperatures. The Moss model performs well at temperatures below 1333 K, but underestimates the ignition delay at higher temperatures.

For the 0.25% initial n-butanol concentration experiments: none of the models capture this dataset well for an extended range of temperatures. The Black model, Moss model, and our model capture the high-temperature experiments well, but overestimate the ignition delay below 1389 K. The Sarathy model overestimates the ignition delay across the entire temperature range.

In summary, the Black model, Sarathy model, and our model match the 1% and 0.5% n-butanol data well over all temperatures and equivalence ratios tested. The Moss model does well for these conditions at lower temperatures, but underestimates the ignition delay at higher temperatures. Finally, none of the models do particularly well at predicting the 0.25% n-butanol experimental data.

5.4.5.3 N-BUTANOL: EXPERIMENTS CONDUCTED BY NOORANI ET AL.

A comparative study on the high-temperature ignition properties of primary alcohols, up to butanol, was performed by Noorani et al. [227]. The reflected shock pressures studied were 2, 10, and 12 atm, and the equivalence ratios investigated were $\phi = 0.5$, 1.0, and 2.0; the fuel percentage ranged from 0.5 to 2.0%. The experimental conditions of this study

are similar to those of Black et al.[181] (see Section 5.4.5.1), though the 10 and 12 atm reflected shock pressures studied here are larger than those of the Black et al. study.
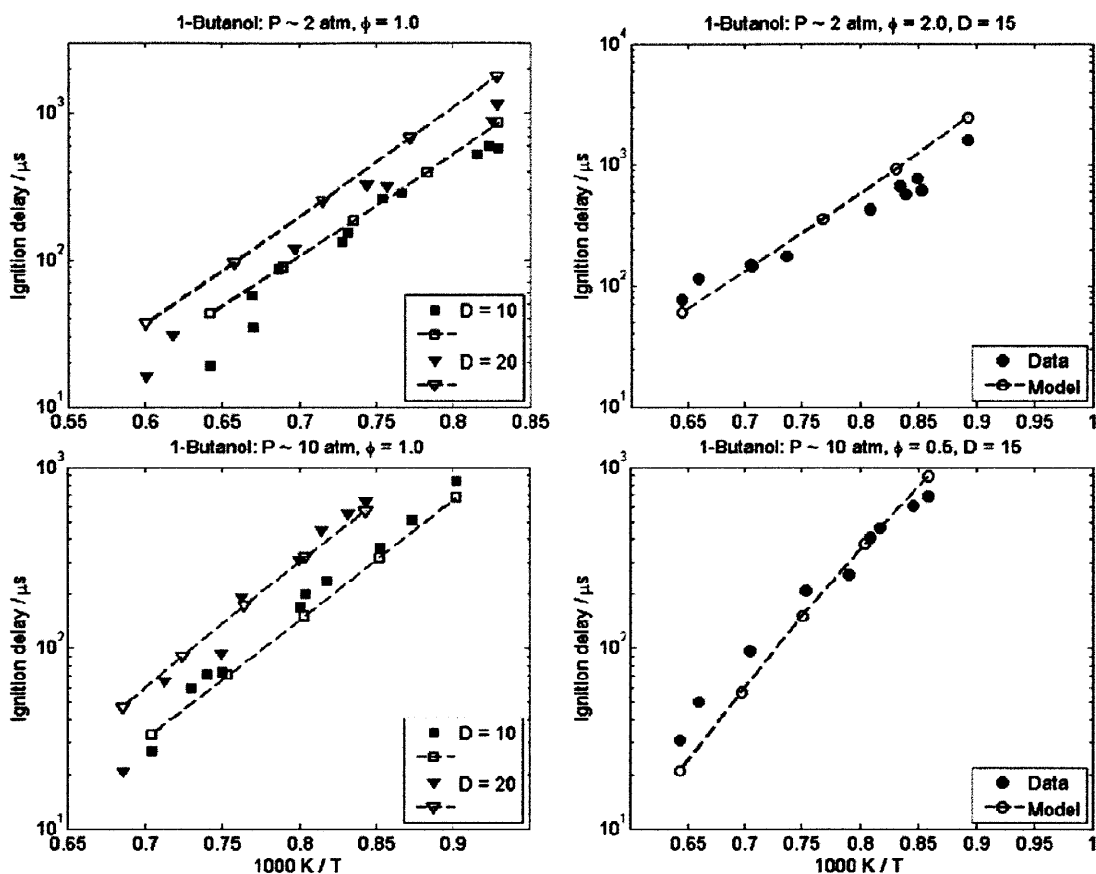
Figure 5-23: The predicted and experimental [227] ignition delay of n-butanol in a high-temperature shock tube study. The simulated pressure, equivalence ratio, and argon-to-oxygen dilution ratio ("D") for each experiment are given in the figure. The fuel percentage of each mixture is 1.5% for the D=10 mixtures, 0.8% for the D=20 mixtures, 0.5% for the D=15 mixture at 10 atm, and 2.0% for the D=15 mixture at 2 atm.

These experiments were modeled in CHEMKIN 10101 assuming an adiabatic, isochoric Closed Homogeneous Batch Reactor. The simulated temperatures, pressures, and fuel mixture compositions are given in Figure 5-23. The ignition delay was defined as the time to the maximum rate of pressure rise (in accord with the study) and was computed independently of CHEMKIN. Overall, the model predicts this experimental dataset very well. At some of the higher temperatures, our predicted ignition delays are longer than the experimental values, but always within a factor of three. The authors do not give explicit uncertainty ranges for the data, but mention that "... at higher temperatures, the

166

experimental scatter is largest due to the increased uncertainty that accompanies the shortest ignition delay times."

Although it is encouraging that the model predicts this dataset well, it is not completely unexpected: at the similar experimental conditions of Black et al., it was concluded that the ignition delay was primarily sensitive to the small molecule chemistry. Thus, there is not as much n-butanol chemistry knowledge to obtain from these sets of experiments that were not already learned from other experiments.

In general, for high-temperature shock tube studies, the most useful future experiments would either: (1) test much larger reflected shock pressures and/or (2) measure speciation data. Our collaborators in Prof. Ron Hanson's group at Stanford University have done and are continuing to perform these exact experiments. This unpublished study (at the time of this thesis) has been especially useful in finding new species thermochemistry and reaction rate coefficients that our model was sensitive to, and which required more accurate thermochemical parameters. Our two groups, in addition to Prof. Kevin Van Geem and Prof. Sung's group at the University of Connecticut, have been accepted to give an oral presentation on this work at the 7th International Conference on Chemical Kinetics [231].

5.4.5.4 N-BUTANOL: EXPERIMENTS CONDUCTED BY HEUFER ET AL.

5.4.5.5 N-BUTANOL: EXPERIMENTS CONDUCTED BY VRANCKX ET AL.

Heufer et al. [228] have measured the ignition delay of n-butanol at 10, 20, and 40 bar, and Vranckx et al. [229] have measured the ignition delay at 80 bar. Both sets of experiments' reflected shock temperatures were in the low-to-intermediate temperature regime. The model's predicted ignition delay for all experiments is shown in Figure 5-24; the ignition delay was defined as the time to the maximum rate of pressure rise. Overall, the model predicts these two experimental datasets very well. However, at the highest temperatures tested in the 80 bar experiments, the model's ignition delay is as

much as 3 times shorter than the experiment. Furthermore, the model has the wrong temperature-dependence at the lowest temperatures, consistent with the model's misprediction of the University of Connecticut's RCM experiments (see Section 5.4.5.6) in the same pressure and temperature range.
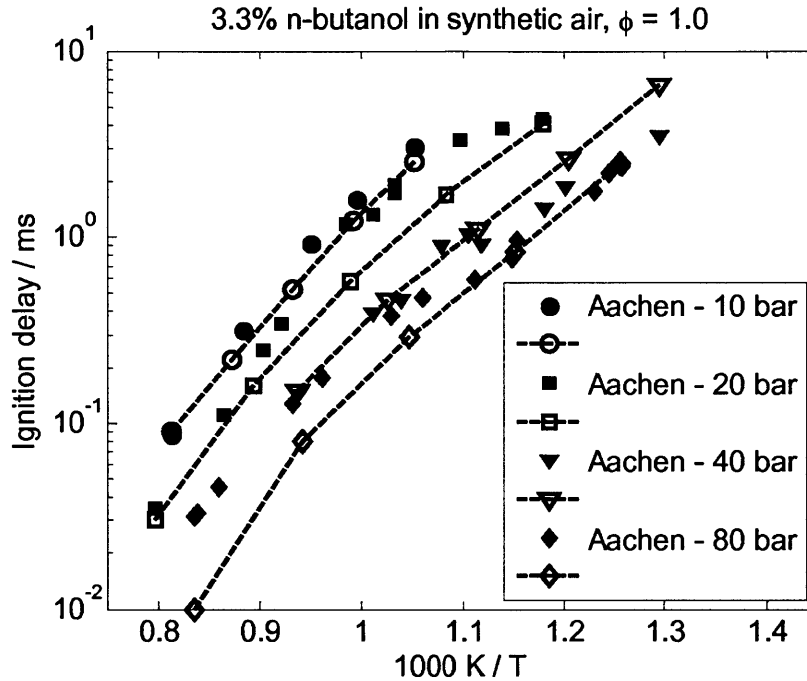
Figure 5-24: Predicted and experimental ([228] for the 10, 20, and 40 bar experiments and [229] for the 80 bar experiments) ignition delay for n-butanol.

5.4.5.6 IGNITION DELAY IN A RAPID COMPRESSION MACHINE

Additional studies on the combustion characteristics of n-butanol have been performed, in particular the ignition delay as measured in a rapid compression machine [230]. The simulations were performed in CHEMKIN-Pro, assuming an adiabatic, isochoric closed homogeneous batch reactor. For this reactor set-up, the adiabatic assumption should be critically analyzed as there is small, yet significant heat loss in these experiments. Without any experimental measurements on Q(t), I have assumed adiabatic conditions as a first approximation.

The predicted ignition delays for eight unique experimental conditions (excluding temperature) are presented in Figure 5-25. Overall, the predictions are in reasonable

agreement with the experimental data. The notable exceptions are the 3.38 mol% n-butanol experiments performed at 15 bar (upper right-hand figure), where the model does not predict the equivalence ratio (phi) dependence; in these experiments, the equivalence ratio is changed by increasing the amount of air. This lack of a trend is strange, especially since similar simulations at 15 bar with 20.3 mol% O_2 (lower right-hand figure) do show a dependency on equivalence ratio; in these experiments, the amount of n-butanol was changed to realize a change in equivalence ratio.
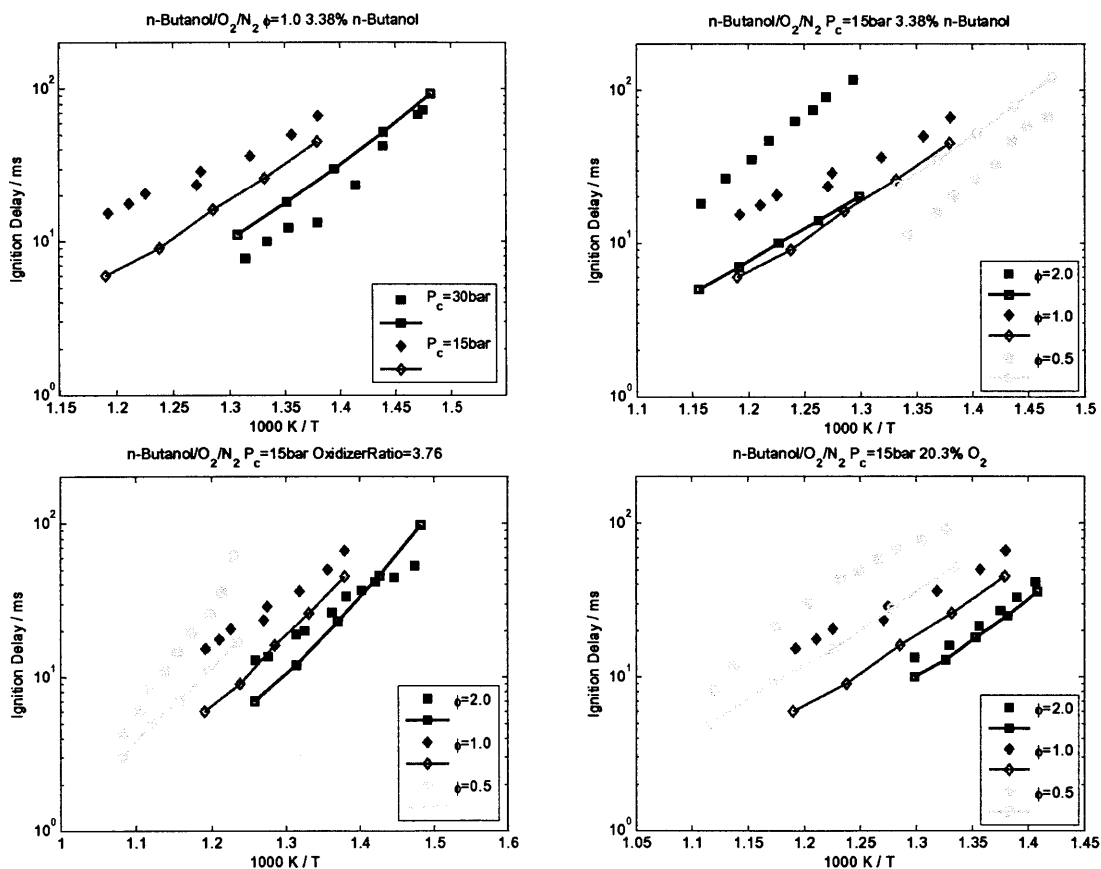
Figure 5-25: Predicted and experimental [230] ignition delays for n-butanol in a rapid compression machine. An adiabatic, isochoric closed homogeneous batch reactor was implemented in modeling the rapid compression machine and the ignition delay was defined as the time to reach 50% of the maximum hydroxyl radical concentration.

Although the model predictions are not as accurate as one may like, all predicted ignition delays are on the same order time scale as the experiments. This is particularly meaningful because all other published n-butanol mechanisms, including our model in

Combustion and Flame, predict ignition delays one-to-three orders of magnitude slower (longer ignition delays) than the experimental data.

An important rate coefficient estimate was improved during this work. In our Combustion and Flame mechanism, the abstraction of n-butanol by hydroperoxy radical was estimated by RMG's "Average of Averages" routine. For the datasets used to validate the model in the Combustion and Flame paper, the model was never deemed to be sensitive to these kinetics. When initially modeling the rapid compression machine, we confirmed with our collaborators that our predicted ignition delays were too long. The first approach in solving this was to determine which reactions the model was most sensitive to at these conditions, temperatures significantly lower and pressures significantly higher than any of the conditions used in the Combustion and Flame manuscript. Running the sensitivity analysis in CHEMKIN-Pro proved futile; the calculations were still running after 7 days, however sensitivity analysis for a similar reactor model at higher temperatures typically took ~1 day.

Performing sensitivity analysis by hand, by manually changing some potential key kinetics, was performed instead. The first reaction to happen under these conditions is hydrogen abstraction of n-butanol by molecular oxygen, so these were the first kinetics tested. Multiplying these kinetics by 1000 did not change the predicted ignition delays, so their values were restored. One of the products of the previous reactions is hydroperoxy radical. The hydrogen abstraction of n-butanol by hydroperoxy radical was then tested; the model proved to be sensitive to these kinetics, dropping the predicted ignition delays by ~two orders of magnitude with an increase in rate coefficient of 1000. The source of the nBuOH+HO2 kinetics were RMG estimates; in fact, RMG estimated the kinetics for the reverse reaction, Radical+H2O2=HO2+nBuOH.

Looking at the H_Abstraction X_H tree in the RMG Dictionary:

    L2: O_H

        L3: O_pri

L3: O_sec

    L4: O/H/NonDeC

    L4: O/H/NonDeO

    L4: O/H/OneDe

H2O2 is classified by RMG as O/H/NonDeO. With no X_H entries in the database matching this node, RMG "fell up the tree" one level to O_sec. Still finding no matches, RMG fell up to the O_H node. Although RMG still had no matches for O_H, RMG does have entries for O_pri and thus estimated the kinetics accordingly. Unfortunately, O_pri represents a hydrogen atom from water. Thus, RMG's estimate for a radical abstracting a hydrogen from H_2O_2 was (essentially) the kinetics for a radical abstracting a hydrogen from H_2O!

The abstraction of each C-H hydrogen from all four butanol isomers was calculated using TST and added to the RMG database. A new L5 node "H2O2" was added beneath the L4 node O/N/NonDeO so all future RMG estimate for a radical abstracting hydrogen from hydrogen peroxide will use an average of these calculations, in the worst-case scenario.

One other aspect to consider when comparing our model's predictions with the data is the assumption of an adiabatic reactor. As mentioned previously, this assumption is known to be flawed as heat loss is measurable during the experiments; if the experimental temperature profile, T(t), or heat loss profile, Q(t), were known, these could be augmented to the current CHEMKIN simulations to model the experiments more accurately. With the predicted T(t) curve overestimating the true experimental value, our kinetic rate coefficients are faster, resulting in a faster build-up of our radical pool and thus shorter ignition delays. Any heat loss will decrease the simulated temperature profile, resulting in slower chemistry and longer ignition delays. Thus, our model predicting shorter ignition delays is reasonable, as these are likely to increase slightly once heat loss is accounted for. However, our collaborators at the University of Connecticut have shown that this effect is not large enough to resolve all of the discrepancies and thus more work on the low-temperature submechanism is still needed.

5.4.5.7 BUTANAL

In addition to validating the n-butanol mechanism, it is important to validate the submechanisms of the model. If certain submechanisms of the total model are inadequate, it is difficult to apply the present mechanism to other species of interest. Although our mechanism is for an alcohol, one of the important intermediates is an aldehyde: butanal. As was shown in the previous sections, a significant fraction of n-butanol reacts to form butanal. Thus, the chemistry of n-butanol is highly correlated with the chemistry of butanal.

The ignition delay time of butanal was measured recently in a shock tube by Davidson *et al.* [182]. The reflected shock conditions spanned temperatures of 1150–1550 K, pressures of 1–4 atm, and the equivalence ratios tested were stoichiometric and fuel rich (ϕ=2.0). Our model's comparison against the data is shown in Figure 5-26. Our model predicts the ignition delay time for three of the four experiments quite well: the stoichiometric mixture with 5.5% O_2 for both pressures tested and the rich mixture at 1.4 atm. Our model slightly overestimates the ignition delay for the remaining case: P=1.8 atm, φ=1.0, with 4% initial O_2. In general, the reactivity of butanal was governed by H-abstraction reactions from butanal by H atom and hydroxyl radical; the $CH_3CH_2CH_2$-CHO C-C bond fission was also a significant pathway.
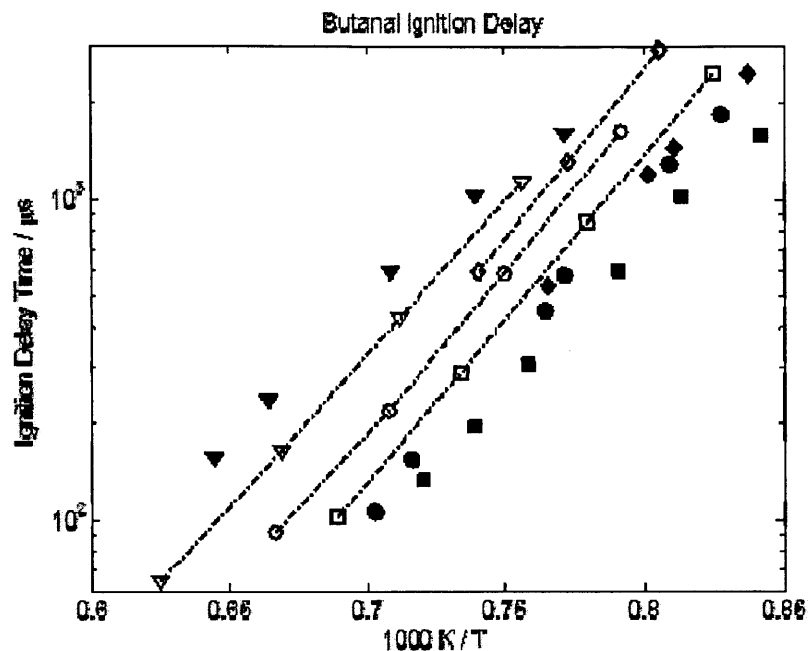
Figure 5-26: Predicted and experimental [182] butanal ignition delay times. The conditions simulated were: P=1.45atm, φ=1.0, 5.5% O_2 (circles), P=2.65atm, φ=1.0, 5.5% O_2 (squares), P=1.4atm, φ=2.0, 2.75% O_2 (triangles), and P=1.8atm, φ=1.0, 4% O_2 (diamonds).

5.4.5.8 N-BUTANOL + OH RATE COEFFICIENTS

The total n-butanol + OH H-Abstraction rate coefficient has been measured by Vasu et al. [232] over the temperature range 1017 – 1269 K, at pressures near 2.25 atm. A comprehensive comparison of their experimental data and many estimates for the total abstraction rate coefficient are shown in Figure 5-27 (this figure is from the Vasu et al. study). As the figure shows, my original butanol model's estimate for the total rate coefficient over these temperatures underestimates the experimental data by as much as a factor of three. The current butanol model uses the G3 calculations of Zhou et al. [233]. In their study, Zhou et al. computed each of the five H-abstraction rate coefficients of n-butanol by OH using transition state theory. An asymmetric Eckart tunneling correction was used, and the low-frequency internal torsional modes were treated as 1-d separable hindered rotors. In their study, the authors state the most stable conformer of the transition states contains Hydrogen-bonding characteristics, i.e. 5-, 6-, and 7-member cyclic structures. The assumption of treating the low-frequency torsional modes as separable should be revisited, as the low-frequency modes in the cyclic Hydrogen-

173

bonding transition state structure are most likely highly coupled. Dr. Sandeep Sharma, formerly of the Green Group, and co-workers have presented a method for handling coupled hindered rotors [234]. Zador et al. have very recently reported a calculation for OH + n-butanol [235] which gives different rate coefficients than those of Zhou et al.
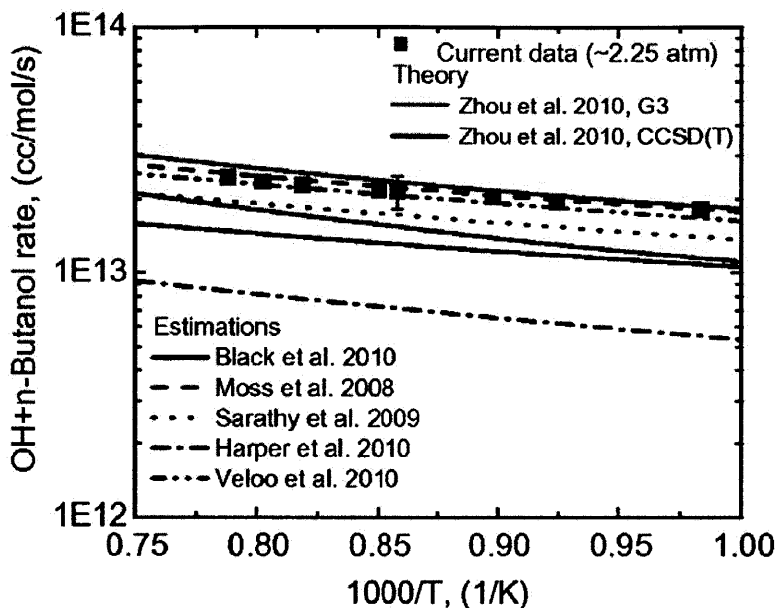
Figure 5-27: Total n-butanol + OH rate coefficient (figure from [233]). The data is from Ref. [232], the Zhou et al. estimates from Ref. [233], the Black et al. estimates from [181], the Moss et al. estimates from [180], the Sarathy et al. estimates from [179], the Harper et al. estimates from [166], and the Veloo et al. estimates from [236].

5.5   CONCLUSIONS

A detailed, robust reaction mechanism for n-butanol has been constructed using an automated, open-source software package, Reaction Mechanism Generator (RMG). The model has been tested against multiple types of experiments – flames, jet-stirred reactors, shock tubes – and varying reaction conditions – diffusion and premixed, rich and lean, over a pressure range of 1-10 atm and a temperature range of 800-1800 K – with great success. For the pyrolysis experiments, the n-butanol chemistry was controlled by the $CH_3CH_2CH_2$-CH_2OH bond fission reaction near the entrance of the reactor; H-abstraction from n-butanol by H atom and methyl radical, forming the 1-hydroxybutyl radical, dominated throughout the remainder of the reactor. In the doped methane flame

174

experiment, the $CH_3CH_2CH_2-CH_2OH$ bond fission again dictated the reactivity of n-butanol. However, H-abstraction rates from n-butanol, primarily by H atom, governed the formation of minor products; both the four-center dehydration reaction and the β-scission of the 1-(hydroxymethyl)propyl radical contributed to the formation of 1-butene. For the opposed-flow diffusion flame, the n-butanol reactivity was governed by H-abstraction by hydroxyl radical and H atom for the first half of the reaction zone and by the $CH_3CH_2CH_2-CH_2OH$ bond fission in the second half. For all shock tube experiments, H-abstraction reactions from the fuel with hydroxyl radical and H atom controlled the ignition delay time; thus, the models for all three shock tube experiments were very sensitive to the reactions controlling the concentration of hydroxyl radical and H atom, namely CH3+HO2=CH3O+OH, C2H3+O2=CH2CHO+O, H+O2=O+OH, and C2H4+H=C2H5. In the jet-stirred reactors, the dominant n-butanol decomposition pathways switched from H-abstraction by H atom in the rich conditions to H-abstraction by hydroxyl radical in the lean conditions; H-abstraction by O atom was also significant at high temperatures and lean conditions. Overall, the mechanism can reproduce the ignition delay of n-butanol quite well across a wide range of temperatures, pressures, and fuel conditions and can reproduce species concentration profiles under many differing reactor conditions, for all major and minor products; the mechanism can also reproduce the ignition delay of butanal very well across a range of experimental conditions. Future work on n-butanol includes exploring the discrepancies in the acetylene and butadiene submechanisms, along with a more thorough analysis on the pathways to benzene and other aromatic compounds. This n-butanol mechanism should be a useful Seed Mechanism for future modeling of n-butanol fuel blends and other butanol isomers.

CHAPTER 6
EXTENDING THE MECHANISM TO
SEC-, TERT-, AND ISO-BUTANOL

Note: Some of the results reported here have been recently presented in Reference [237].

6.1   INTRODUCTION

The study and use of oxygenated hydrocarbons, or biofuels, has become prevalent in the twenty-first century as the world searches for renewable energy sources. Some typical industrial examples are ethanol and n-butanol. While ethanol has been the primary commercially-used fuel additive, recent research has been shifting towards the study of longer-chain alcohols; some properties that make long-chain alcohols advantageous over short-chain alcohols are: larger energy densities; lower miscibility in water, which cause less problems in the event of contamination; their greater compatibility when blended with conventional fuels or utilized in conventional engines; their lower vapor pressure, which reduces fugitive emissions; and their lower heat of vaporization, which is important for "cold starts."

To better understand the chemistry of different oxygenated fuels over a range of temperatures, pressures, and equivalence ratios, one tried and true approach is through pure experimentation. Burning each of the potential fuels across a range of temperatures and pressures, in every engine of interest, would undoubtedly reveal the solution; however this approach is quite expensive and requires accurate predictions of future engine designs. Alternatively, it would be beneficial to have a kinetic model which describes the fuel's reactivity, before running any experiments. In this way, a design of experiments may be carried out on a computer and only the promising fuel compositions need be explored experimentally. Shifting from *a posteriori* to *a priori* knowledge would improve the efficiency of the validation process, in particular by limiting the amount of resources necessary to conduct experiments. *A priori* knowledge requires extracting as much useful information out of the already available, yet limited data. For example, the

177

validated combustion chemistry for normal- and iso-propanol [24] could serve as a tool to predict the behavior of primary and secondary alcohols. Similarly if one possessed validated pyrolysis and combustion networks for normal-, sec- and tert-butanol, i.e. the smallest oxygenated hydrocarbon system that contains a primary, secondary, and tertiary alcohol, then one should have many of the necessary tools to predict the behavior of larger alcohols, regardless of their structure's complexity.

Bio-butanol is one of the emerging fuel additives because it could be 100% renewably sourced from agriculture feedstocks such as corn, wheat, and sugar cane or from biomass waste. Bio-butanol can be produced by bacterial fermentation of biomass, and several reports suggest this process will soon be commercialized [189, 202, 238]. Tremendous effort is currently being placed on understanding the reaction pathways of the different butanol isomers under pyrolysis and combustion conditions. Recent emphasis is on exploring the possibilities of utilizing not only n-butanol but also sec- and tert-butanol produced from fermentation as either a fuel additive or alternative fuel. Currently, sec-butanol is produced primarily as a precursor to methyl ethyl ketone while tert-butanol is an industrial solvent produced for paint removal or the production of methyl tert-butyl ether (MTBE). tert-Butanol is also used as an octane enhancer.

The first study of tert-butanol pyrolysis was reported by Schultz and Kistiakowsky [239]. The authors concluded that the thermal decomposition of tert-butanol was unimolecular over the temperature range 760-828 K, reacting to form water and isobutene, with a rate expression of $k = 4.8 \times 10^{14} \exp(-273790 \text{ J/mol} / RT) \text{ s}^{-1}$; the authors also report a fall-off effect beginning at 2.66×10^{-3} bar. Barnard investigated the pyrolysis of tert-butanol [240] over the temperature range 760-893K, for initial pressures from 2.66×10^{-2} to 5.33×10^{-1} bar and also concluded that the decomposition of tert-butanol was homogenous and proceeded mainly through the water + isobutene route; this was confirmed by noticing no difference in the rate of decomposition when introducing nitric oxide (a free radical trap) to the system. The overall tert-butanol decomposition rate expression reported was $k = 10^{11.51(\pm 0.45)} \exp(-227810 \text{ J/mol} / RT) \text{ s}^{-1}$. Smith et al. studied diffusion flames of the four butanol isomers [171]. For all four isomers, those authors concluded that the dominant

decomposition route was through hydrogen abstraction of the parent molecule; the direct pathway from a butanol isomer to water + alkene was not discussed.

McEnally and Pfefferle studied the butanol isomers by doping a methane diffusion flame and measuring the centerline C1-C12 mole fraction profiles using electron-impact and 118 nm photoionization mass spectrometry [172]; this enabled the detection of species with molecular weight M_m between 17 and 200 amu, although the individual isomers could not be distinguished. One focus of this study was gaining a better understanding of the competition between the different decomposition pathways: unimolecular water elimination, bond fission, and hydrogen abstraction. Using a simple kinetic model, the authors estimated the flux for tert-, sec-, and n-butanol through the water elimination reaction to be 87, 28, and 1%, respectively; the remaining flux for each isomer was estimated to be primarily through C-C bond fissions, with little-to-no flux through hydrogen abstractions. Yang et al. studied the four butanol isomers in premixed, fuel-rich (initial equivalence ratio of 1.71) butanol-oxygen flames at 0.04 bar [173]. Using a molecular beam photoionization mass spectrometer, species with a mass-to-charge ratio from 15 to 106 were detected, including some radical species. Equally important, the study determined the identity of most isomers in each flame, e.g. the majority of the C_4H_8 species detected in the tert-, sec-, and n-butanol flames were isobutene, 2-butene, and 1-butene, respectively. The study also concluded that the position of the alcohol in the fuel had an important role in enol formation; a reaction network was not proposed.

The first detailed chemistry model for the four butanol isomers was reported by Moss et al. [180]. The joint reaction network, containing 158 species and 1250 reactions, was validated against shock tube ignition delay measurements for the four butanol isomers. The reflected shock temperatures and pressures tested ranged from 1200-1800 K and 1-4 bar, respectively, and the equivalence ratios tested were 1.0 (with 1, 0.5, and 0.25 mol% butanol in argon), 0.5 (with 1 and 0.5 mol% butanol in argon), and 0.25 (with 1 and 0.5 mol% butanol in argon) for each isomer. Experimentally, the authors observed the reactivity of the isomers, from least to most reactive, to be: tert-butanol, sec-butanol, iso-butanol, and n-butanol. Computationally, the authors determined that the difference in

reactivity was due to the difference in the butanol decomposition pathways: while n-butanol was consumed primarily by hydrogen abstraction of the parent molecule by hydrogen atom and hydroxyl radical, the dominant routes through tert- and sec-butanol were through the four-centered water elimination reaction. The alkenes formed by water elimination lead to resonantly-stabilized radicals thus retarding the ignition delay. The kinetic parameters for the water elimination reactions, while being based on values reported in the literature, were adjusted to match the data. While extensive, the network does not contain enol species, which have been shown to be common intermediates in the oxidation of hydrocarbons [174], and ignores falloff effects.

Given the importance that capturing the competing pathways' reaction rates has on predicting the fuel chemistry over a range of temperatures and pressures, herein we report a detailed, pressure-dependent reaction network for tert- and sec-butanol whose water elimination kinetics, in addition to the kinetics for hydrogen abstraction of butanol by hydrogen atom and methyl radical, have been computed using quantum chemistry. The network, generated by an open-source software package Reaction Mechanism Generator (RMG) [183], is validated against the doped methane diffusion flame of McEnally and Pfefferle, the shock tube ignition delay data of Moss et al, and newly reported pyrolysis data measured at the Laboratory for Chemical Technology. Section 6.2 describes the experimental and analytical apparatus used in the pyrolysis experiments, in addition to describing how each of the reactor setups was modeled. The automated construction of the reaction network, including its refinement via statistical mechanics and quantum chemistry, is explained in Section 6.3. The comparison between the model's predictions and all experimental data, including pathways to benzene and other small aromatic molecules, is illustrated in Section 6.4; combining the present study with one previously reported for n-butanol [166], the different pathways and reactivity for the primary, secondary, and tertiary alcohol are also discussed. Finally, our conclusions and future directions in constructing reaction networks for alternative fuels are presented in Section 6.5.

6.2 EXPERIMENTAL AND COMPUTATIONAL PROCEDURES

6.2.1 PYROLYSIS EXPERIMENTS

Experiments studying the pyrolysis of the butanol isomers were conducted in the bench-scale set-up of the Laboratory for Chemical Technology (LCT) of Ghent University. For details of the experimental apparatus and the analytical techniques, the reader is directed to the manuscript mentioned at the beginning of this chapter.

6.2.2 MODELING: PYROLYSIS

The pyrolysis reactor was modeled using the CHEMKIN-Pro software package [240]. Initially, the LCT's laminar flow reactor was modeled using CHEMKIN's Cylindrical Shear Flow Reactor model. As the computed temperature and concentration profiles exhibited only small radial gradients throughout the length of the reactor, for both the tert- and sec-butanol pyrolysis simulations, we concluded modeling the reactor as plug flow, as was assumed by Chen and Froment [194] and in our previous study on n-butanol [166], was valid. As the length-to-diameter ratio is greater than 200, entrance effects can be neglected [241]. The calculated Peclet number is on the order of 10^3 hence back-mixing is not important.

For all results reported, we implemented CHEMKIN's Plug Flow Reactor module. The momentum equation and residence time calculation were turned off. The experimentally measured temperature profile was supplied, as was the COP; the reactor dimensions used were those reported in Section 6.2.1. The mass flow rates of tert- and sec-butanol, for all simulations, were 6.556×10^{-2} and 6.721×10^{-2} grams per second, respectively. The default absolute and relative tolerances were sufficient for convergence. In addition to having CHEMKIN return the species mass fraction profiles along the length of the reactor, the normalized sensitivity coefficients for each species, defined in Equation (4.1), was also reported. Since the reactions reported in our network are reversible, the forward and reverse pre-exponential factors are changed in concert to ensure thermodynamic equilibrium.

$$\tilde{s}_{ij} = \frac{A_j}{X_i} \frac{\partial X_i}{\partial A_j} = \frac{\partial (\ln X_i)}{\partial (\ln A_j)} \tag{4.1}$$

6.2.3 MODELING: DOPED METHANE DIFFUSION FLAME

The McEnally and Pfefferle doped methane diffusion flame was modeled using a solver developed by Sharma et al. in their study on hexadienes [190]; this solver will be referenced as the "Sharma flame solver" throughout the remainder of the article. A brief description of the reactor model ensues; we refer the reader to the reference for a more detailed explanation.

To model the doped methane flame, the system was assumed to be at steady-state; the geometry was assumed to be axisymmetric. In general, solving this problem requires computing the temperature, axial and radial velocities, and species concentrations as a function of r and z. Bennett et al. solved this problem for the undoped case [198], for the same reactor geometry, using the local rectangular refinement solution-adaptive gridding method [242], using the GRI-Mech 2.11 reaction network [243]. Additionally, McEnally and Pfefferle have demonstrated that the experimental centerline temperature profiles of the doped and undoped flames, for the small amount of dopant used, are equivalent [172, 199, 200]. Thus, rather than compute the temperature profile, the Sharma flame solver utilizes the numerically-determined temperature profile of Bennett et al.; the Sharma flame solver also utilizes Bennett's computed axial and radial velocity profiles. Thus, the only unknown quantities, which the Sharma flame solver computes, are the species concentration profiles.

To solve for the concentration profiles, the Sharma flame solver starts with the mass conservation equation, Equation (4.2). ρ is the total density, v_z and v_r are the axial and radial velocity, Y_i is the mass fraction of species i, γ_i and $M_{m,i}$ are the molar rate of production and molecular mass of species i, and the radial diffusive flux is defined in Equation (4.3), where D_i is the multi-component diffusivity coefficient for species i; the axial diffusive flux is defined similarly. CHEMKIN-II [205], modified to handle the Chebyshev formatted fall-off effects [186], was used to estimate species thermochemistry and reaction rates; the Sandia Transport subroutine [206] was used to estimate species transport properties.

$$\rho v_z \frac{\partial Y_i}{\partial z} + \rho v_r \frac{\partial Y_i}{\partial r} = \gamma_i M_{m,i} - \frac{1}{r}\frac{\partial}{\partial r}\left(r\rho v_{r,i}Y_i\right) - \frac{\partial}{\partial z}\left(\rho v_{z,i}Y_i\right) \tag{4.2}$$

$$v_{r,i}Y_i = -D_i\left(\underline{Y}\right)\frac{\partial Y_i}{\partial r} \tag{4.3}$$

The Dufour and Soret effects are neglected. The axial diffusive term is also neglected; the significance of this assumption, particularly with respect to oxygen entrainment, is discussed in detail elsewhere [190]. In this flame geometry, the important diffusion effects are perpendicular to the flow. Moving the radial convection term to the right-hand side of Equation (4.2) isolates all r-dependent terms to one side of the equation; this problem can now be solved using the Method of Lines [201]. By approximating the partial derivatives with respect to r using finite differences, the partial differential equation is converted to an ordinary differential equation (ODE). This system of ODEs is solved using the commercially available ODE solver package DASPK-3.1 [202]; the species mass fractions leaving the burner reported in the McEnally and Pfefferle study [172] are supplied as the initial conditions. Despite supplying the temperature and velocity profiles to the Sharma flame solver, the computation is still very demanding. The number of state variables to solve for is N$_{species}$ * N$_{radial grid points}$ with 70 grid points being a typical value, so for a 281 species model there are 19,670 coupled stiff differential equations. Thus, to accelerate the computation, the Jacobian matrix was computed analytically using parallel computing. Computing the concentration profiles for the 2-D diffusion flame for our network took ~8 hours to solve across eight CPUs.

Normalized sensitivity coefficients were also computed for this reactor model, by using a centered finite differencing scheme, Equation (4.4); the a_{11} parameter is the coefficient in the Chebyshev format whose polynomial term is constant, i.e. temperature- and pressure-independent. This truncation of the normalized sensitivity coefficient is similar to approximating dc_i/dk_j as dc_i/dA_j when k_j is represented by a modified Arrhenius expression, where the effects of the temperature exponent and activation energy are not considered (or are constant for an isothermal system).

$$\tilde{s}_{ij} \equiv \frac{d\ln c_i}{d\ln k_j} = \frac{k_j}{c_i}\frac{dc_i}{dk_j} \approx \frac{k_j(a_{11})}{c_i[k_j(a_{11})]}\frac{c_i[k_j(a_{11}+\Delta a_{11})]-c_i[k_j(a_{11}-\Delta a_{11})]}{k_j(a_{11}+\Delta a_{11})-k_j(a_{11}-\Delta a_{11})} \tag{4.4}$$

6.2.4 MODELING: SHOCK TUBE EXPERIMENTS

The shock tube experiments were modeled in CHEMKIN-v4.1.1 [244] using the Closed Homogeneous Batch Reactor module. The energy equation was solved, constraining the reactor's volume. The initial temperatures, pressures, and mole fractions simulated are provided in Table S2 of the Supplementary Material. The default absolute and relative tolerances were employed. The ignition delay times were computed independently of CHEMKIN and were defined as the time at which the OH concentration reached 10% of the maximum OH concentration; this calculation method is in accord with the Moss et al. study [180]. The time-dependent normalized sensitivity coefficients for the butanol isomers were computed for certain simulation conditions; the absolute and relative tolerances for these simulations were relaxed to 1×10^{-10} and 1×10^{-4} respectively.

6.2.5 MODELING: LAMINAR BURNING VELOCITIES

This study also reports the predicted laminar burning velocity for stoichiometric mixtures of the 1-, 2-, and tert-butanol isomers with air. The laminar burning velocity was computed in CHEMKIN-MFC [64] using the Premixed Laminar Flame-Speed Calculation module. The temperature profile was estimated from equilibrium and the unburnt gas temperature was set to 343 K, at atmospheric pressure. Thermal diffusion, mixture-averaged diffusivity coefficients, and a windward differencing scheme were employed. The maximum number of grid points was set to 500 and the adaptive grid control based on solution gradient and curvature were both set to 0.15. The absolute and relative tolerances were set to 1×10^{-9} and 1×10^{-4}, respectively.

6.3 CONSTRUCTING THE REACTION NETWORK

6.3.1 AUTOMATED NETWORK GENERATION

The reported reaction network was constructed using the open-source software package Reaction Mechanism Generator (RMG) [183], originally developed by Jing Song [49]. RMG is a rate-based [57], automated reaction network generator that constructs pressure-dependent networks for isothermal, isobaric batch systems. Thermochemistry is estimated using Benson's group additivity scheme [58] and a reaction's high-pressure-limit rate expression is estimated using RMG-defined reaction family templates [49, 245]; In total, the RMG database has 40 reaction family templates, including H-

abstraction, β-scission, and recombination, from which to make reactions; the complete list of reaction family templates may be found elsewhere [183]. Fall-off effects may be estimated using the Modified Strong Collision approach of Chang et al. [185] or the Steady-state Master Equation method of Green and Bhatti [184]. Most of the pressure-dependent networks' rate coefficients (132 of the 147 reported in the mechanism) have been calculated using the steady-state master equation method of Green and Bhatti. The remaining 15 networks' rate coefficients are still solved using the Modified Strong Collision approximation, because the matrices formed when implementing the Green and Bhatti approach ran into stiffness problems.

The required inputs for a RMG simulation are: the system temperature and pressure; the initial species, in the form of a graph, and their initial concentrations; and the termination criteria, either the desired conversion or reaction time. The output from each RMG simulation includes a CHEMKIN chemistry and transport input file. The name of the reaction family template, in addition to information regarding how the rate coefficient was estimated, accompanies each reaction present in the chemistry input file. In Section 6.4, some of the more important reactions' rate coefficients will be mentioned and cited specifically; although not every reaction's rate coefficient will be referenced directly in this text, all references may be found in the provided chem.inp file in the Supplemental Information. Furthermore, similar bibliographic information is provided for each species' estimated thermochemistry and transport properties. All reactions in the CHEMKIN chemistry input file are defined as reversible reactions; thus, the CHEMKIN pre-processor will determine the reverse reaction rate coefficients, k_{rev}, from the forward reaction rate coefficients k_{for} and the thermochemistry for all simulations. The kinetic models produced by RMG have been validated against the pyrolysis and oxidation of hydrocarbons [166, 187, 189, 190].

A user may override RMG's estimation routines by supplying their own species thermochemistry and reaction rate coefficient expressions. An RMG simulation may also be seeded with an entire reaction network; if RMG is seeded with a network, the initial model contains the species in the input file, in addition to every species and reaction

185

listed in the seed network, and then expands the network using the rate-based algorithm. Using this approach, a network valid for a particular set of conditions, e.g. low-temperature oxidation, can be extended to be valid for a different set of conditions, e.g. high-temperature pyrolysis. The network reported in our previous work on n-butanol [166] was constructed in this fashion.

The reported sec- and tert-butanol network was generated using RMG, by supplying the n-butanol reaction network as a seed network. The first set of RMG simulations matched the experimental conditions of the pyrolysis reactor: 900 K and 1.5 atm, with an initial mass fraction of 1.0 for sec-butanol. The resulting network was supplied as the seed network to the next RMG simulation: 950 K and 1.5 atm, with an initial mass fraction of 1.0 for sec-butanol. This sequence was repeated until a temperature of 1200 K was reached. The network was expanded further by performing the following sets of simulations:

- sec-butanol oxidation: These simulations were run at 1 bar over a temperature range of 700–1800 K, for initial mole fractions of 0.01, 0.24, and 0.75 for sec-butanol, oxygen, and argon, respectively. These conditions were meant to emulate the lean experiments performed by Moss et al. [180]
- tert-butanol pyrolysis: These simulations mirrored the sec-butanol pyrolysis simulations mentioned previously, with tert-butanol replacing sec-butanol.
- tert-butanol oxidation: These simulations mirrored the sec-butanol oxidation simulations mentioned previously, with tert-butanol replacing sec-butanol.

The species transport properties were estimated independently of the RMG software. The Lennard-Jones parameters were calculated using empirical correlations based on the species' critical properties, which were estimated using a group-additivity scheme; more details are provided elsewhere [166].

Lastly, flux and sensitivity analysis from the reactor model simulations mentioned in Sections 6.2.2-6.2.4 identified important species and reactions for which to obtain more accurate thermochemical parameters. These refined parameters were either taken from

the literature or computed using quantum chemistry calculations, described in the next section. The final network, including the n-butanol chemistry, contains 281 species and 3608 reactions.

6.3.2 QUANTUM CHEMISTRY AND STATISTICAL MECHANICS

For some important species, the enthalpy difference relative to absolute zero, entropy, and heat capacity were computed using the standard statistical mechanics equations. In particular, the properties desired were the enthalpy of formation and entropy at 298 K, and the heat capacity at the following temperatures: 300, 400, 500, 600, 800, 1000, and 1500 K. These parameters were then fit to the NASA-7 polynomial format, for use in the CHEMKIN chemistry input file. The electronic energies, vibrational frequencies, and moments of inertia were computed using CBS-QB3 calculations [68, 216, 217] in the Gaussian03 software suite [69]. The frequencies given by the CBS-QB3 calculations were calculated using the B3LYP/CBSB7 method and were scaled by a factor of 0.99 [70]. The RRHO approximation with 1-D hindered rotor corrections was implemented. For each hindered rotor, i.e. for each heavy atom-heavy atom dihedral angle, its contribution to the vibrational partition function was replaced by the canonical partition function [55]. To compute the necessary energy levels, ε_i, a scan at dihedral increments of 10° was performed using the B3LYP/6-31G(d) method, optimizing the geometry at each step. The resulting energies as a function of dihedral angle, $V(\phi)$, were fit to a Fourier series, Equation (4.5).

$$V(\phi) = \sum_{m=0}^{5} A_m \cos(m\phi) + B_m \sin(m\phi) \qquad (4.5)$$

The reduced moment of inertia $I^{(2,3)}$ of the equilibrium geometry was computed [75] and the resulting one-dimensional Schrodinger equation was solved for the lowest 200 energy levels, ε_i. These energies were substituted into the canonical partition function and the desired thermodynamic quantities were computed. The fit to the Fourier series, the calculation of $I^{(2,3)}$, and solving the 1-D Schrodinger equation were performed using an in-house code, CANTHERM [74]. For the enthalpy of formation at 298 K, Bond Additivity Corrections and spin orbital corrections were applied [218]. The list of species and their calculated thermochemistry is reported in Table 6-1.

Table 6-1: Species thermochemistry properties, calculated using CBS-QB3 with 1D hindered rotor corrections. Enthalpy has units of kcal mol^{-1}; entropy and heat capacity have units of cal mol^{-1} K^{-1}

	$H_{f,298}$	S_{298}	$C_{P,300}$	$C_{P,400}$	$C_{P,500}$	$C_{P,600}$	$C_{P,800}$	$C_{P,1000}$	$C_{P,1500}$
sBuOH	-70.51	83.05	28.21	34.50	40.21	45.08	52.80	58.62	67.90
CH2CH[OH]C2H5	-20.29	85.12	28.32	34.19	39.30	43.58	50.27	55.31	63.42
CH3C[OH]C2H5	-28.11	85.48	27.09	32.67	37.82	42.25	49.33	54.67	63.16
CH3CH[O]C2H5	-16.68	81.26	27.15	33.15	38.50	43.06	50.30	55.76	64.36
CH3CH[OH]CHCH3	-22.93	85.73	29.60	34.49	38.99	42.99	49.61	54.76	63.12
CH3CH[OH]CH2CH2	-21.44	85.19	28.95	34.38	39.34	43.58	50.30	55.39	63.54
HOCHC2H5	-18.03	77.53	20.59	25.27	29.45	32.98	38.48	42.60	49.12
HOCHCH3	-13.27	68.07	15.60	18.61	21.40	23.78	27.55	30.37	34.91
CH3CH[OH]CH2	-15.05	76.17	22.88	27.27	31.04	34.18	39.13	42.92	49.13
tBuOH	-75.87	78.30	28.26	35.02	40.83	45.65	53.18	58.85	67.96
OC[CH3]3	-21.12	76.85	27.25	33.57	38.95	43.42	50.47	55.80	64.28
HOC[CH2][CH3]2	-24.74	81.50	29.21	35.23	40.22	44.31	50.69	55.53	63.46
tC4H9	12.48	76.49	21.47	26.48	31.51	36.05	43.52	49.21	58.13
HOC[CH3]2	-23.50	74.70	21.59	25.81	29.71	33.10	38.53	42.63	49.16

Additionally, some high-pressure-limit reaction rate coefficients were computed using transition state theory, Equation (4.6).

$$k = \kappa(T) \frac{k_B T}{h C^\circ} \exp\left(-\frac{G_{TS} - \sum G_{reactants}}{RT} \right)$$ (4.6)

k is the reaction rate coefficient, k_B and h are the Boltzmann and Planck constants, R is the universal gas constant, T is the absolute temperature, C° is the standard-state concentration, and G_i is the gas-phase Gibbs free energy of species i at concentration C°. The Gibbs free energy, G_i, was calculated using the standard $G_i = H_i - T^*S_i$ formula. $\kappa(T)$ is the asymmetric Eckart tunneling correction [71] and was calculated using the methodology presented by Johnston and Heicklen [215], with their Equation (15) replaced by the formula given in Equation (4.7), as noted by Garrett and Truhlar [73].

$$2\pi b = \frac{2\sqrt{(\xi-1)\alpha_1 + \alpha_2}}{\alpha_1^{-1/2} + \alpha_2^{-1/2}}$$ (4.7)

The rate coefficient was calculated for a series of temperatures (from 600 K to 2000 K, in 200 K increments) and the data was fit to the modified Arrhenius expression using least-

squares regression. The list of reactions and their calculated Arrhenius parameters are reported in Table 6-2. These high-pressure-limit rate coefficient calculations were also performed within CANTHERM [74].

Table 6-2: Modified Arrhenius rate coefficient parameters, computed using transition state theory at CBS-QB3, for important reactions involving sec-butanol, tert-butanol, and the butene isomers. The rate coefficient expression is $k = A (T/K)^n \exp(-E/RT)$ where A has units of s^{-1} and $cm^3\ mol^{-1}\ s^{-1}$ for unimolecular and bimolecular reactions, respectively, and E has units of kcal/mol.

	A	n	E
sBuOH + H = H2 + CH2CH[OH]C2H5	5.68E+06	2.21	7.50
sBuOH + H = H2 + CH3C[OH]C2H5	4.14E+05	2.34	2.68
sBuOH + H = H2 + CH3CH[O]C2H5	5.01E+04	2.64	7.15
sBuOH + H = H2 + CH3CH[OH]CHCH3	8.65E+05	2.30	4.68
sBuOH + H = H2 + CH3CH[OH]CH2CH2	1.68E+06	2.21	9.58
sBuOH + CH3 = CH4 + CH2CH[OH]C2H5	1.42E+00	3.60	11.05
sBuOH + CH3 = CH4 + CH3C[OH]C2H5	3.89E-01	3.53	4.01
sBuOH + CH3 = CH4 + CH3CH[O]C2H5	1.53E-02	3.92	7.89
sBuOH + CH3 = CH4 + CH3CH[OH]CHCH3	1.21E+01	3.43	9.58
sBuOH + CH3 = CH4 + CH3CH[OH]CH2CH2	1.59E+00	3.62	13.43
tBuOH + H = H2 + OC[CH3]3	9.59E+04	2.56	10.71
tBuOH + H = H2 + HOC[CH2][CH3]2	7.86E+06	2.30	9.43
tBuOH + CH3 = CH4 + OC[CH3]3	2.99E-01	3.73	10.80
tBuOH + CH3 = CH4 + HOC[CH2][CH3]2	1.32E+01	3.40	11.97
C4H8-1 + H = H2 + CH3CHCHCH2	4.50E+04	2.67	3.48
C4H8-2 + H = H2 + CH3CHCHCH2	6.70E+03	3.14	4.29
C4H8-i + H = H2 + CH2C[CH3][CH2]	5.03E+03	3.18	4.37
C4H8-1 + CH3 = CH4 + CH3CHCHCH2	2.04E-01	3.99	6.27
C4H8-2 + CH3 = CH4 + CH3CHCHCH2	1.45E-01	4.25	7.53
C4H8-i + CH3 = CH4 + CH2C[CH3][CH2]	1.19E-01	4.26	7.55
sBuOH = H2O + C4H8-1	3.63E+04	2.54	61.39
sBuOH = H2O + (Z)-C4H8-2	4.78E+05	2.15	63.90
sBuOH = H2O + (E)-C4H8-2	2.71E+05	2.22	62.63
tBuOH = H2O + C4H8-i	1.37E+07	2.26	62.42

6.4 RESULTS

6.4.1 PYROLYSIS

Our experimental pyrolysis data show that at similar experimental conditions significant differences in conversion of the butanol isomers are observed as illustrated in Table 6-3.

Table 6-3: Comparison between simulated product yields (wt%) and experimental data for n-, sec- and tert-butanol pyrolysis.

	n-butanol		sec-butanol		sec-butanol + H_2O		tert-butanol	
Conditions								
$F_{0,C_4H_{10}O}$	0.06750 g s^{-1}		0.06721 g s^{-1}		0.04996 g s^{-1}		0.06721 g s^{-1}	
F_{0,H_2O}	-		-		0.0050 g s^{-1}		-	
T_{avg}	1005 K		1005 K		1005 K		998 K	
P	1.72 bar		1.72 bar		1.72 bar		1.72 bar	
Residence time	0.71 s		0.74 s		0.74 s		0.78 s	
	Sim.	Expt.	Sim.	Expt.	Sim.	Expt.	Sim.	Expt.
H2	1.00	0.99	0.44	0.59	0.41	0.42	0.15	0.20
CO	13.45	13.32	9.27	9.45	8.78	8.98	0.73	0.45
CH4	9.55	10.03	15.23	15.03	13.91	14.11	4.27	4.19
CH2O	1.28	1.46	0	0	0	0	0	0
CH3OH	1.37	1.48	0	0	0	0	0	0
C2H2	0.47	0.22	0.22	0.14	0.22	0.14	0.01	0.02
C2H4	15.50	15.76	11.0	10.58	10.9	11.08	0.31	0.66
C2H6	5.77	5.45	2.26	2.47	1.86	2.00	0.05	0.09
CH3CHO	6.66	6.82	2.62	2.99	2.62	2.99	0	0.03
C3H4(MA)	0.09	0.07	0.12	0.18	0.11	0.16	0.40	0.3
C3H4(PD)	0.12	0.09	0.12	0.05	0.09	0.07	0.61	0.51
C3H6	10.03	10.18	5.0	4.61	4.1	4.31	2.40	2.59
C3H8	0.28	0.50	0.11	0.25	0.07	0.18	0.10	0.25
C3H6O(ketone)	0	0	12.01	11.16	10.01	10.00	4.54	4.79

1,3-C4H6	1.53	1.26	4.47	4.52	4.17	4.12	0.05	0.16
1-C4H8	1.76	2.50	2.77	2.94	2.57	2.54	0.05	0.12
2-C4H8	0.78	0.61	5.04	4.81	4.24	4.31	0.01	0.06
i-C4H8	0.24	0.23	0.42	0.13	0.42	0.17	54.65	53.12
C4H8O(aldeh.)	0.38	0.25	0	0	0	0	0	0
C4H8O(ketone)	0	0	2.78	2.24	2.31	2.22	0	0
1,3-C5H8	0.11	0.11	0.22	0.21	0.16	0.22	2.18	2.3
C6H6	0.68	0.61	1.26	1.02	1.27	1.32	0.11	1.15
C7H8	0.02	0.08	0. 10	0.23	0.11	0.20	0.02	1.42
H2O	6.34	6.61	9.28	9.01	17.61	17.81	19.86	20.2
$X_{butanol}$	80.78	80.83	88.33	88.26	88.41	88.56	91.44	92.21

Under the specified conditions tert-butanol has the highest conversion, followed by sec-butanol and finally n-butanol. The difference in conversion is strongly related to the dehydration reaction of the different butanol isomers; the high pressure rate coefficients for the different butanol isomer dehydration reactions may be found in Table 6-2. The dehydration reaction of tert-butanol is approximately ten times faster than the dehydration reactions of sec-butanol or n-butanol. Hence, tert-butanol decomposes almost entirely to isobutene and water before radical reactions start to become important, while for sec- and n-butanol the radical reactions are the dominant decomposition pathways. The same is found when using the reaction network of Moss et al. At tert-butanol conversions above 85%, the concentrations of radicals have grown sufficiently to have a noticeable effect on conversion and product yields. Table 6-3 shows a comparison between simulated and experimentally measured product yields at a tert-butanol conversion of 91%. Good agreement between experimentally measured and simulated product yields is observed. During the cracking of tert-butanol, a small amount of acetone is formed. The rate of production analysis shows that the 2-hydroxy-2-methylpropyl radical is formed via hydrogen abstraction of tert-butanol by methyl radical; the 2-hydroxy-2-methylpropyl radical decomposes to propen-2-ol and methyl radical via β-

191

scission. The propen-2-ol then undergoes tautomerization to form acetone. The isobutene reacts further to propene via the addition of H atom to isobutene to form isobutyl radical, followed by the β-scission of isobutyl to propene and methyl radical. Isobutene also leads to the formation of methylacetylene and propadiene: methyl radical abstracts one of the primary hydrogens of isobutene forming methane and 2-methylallyl radical; 2-methylallyl radical undergoes a β-scission resulting in propadiene and methyl radical. Some of the propadiene then isomerizes to methylacetylene. Significant amounts of 2-methyl-1,3-butadiene are formed via the recombination of methyl and 2-methylallyl radicals, followed by a hydrogen abstraction and β C-H scission. At tert-butanol conversions above 90%, significant amounts of benzene and toluene are formed, see Table 6-3. In our mechanism, the dominant reaction pathway to benzene for tert-butanol pyrolysis is the recombination of two propargyl radicals; for toluene, it is the recombination of a propargyl radical with the 2-methylallyl radical. The latter is in agreement with the results obtained by Yasunaga et al. [246] on isobutene combustion and oxidation. However the former is significantly different from the dominant benzene formation pathway when pyrolyzing n-butanol, i.e. addition of vinyl radical to 1,3-butadiene followed by cyclization and β C-H scission [166]. Note that the proposed pathways for the formation of aromatics for tert-butanol pyrolysis are clearly insufficient to explain all the observed toluene and benzene. Further research is necessary on the conversion of isobutene and 2-methyl-1,3-butadiene to aromatic hydrocarbons. This is also important to better understand the formation of polycyclic aromatic hydrocarbons during pyrolysis and combustion of fuels containing significant amounts of branched olefins.
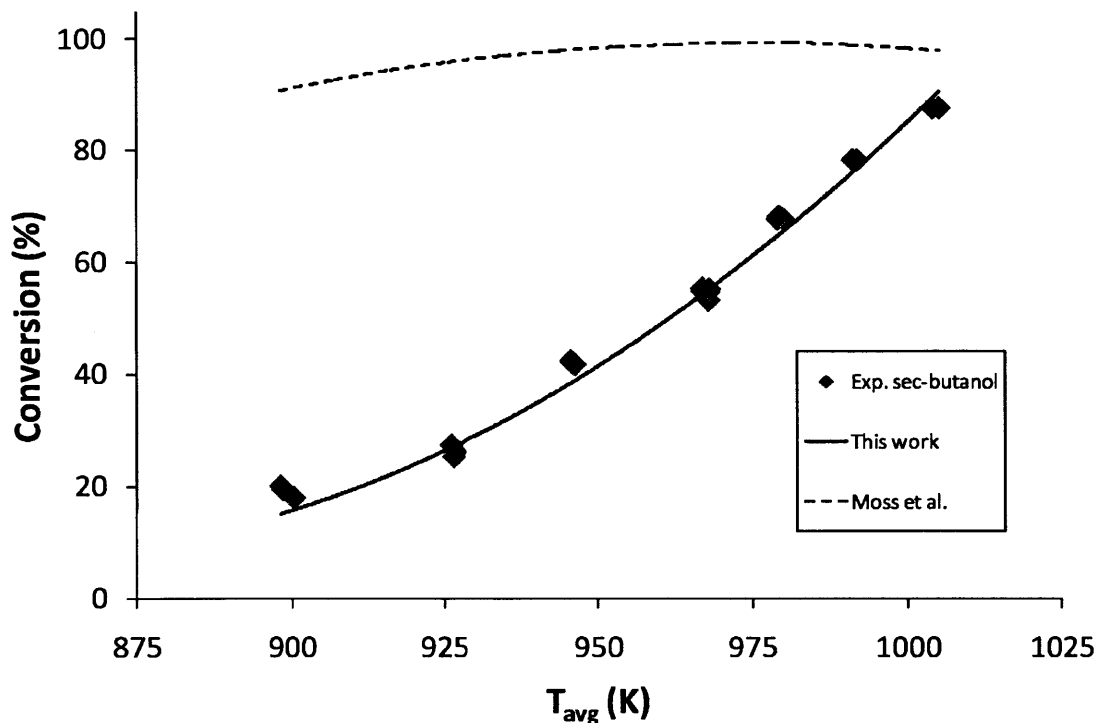
Figure 6-1: Comparison between measured and simulated conversion for sec-butanol in the pyrolysis reactor as a function of the axial averaged temperature. $F_0 = 0.06721$ g s^{-1}, P = 1.70x10^5 Pa.

The results in Table 6-3 also show that for sec-butanol a good agreement is observed between experimental and simulated data for the major and minor products. The measured and predicted conversions of sec-butanol as a function of the maximum temperature measured in the reactor are plotted in Figure 6-1. Our reaction network's predictions match the data well, within 10% over the entire temperature range. However, using the reaction network of Moss et al. gives almost complete conversion of sec-butanol, even at low temperatures. Clearly there is room for improving the Moss et al. chemistry under pyrolysis conditions for sec-butanol. For tert-butanol, the model of Moss et al. predicts the trend for the conversion with reasonable accuracy.
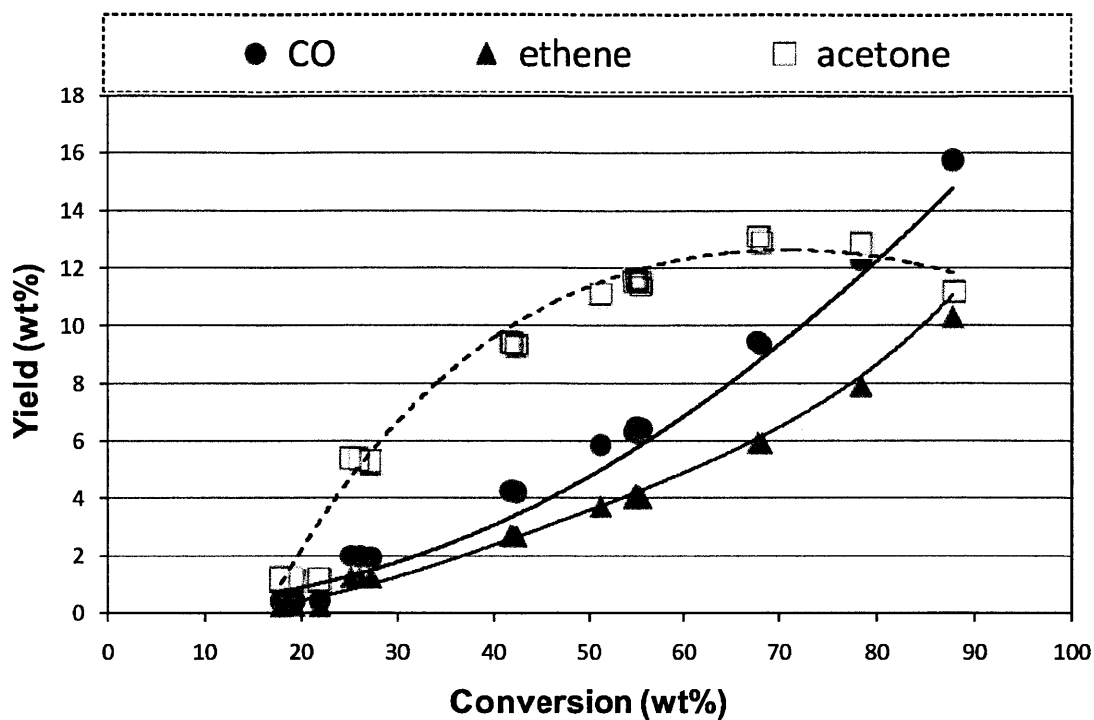
Figure 6-2: Measured (shapes) and simulated (lines) yields for acetone, ethene, and CO as a function of the sec-butanol conversion in the pyrolysis reactor.

Our model's ability to predict the sec-butanol dataset is further illustrated in Figure 6-2 where the yields of acetone, CO, and propene are plotted as a function of the maximal temperature observed during the experiment. The mechanism of Moss et al. has difficulties predicting the trends for these main products because of the very high simulated conversion for sec-butanol and therefore is not included in Figure 6-2. The chemistry of sec-butanol is significantly more complex under pyrolysis conditions than for tert-butanol.
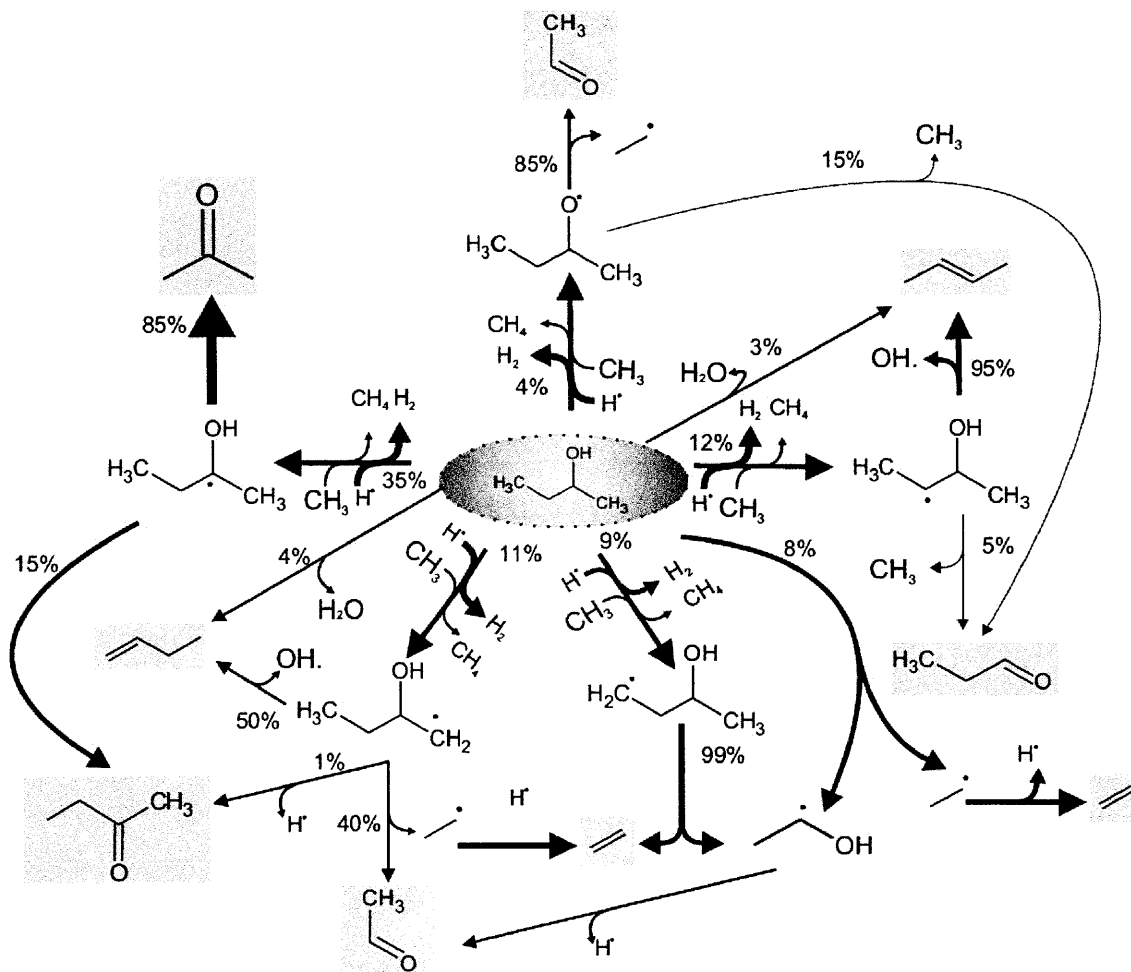
Figure 6-3: Reaction pathway analysis for sec-butanol pyrolysis towards the main products performed at the maximum temperature along the reactor coil. The arrow thickness and percentages represent the reaction rate of decomposition for that species. T_{inl} = 673 K, T_{max} = 1093 K, P = 1.7x10^5 Pa, F_0 = 6.721x10^{-2} g s^{-1}.

Figure 6-3 shows the results of a rate of production analysis for sec-butanol pyrolysis. The dominant pathway in this case is a set of hydrogen abstractions by methyl and hydrogen atom producing the 1-hydroxy-1-methylpropyl radical. This radical decomposes into methyl radical and propen-2-ol, which then undergoes tautomerization to form acetone. Note that the dehydration reactions of sec-butanol to form butenes are significantly less important than the hydrogen abstraction reactions, which was the opposite for tert-butanol pyrolysis. The formation of 2- and 1-butene occurs mainly through a radical pathway. Note that propene is not present in Figure 6-3. Propene is indirectly formed from sec-butanol via the decomposition of 1-butene. This explains the

relatively small amount of propene observed experimentally. The large concentrations of butene result in significant amounts of 1,3-butadiene, see Table 6-3. Addition reactions of vinyl radical to 1,3-butadiene, followed by cyclization and β C-H scissions lead to the formation of benzene.

Table 6-3 further illustrates that our model is also able of predicting cracking of 2-butanol diluted with water. For the dilutions tested, the addition of water has no significant effect on the conversion if the residence time is kept fixed and the average temperature and pressure are identical. On the other hand the addition of water increases the selectivity for ethene and decreases the selectivity for methane. This is in line with what is generally observed in steam cracking of hydrocarbons. In the steam cracking process water is added to increase the selectivity to ethene and decrease the selectivity to secondary products [247]. Diluting the feedstock with water decreases the partial pressures of all species, and hence results in an increase of the reaction rate of the unimolecular reactions (e.g. β-scissions giving ethene) to the reaction rate of the bimolecular reactions (e.g. hydrogen abstractions by the methyl radical giving methane [248]). The selectivity to the other products is only marginally affected as can be observed from the results presented in Table 6-3.

The results of the sensitivity analysis for sec-butanol, presented in Table 6-4, give a different view than the results obtained via the rate of production analysis.

Table 6-4: Reactions with the largest normalized sensitivity coefficients affecting major species from sec-butanol pyrolysis at operating conditions: F_0 = 0.06721 g s^{-1}, T_{max} = 1093 K, P = 1.70x10^5 Pa; values reported are at an axial distance of 44 cm from the reactor inlet.

Reaction equations	Sensitivity coefficient ($\times 10^2$)					
	CO	$=$	acetone	benzene	butanone	sec-butanol
sBuOH = H2O + C4H8-1	0	0	0	12	0	10
sBuOH = H2O + C4H8-2	0	0	0	2.7	0	4
propen-2-ol = acetone	0	0	36	0	0	0
C2H5 = H + C2H4	9	23	9	34	3	0
sBuOH = CH3CHOH + C2H5	95	52	78	230	43	-25
sBuOH + H = H2 + CH2CH[OH]C2H5	-4	4	-17	10	-3	-7

sBuOH + H = H2 + CH3C[OH]C2H5	-21	-12	-25	-37	-2	-10
sBuOH + H = H2 + CH3CH[O]C2H5	4	0	-6	-16	-2	-8
sBuOH + H = H2 + CH3CH[OH]CHCH3	0	2.5	-19	9	-2	-7
sBuOH + H = H2 + CH3CH[OH]CH2CH2	0	8	-11	0	0	-5
sBuOH + CH3 = CH4 + CH3C[OH]C2H5	21	1.6	62	21	43	-18

It is obvious that the C-C scission reactions and the dehydration reactions are important for sec-butanol. However, the normalized sensitivity coefficients indicate that sec-butanol is more sensitive to the hydrogen abstraction by hydrogen atom and methyl radicals than to the dehydration reactions. Not surprising is the sensitivity of ethene to the β-scission of the ethyl radical as can be seen from Table 6-4. The β C-H scission of the ethyl radical is also important as it provides the H atoms which drive the free radical chemistry; it also plays a crucial role in the formation of ethene and ethane. CO is mainly sensitive to the C-C bond fission reaction of sec-butanol forming ethyl and 1-hydroxyethyl radical and, to a lesser extent, to the hydrogen abstraction reactions forming 1-hydroxy-1-methylpropyl radical. The trends are similar for acetone, with the exception of acetone having sensitivity to the tautomerization of propen-2-ol, shown in Table 6-4. Benzene is very sensitive to the dominant C-C bond fission reaction of sec-butanol and, to a lesser extent, to the β C-H scission of the ethyl radical.

Finally the proposed reaction network is also able to predict the pyrolysis behavior of n-butanol. The dominant reaction pathways for decomposition of n-butanol under pyrolysis conditions have been previously identified [166]. Looking at the trends of the products propene, CO, and acetaldehyde shown in Figure 6-4, our mechanism's predictions match the data well. This illustrates the potential of the proposed methodology, starting from an extensively validated seed reaction network and expanding the network using the rate-based algorithm.
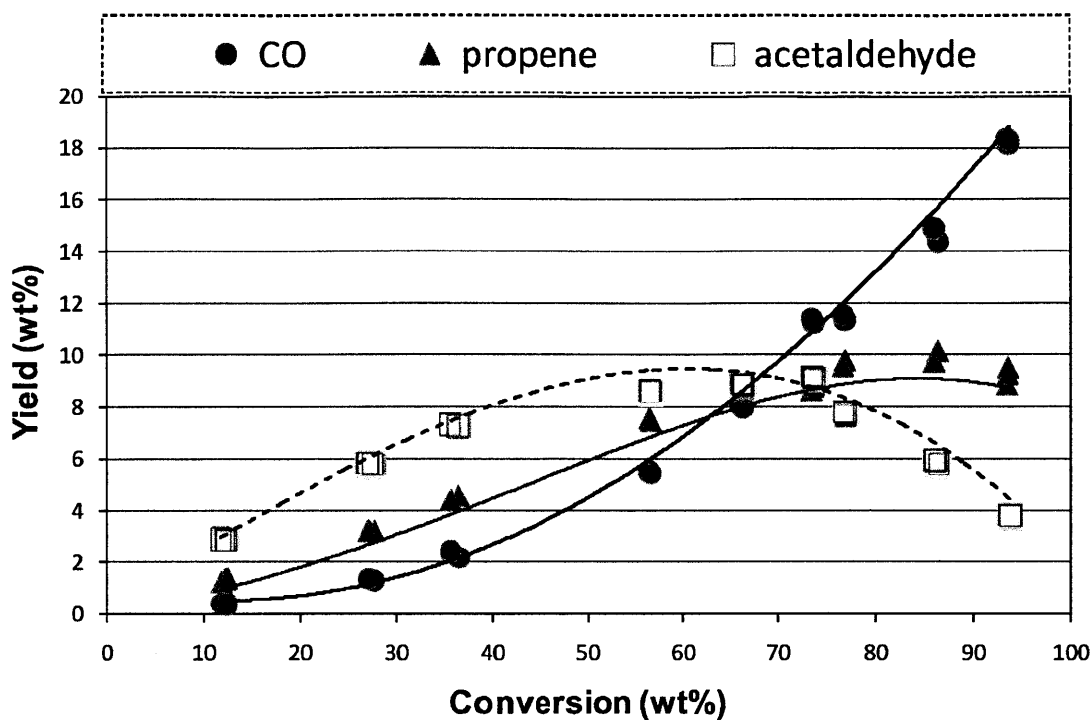
Figure 6-4: Measured (shapes) and predicted (lines) yields for CO, propene, and acetaldehyde as a function of the n-butanol conversion in the pyrolysis reactor.

6.4.2 Doped methane diffusion flame

The new network was further tested against the butanol-doped methane diffusion flame experiments, using the Sharma flame solver. Validating our model against this set of experiments expands not only the validated range of equivalence ratios, but also the range of temperatures; in these experiments, the measured temperature ranged from 445 to 1898 K, whereas the pyrolysis experiments were conducted over a temperature range of 673 to 1010 K. The centerline concentration profiles of butanol are shown in Figure 6-5.
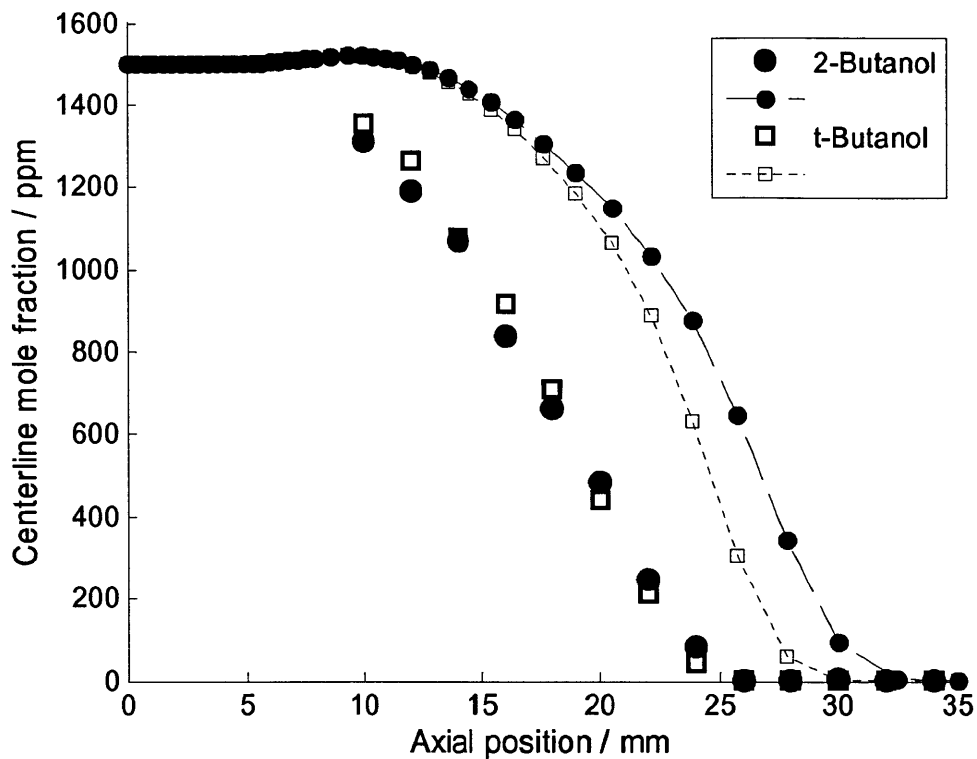
Figure 6-5: The experimental [172] and simulated centerline mole fraction profiles of sec- (circles) and tert-butanol (squares) in the doped methane flame. The shapes connected with lines are the simulated results.

In the experiments, the centerline butanol concentration drops to zero at an axial position of 26 mm from the burner, for both butanol isomers. The simulated concentration profiles drop to zero at 33 and 30 mm for sec- and tert-butanol, respectively. We believe these discrepancies are explained by examining the experimental and simulated centerline temperature profile, Figure 6-6. The simulated temperature profile comes from the study by Bennett et al. in which the uncertain temperature boundary condition at the burner exit was assumed to be 300 K; with this assumption, the simulated temperature profile is underestimated by 60-260 K throughout the flame (axial positions ≤ 62 mm from the burner). If the simulated temperature field is shifted upstream by 4 mm in the post-processing, the difference between the experimental and simulated temperature is no greater than 27 K in the region 10 to 50 mm downstream of the burner; the reported uncertainty in the temperature measurements is ±65 K. Taking this shift into account in the post-processing, the simulated concentration profiles drop to zero at 29 and 26 mm

for sec- and tert-butanol, respectively, which match the experimental values reasonably well; the reported spatial resolution for the gas sample probe is 1 mm.
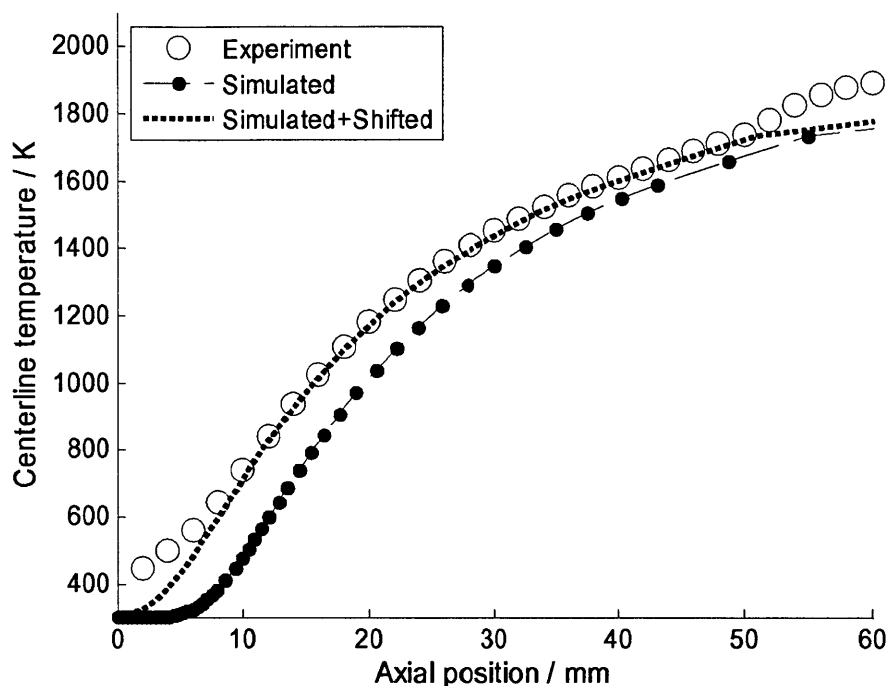
Figure 6-6: The experimental [172] and simulated [198] centerline temperature profile in the sec-butanol doped methane flame. The dotted line is the simulated profile, shifted upstream by 4 millimeters.

6.4.2.1 BUTANOLS: FLUX AND SENSITIVITY ANALYSIS

The centerline flux analysis for the butanol isomers in the doped methane flame is presented in Figure 6-7. The main decomposition route of sec-butanol in the flame is the C-C bond fission leading to ethyl and 1-hydroxyethyl radical. Ethyl radical undergoes a β-scission to H atom and ethene while 1-hydroxyethyl radical undergoes a β-scission to form H atom and acetaldehyde or, to a lesser extent, H atom and vinyl alcohol. Other significant sec-butanol consumption pathways are the dehydration reactions to water and 1-butene, or water and 2-butene, and the C-C bond fission to form methyl and 1-hydroxypropyl radical; the 1-hydroxypropyl radical readily undergoes a β-scission to form vinyl alcohol and methyl radical.
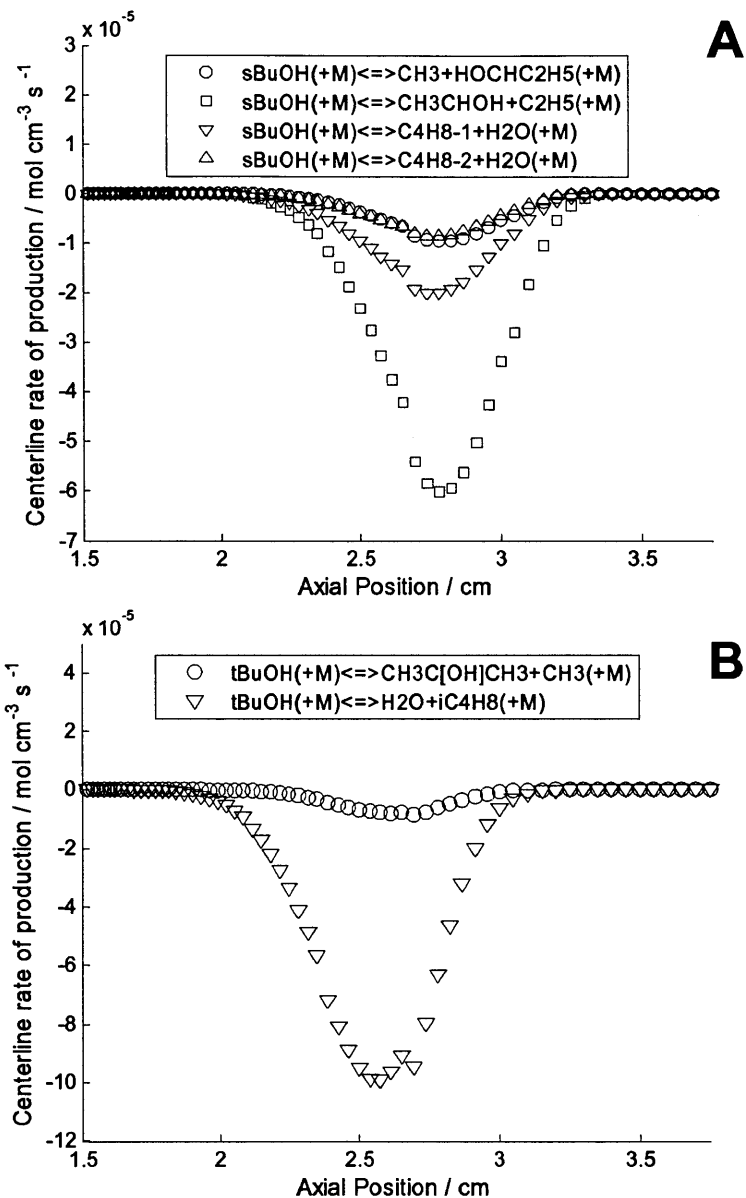
Figure 6-7: Centerline rate of production for (A) sec- and (B) tert-butanol in the doped methane flame. For both plots, the absolute rate of production for all other pathways is less than 5×10^{-6} mol cm^{-3} s^{-1}.

For both of the C-C bond fission reactions, the high-pressure-limit rate coefficient was computed by multiplying the reverse rate coefficient (a temperature-independent rate of 2×10^{13} cm^3 mol^{-1} s^{-1} was assumed for these radical recombination reactions) by the equilibrium constant. The species thermochemistry was either computed using the methodology described in Section 6.3.2, or comes from the Third Millennium Ideal Gas and Condensed Phase Thermochemical Database for Combustion with Updates from

Active Thermochemical Tables [109]. The high-pressure-limit rate coefficients for the dehydration reactions were computed using the methodology described in Section 6.3.2. For the dehydration to 2-butene and water, the rate coefficient to both (Z)-2-butene and (E)-2-butene were computed; since the present network does not distinguish between the two isomers, the two rate coefficients were summed and fit to a modified Arrhenius expression. The pressure-dependent rate coefficients were then computed within the RMG software, using the steady-state master equation approach.

The dominant decomposition route of tert-butanol is the dehydration reaction to isobutene and water; a minor pathway is the C-C bond fission reaction forming methyl and 1-hydroxy-1-methylethyl radical. The 1-hydroxy-1-methylethyl radical readily undergoes a β-scission to form acetone and H atom; a minor decomposition route is also through a β-scission, leading to H atom and propen-2-ol. The C-C bond fission rate coefficient was also computed by multiplying the reverse rate coefficient (assumed to be a temperature-independent 2×10^{13} cm^3 mol^{-1} s^{-1}) with the equilibrium constant. The high-pressure-limit rate coefficient for the dehydration reaction, and the pressure-dependent rate coefficients, was computed in the same manner as described in the previous paragraph.

The normalized sensitivity coefficients for the centerline butanol mole fraction with respect to the unimolecular reaction rate coefficients, i.e. the C-C bond fissions and dehydrations, are presented in Figure 6-8. The equation for normalized sensitivity coefficients, Equation (4.4), contains the mole fraction of butanol in the denominator and thus yields unphysical results when the butanol concentration approaches zero, after 33 and 30 mm for the sec- and tert-butanol simulations, respectively.
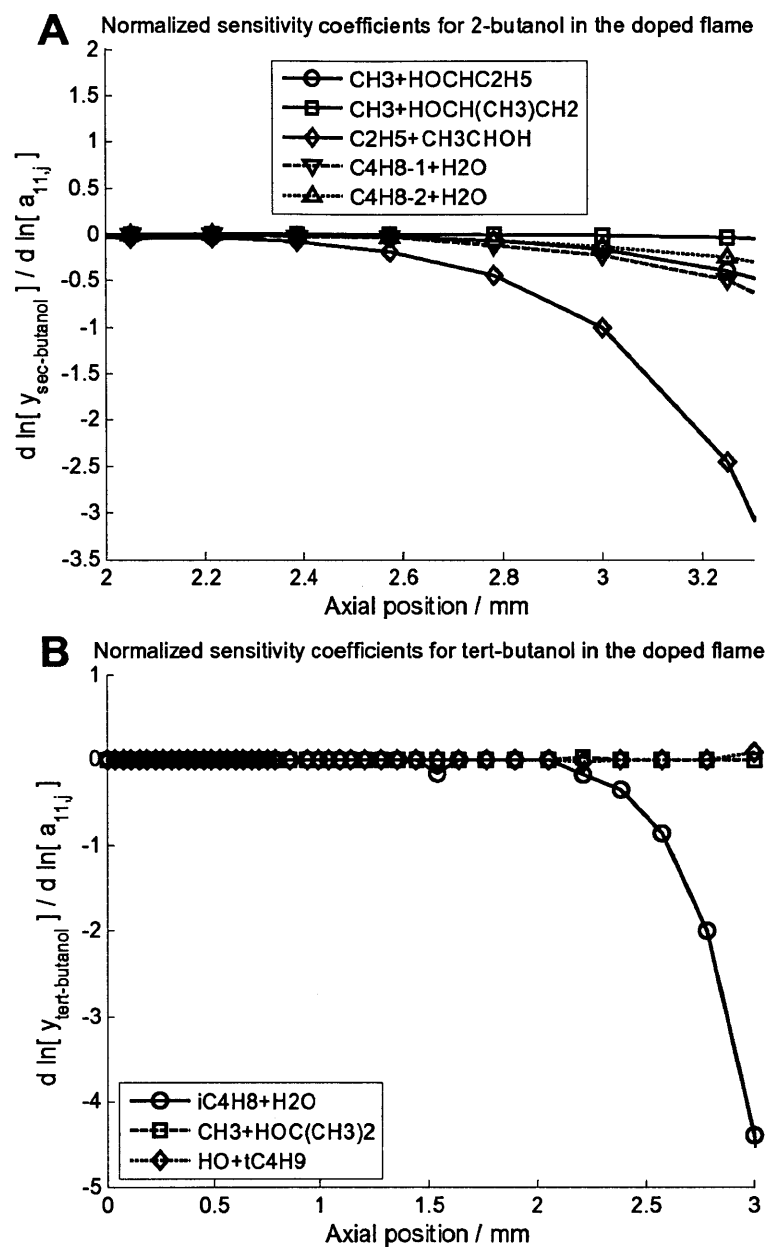
Figure 6-8: Normalized sensitivity coefficients for the centerline concentration of (A) sec- and (B) tert-butanol in the doped methane flame, with respect to the unimolecular reaction rate coefficients.

For the sec-butanol simulations, the centerline concentration is sensitive to the C-C bond fission producing ethyl and 1-hydroxyethyl radicals; the concentration is also sensitive to the C-C bond fission producing methyl and 1-hydroxypropyl radicals and both dehydration reactions. As mentioned previously, the C-C bond fission high-pressure-limit rate coefficients were computed using the assumed temperature-independent reverse rate coefficient and the equilibrium constant; the thermochemistry for sec-butanol and 1-

hydroxyethyl were computed in this study and the thermochemistry of ethyl was taken from the literature [109]. The pressure-dependent rate coefficient was then computed in RMG, using the steady-state master equation method. A more accurate radical recombination rate coefficient, in addition to solving the full master equation, would further assist our modeling efforts. However calculating said rate coefficients are non-trivial [249], and were considered beyond the scope of this work.

For the tert-butanol doped flame simulations, the centerline concentration is only sensitive to the dehydration reaction. Although the high-pressure-limit rate coefficient was computed using the CBS-QB3 calculations, quantum calculations using even more accurate methodology would benefit the kinetic model given tert-butanol's considerable sensitivity to this single reaction.

The normalized sensitivity coefficients for the centerline butanol mole fraction with respect to the species' transport properties, in particular the Lennard-Jones collision diameter, are presented in Figure 6-9. The equation used to compute these normalized sensitivity coefficients is given in Equation (4.8).

$$\tilde{s}_{ij} \equiv \frac{d \ln c_i}{d \ln \sigma_j} = \frac{\sigma_j}{c_i} \frac{dc_i}{d\sigma_j} \approx \frac{\sigma_j}{c_i[\sigma_j]} \frac{c_i[\sigma_j + \Delta\sigma_j] - c_i[\sigma_j - \Delta\sigma_j]}{2\Delta\sigma_j} \tag{4.8}$$

For each isomer, the butanol concentration is sensitive to its respective collision diameter. In general, many species concentration profiles are also sensitive to the collision diameter of the dopant. In the CHEMKIN-II transport subroutines, the binary diffusion coefficient scales as the inverse square of the reduced collision diameter, $\sigma_{mn} = 0.5*(\sigma_m + \sigma_n)$. An increase in the butanol collision diameter decreases all its binary diffusivity coefficients, reducing its radial diffusion. This results in an increased centerline butanol concentration and would thereby increase the centerline concentrations of all butanol-derived species. The values of the collision diameter used for sec- and tert-butanol in this study are 5.667 and 5.654 Å, respectively, as estimated by the group contributions scheme; both of these are within 10% of those reported in the literature [250, 251]. The butanol concentration is not sensitive to the species' Lennard-Jones potential well depth parameters; the normalized sensitivity coefficients are effectively zero throughout the domain.

The centerline butanol concentration is also sensitive to the collision diameters of N_2 and CH_4. In general, most centerline concentration profiles in the doped flame are sensitive to the collision diameters of nitrogen and methane as these species have large mole fractions throughout the flame; the values used in this mechanism are those reported in the GRI-Mech 3.0 mechanism [191].
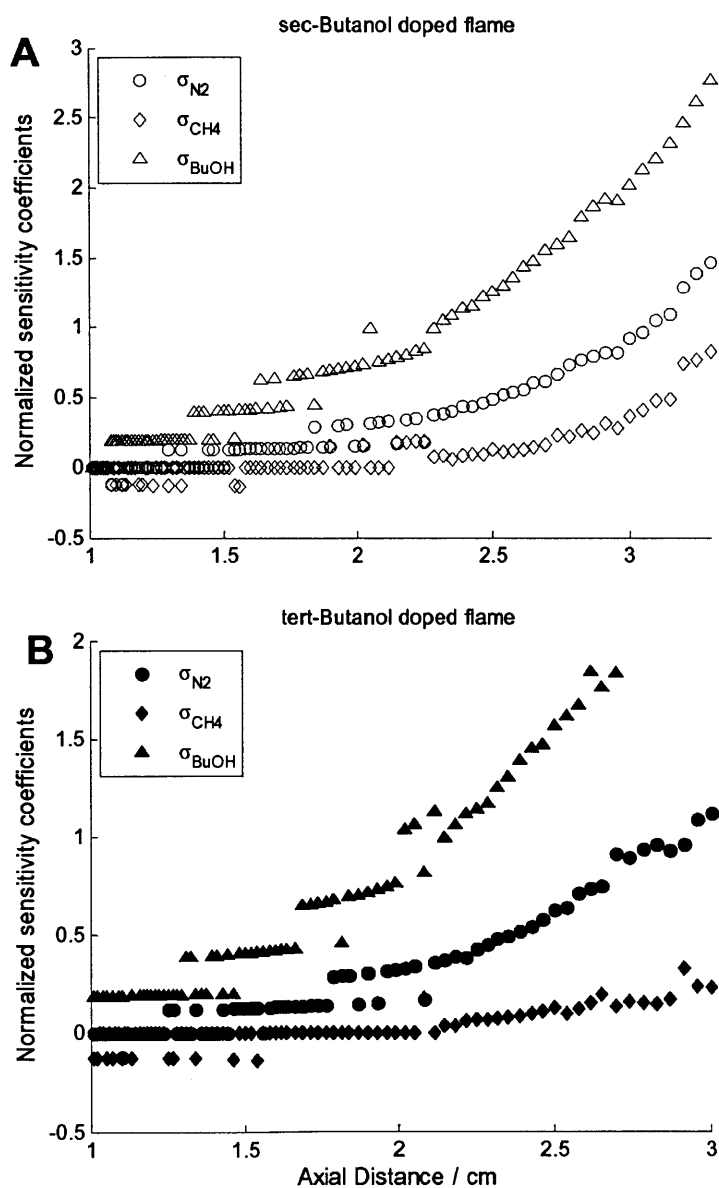
Figure 6-9: Normalized sensitivity coefficients for the centerline butanol concentration profile in the doped methane flame for (A) sec- and (B) tert-butanol with respect to certain species' Lennard-Jones collision diameters.

6.4.2.2 BUTANOL PRODUCTS: CONCENTRATIONS, FLUX AND SENSITIVITY ANALYSIS

The centerline concentration profiles of some of the butanol-derived products are presented in Figure 6-10; the corresponding centerline flux analysis for the sec-butanol and tert-butanol derived species are presented in Figure 6-11 and Figure 6-12, respectively. In their study, McEnally and Pfefferle put a conservative estimate of +100/-50% uncertainty in their reported mole fraction profiles. In general, our mechanism predicts this dataset well, with the exception of the $M_m=54$ profiles which are discussed below.
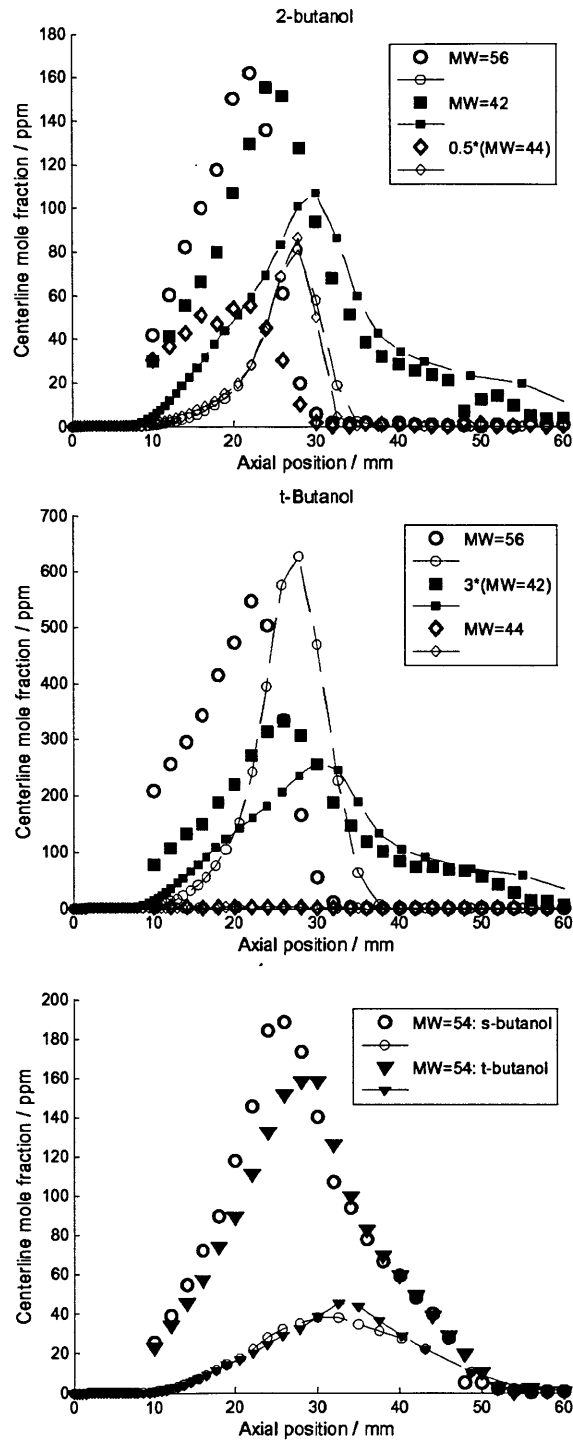
Figure 6-10: Simulated (shapes connected by lines) and experimental [172] (shapes) centerline mole fraction of butanol-derived products in the doped methane diffusion flame. Some of the concentrations have been multiplied by a constant to improve the readability.

For the sec-butanol experiments, our mechanism predicts the $M_m = 42$ (propene + ketene), $M_m = 44$ (acetaldehyde + vinyl alcohol), and $M_m = 56$ (1-butene, 2-butene, and isobutene) profiles reasonably well. The flux analysis for acetaldehyde and vinyl alcohol is located in Figure 6-11A and B. The main routes to vinyl alcohol are the β-scission reactions from the 1-hydroxyethyl and 1-hydroxypropyl radicals, which come directly from sec-butanol. Vinyl alcohol primarily forms acetaldehyde through the tautomerization reaction; the rate coefficient utilized for this reaction is $k = 8.59 \times 10^{11}\ T^{0.318}\ \exp(-55900\ \mathrm{cal/mol}\ /\ \mathrm{RT})\ s^{-1}$, as recommended by da Silva et al. [220]. The primary decomposition route of acetaldehyde under these conditions is the C-C bond fission to form methyl and formyl radical; H-abstraction reactions of acetaldehyde to form acetyl radical do not play a significant role in the doped flame.
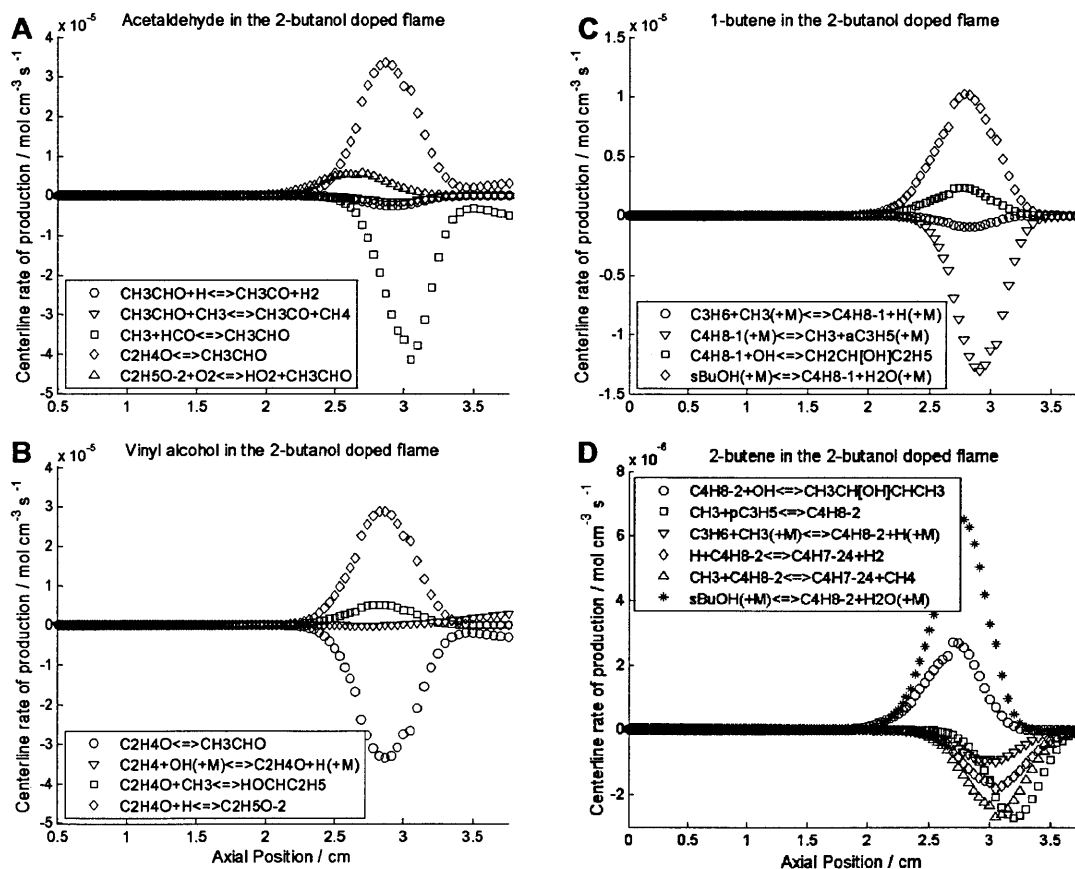
Figure 6-11: Simulated centerline rate-of-production for: (A) acetaldehyde, (B) vinyl alcohol, (C) 1-butene, and (D) 2-butene in the sec-butanol doped methane flame. The plotted pathways to and from each species are the pathways with the largest rates.

The flux analysis for 1- and 2-butene is located in Figure 6-11C and D. The major route to both alkenes is through the dehydration reaction of sec-butanol. Other significant pathways are through β-scissions of radicals of the parent sec-butanol molecule: 1-butene is formed by the β-scission of the 2-hydroxybutyl radical while 2-butene is formed by the β-scission of the 2-hydroxy-1-methylpropyl radical. The main decomposition pathway of 1-butene is the C-C bond fission forming methyl and allyl radical. 2-butene has three significant decomposition pathways: the C-C bond fission forming methyl and 1-propenyl radical and the H-abstraction of one of the primary hydrogens by either H atom or methyl radical. The former's rate coefficient was estimated by the RMG software using the reverse rate coefficient and equilibrium constant; the reverse rate coefficient was estimated as $k = 7.23 \times 10^{13}$ cm^3 mol^{-1} s^{-1}, the rate coefficient recommended by Fahr et al. [252] for the recombination of methyl and vinyl radical. The latter two were calculated in this study.

Our mechanism predicts the M_m =42, M_m =44, and M_m =56 curves very well for the tert-butanol doped methane flame. The flux analysis for isobutene and 2-methylallyl radical are presented in Figure 6-12. The main route to isobutene is the dehydration reaction of tert-butanol. The major routes from isobutene are the H-abstraction reactions by H atom and methyl radical to form 2-methylallyl radical; the rate coefficients for both of these reactions were computed in this study. A minor route is through the C-C bond fission to form methyl and 1-methylethenyl radicals. The dominant route from 2-methylallyl is the β-scission reaction to form propadiene and methyl radical.

209
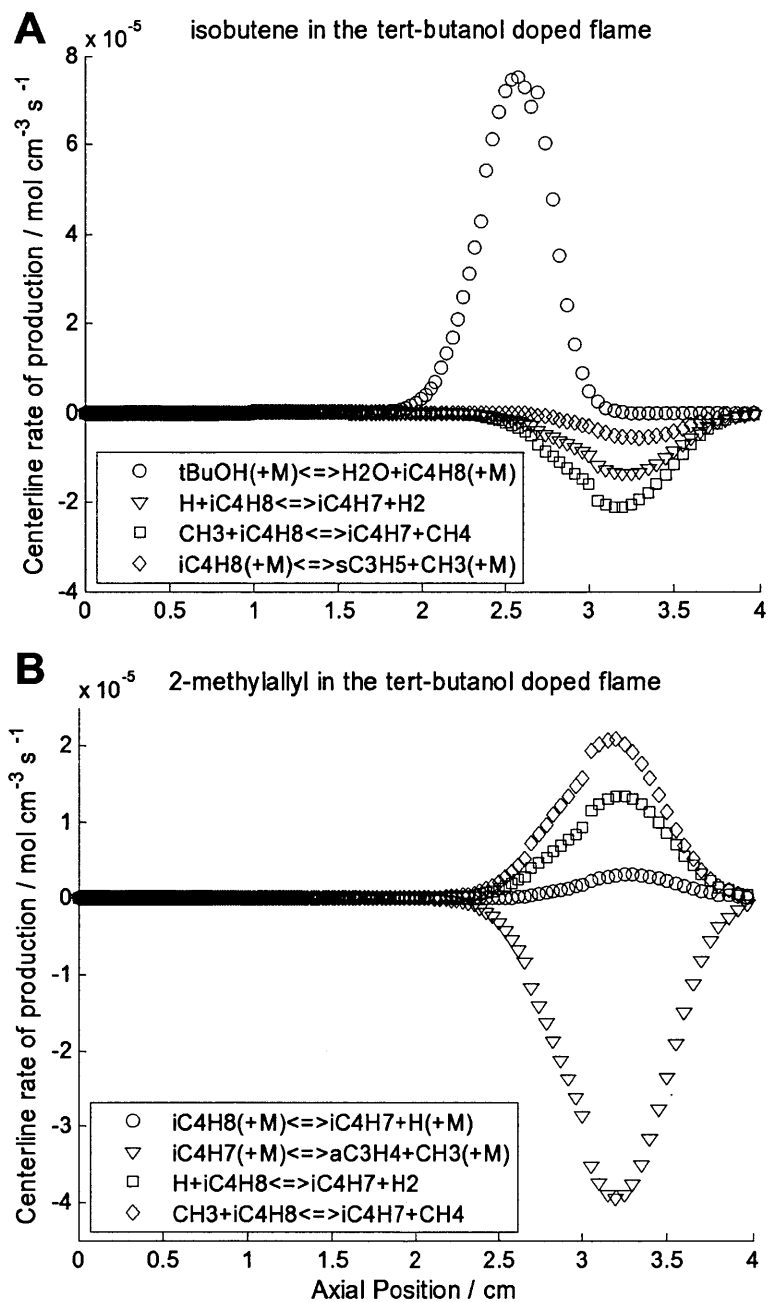
Figure 6-12: Simulated centerline rate-of-production for: (A) isobutene and (B) 2-methylallyl radical in the tert-butanol doped methane flame.

As mentioned previously, one experimental curve our mechanism does not predict well is the $M_m=54$ (1,2-butadiene, 1,3-butadiene, 1-butyne, and 2-butyne) curve. Our mechanism underestimates the maximum concentration by a factor of 5 and 3.5 for the sec-butanol and tert-butanol doped methane flame, respectively. We have performed (but have not presented) sensitivity analysis for the $M_m=54$ concentrations with respect to the C_4H_6

(and related) species thermochemistry and transport properties, reaction rate coefficients, and initial butanol concentration, however the concentration is not sensitive to any of the tested parameters. This discrepancy is in agreement with previous studies using the Sharma flame solver + RMG software [166, 190]. Our mechanism most likely is missing important C_4H_6 pathways or has erroneous thermochemistry. Other than this exception, our mechanism predicts the centerline mole fraction profiles for the sec-butanol and tert-butanol doped methane flames very well.

6.4.3 JET-STIRRED REACTOR SPECIATION DATA: 10 ATM

6.4.3.1 2-BUTANOL RESULTS

Togbé et al. have measured speciation data for 2- and iso-butanol in a jet-stirred reactor at 10 atm, from $770 - 1250$ K, for equivalence ratios $\phi = 0.5, 1.0, 2.0,$ and 4.0 [253]. The reactor was 30.5 cm^3 in volume and was insulated to create an isothermal system. The residence time for all experiments was 0.7 seconds.

The reactor was modeled using CHEMKIN 10101 assuming an isothermal Perfectly-Stirred Reactor. The reactor conditions stated above were supplied to CHEMKIN. The fuel percentage was 0.1% for the $\phi = 0.5, 1.0,$ and 2.0 simulations with N_2 as the bath gas; the fuel percentage was 0.15% for the $\phi = 4.0$ simulations. The default tolerances were employed.

The model's predicted species concentration profiles for all four equivalence ratios are presented in Figure 6-13 through Figure 6-16; the model's predictions are in reasonable agreement with the experimental data.

211
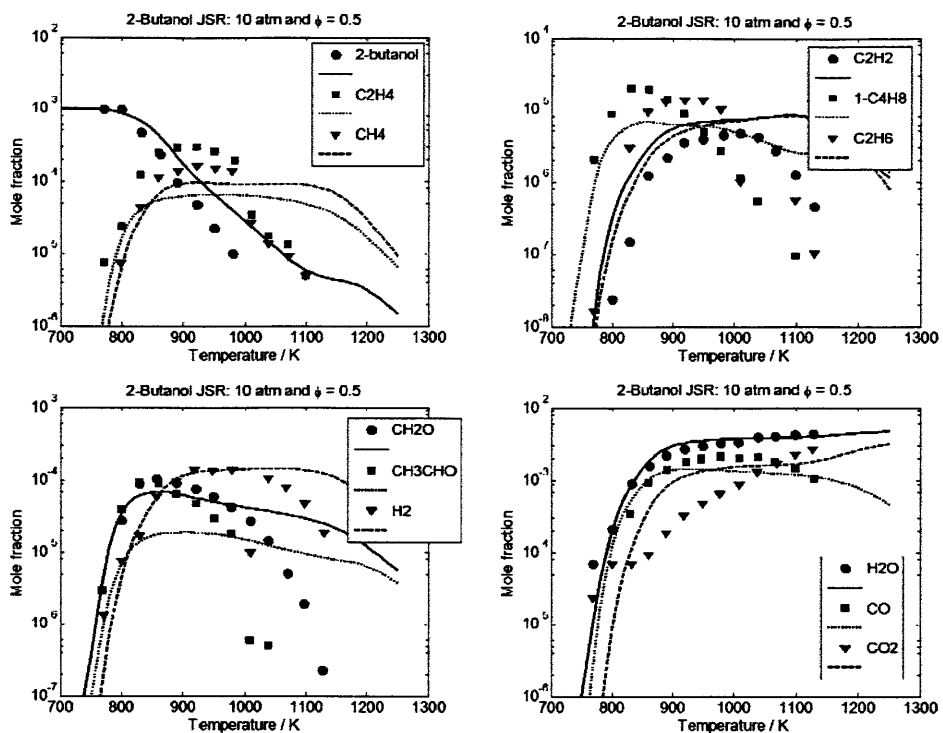
Figure 6-13: Predicted and experimental [253] speciation data for 0.1% 2-butanol oxidation in a 10 atm perfectly-stirred reactor for an equivalence ratio of 0.5. The "CH3CHO" curve is a summation of acetaldehyde and ethanol.

Figure 6-14: Predicted and experimental [253] speciation data for 0.1% 2-butanol oxidation in a 10 atm perfectly-stirred reactor for an equivalence ratio of 1.0. The "CH3CHO" curve is a summation of acetaldehyde and ethanol. Note: the H2 curves have been divided by two.

Figure 6-15: Predicted and experimental [253] speciation data for 0.1% iso-butanol oxidation in a 10 atm perfectly-stirred reactor for an equivalence ratio of 2.0. The "CH3CHO" curve is a summation of acetaldehyde and ethanol. Note: the H2 curves have been divided by four.

Figure 6-16: Predicted and experimental [253] speciation data for 0.15% 2-butanol oxidation in a 10 atm perfectly-stirred reactor for an equivalence ratio of 4.0. The "CH3CHO" curve is a summation of acetaldehyde and ethanol. Note: the H2 curves have been divided by eight.

213

Of particular note are the species CO_2 and 1-butene. For all equivalence ratios, the model overestimates the concentration of CO_2 at lower temperatures, particularly between 850 - 1050 K. This observation of the final combustion product peaking too soon generally suggests that the fuel is reacting away too quickly. For the rich experiments (ϕ = 2.0 and 4.0), this is indeed the case with the model not predicting the experimental 2-butanol curve particularly well between 900 - 1100 K.

For 1-butene, the model consistently underestimates the concentration profile, for all equivalence ratios and temperatures tested. The main routes to 1-butene are the unimolecular decomposition from 2-butanol to 1-butene and water, and the β-scission of the *CH_2-CH(OH)-C_2H_5 radical. I have calculated the high-pressure-limit kinetics for the former, whereas the latter's kinetics are RMG estimates. Both reactions' kinetics appear as pressure-dependent kinetics in the mechanism, and were estimated using the steady-state master equation method of Green and Bhatti [184]. In the experiments of Togbé et al., several analytical techniques were employed to measure the species profiles, including online FTIR. Although the maximum mole fraction for cis- and trans-2-butene is reported for the ϕ = 0.5, 1, and 2 experiments – in fact, the maximum 2-butene mole fraction is 2-3 times greater than the maximum 1-butene mole fraction – no speciation data for 2-butene as a function of temperature was reported. The model predicts significant amounts of 2-butene forming in the oxidation of 2-butanol, see Figure 6-17 and Table 6-5; the primary routes to 2-butene are through the unimolecular decomposition of 2-butanol to 2-butene and water, and the β-scission of the CH3-CH(OH)-*CH-CH3 radical.

Table 6-5: Predicted and experimental [253] maximum mole fractions, in parts per million, of 1- and 2-butene (summation of cis- and trans-) for 2-butanol oxidation in a 10 atm perfectly-stirred.

	ϕ=2	ϕ=1	ϕ=0.5
2-butene (model)	79	45	26
2-butene (expt.)	61	54	41
1-butene (model)	9	8	7
1-butene (expt.)	34	24	20

The model overestimates the maximum mole fraction of 2-butene by 30% at the rich condition and underestimates the maximum by 50% at the lean condition. If the butene concentrations are summed, the model still underestimates the total maximum butene mole fraction. Thus, more work is needed on the formation and depletion of the butene isomers in the oxidation of 2-butanol, in particular the 1-butene isomer.
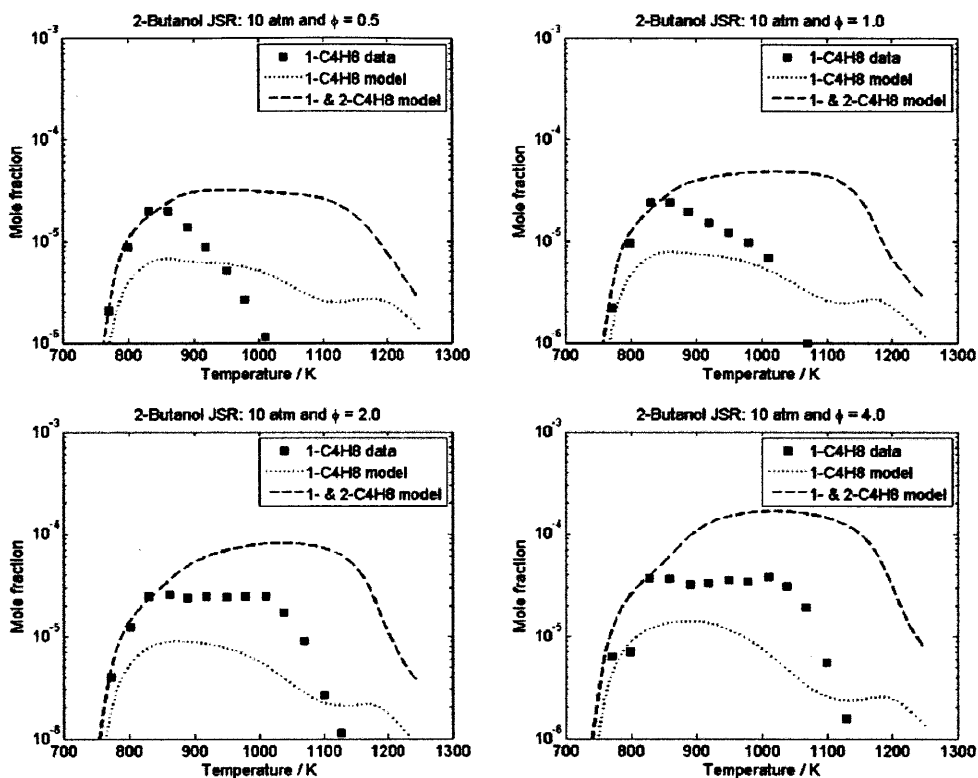
Figure 6-17: Predicted and experimental [253] butene speciation data for 2-butanol oxidation in a 10 atm perfectly-stirred. The dotted lines are the model's 1-butene predictions and the dashed lines are the model's 1-butene + 2-butene predictions.

6.4.3.2 ISO-BUTANOL RESULTS

The model comparisons for each equivalence ratio tested are shown in Figure 6-18 through Figure 6-21. Overall, the model's predicted species concentrations are in reasonable agreement with the data. Two species to point out are iso-butanol and iso-butene. For iso-butanol, for all equivalence ratios tested, the predicted concentration profiles do not drop-off as quickly as the experimental data. For iso-butene, the model does not predict the peak concentration (near 800 K) for $\phi = 0.5$ or 1.0. The two

215

dominant pathways to iso-butene are through the β-scission of the HO-CH₂-*C-(CH₃)₂ radical and the unimolecular decomposition of iso-butanol to iso-butene and water. A detailed pathway and sensitivity analysis for this dataset has not been performed. However, future work in this regard would benefit the model greatly.
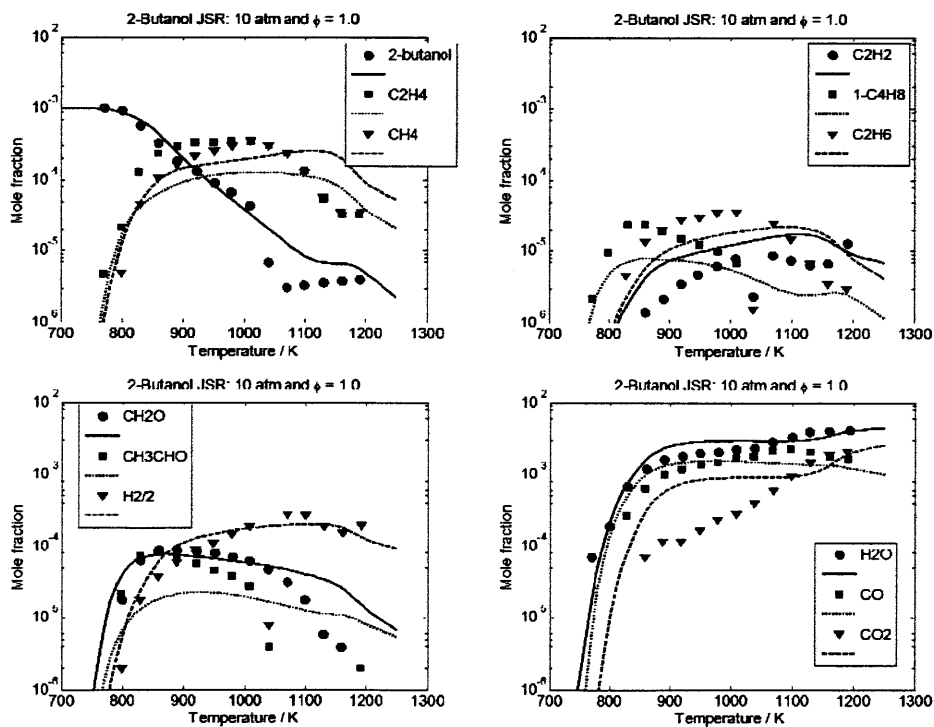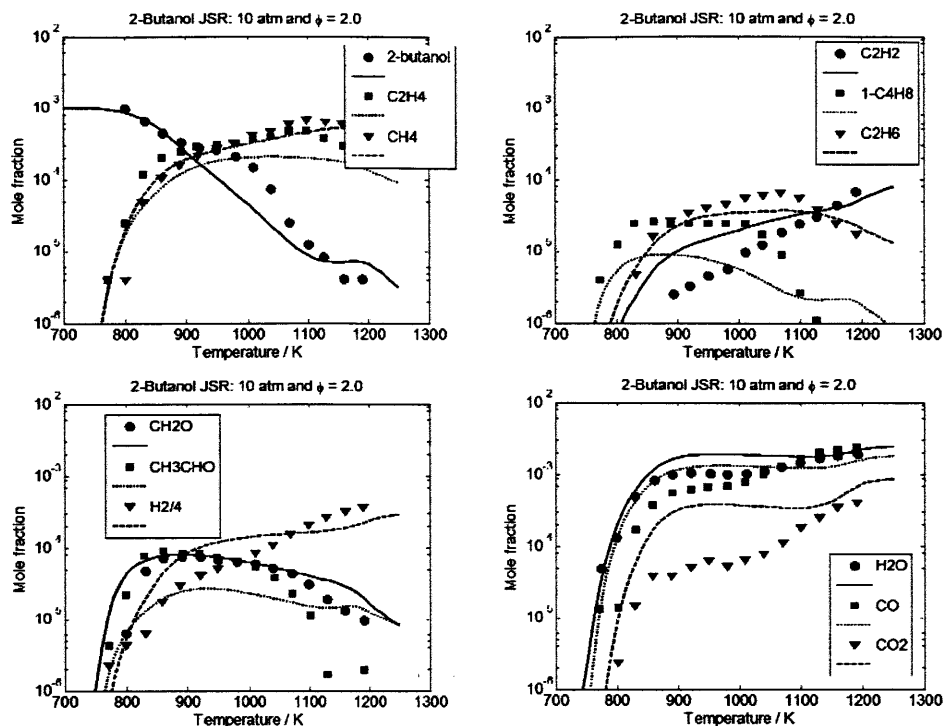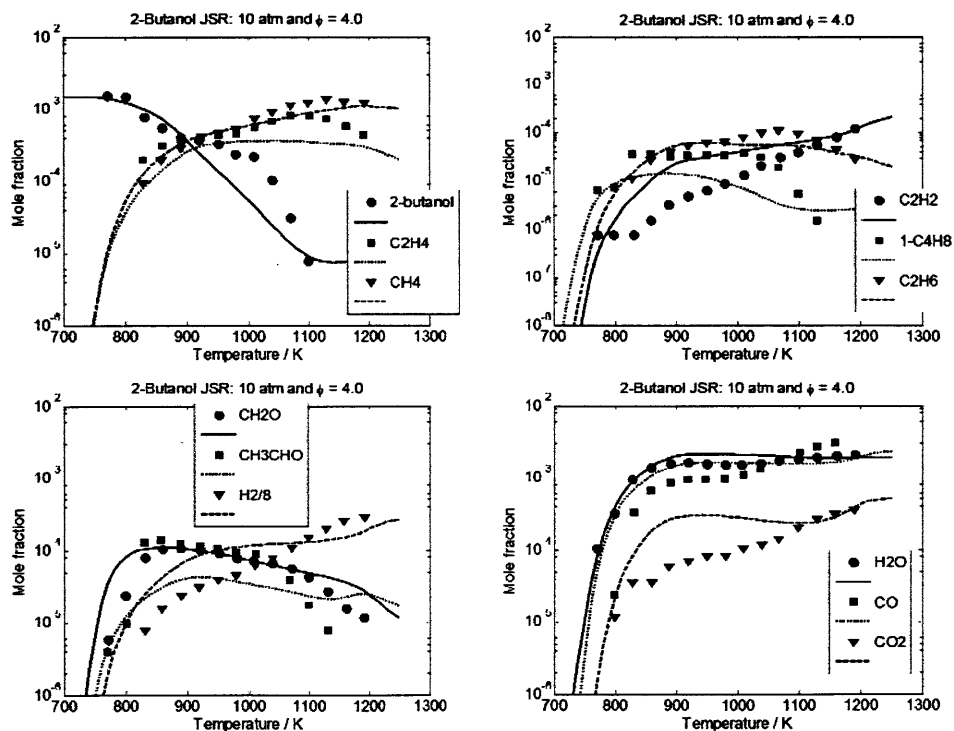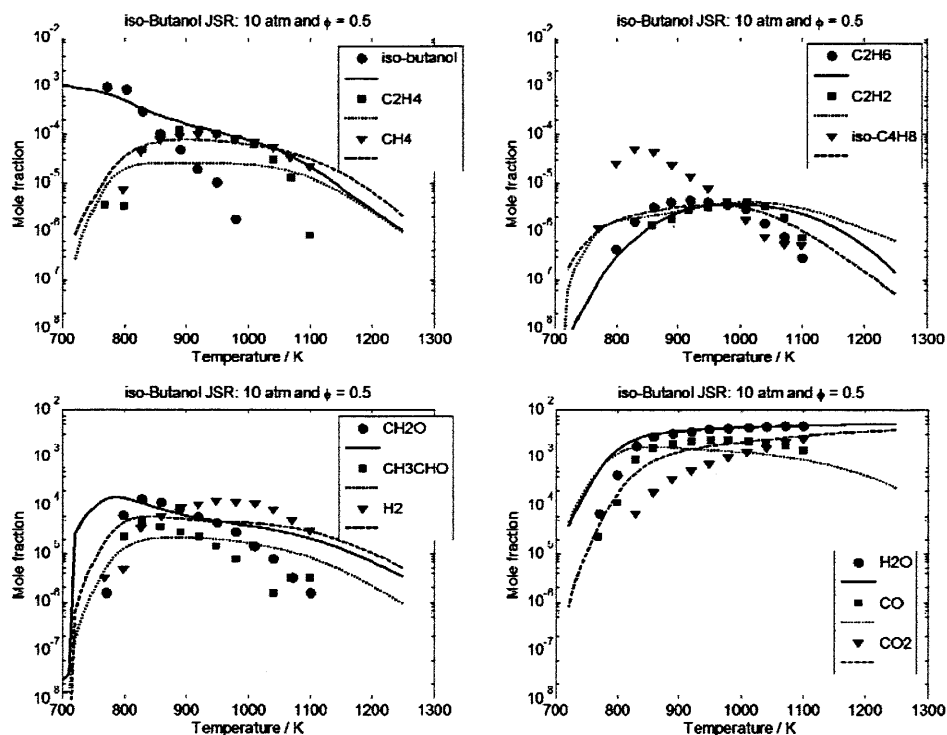

Figure 6-18: Predicted and experimental [253] speciation data for 0.1% iso-butanol oxidation in a 10 atm perfectly-stirred reactor for an equivalence ratio of 0.5. The "CH3CHO" curve is a summation of acetaldehyde and ethanol.
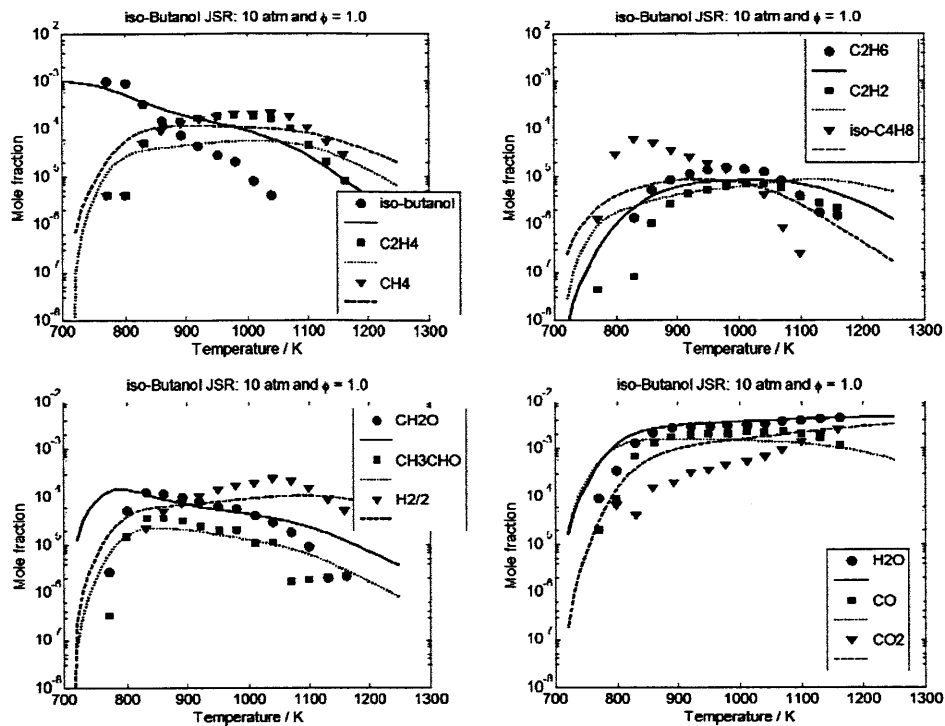
Figure 6-19: Predicted and experimental [253] speciation data for 0.1% iso-butanol oxidation in a 10 atm perfectly-stirred reactor for an equivalence ratio of 1.0. The "CH3CHO" curve is a summation of acetaldehyde and ethanol. Note: the H2 curves have been divided by two.
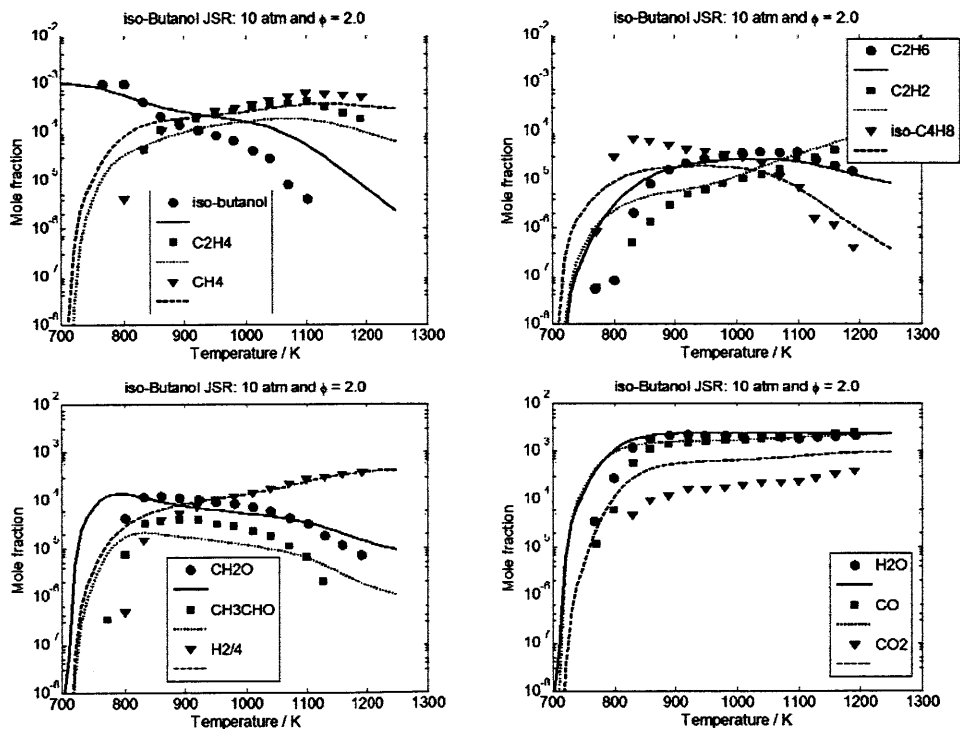
Figure 6-20: Predicted and experimental [253] speciation data for 0.1% iso-butanol oxidation in a 10 atm perfectly-stirred reactor for an equivalence ratio of 2.0. The "CH3CHO" curve is a summation of acetaldehyde and ethanol. Note: the H2 curves have been divided by four.

217
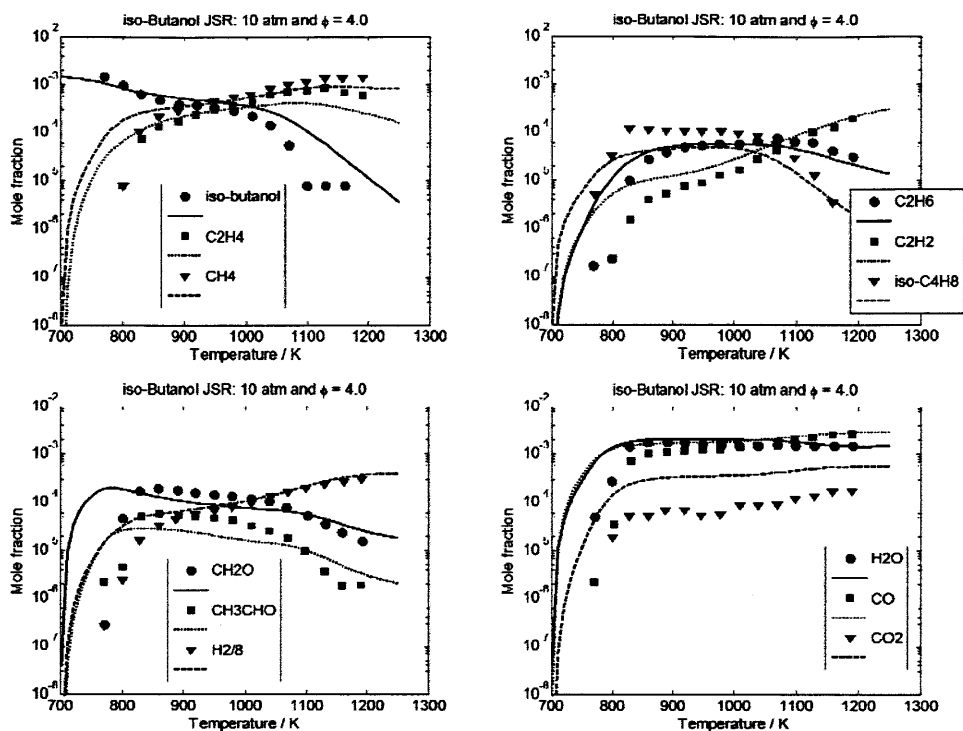
Figure 6-21: Predicted and experimental [253] speciation data for 0.15% iso-butanol oxidation in a 10 atm perfectly-stirred reactor for an equivalence ratio of 4.0. The "CH3CHO" curve is a summation of acetaldehyde and ethanol. Note: the H2 curves have been divided by eight.

6.4.4 LOW-PRESSURE, FUEL-RICH, PREMIXED FLAME SPECIATION DATA

Oβwald et al. measured species concentration profiles in low-pressure (P = 30 torr), premixed, fuel rich (ϕ = 1.71) butanol flames using electron-impact ionization and photoionization mass spectrometry [254]. These experiments were modeled in CHEMKIN-MFC, using the PREMIX reactor model. The experimentally-measured temperature profile was supplied as input. The inlet mixture composition was 16.6% butanol, 58.4% oxygen, and 25% argon. Some of the model's predicted concentration profiles, for all four butanol isomers, are compared against the electron-impact ionization experimental data in Figure 6-22 through Figure 6-28. Overall, the model does reasonably well at predicting the mole fraction profiles: the predicted peak for most species is within a factor of three, and the trends between the four isomers are captured for most species. However, the model generally predicts the peak concentrations to occur ~5 mm closer to the burner than the experimental data. One possible explanation for this discrepancy is that the probe used to measure the temperature profile could distort the

218

flame and thus yield a measurement different from the "true" experimental value. One way most modelers treat this probe effect is by shifting all simulated profiles. Some of the more interesting species comparisons are discussed in the coming paragraphs.

Of particular interest for modelers and experimentalists, especially in these low-pressure flames where structural isomers may be resolved (e.g. acetaldehyde and ethenol), are the aldehyde and corresponding enol species. For the butanol isomer system, the acetaldehyde/ethenol (Figure 6-23), propanal/1-propenol, acetone/propen-2-ol, butanal/1-buten-1-ol, and 2-methylpropanal/2-methyl-1-propen-1-ol (Figure 6-26) combinations are relevant.

The model predicts the overall C_2H_4O profile well for 2-, iso-, and tert-butanol; the model also predicts the distribution between ethenol and acetaldehyde well for these three isomers (not shown). However, the model underestimates the overall C_2H_4O profile for 1-butanol; this is caused by the model underestimating the amount of acetaldehyde present in the flame (not shown). In the model acetaldehyde comes exclusively from ethenol: both the unimolecular tautomerization and the H-assisted tautomerization – H+C2H4O(+m)=H+CH3CHO(+m) – are significant pathways. One pathway that is not predicted to be significant is the recombination of methyl and formyl radical. Under these low-pressure conditions, fewer collisions occur on average and radicals therefore have unusually high concentrations; hence, it is not unreasonable to imagine the methyl + formyl pathway being a significant pathway to acetaldehyde.
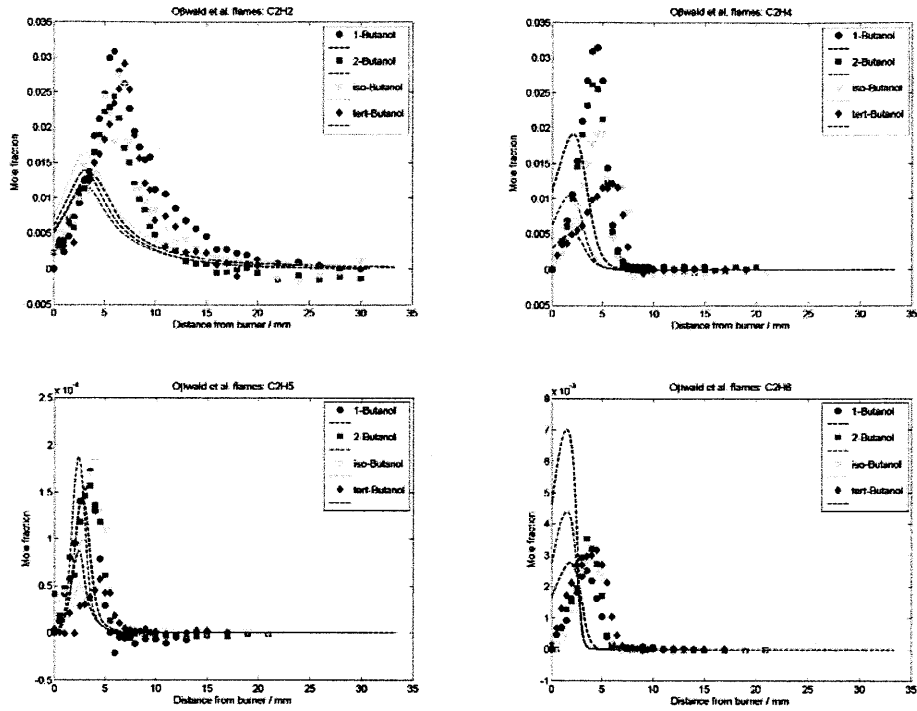
Figure 6-22: Predicted and experimental [254] mole fraction profiles for C_2H_x species in low-pressure, fuel-rich, premixed butanol/O_2/Ar flames. The data presented is the electron-impact ionization measurements.
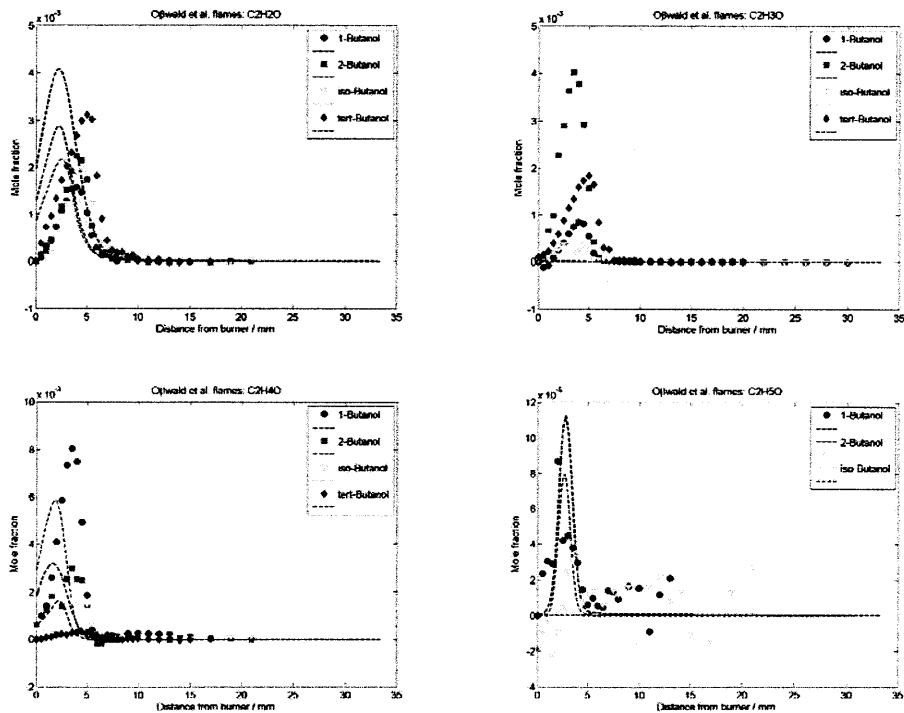
Figure 6-23: Predicted and experimental [254] mole fraction profiles for C_2H_xO species in low-pressure, fuel-rich, premixed butanol/O_2/Ar flames. The data presented is the electron-impact ionization measurements.

For the 1-, 2-, and iso-butanol flames, the model underestimates the C_3H_6O isomer profile and overestimates the C_4H_8O isomer profile. For the C_3H_6O isomers, the model again predicts the enol (1-propenol for 1- and iso-butanol and propen-2-ol for 2-butanol, respectively) species profile very well, but greatly underestimates the aldehyde (propanol for 1- and iso-butanol) and ketone (acetone for 2-butanol) profiles.
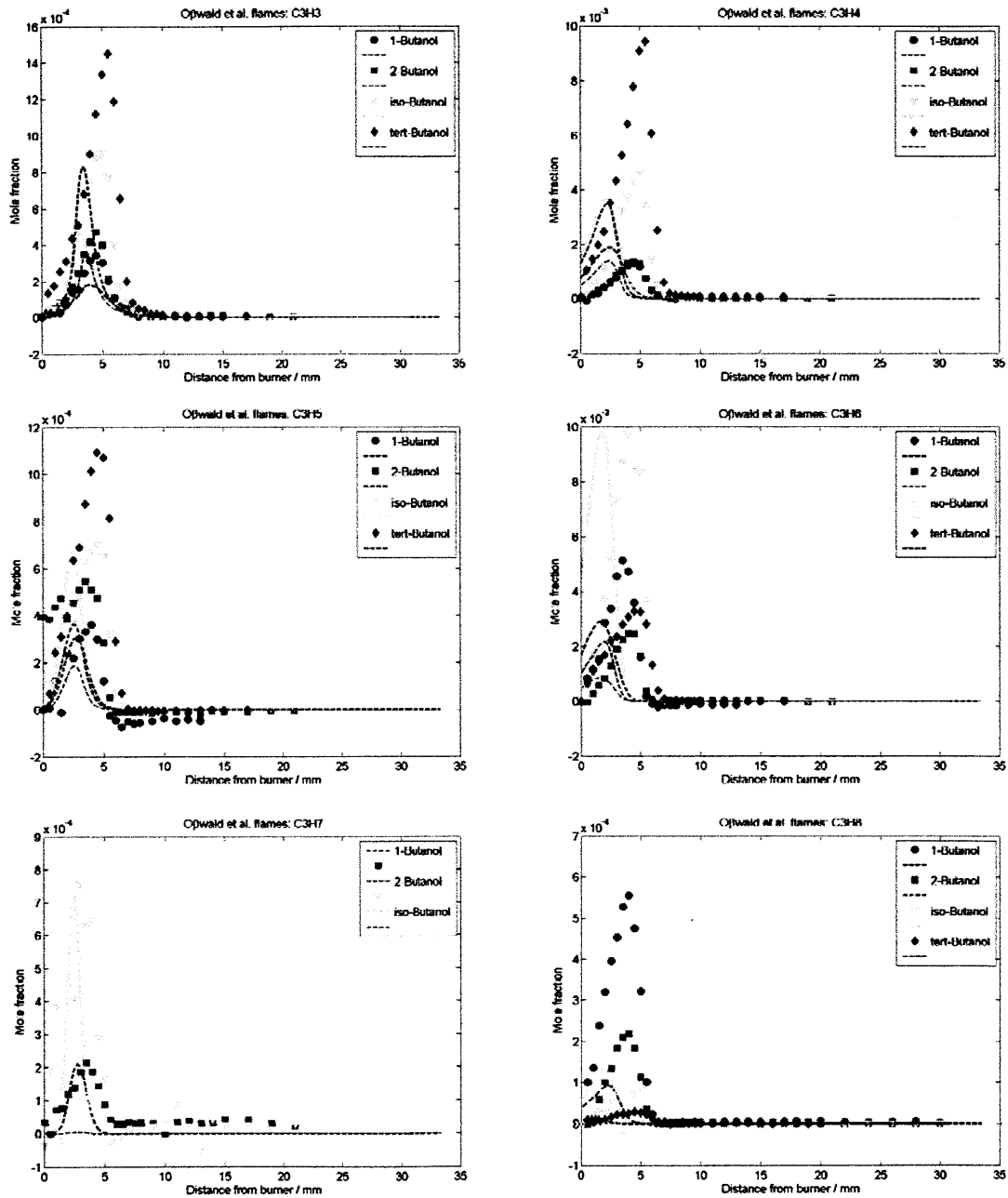
Figure 6-24: Predicted and experimental [254] mole fraction profiles for C_3H_x species in low-pressure, fuel-rich, premixed butanol/O_2/Ar flames. The data presented is the electron-impact ionization measurements.

In general, the model does not predict the C_4H_x species profiles well, for any of the butanol isomers (Figure 6-25). One possible explanation is the fate of the C_4H_9O radicals (formed from a Hydrogen abstraction of the fuel). Under these low-pressure, high oxygen concentration conditions, the model predicts these radicals to react directly with oxygen (or HO_2) to form a C_4H_8O isomer and HO_2 (or H_2O_2); this explains the high C_4H_8O predicted concentrations for each fuel. The most dominant C_4H_9O radical formed has the radical alpha to the hydroxyl group (with the exception of tert-butanol, which has no alpha hydrogens to abstract). These radicals can then either lose a hydrogen to form the aldehyde / ketone, or can undergo β-scission forming the C_2 and C_3 enol species.
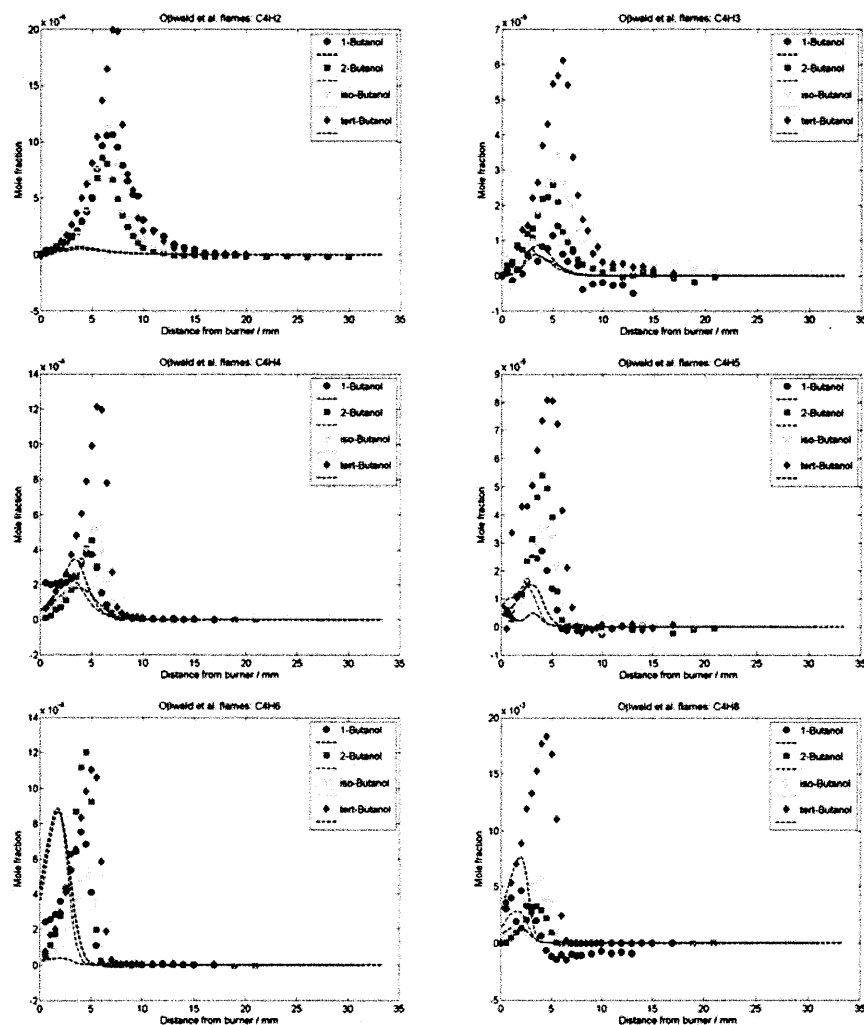
Figure 6-25: Predicted and experimental [254] mole fraction profiles for C_4H_x species in low-pressure, fuel-rich, premixed butanol/O_2/Ar flames. The data presented is the electron-impact ionization measurements.

222
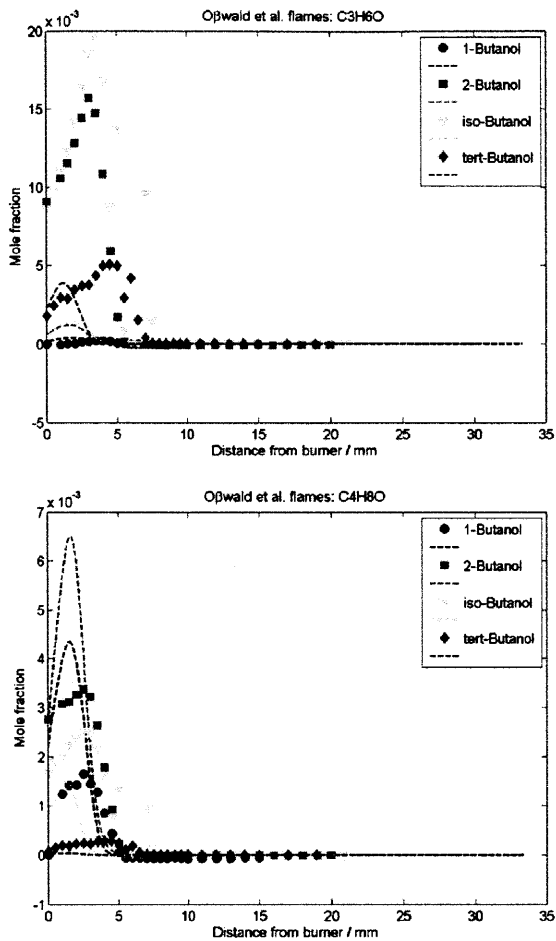
Figure 6-26: Predicted and experimental [254] mole fraction profiles for C_3H_6O and C_4H_8O species in low-pressure, fuel-rich, premixed butanol/O_2/Ar flames. The data presented is the electron-impact ionization measurements.
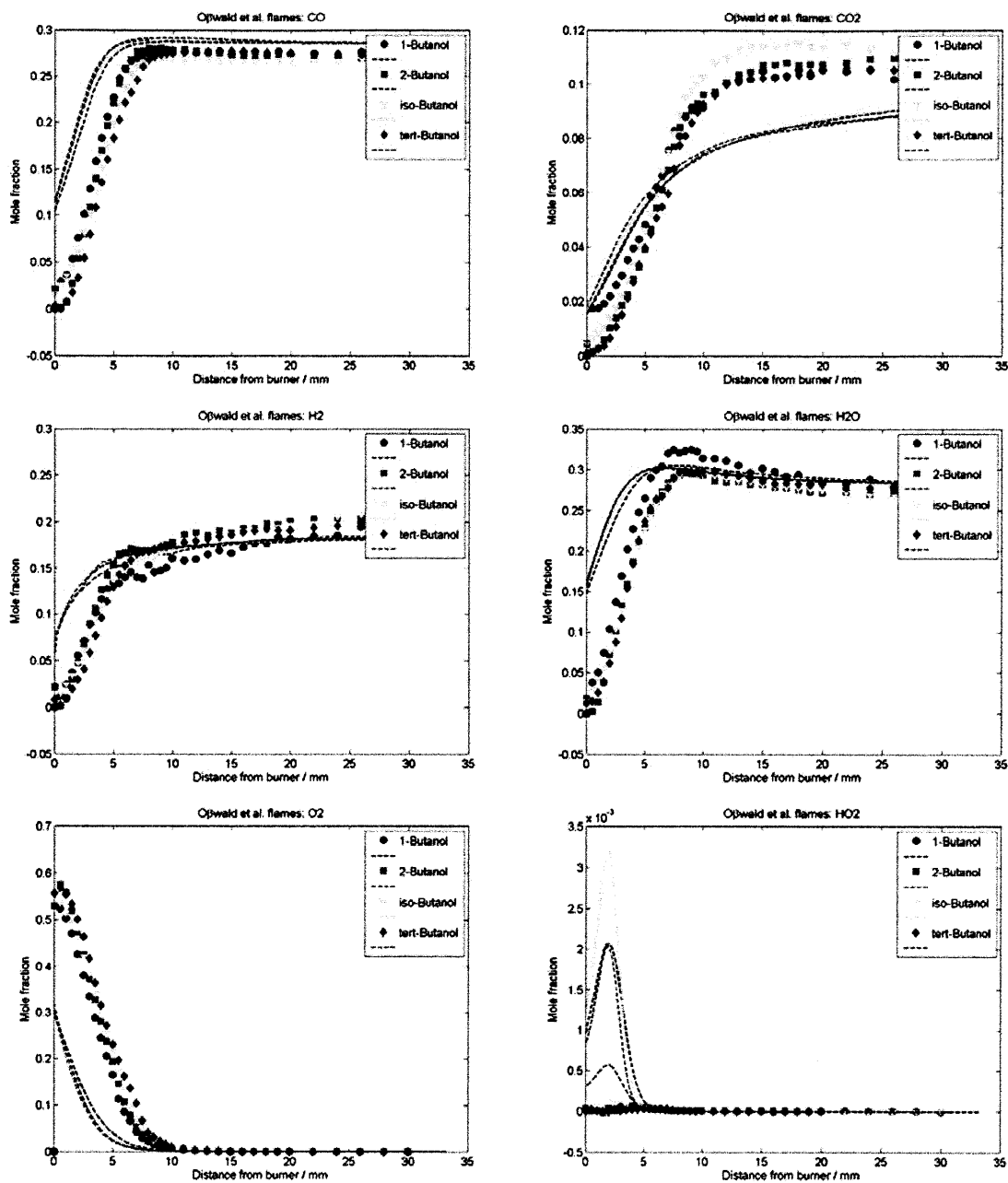
Figure 6-27: Predicted and experimental [254] mole fraction profiles for CO, CO_2, H_2, H_2O, O_2, and HO_2 species in low-pressure, fuel-rich, premixed butanol/O_2/Ar flames. The data presented is the electron-impact ionization measurements.

With few exceptions, the model predicts the small molecule species' profiles ($C_0 - C_2$) well for all butanol isomers. The CO_2 profile as shown in Figure 6-27 would suggest otherwise, but the model's predictions agree very well with the CO_2 profile measured using photoionization (not shown).
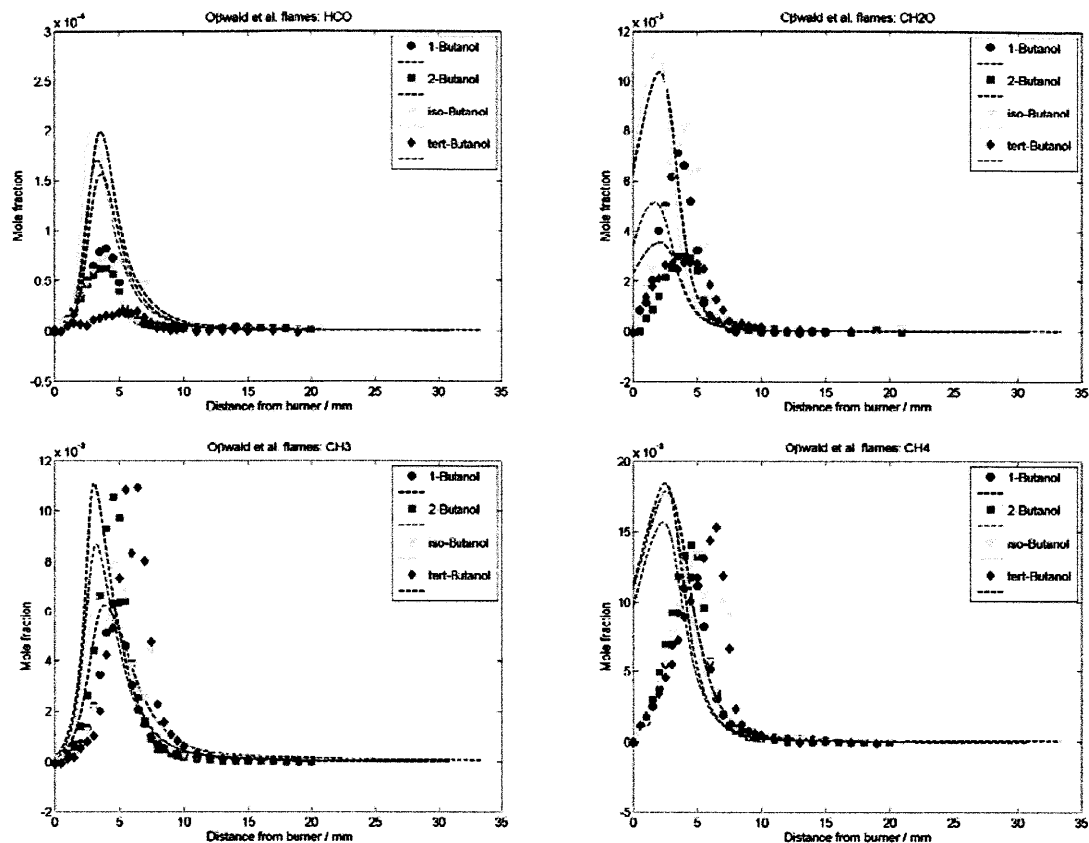
Figure 6-28: Predicted and experimental [254] mole fraction profiles for HCO, CH_2O, CH_3, and CH_4 species in low-pressure, fuel-rich, premixed butanol/O_2/Ar flames. The data presented is the electron-impact ionization measurements.

6.4.5 SHOCK TUBE IGNITION DELAY TIMES

Our mechanism was further tested against the ignition delay measurements conducted by Moss et al.; a direct comparison between the data, our mechanism's predictions, and the Moss mechanism's predictions, is located in Figures S1-S6 of the Supporting Information. As mentioned in Section 6.2.4, the ignition delays were computed independently of CHEMKIN and were defined as the time at which the OH concentration reached 10% of the maximum OH concentration; this calculation method is in accord with the Moss et al. study [180]. In comparing our mechanism against the dataset, the relative difference as defined by $(\tau_{predicted} - \tau_{experimental}) / \tau_{experimental}$ will be mentioned prevalently.

6.4.5.1 SEC-BUTANOL

Our network's predictions, compared against the entire sec-butanol ignition delay dataset obtained by Moss et al., are presented in Figure 6-29.
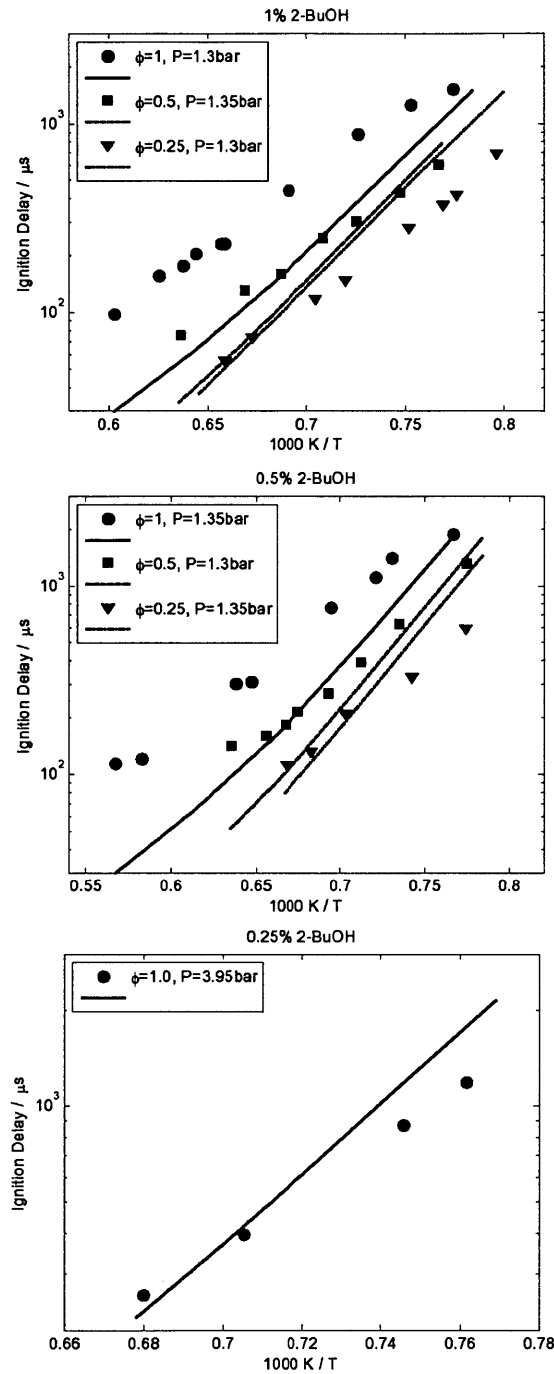
Figure 6-29: Experimental [180] and simulated autoignition delay of sec-butanol; the stated pressures correspond to the pressures used in modeling the shock tube experiments.

For the 1% initial mole fraction experiments, the mechanism predicts the data reasonably well over all experimental conditions. For the $\phi=1$ experiments, the Moss mechanism's predictions are consistently better across the entire temperature range. Our mechanism underestimates the ignition delay across the entire temperature range, by as much as 85%. For the $\phi=0.5$ experiments, our mechanism predicts the data well for initial temperatures ≤ 1496 K; both mechanisms' predictions are in error by more than 50% for high temperatures. For the $\phi=0.25$ experiments, our mechanism's predictions, in comparison to the Moss mechanism's predictions, are in better agreement with the data across the entire temperature range. Our mechanism's predictions are within 30% for initial temperatures ≥ 1419 K; we differ by as much as 85% at lower temperatures.

The comparisons for the 0.5% initial mole fraction experiments are similar to those made for the 1% initial mole fraction dataset. For the $\phi=1.0$ conditions, the Moss mechanism's predictions are in better agreement with the experimental data across the entire temperature range. Our mechanism predicts the ignition delay within 50% for initial temperatures ≤ 1545 K and is no worse than 75% for the higher temperatures. For the $\phi=0.5$ conditions, the Moss mechanism predicts the high-temperature data better and our mechanism predicts the low-temperature experiments better. Once again, our mechanism is no worse than 50% different for initial temperatures ≤ 1525 K and no worse than 70% across all temperatures. For the $\phi=0.25$ experiments, our mechanism predicts most of the data very well, particularly the high temperature chemistry. The relative difference between our predictions and the experiments are no worse than 50% at temperatures $\geq$ 1347 K; we differ by as much as 85% at lower temperatures.

Our mechanism predicts the 0.25% initial mole fraction data very well across the entire temperature range; our prediction's relative difference from the data is no greater than 45%. Our model's predictions are consistently in better agreement with the data for these experiments, compared to the Moss model's predictions. Clearly, both mechanisms have conditions where they predict the dataset well and where they need improvement: the Moss mechanism tends to predict the high temperature and stoichiometric conditions well

whereas our mechanism tends to predict the low temperature, lean, and high pressure conditions well.

A flux and sensitivity analysis for one of the sec-butanol shock tube simulations is presented in Figure 6-30A-B; the simulated conditions are: 1% initial mole fraction of sec-butanol, ϕ=1.0, P = 1.3 bar, and T = 1450 K. For this simulation, the C-C bond fission forming ethyl and 1-hydroxyethyl radical is the dominant decomposition route during the first 20 μs. From 20 to 70 μs, the flux through the H-abstraction of sec-butanol by H atom forming either the 1-hydroxy-1-methylpropyl or 2-hydroxybutyl radical is equally dominant; the H-abstraction of sec-butanol by H atom forming the 2-hydroxy-1-methylpropyl radical also contributes significantly to the decomposition during this time. From 70 to 150 μs, i.e. the time at which the sec-butanol decomposition is complete, the H-abstraction of sec-butanol by O atom forming either the 2-hydroxybutyl or 3-hydroxybutyl radical also contributes significantly to the decomposition. The H-abstraction reaction rate coefficients by H atom were computed in this study; the H-abstraction reactions by O atom were estimated by RMG and based on the kinetics reported by Curran et al. [255].

For this simulation, the sec-butanol concentration is sensitive mainly to small-molecule reactions, e.g. $H+O_2=OH+O$, $CH_3+CH_3=C_2H_6$, $CH_3+OH=H_2O+CH_2(S)$, and $HO_2+CH_3=CH_3O+OH$. The kinetics for these reactions come from Miller et al. [209], Klippenstein et al. [107], the GRI-Mech 3.0 mechanism [191], and Jasper et al. [212], respectively. Our kinetic network would be improved if more accurate rate coefficients for the reaction $CH_3+OH=H_2O+CH_2(S)$, such as those reported by Jasper et al. [256], were implemented; unfortunately, the version of CHEMKIN employed here does not recognize the modified Troe rate coefficient expression reported by Jasper et al. Additionally, the sec-butanol concentration is also sensitive to the C-C bond fission forming ethyl and 1-hydroxyethyl radical. As mentioned previously, more accurate kinetics for the radical recombination is necessary to refine our kinetic network.
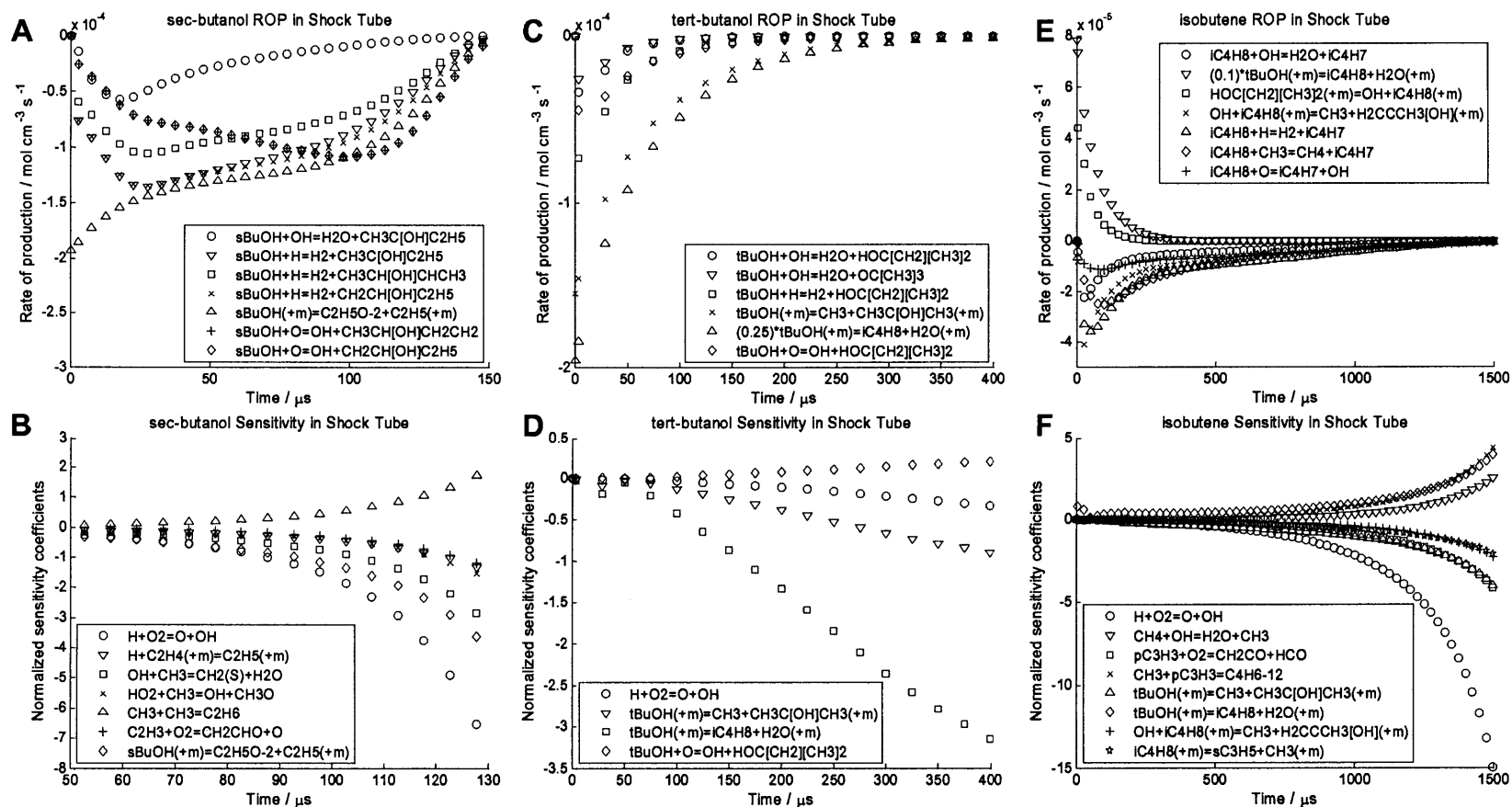
Figure 6-30: Rate-of-production analysis and normalized sensitivity coefficients for: (A-B) sec-butanol in an autoignition delay calculation for sec-butanol and (C-D) tert-butanol and (E-F) isobutene in an autoignition delay calculation for tert-butanol. See text for details. Also, please note that one rate-of-production in both figures (C) and (E) has been mutlpiled by a constant value, to better display both the dominant and minor pathways.

229

6.4.5.2 TERT-BUTANOL

Our network's predictions, compared against the entire tert-butanol ignition delay dataset obtained by Moss et al., are presented in Figure 6-31; overall, the model predicts this dataset very well. The following analysis is regarding the 1% initial mole fraction experiments. For the $\phi=1$ experiments, our predictions are consistently within 30% of the data for initial temperatures ≤ 1646 K; the predictions are within 45% across the entire temperature range. For the $\phi=0.5$ experiments, our predictions are within 35% across the entire temperature range. For the $\phi=0.25$ experiments, our predictions are within 25% for initial temperatures ≤ 1447 K; we underestimate the ignition delay by as much as 40% at the highest temperature reported.
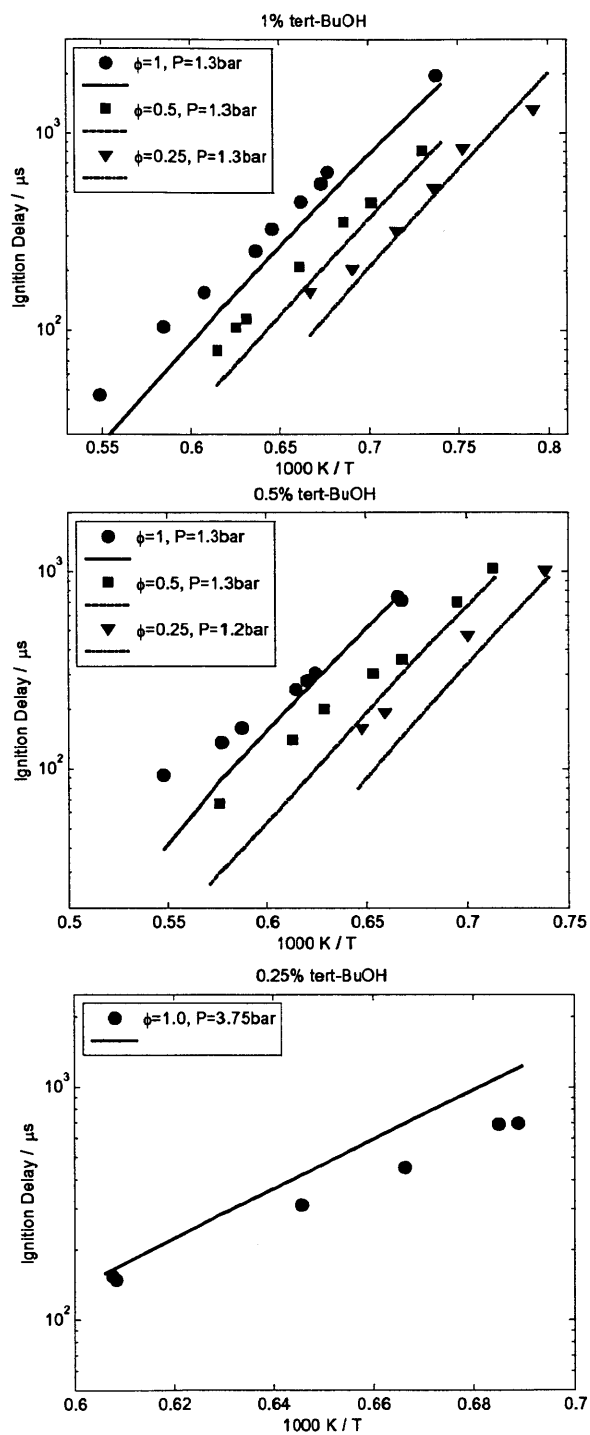
Figure 6-31: Experimental [180] and simulated autoignition delay of tert-butanol; the stated pressures correspond to the pressures used in modeling the shock tube experiments.

Our mechanism also predicts the 0.5% initial mole fraction experiments well. For the $\phi=1$ experiments, the model's predictions are within 30% for the majority of the temperature range; the model underestimates the ignition delay by as much as 50% at temperatures $\geq$

231

1710 K. Our model predicts this data better than the Moss model over all temperatures. For the φ=0.5 experiments, the model is within 30% for initial temperatures ≤ 1531 K; the model deviates by as much as 55% for the higher temperatures. For these experiments, our model's predictions are consistently in better agreement with the ignition delay experimental data in comparison to the Moss mechanism's predictions. For the φ=0.25 experiments, our mechanism consistently underestimates the ignition delay, by as much as 45%. The two models perform equally well for these experiments.

The Moss mechanism's predictions match the experimental ignition delay more consistently than our model's predictions for the 0.25% initial mole fraction experiments. At initial temperatures ≤ 1549 K, our mechanism overestimates the ignition delay by as much as 70%; our model performs equally well with the Moss mechanism at higher temperatures. Overall, our mechanism's predictions are in better agreement with the data than the Moss mechanism's predictions for most experiments performed near 1 bar; however, the Moss mechanism is more accurate for the high pressure dataset.

A flux and sensitivity analysis for one of the tert-butanol shock tube simulations is presented in Figure 6-30C-D; the simulated conditions are: 0.25% initial mole fraction of tert-butanol, φ=1.0, P = 3.75 bar, and T = 1450 K. For this simulation, the predominant decomposition route is through dehydration to isobutene and water; a minor pathway is the C-C bond fission forming methyl and 1-hydroxy-1-methylethyl radical. Sensitivity analysis reveals the same conclusions as the rate-of-production analysis, namely that the concentration of tert-butanol is very sensitive to the dehydration kinetics and, to a lesser extent, to the C-C bond fission kinetics. Once again, more accurate kinetics for the C-C bond fission reaction would greatly assist our modeling efforts.

Since the tert-butanol reacts rapidly away to isobutene, the measured autoignition delay is as indicative of a measure of the reactivity of isobutene as it is a measure of the reactivity of tert-butanol. Thus, for the same simulation conditions described in the previous paragraph, the rate-of-production and sensitivity analysis for isobutene is presented in Figure 6-30E-F. The major route to isobutene is clearly the dehydration of tert-butanol; a minor channel is the β-scission of the 2-hydroxy-2-methylpropyl radical, forming

isobutene and hydroxyl radical. The major decomposition routes are through the H-abstraction reactions of isobutene by H atom, methyl, and hydroxyl radical, and via the chemically-activated reaction OH+iC4H8(+m)=CH3+H2CCCH3[OH](+m) where isobutene and hydroxyl radical form an adduct before falling apart to propen-2-ol and methyl radical; this pressure-dependent rate coefficient was computed in this study, using the steady-state master equation option in the RMG software. The H-abstraction rate coefficients of isobutene by H atom and methyl radical were computed in this study; the H-abstraction rate coefficient by hydroxyl radical was estimated by RMG.

The isobutene concentration is sensitive to many reactions, both small-molecule and the fuel chemistry. Isobutene is sensitive to the following small-molecule reactions: $H+O_2=O+OH$, $CH_4+OH=H_2O+CH_3$, $pC_3H_3+O_2=CH_2CO+HCO$, $CH_3+pC_3H_3=C_4H_6$-12; the rate coefficients employed come from Miller et al. [209], Srinivasan et al. [211], Marinov [192], and Davis et al. [257]. The isobutene concentration is also sensitive to: the dehydration of tert-butanol, the C-C bond fission of tert-butanol forming methyl and 1-hydroxy-1-methylethyl radical, the C-C bond fission of isobutene forming methyl and 1-methylethenyl radical, and the chemically-activated reaction mentioned in the previous paragraph, i.e. isobutene and hydroxyl radical forming propen-2-ol and methyl radical. These rate coefficients are from this study: the dehydration was computed using the methodology described in Section 3.2 and the C-C bond fissions were computed using the reverse rate coefficients and equilibrium constants. A more accurate potential energy surface and master equation solution for the C_4H_9O system would benefit our kinetic model greatly.

6.4.5.3 ISO-BUTANOL

The predicted ignition delay, as defined by the time to reach 50% of the maximum hydroxyl radical concentration, for iso-butanol for a range of temperatures, pressures, and fuel conditions is shown in Figure 6-32 and Figure 6-33. The model predictions of Moss et al. and Grana et al. are also presented. Overall, our model's predictions are in very good agreement with the Moss et al. experimental data. The predictions of the experiments near 1 bar, Figure 6-32, are always within a factor two of the experimental measurements. All three models predict the lower temperature experiments reasonably

well, but the Moss et al. and Grana et al. predictions are too fast (shorter ignition delay) at higher temperatures. None of the models predict the experiments near 4 bar, Figure 6-33, well over the entire temperature range. The Moss et al. model and our model predict longer ignition delays than the experimental measurements over the entire temperature range; the predictions are always within a factor two though and the predicted power law is similar to the experimental observation. The Ranzi et al. model predicts the higher temperature chemistry correctly but is too slow (longer ignition delays) at lower temperatures.

Using our model, the predicted dominant decomposition pathways for the experiments performed near 1 bar are through the bond fissions of iso-butanol – forming 2-propyl and hydroxymethyl radicals or methyl and 2-hydroxy-1-methylethyl radicals. 2-propyl and molecular oxygen undergo disproportionation to form propene and hydroperoxy radical whereas 2-hydroxy-1-methylethyl radical forms 2-propen-1-ol through disproportionation with molecular oxygen or propene and hydroxyl radical through β-scission; propene loses a Hydrogen atom to hydroxyl radical, forming allyl radical. Allyl and Hydrogen atom react to vinyl and methyl radical through chemical activation; vinyl reacts with molecular oxygen to form formaldehyde and formyl radical through chemical activation, with the formyl radical reacting to CO and eventually to CO_2.
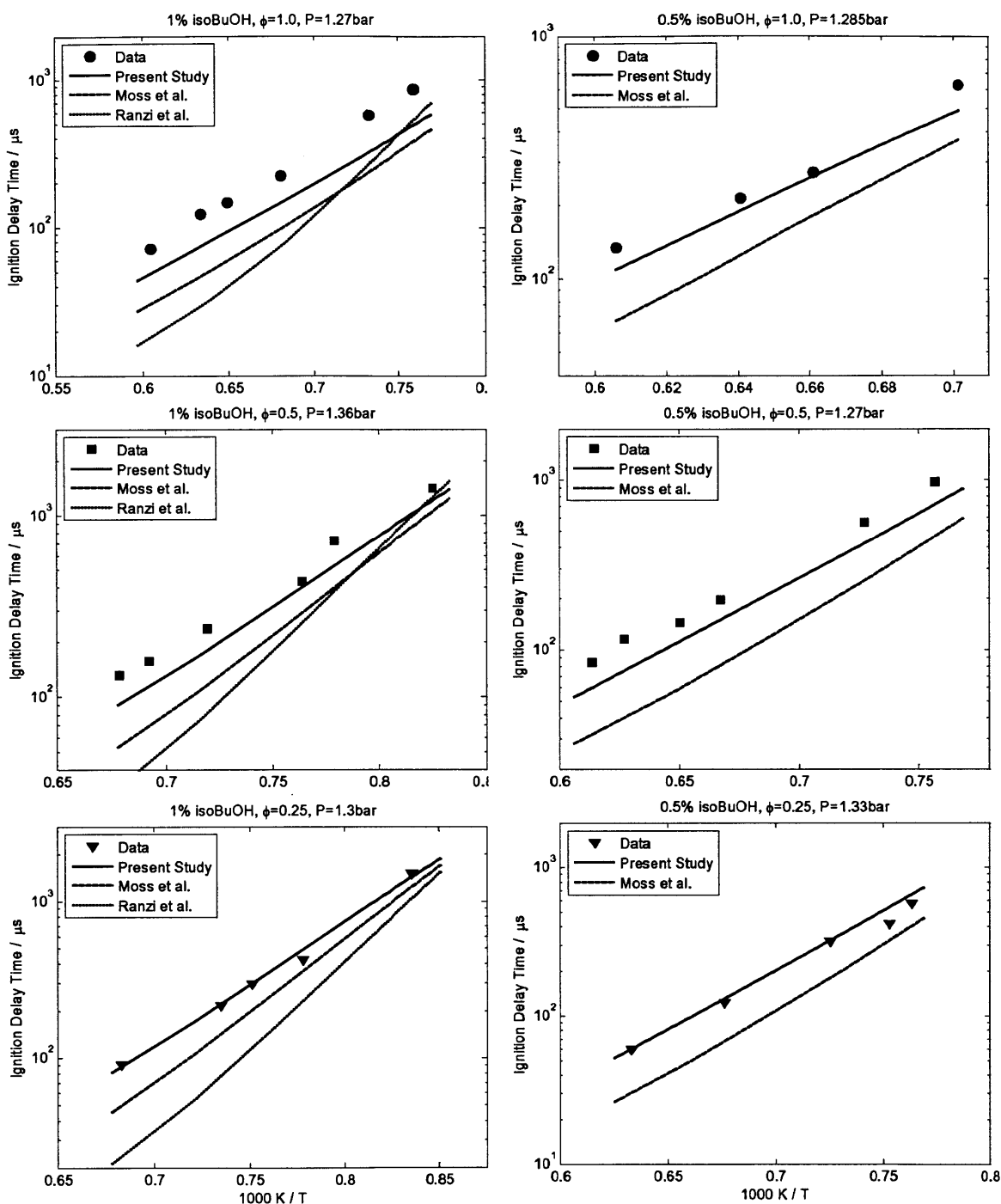
Figure 6-32: Predicted and experimental [180] ignition delay of iso-butanol. The left-hand column is for 1 mol% initial fuel while the right-hand column is for 0.5 mol% initial fuel. The figures are for equivalence ratios of 1, 0.5, and 0.25 moving from top to bottom. The "Moss et al." [180] and "Ranzi et al." [258] predictions are other butanol mechanism predictions.

For the experiments run near 4 bar, the dominant iso-butanol decomposition pathway is also the bond fissions. The 2-hydroxy-1-methylethyl radical goes exclusively to 2-

235

propen-1-ol through disproportionation with molecular oxygen; the propenol isomer loses a hydrogen atom via abstraction to form 3-hydroxy-2-propenyl radical. This radical forms 2-propenal through disproportionation with molecular oxygen; 2-propenal reacts with hydrogen atom to form ethylene and formyl radical through chemical activation.
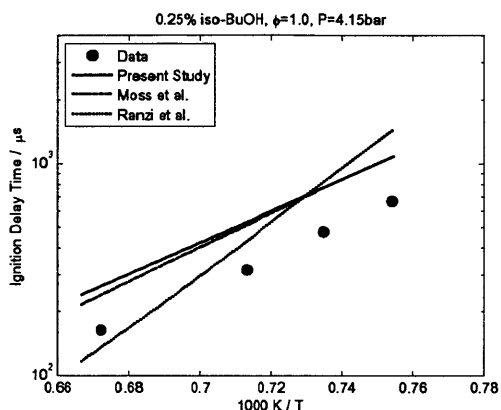
Figure 6-33: Predicted and experimental [180] ignition delay for 0.25 mol% initial iso-butanol, for a stoichiometric equivalence ratio. The "Moss et al." [180] and "Ranzi et al." [258] predictions are other butanol mechanism predictions.

6.4.5.4 ETHANOL

One of this study's objectives is gaining a better understanding of how a molecule's structure affects its combustion properties; in this case, the study focuses on the reactivity differences between a primary-, secondary-, and tertiary alcohol using the butanol isomers. In addition to comparing the reactivity differences between the three types of alcohols, it would also be illuminating to compare the reactivity differences within a class of alcohols, e.g. examining ethanol and n-butanol, two examples of primary-alcohols. To examine the trends between different alcohol classes, and between different structures within the same alcohol class, the predicted ignition delay for n-, sec-, tert-butanol, and ethanol are compared and discussed herein.

Before presenting this comparison, the ethanol submodel will be validated against the ignition delay measurements of Dunphy and Simmie [259]. In these experiments, the ignition delay of ethanol-oxygen-argon mixtures was determined for equivalence ratios of 0.25, 0.5, 1.0, and 2.0. The reflected shock temperatures and pressures spanned 1080-

1660 K and 1.8-4.6 bar. The ignition delay was determined experimentally based on light emission at 366 nm; in their study on modeling high-temperature ethanol oxidation [260], the authors estimated the ignition delay by finding the time that maximized the [CO]*[O] curve.

Table 6-6: Experimental [259] and predicted ignition delay, in microseconds, of ethanol-oxygen-argon mixtures; temperature has units of Kelvin. The predicted ignition delay corresponds to the time that maximized the [CO]*[O] curve.

	Temperature	P = 2.0 bar		P = 3.3 bar		P = 4.6 bar	
		$\tau_{experiment}$	$\tau_{prediction}$	$\tau_{experiment}$	$\tau_{prediction}$	$\tau_{experiment}$	$\tau_{prediction}$
1.25% Ethanol, ϕ = 0.5	1250	593	1186	412	855	294	691
	1429	130	114	83	82	73	67
	1667	28	20	16	13	18	10
1.25% Ethanol, ϕ = 1.0	1250	904	1406	638	974	481	816
	1429	208	151	142	104	112	88
	1667	57	32	31	20	26	16
2.50% Ethanol, ϕ = 2.0	1250	923	994	542	702	423	484
	1429	234	168	150	119	118	96
	1667	59	41	41	28	33	22

The present model's ignition delay predictions for ethanol are presented in Table 6-6. The Dunphy and Simmie shock tube experiments were modeled using the same methodology as presented in Section 6.2.4, with the exception of how the ignition delay was estimated. For these experiments, the estimated ignition delay corresponds to the time that maximized the [CO]*[O] curve. Overall, the model's predictions are in good agreement with the experimental data. The worst-case predictions are for the lowest-temperature experiments for the ϕ = 0.5 and 1.0 experiments, in which the model overestimates the ignition delay by as much as a factor of 2.4; all other ignition delays are predicted within a factor of 1.5.

A direct comparison of the present model's predicted ignition delay for n-, sec-, tert-butanol and ethanol, at the same reactor conditions, is presented in Figure 6-34. The reactivity of the tertiary alcohol is clearly different from those of the secondary and primary alcohol. As mentioned in previous sections, this slower reactivity is attributed to the dehydration reaction controlling the tert-butanol decomposition; a radical then

237

abstracts a hydrogen atom from isobutene, forming the resonantly-stabilized 2-methylallyl radical.
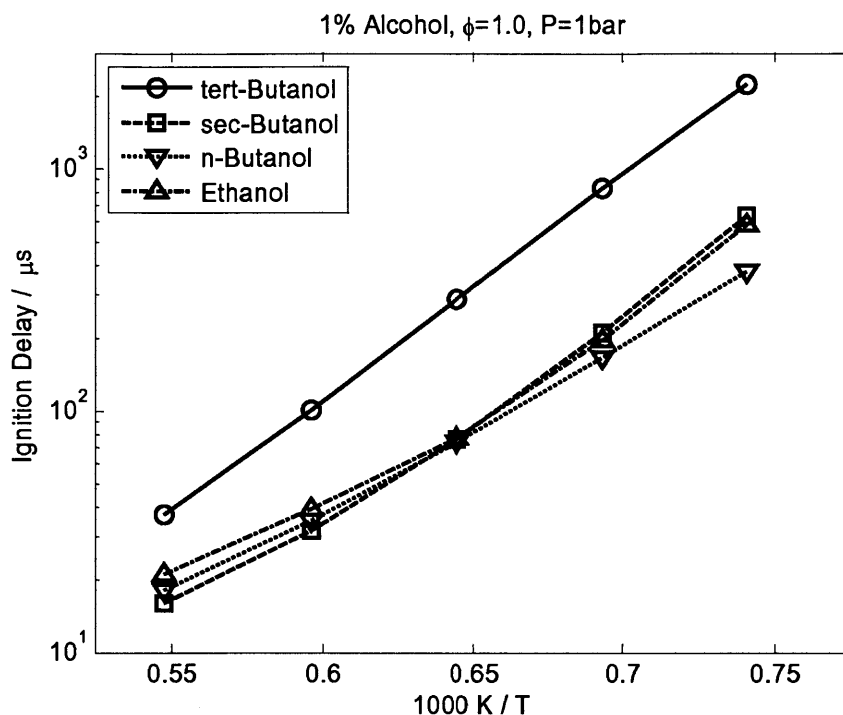
Figure 6-34: Predicted ignition delay of ethanol, n-, sec-, and tert-butanol for stoichiometric 1% butanol-oxygen-argon mixtures at a reflected pressure of 1 bar. The reported ignition delay is the time at which the predicted [OH] concentration reached half its maximum value.

Comparing sec- and n-butanol directly, the predicted ignition delays are essentially equivalent at initial temperatures > 1550 K; at lower temperatures, the ignition delay of n-butanol is less than the ignition delay of sec-butanol. This phenomenon can be explained by the competition between the dehydration and bond fission pathways of the fuel. At lower temperatures, the dehydration of sec-butanol is significant, resulting in either 1- or 2-butene; H-abstraction of either of these isomers results in the resonantly-stabilized 1-buten-3-yl radical. At higher temperatures, the dominant decomposition pathway switches from dehydration to bond fission; bond fission is the major decomposition pathway for n-butanol across all temperatures tested, hence the equivalent predicted ignition delays at higher temperatures for n- and sec-butanol.

Comparing the two primary alcohols directly reveals that ethanol and n-butanol effectively have identical ignition delays across all temperatures, except for the lowest temperature tested, at which the ethanol ignition delay is greater by a factor of 1.5. This

anomaly can be explained by recalling the present model overestimates the ignition delay at the lowest temperatures studied by Dunphy and Simmie. Capturing the trends within a given class of alcohols further demonstrates the potential of the methodology employed in constructing the reported butanol model.

6.4.6 LAMINAR BURNING VELOCITIES

The predicted laminar burning velocity for stoichiometric mixtures of each butanol isomer in air is presented in Table 6-7. The predicted laminar burning velocities for 1- and 2-butanol are similar, whereas the predicted value for tert-butanol is significantly lower. This difference can be attributed to the different decomposition pathways. 1- and 2-butanol are depleted exclusively through H-abstraction reactions; this results in the formation of C_4H_9O radicals, which undergo β-scissions to form alkenes and smaller radicals. Conversely, ~15% of tert-butanol undergoes dehydration, forming isobutene and water; <4% of 1- or 2-butanol undergoes dehydration. H-abstraction of isobutene produces the resonantly-stabilized 2-methylallyl radical, thus decreasing the laminar burning velocity.

Table 6-7: Predicted laminar burning velocity for stoichiometric mixtures of each butanol isomer in air, for an unburnt gas temperature of 343 K, at atmospheric pressure.

	$S_u°$ [=] cm/s
1-butanol	43.80
2-butanol	45.11
tert-butanol	37.88

The model's prediction for the laminar burning velocity of a stoichiometric mixture of 1-butanol in air is in reasonable agreement with the experimentally-determined values reported by Sarathy et al. [179] and Veloo et al. [236]. The Sarathy et al. study reports a laminar burning velocity of ~44 cm/s for an unburnt gas temperature of 350 K and pressure of 0.89 atm; the Veloo et al. study reports a value of 49.8 cm/s for an unburnt gas temperature of 343 K and pressure of 1 atm. The model's predictions for the 2- and tert-butanol isomers are also in good agreement with the experimentally-determined values reported by Veloo et al. [261]; the reported laminar burning velocities for sec- and

tert-butanol, for an unburnt gas temperature of 343 K at atmospheric pressure, are 47.38 and 36.11 cm/s, respectively.

6.4.6.1 LAMINAR BURNING VELOCITY

The predicted laminar burning velocity of iso-butanol at atmospheric pressure, for an unburnt gas temperature of 343 K, is shown in Figure 6-35. The simulations were performed in CHEMKIN-MFC using the PREMIX reactor model. The Soret effect (thermal diffusion), a mixture-averaged diffusion, and a windward differencing scheme were incorporated. The default absolute and relative tolerances were utilized. The final GRAD and CURV tolerance criteria were 0.2.

Over most equivalence ratios, the model adequately predicts the experimental data; the model underestimates the laminar burning velocity at rich equivalence ratios. The maximum burning velocity and the equivalence ratio corresponding to the maximum are predicted by the model. Comparing the two primary butanol alcohols, n- and iso-butanol, reveals a similar trend in both the experiment and model, with the exception being n-butanol's faster maximum burning velocity, peaking at 50 cm/s. The difference can be attributed to the branched hydrocarbon backbone of iso-butanol. The dominant reaction pathway for both butanol isomers is the abstraction of a C_α-H hydrogen atom. β-scission from the n-butanol radical produces ethenol and ethyl radical, which readily form ethylene and H atom; β-scission from the iso-butanol radical produces 1-propen-1-ol and methyl radical. With H atom being a more aggressive abstractor than methyl, the overall propagation of n-butanol oxidation is faster than iso-butanol oxidation, resulting in the faster laminar burning velocity for n-butanol.

Although the combustion characteristics of a primary and secondary (sec-butanol) alcohol may not be expected to have similar combustion characteristics, this is exactly the case for these laminar burning velocity experiments. Exploring the sec-butanol's reaction pathway reveals the abstraction of the C_α-H hydrogen atom, followed by the β-scission

240

forming 1-propen-2-ol and methyl radical to be the dominant pathway. Thus, the only difference between iso- and sec-butanol combustion is the isomer of propenol formed.
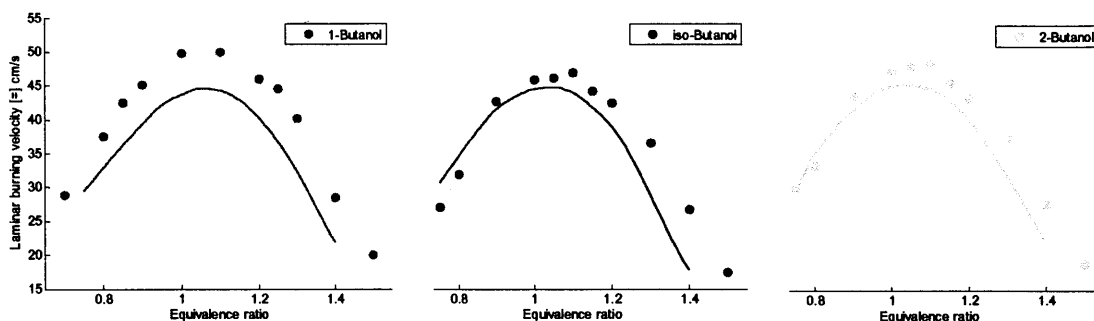
Figure 6-35: Predicted and experimental (1-Butanol: [236], iso- and 2-Butanol: [261]) laminar burning velocity of 1-, iso-, and 2-butanol (left to right) at atmospheric pressure and T_u = 343 K.

6.5 CONCLUSION

A detailed, robust reaction network for n-butanol, sec-butanol and tert-butanol has been constructed using an automated, open-source software package, Reaction Mechanism Generator (RMG). The model has been tested against multiple types of experiments – flames, shock tubes, and pyrolysis experiments – and varying reaction conditions – diffusion and premixed, rich and lean, over a pressure range of 1-4 bar and a temperature range of 900-1800K – with great success.

For the pyrolysis experiments, the sec-butanol chemistry was controlled by the HOCH(CH₃)-CH₂CH₃ bond fission reaction and the dehydration reactions near the entrance of the reactor; the H-abstraction of sec-butanol by H atom and methyl radical, forming the 1-hydroxy-1-methylpropyl radical, dominated throughout the remainder of the reactor. The tert-butanol chemistry was completely controlled by the dehydration reaction, and H-abstraction of tert-butanol by H atom and methyl radical were minor.

In the doped methane flame experiment, the C-C bond fission reactions, in addition to the water elimination reactions, dictated the reactivity of the butanol isomers. In the sec-butanol doped methane flame, both the dehydration reaction and β-scission of a butanol-derived C4H9O radical contributed to the formation of 1- and 2-butene; in the tert-butanol doped methane flame, only the dehydration reaction contributed to the formation of isobutene.

241

For the sec-butanol shock tube experiments, the fuel concentration was sensitive mainly to small-molecule chemistry (whose kinetics have been taken from the literature), but also to the C-C bond fission of sec-butanol to form ethyl and 1-hydroxyethyl radical. For the tert-butanol shock tube experiments, the fuel concentration was sensitive only to the tert-butanol dehydration kinetics; consequently, the autoignition delay was governed by the chemistry of isobutene. The isobutene chemistry was sensitive to both small-molecule chemistry and the fuel chemistry. Furthermore, the reactivity of the primary and secondary alcohols were similar for the high temperature shock tube experiments, specifically that free radical chemistry controlled the fuel's decomposition. At the lower temperatures, the dehydration of the secondary alcohol was significant, resulting in butene and thus resonantly-stabilized radical formation, causing more delayed ignition. The tertiary alcohol chemistry in the shock tube was drastically different from the primary and secondary alcohol chemistry, namely that the dehydration reaction was significant throughout the temperature range tested, resulting in larger ignition delays. Overall, the network can reproduce the ignition delay of sec- and tert-butanol across a wide range of temperatures, pressures, and fuel conditions quite well and can reproduce species concentration profiles under differing reactor conditions, for all major and minor products. It should be noted that the models have only been validated at temperatures above the negative temperature coefficient regime. Experiments of the butanol isomers in the low-temperature regime would greatly assist future modeling efforts in gaining a better understanding of the butanol isomers' behavior in the low- and negative temperature regime. Future work on butanol should resolve the discrepancies in the butadiene and butyne sub-networks, along with a more thorough analysis on the pathways to benzene and other aromatic compounds.

CHAPTER 7
RMG IMPLEMENTATIONS

7.1   THE EXTENT OF C/H/O HARDCODING IN THE RMG SOFTWARE AND DATABASE

As mentioned previously, the RMG software was hardcoded with specific functional groups for carbon, hydrogen, and oxygen (C/H/O) chemistry. Looking only at carbon, the hardcoded functional groups are: Cs, Cd, Cdd, CO, Ct, Cb, Cbf. A pictorial representation of each of these functional groups is located in Figure 7-1. The two primary purposes of these functional groups are: a shortcut notation for entries in the database, and a means of telling the RMG algorithm how to construct the reverse reaction template, if necessary.
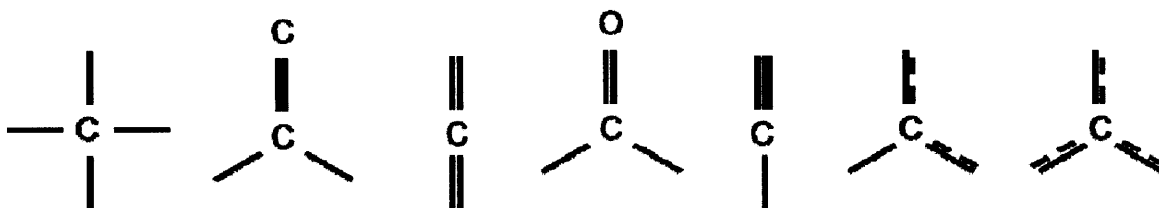
Figure 7-1: The RMG hardcoded "C" functional groups (from left to right): Cs (a carbon with four single bonds), Cd (a carbon with two single bonds and one double bond to a Carbon), Cdd (a carbon with two double bonds), CO (a carbon with two single bonds and one double bond to an Oxygen), Ct (a carbon with one single and one triple bond), Cb (a carbon with one single and two "benzene" bonds), and Cbf (a carbon with three "benzene" bonds).

The definition of Cs is a carbon atom with four single bonds attached to it (note, a free electron may replace a single bond), not the element cesium. This Cs nomenclature allowed multiple advantages in RMG, particularly regarding a simulation's runtime. First, this shorthand notation allowed for simpler definitions in the RMG database. For example, a "Cb" refers to a carbon within a single benzene bond, i.e. not the bridged carbon in naphthalene. Thus, in defining a benzylic hydrogen, one only needs the following definition:

1 H 0 {2,S}

2 C 0 {1,S} {3,S}

243

3 Cb 0 {2,S}

If one wanted to write the full definition of the benzylic hydrogen functional group, it would look like the following:

1 H 0 {2,S}

2 C 0 {1,S} {3,S}

3 C 0 {2,S} {4,B} {8,B}

4 C 0 {3,B} {5,B}

5 C 0 {4,B} {6,B}

6 C 0 {5,B} {7,B}

7 C 0 {6,B} {8,B}

8 C 0 {7,B} {3,B}

With the long list of nodes required to specify the benzylic hydrogen exactly, one can quickly see why representing the benzene ring as "Cb" would be beneficial. Another benefit of having the specific functional groups hardcoded into RMG is the runtime. Since the original RMG developer knew the functional groups would be utilized in the database, she could take advantage of this aspect in the software. For instance, when a new species is created (suppose the user supplied benzene), the RMG software will label each node with its functional group. This becomes very convenient as all of RMG's estimation routines (thermodynamics, kinetics, etc.) are based on identifying functional groups. With the manner that RMG was written, this action would be performed once. Then, any look-up within the RMG database would simply compare the functional groups of the molecule to the functional group definitions within the RMG tree.

Moreover, using the functional groups to compare species was a relatively fast process. Imagine RMG wished to check if formaldehyde and ethylene were the same species. Suppose further that RMG starts with the starred "*" atoms.

Formaldehyde

1 * CO 0 {2,S} {3,S}

2 H 0 {1,S}

3 H 0 {1,S}

Ethylene

1 * Cd 0 {2,D} {3,S} {4,S}

2 Cd 0 {1,D} {5,S} {6,S}

3 H 0 {1,S}

4 H 0 {1,S}

5 H 0 {2,S}

6 H 0 {2,S}

Using the functional group notation, RMG would immediately determine the two species are different, given that Cd and CO are mutually exclusive (Cd assumes carbon has a double bond to a carbon, whereas CO assumes carbon has a double bond to an oxygen). If we generalize the functional groups, i.e. change the Cd to C and change the CO to C, in addition to adding the oxygen atom exclusively, RMG would require many additional steps to determine the two species are different.

Despite the benefits of having hardcoded functional groups, there are disadvantages. As mentioned previously, this is not a robust means of handling chemistry, especially as the Green Group and our collaborators look to utilize RMG for systems other than hydrocarbons and oxygenated hydrocarbons. New functional groups would have to be constructed for each new element, and additional rules would need to be written into the software to recognize which set of functional groups each functional group is allowed to react to; this will be explored further in the section on aromatic chemistry. Furthermore, with how RMG was structured, it would be very difficult for even the most seasoned RMG developer to add a "multi-valent" element, e.g. nitrogen. The implementation would be extremely chemistry-dependent (can a "N3d" react to a "N5t"); however, this defeats the purpose of having the database separate from the software.

Another disadvantage of these functional groups is the extensibility regarding the database. For some elements, the RMG database has the {Cs,O} notation. What this list of functional groups is meant to represent is a non-hydrogen, non-delocalized group; essentially the neighboring atom must have only single bonds connected to it. Thus, when adding a new element to RMG, one should add the appropriate non-delocalized functional group to every instance of this set in the database, e.g. {Cs,O,N3s}. These unions of functional groups also crop up with aromatic structures. RMG's database assumes that aromatic structures will only consist of benzene rings. Re-consider our benzylic hydrogen example. Although the hydrogen abstraction kinetics stored in the database are specifically for benzyl radical abstracting from a stable species, the chemically-important information is that the abstracting radical is a resonantly-stabilized radical, next to an aromatic structure. Thus, if RMG needed to estimate the kinetics for 2-furanylmethyl abstracting a hydrogen from a stable species, a good approximation would be the kinetics of benzyl abstracting a hydrogen from that same species. The same would apply for 2-thiophenylmethyl, 2-(1H)pyrrolylmethyl, etc. Having a way to represent each of these species, without having to specify each structure exactly in the database, would enable RMG to utilize the beauty of the tree structure - kinetics estimation routine, i.e., that the chemistry (especially for hydrogen abstraction reactions), is primarily governed by the localized chemistry.

One final point to make, particularly with benzene chemistry as implemented in RMG, is that benzene bonds could not be created or destroyed (according to the RMG algorithm). The hardcoded rules in the RMG software only allowed a "Cb" functional group to remain a "Cb" or react to a "Cbf." Similarly, the only functional groups that could create a "Cb" were a "Cb" or "Cbf."

Fortunately, the solution to implement a robust means of handling both heteroatom and aromatic chemistry is the same: remove the element-specific functional groups.

7.2 REMOVING THE C/H/O HARDCODING FROM THE RMG DATABASE

As mentioned in the previous section, all functional groups can be expanded to their complete (i.e. definitions containing only chemical elements) definitions. In implementing this expansion of functional groups, a few important issues arose. To guide the discussion, consider expanding the functional group "Cs":

Cs

1 Cs 0

into the more robust definition:

Cs

1 C 0 {2,S} {3,S} {4,S} {5,S}

2 X Y {1,S}

3 X Y {1,S}

4 X Y {1,S}

5 X Y {1,S}

7.2.1 GENERAL FREEELECTRON GROUPS

In the robust "Cs" definition from above, notice that the FreeElectron field (the third entry in each row) for nodes 2-5 contains an unspecified "Y" group. Originally, I placed zeros in this field. However, this was not in accordance with the original "Cs" definition: a carbon with four single bonds attached to it. The original definition made no mention of the state of the node (element) attached to those four bonds. In order to preserve the definition of the original hard-coded groups, I changed Y to {0,1,2,2S,2T,3}:

Cs

1 C 0 {2,S} {3,S} {4,S} {5,S}

2 X {0,1,2,2S,2T,3} {1,S}

3 X {0,1,2,2S,2T,3} {1,S}

4 X {0,1,2,2S,2T,3} {1,S}

5 X {0,1,2,2S,2T,3} {1,S}

247

This allows the neighboring atoms to have one, two, or three free electrons associated with them (note: the "2S" and "2T" are two electrons with either a "singlet" or "triplet" spin multiplicity). However, before implementing this approach in the database, I needed to implement the approach in the software: RMG assumed each node had a single FreeElectron, and not a set of FreeElectrons, associated with it.

The first step was to have RMG read in the possibility of multiple FreeElectrons per node. A similar approach is already available for the ChemElement (the second entry in each node's line): the user is free to specify as many ChemElements are necessary, so long as they are enclosed in braces, e.g. {C, H, O}. Internally, RMG creates a HashSet of ChemElements instead of a ChemElement. I implemented a similar approach, where a HashSet of ChemElements will now be created in the event multiple ChemElements or FreeElectrons are passed into RMG. The details are straightforward and may be found in the RMG source code here: $RMG/source/RMG/jing/ChemParser.readChemNodeElement().

The other significant step in implementing multiple FreeElectrons was updating RMG's algorithm for determining if one node is a child of another node. Before my additions, RMG would check the order of the FreeElectron (the integer value corresponding to the number of FreeElectrons). If they were not the same, the function returned false. If they were the same, and the order was two, RMG then checked the spin multiplicities:

- "2" could be a parent to "2", "2S", and "2T"
- "2S" could be a parent to "2S" only
- "2T" could be a parent to "2T" only

The updated algorithm is no different: When comparing the FreeElectrons, RMG will check if each FreeElectron instance in the child node is found in the parent node. If all FreeElectron instances in the child node are accounted for in the parent, the algorithm returns true; otherwise, the algorithm returns false;

248

With the unspecified "Y" groups now resolved in our robust "Cs" definition, we turn to the unspecified "X" groups.

7.2.2 GENERAL "R" GROUPS

The question now becomes what replace the unspecified X groups with? The original implementation of RMG had a hardcoded "R" group to represent any chemical element or functional group. I agree with the idea of the "R" group but believe it can be made extensible; the "R" was hardcoded into the RMG software. I have constructed an additional database file, the purpose of which is to define whatever extensible functional groups you like. For example, if a RMG user was only concerned with C/H/O chemistry, their database file would appear as follows:

R　　　{C, H, O}

The idea is that the user can now define what "R" means. The default values will be assigned by the RMG developers, but the user is free to mix-and-match to their liking. Another example of a hardcoded functional group within RMG is "R!H," anything except a hydrogen. This hardcoding can easily be extended to the new database file:

R!H　　{C,O}

In this way, if the user wanted to change the definition of "R!H," wanted to add additional constrained functional groups, e.g. "R!C," or was not aware of the RMG syntax, it would be straightforward to edit and/or contribute to their own database.

Presently, the additional database file is called FGElements.txt (for _F_unctional _G_roup Elements) and is located in the home directory of any RMG database, e.g. $RMG/databases/RMG_database_MRH. The file currently consists of the following six functional groups.

R   {C,Cl,H,N,O,Si,S}

R!H   {C,Cl,N,O,Si,S}

R!C   {Cl,H,N,O,Si,S}

R_min2valency   {C,O,N,Si,S}

R_min3valency   {C,N,Si}

R_min4valency   {C,Si}

The premise of the first three functional group elements was discussed in this section. The reasoning for the last three groups are discussed forthwith.

7.2.3 GENERAL "R_MINXVALENCY" GROUPS

The idea of "R" and "R!H" could be extended to any functional group the user may imagine. One example that the current RMG database can benefit from is some way of representing an element that can participate in a double bond. The current notation, for C/H/O chemistry, is {CO,Cd}, meaning a carbon with a double bond, either to an oxygen or carbon atom. This definition would look like:

1 {CO,Cd} 0

Expanding this definition to include only elements or the previously discussed "R" and "R!H" functional group elements:

1 C 0 {2,D} {3, S} {4,S}
2 {C,O} 0 {1,D}
3 R 0 {1,S}
4 R 0 {1,S}

The above definition is extensible; if a RMG developer/user wished to add nitrogen chemistry, they could replace all {C,O} with {C,N,O}. Again, this is not the most robust manner of writing the definition, as every {C,O} in the RMG database would need to be changed to {C,N,O}. What I have proposed and implemented in RMG is the functional group "R_minXvalency". For the example above, I would define the following functional group in the new database file:

R_min2valency {C,O,N,S,Si,etc.}

The idea behind this functional group is that we do not want any halogens or hydrogen. If the user wished to include these, they may. This could be extended to R_min3valency – any element allowed to participate in triple bonds – and to any other specific functional

group the user may require: R!C, R!C!O, etc. By removing the hardcoding of these "R" functional groups from the RMG software, more of the chemistry assumptions are transparent to the user. Most importantly, this new syntax allows a user to quickly and easily add their own chemistry without having to be an RMG expert.

While the original intent of this new database file was to remove all chemistry-related hardcoding from the software, unfortunately, I found myself unable to do so for the following functional group.

7.2.4 GENERAL "R_NONDELOCALIZED" GROUP

As mentioned in a previous section, one of the special functional groups in the RMG database is {Cs,O}. This definition exists to represent a non-hydrogen, non-delocalized group. The chemically significant portion of this functional group means any non-hydrogen element with only single bonds attached to it. Unfortunately, this definition does not extend to its "full" definition without excluding possible delocalized elements. For example, if we wrote out the common features of the Cs and O functional groups, we would generate the following ChemGraph:

{Cs,O}
1 R!H 0 {2,S} {3,S}
2 R 0 {1,S}
3 R 0 {1,S}

The problem with this definition is that carbon fits node 1, yet a double-bonded carbon also matches node 1 (assuming the default valency of four for carbon). If we try to exclude this double bond, by defining a third single bond, this definition is now suitable for carbon, however it no longer defines oxygen (assuming the default valency of two, which is typical for gas-phase oxygen):

{Cs,O}
1 R!H 0 {2,S} {3,S} {4,S}
2 R 0 {1,S}

251

3 R 0 {1,S}
4 R 0 {1,S}

Furthermore, these specific attempts to resolve the non-delocalized chemistry do not consider other elements, i.e. elements with valencies other than two or four.

To resolve this, I have elected to **_hardcode_** a "R_nondelocalized" functional group in the RMG software. When reading in the database, RMG would normally expect to find an element or a general functional group element, as defined in the new external database files. However, in the event the "element" does not match any of these definitions, it will check the limited list of hardcoded functional groups (in the original RMG software, these functional groups included "R" and "R!H"). If it matches one of these hardcoded functional groups, the algorithm will continue as normal; if not, the software prints an error message and immediately terminates. This termination would occur within the first minute of any RMG simulation, so, when a RMG user is testing out new database files, they will quickly know if the RMG software is reading in the database properly.

The definition of this "R_nondelocalized" functional group is now hardcoded in the RMG software. However, un-hardcoding this functional group may also prove possible. For example, one may utilize the "Union" function already recognized by RMG to split a "R_nondelocalized" functional group into several children, each representing a particular valency. Using our {Cs,O} example from above, one could generalize this to the following Union:

{Cs,O}
Union(R_nondelocalized_2valency, R_nondelocalized_4valency)

R_nondelocalized_2valency
1 R_2valency 0 {2,S} {3,S}
2 R 0 {1,S}
3 R 0 {1,S}

252

R_nondelocalized_4valency

1 R_4valency 0 {2,S} {3,S} {4,S} {5,S}

2 R 0 {1,S}

3 R 0 {1,S}

4 R 0 {1,S}

5 R 0 {1,S}

The "R_2valency" and "R_4valency" wildcards would need to be defined in the new input file, similar to the wildcards discussed in the previous two sections. Although I've only shown examples for di- and tetra-valent elements, this method would be easily extensible to any valency. This methodology would also handle multi-valent elements, e.g. sulfur and nitrogen, as sulfur would be part of the R_2valency wildcard (sulfur cannot have more than 2 S-H bonds) and nitrogen would be part of the R_3valency wildcard (nitrogen cannot have more than 3 N-H bonds, at least in the gas phase).

Originally, I was also thinking of having a "R_delocalized" hardcoded functional group as well; in the original RMG database, these appeared as:

1 R 0 {2,S}

2 {Cd,CO,Ct,Cb} 0 {1,S}

However, there is a more robust means of accomplishing this task:

1 R 0 {2,S}

2 R_min3valency 0 {1,S} {3,{D,T,B}}

3 R_min2valency 0 {2,{D,T,B}}

The R_min3valency group allows any element with at least 3 valency (one of which must be involved in the single bond to node 1, and at least two of which must be involved in the bond to node 3) to capture the proposed "R_delocalized" group. RMG already recognizes the {D,T,B} syntax, so the two software hurdles were: (1) Having RMG read in the dictionary files correctly (i.e. recognizing what the acceptable functional group

elements are) and (2) Updating RMG's algorithm for determining if one node is a child of another node. These issues will be discussed in Section 7.3.

7.2.5 GENERAL "R_AROMATIC" GROUP

Originally, I proposed to include a "R_aromatic" hardcoded functional group, thinking this was a necessary (but unfortunate) hardcoding. However, in addition to having single ("S"), double ("D"), and triple ("T") bonds in its arsenal, RMG also recognizes a benzene ("B") bond, meant to represent aromatic bonds. Thus, rather than have the node (the elements or functional group elements) reflect the aromaticity, I elected to have the arc (the bond) reflect the aromaticity.

Recall the benzylic carbon example from before. The actual benzyl radical could be specified exactly. However, the kinetics listed in the database is probably meant to represent any methylene group adjacent to an aromatic (resonantly-stabilized) group. Thus, a furanyl, thiophenyl, pyrrolyl, etc. group should also fall into this group. The parent node of these groups would look like:

1 H 0 {2,S}

2 C 0 {1,S} {3,S}

3 R_min4valency 0 {2,S} {4,B} {5,B}

4 R_min2valency 0 {3,B}

5 R_min2valency 0 {3,B}

If the user has a more specific definition of the stable group, all which is needed is one additional level in the tree. This additional level would allow the user to distinguish between toluene, 2-methylfuran, 3-methylfuran, etc.

This choice of representing "benzene" carbons easily translates to the previously-hardcoded "Cb" and "Cbf" functional groups:

Cb

1 R_min4valency 0 {2,B} {3,B} {4,S}

2 R_min2valency 0 {1,B}

3 R_min2valency 0 {1,B}

4 R 0 {1,S}

Cbf

1 R_min4valency 0 {2,B} {3,B} {4,B}

2 R_min2valency 0 {1,B}

3 R_min2valency 0 {1,B}

4 R_min2valency 0 {1,B}

In the RMG database, most of the definition in the Dictionary.txt file are not complete structures, i.e. are functional groups. Thus, the RMG user/developer must take care in using the "B" bond when adding thermochemical, kinetics, frequency, or transport groups to the RMG database.

However, in terms of the input file where all species must be specified in full, the user should not be forced to decide what species are aromatic or not; the computer should be able to handle that, i.e., if a user inputs benzene in the Kekule form, our software should be robust enough to recognize it as aromatic and apply the correct thermochemistry parameters to it. This leads into a discussion of what is an aromatic species and how can a computer program determine this automatically.

7.2.6 AROMATICITY ALGORITHM

An aromatic species must have the following four properties

- Cyclic
- Delocalized, conjugated π system
- $4n+2$ electrons in the conjugated π system
- Planar

Looking at the RMG source code, there was certainly an attempt in the past to implement an isAromatic() function. However, the code has not been working since January 2006 (when I first joined the Green Group), and after further inspection, appears to be

incomplete. In the following sections, I describe how I implemented a robust (i.e. heteroatom-friendly) isAromatic() function within RMG.

7.2.6.1 RMG AROMATICITY: IS MOLECULE CYCLIC?

RMG has an algorithm to determine if a species is cyclic – the smallest set of smallest rings (SSSR) – and returns each cycle present in each species. This work was performed by previous RMG developers. If no cycles exist in the molecule of interest, the algorithm returns false.

7.2.6.2 RMG AROMATICITY: ARE 4N+2 ELECTRONS IN π SYSTEM?

To determine if 4n+2 electrons are present in the cycle, RMG iterates over all GraphComponents (Nodes and Arcs) in the cycle. For each GraphComponent:

- If the GraphComponent is an Arc (Bond), RMG added the Bond's "piElectrons" to a running counter. A single bond is assumed to contribute zero piElectrons, a double contributes two, a triple contributes two (two electrons contribute to the potential conjugated π system and the other two contribute to the p orbitals perpendicular to the potential conjugated p system and s orbitals), and a benzene bond contributes one.

- If the GraphComponent is a Node (Element)

  o RMG checks if the Element is a biradical (contains two FreeElectrons). If so, RMG counts two electrons towards the π system. This function is meant to capture the ability of unpaired electrons to contribute to π systems, e.g. cyclopentadienyl anion.

  o RMG checks if the Element is not a radical. If so, RMG calculates the elements available valency, determined by subtracting the bonding valency (i.e. a single bond contributes one, a double bond two, etc.) from the total valency (see Section 7.3.1). If the difference is at least two, RMG considers two to participate in the π system. This function is meant to capture the ability of heteroatom's lone pairs to contribute to π systems, e.g. furan, thiophene, and pyrrole.

256

If the sum of the running counter does not follow Hückel's rule, the algorithm returns false.

7.2.6.3 RMG AROMATICITY: IS π SYSTEM CONJUGATED?

If the algorithm has not failed at this point, the next check is whether the π system of electrons is conjugated.

Before the previous algorithm starts, a vector of Boolean variables, whose length is equal to the number of GraphComponents within the cycle, is initialized to false. During the algorithm, if an Arc or Node is determined to contribute at least one electron to the π system, the Boolean is set to true.

After the algorithm, RMG iterates over all nodes in the cycle:

- If the node contributed electrons to the π system, the algorithm continues
- If the node did not contribute electrons, the arcs (within the cycle) attached to that node are inspected. If neither of the arcs contributed electrons to the π system, the algorithm returns false. Otherwise, the algorithm continues.

If the algorithm has not failed by this point, the final criterion is checked.

7.2.6.4 RMG AROMATICITY: IS MOLECULE PLANAR?

At this current time, if RMG reaches this step, I assume the molecule to be aromatic, i.e. the question of planarity is assumed to always hold. While this will not always be true in nature, it is generally true, e.g. a five-member ring will distort its natural "puckered" envelope shape if the resulting strain will delocalize a set of 4n+2 electrons. Furthermore, RMG has no current, simple way of computing an accurate three-dimensional geometry for any given molecule. Greg Magoon has implemented some on-the-fly quantum chemical calculations within RMG, using PM3 calculations; perhaps this, or something similar, could be utilized in the future to test for the planarity criterion. However, at this point in time, the time to run a quantum chemistry job and perform the analysis is

relatively long and thus not amenable when expecting to run this "isAromatic" function ~40,000 times over the course of a simulation.

7.2.6.5 RMG AROMATICITY: KEKULIZING THE MOLECULE

Lastly, a "kekulize" function needed to be written. If the molecule is determined to be aromatic, RMG iterates over the arcs within the cycle. Each arc's value is changed to "B" to reflect that the bond is aromatic. This ChemGraph is then set as the primary ChemGraph for this molecule: in general, when RMG estimates the thermochemistry of a species with resonance isomers, it chooses the primary ChemGraph based on which resonance structure yields the lowest enthalpy of formation at 298 K. While this method should always produce the aromatic ChemGraph as the primary one, I have forced RMG to recognize this feature.

After setting the aromatic ChemGraph as the default value, and setting the previous ChemGraph as a resonanceIsomer, the kekulize() function is called:

- If the cycle contains an even number of arcs, the first is assigned as a single bond, the next as a double, and so on until all arcs have been assigned. This ChemGraph is added to the list of resonanceIsomers (if not already present). The procedure is then repeated, with the first Arc being assigned a double bond, the next a single bond, etc.

- If the cycle contains an odd number of arcs
    - o If the cycle contains a biradical: RMG already has a generateResonanceIsomers() function that handles FreeElectrons next to non-single bonds. In the event a biradical is present, this function, written by a previous RMG developer, is called.
    - o If the cycle does not contain a biradical: The lone pairs from a heteroatom thus contributed to the conjugated π system. RMG iterates over the arcs, starting from the Node with two single bonds attached to it (the heteroatom) and assigns bonds in an alternating fashion – double, single, double, single, etc. – for all but the final Arc; the final Arc is set to single.

258

The final node in the cycle is assigned a FreeElectron (technically, this would be an anion, but RMG cannot currently handle this). If this structure is valid (see Section 7.3.1), RMG will add it to the list of resonanceIsomers and generate potential further isomers using the generateResonanceIsomers() function mentioned previously. The direction of assigning the alternating bonds is then switched and the algorithm is repeated.

When comparing a species against all reaction family templates in the RMG database, all "resonance" structures are considered. When comparing an aromatic species against each reaction family in the RMG database, RMG first compares the primary (aromatic) structure. If any reactions are found, RMG utilizes these kinetics in its mechanism generation (and the remaining isomers are ignored). However, if RMG returns no hits for the primary structure, all other resonance isomers will be reacted against that particular RMG reaction family (and would normally be done for non-aromatic species).

7.2.6.6   RMG AROMATICITY: KNOWN ISSUES

One known issue to me is the molecule benzyne, Figure 7-2. The structure on the left is recognized as aromatic by the current algorithm; however, the structure on the right is recognized as being not aromatic (due to RMG counting 8 electrons in the π system). The algorithm could be updated, to check for consecutive double bonds, but at this time the algorithm as implemented cannot handle the benzyne structure properly.
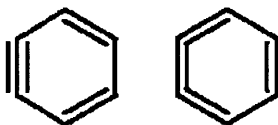
Figure 7-2: Two Lewis dot structure representations for the molecule benzyne.

259

7.3 REMOVING THE C/H/O HARDCODING FROM THE RMG SOFTWARE

7.3.1 CHEMICAL ELEMENTS AND NON-HARDCODED FUNCTIONAL GROUPS

All of the original RMG functional groups have been removed from the software. However, without these functional groups, RMG no longer knows what a "carbon," "hydrogen," or "oxygen" atom is. In thinking of applying RMG to any chemical element, I have created a new database file which allows a user to inform RMG of any chemical element they wish, given they specify the following information:

C   4   4   4   4   12.011   Carbon

- The first column is the element symbol. This one-or-two letter symbol needs to be consistent with the remaining RMG database files. The default values supplied in this file will be consistent with the standard RMG database.

- The second column is the maximum number of arcs allowed to/from this node; a double or triple bond is considered one connection.

- The third column is the maximum number of hydrogen "nodes" allowed to be connected to the central node.

- The fourth column is the maximum cumulative bond strength, or the total order of connections allowed to be connected to the central node, i.e. Carbon can have four arcs from it but they cannot all be triple bonds.

- The fifth column is the number of valence electrons

- The sixth column is the atomic mass, in units of amu.

- Any remaining information is considered a comment within the RMG software (the "//" double forward slash is interpreted within RMG as the delimiter for comments).

The second, third, fourth, and fifth columns allow RMG to handle any element, regardless of the complexity of its valency. Consider a larger list of potential elements:

C	4	4	4	4	12.011	Carbon
Cl	4	1	7	7	35.453	Chlorine
H	1	1	1	1	1.0079	Hydrogen
N	4	3	5	5	14.0067	Nitrogen
O	2	2	2	6	15.9994	Oxygen
Si	4	4	4	4	28.0855	Silicon
S	6	2	6	6	32.06	Sulfur

Consider carbon and silicon, two species in the same column on the periodic table. Chemically, these species are the same: a maximum valency of four, never have more than four connections, and never have more than four hydrogens attached to them. Now consider oxygen and sulfur, two elements that are also in the same column and thus have the same valency. While the chemistry of the two elements is similar, there are differences between the two, due to sulfur having unfilled d orbitals that can participate in π bonding. Notice the valency and maximum number of hydrogens columns are the same for oxygen and sulfur, however, the maximum number of connections and the maximum cumulative bond strength has been increased from two to six. This ability to allow six connections to sulfur is especially important in modeling desulfurization. One way to remove the sulfur from crude oil is through oxidation; if a species like dibenzothiophene can be oxidized twice to dibenzothiophene 5,5-dioxide (Figure 7-3), the molecule becomes polar enough with respect to the crude oil to phase separate.
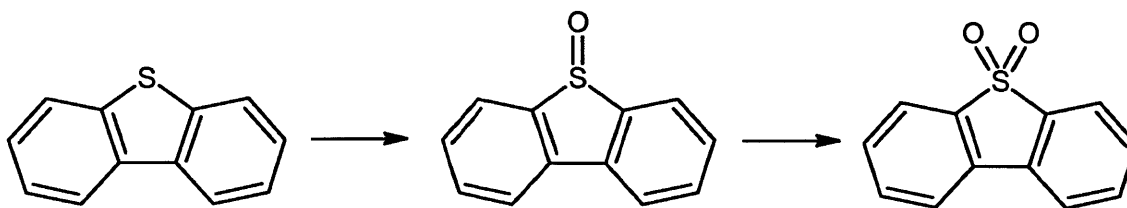
Figure 7-3: Oxidation of dibenzothiophene to dibenzothiophene 5,5-dioxide

One potential caveat is the perchlorate ion; although RMG cannot handle ionic chemistry at the moment (lack of thermochemistry in the database and no means of representing charges), chlorine does not behave as a "normal" gas-phase halide, i.e. one single bond and three sets of lone pairs. For perchlorate anion, the chlorine has four separate double bonds to oxygen.

Looking at the definition of chlorine:

Cl   4   1   7   7   35.453   Chlorine

This syntax would allow up to four different arcs to the chlorine atom (check), would still not allow more than one hydrogen be attached to any chlorine in any molecule (check), but would limit the chlorine total bond strength to 7 (check). Thus, the perchlorate anion could be modeled in RMG.

Perchlorate
1 Cl 0 {2,D} {3,D} {4,D} {5,S}
2 O 0 {1,D}
3 O 0 {1,D}
4 O 0 {1,D}
5 O 0 {1,S}

The caveat extends to any ionic species, e.g. hydronium ion. Clearly, the maximum number of connections and maximum number of hydrogens to any oxygen atom would need to be increased to three.

7.3.2 HARDCODED FUNCTIONAL GROUPS

As mentioned in the previous subsections, I found it necessary to include one hardcoded functional group within the RMG software: R_nondelocalized. The footprint of this functional group exists in two places:

- $RMG/source/RMG/jing/chem/FGElement.java: When RMG reads in the entire database at the beginning of a simulation, it verifies that all database files have the proper syntax. When reading in the chemical element token (the second column of every row within a ChemGraph), RMG expects to find:
    - an exact element, as defined in the new database file Elements.txt
    - a functional group, as defined in the new database file FunctionalGroups.txt

262

- a hardcoded functional group

The "R_nondelocalized" keyword is located here. This hardcoding simply allows RMG to read and store the specific functional groups to the assigned definition in the RMG database.

- $RMG/source/RMG/jing/chemUtil/Node.java: After RMG reads in the database, it also confirms if the structure of the tree (the parent-child relationship) is correct. In general, RMG will check the Element (in addition to the FreeElectron and bonding) field to confirm the tree's structure.

If "R_nondelocalized" is a parent, I updated the "isChild" function to check if the potential child:

- Is a Hydrogen atom. If so, the function returns false
- Has any Arcs that are not single bonds. If so, the function returns false.
- All other instances return true

If "R_nondelocalized" is a child, I updated the "isChild" function to check if the potential parent:

- Contains at least one non-Hydrogen atom. If not, the function returns false
- Has any Arcs that are not single bonds. If so, the function returns false.
- All other instances return true

These are now the only files containing any instances of hardcoded chemistry in the RMG software.

7.3.3 CALCULATING MOLECULAR FORMULA

The algorithm to calculate each species molecular formula has been updated according. Before, RMG would iterate over each node and pass through a series of if/elseif statements to determine what element the atom was. The nested if/elseif statement has

been replaced with a nested for loop, which loops over the elements listed in the Elements.txt file.

7.3.4 CALCULATING SYMMETRY NUMBERS

The algorithm to compute a molecule's symmetry numbers (RMG has several symmetry numbers it calculates) relied heavily on knowing the previously-hardcoded functional groups, e.g. "Cs". These algorithms have been updated accordingly, and are now robust in that the symmetry numbers are calculated based on the Arcs and Nodes attached to the central node; thus, when a new element is introduced to RMG (e.g. Nitrogen), this function returns the appropriate values as is.

7.4   ADDING FEATURES TO RMG

The following contains some features I have added to RMG over the years. Although documented in the source code, version control software, or the database, I decided to compile the main functions of each feature in one document.

7.4.1 PRIMARY THERMO LIBRARY

This feature was available to the user before I joined the group. However, I have expanded both the software and the database aspects. Firstly, a user may specify multiple libraries now. In the past, only a single library would be read, and the user would need to add all of their preferred thermochemistry values to a single file. While nothing is technically wrong with this, it was inconvenient when trying to document many different distinct datasets within one file. For instance, one aspect I have added to the database is the PrIMe recommended species thermochemistry. Rather than have to replace the RMG default H and H2 thermochemistry, I now have the PrIMe recommended values in its own separate folder.

One question that may come up is what happens if the same species is listed in multiple families. Firstly, if the same species ChemGraph is present in the same library, the RMG software will fail and state which species are in duplicate. The user may then fix the database as necessary. However, if the same species appears in multiple libraries, the

264

order of the libraries takes precedence. In this respect, the user should be aware of what is present in each library. However, in the reported chem.inp file, the source of the thermo is tagged with the thermochemistry of the species (in the THERMO section).

7.4.2 MAX ELEMENTS PER SPECIES

Over the last six years, one of RMG's biggest problems has been the memory allocation: jobs will typically fail not because of a bug, but because the mechanism becomes so large that the memory required to call external programs causes RMG to run out of memory. One idea (very early on) was to give the user the option to restrict the size of the species generated in the mechanism. For instances if one were interested in how a fuel burns (i.e. breaks down) and not in soot formation, there is no need to generate and store species with 50 carbon atoms (e.g. if your fuel only contains 4 carbons atoms). Thus, the user could override the default max elements per molecule (which was hard-coded in RMG) in order to restrict the number of species that were generated in an RMG run (which is the most memory consuming aspect of any RMG run).

7.4.3 RESTART FILES

Another issue that arose when group members ran RMG was that jobs would fail for silly reasons (the RMG.jar file was re-built during the middle of a job, the server would go down for no reason, the maximum allotted time for the job was up, but the simulation was still running, etc.). In these cases, it was very inconvenient to restart the entire job, from scratch. What would be nice was to have "restart" files that would quickly (in comparison to the jobs total runtime) restore the RMG simulation to its last known (and stable) state. Thus, I resurrected the Restart files. However, many of the unused functions were not obsolete, as RMG had changed aspects of what it stores for reactions and species. Furthermore, there was nothing to save the pressure-dependent networks, which is a main staple of the current version of RMG.

For the species, the only information that is written to these restart files are the chemkinName (a 16 or less ASCII string that assigns a unique name to every species in

the model, be it core or edge) and the ChemGraph. Although many other properties are associated with a species – thermochemistry, transport properties, frequencies, etc. = estimating these properties are relatively fast; essentially, it was more trouble (from a time and memory standpoint) to write this information to a file (but more importantly, to read it from a file). For reactions, the structure was stored (reactants, products, and whether it was reversible or irreversible), along with the kinetics. One reason the kinetics were also stored (whereas the species auxiliary information was not) is because of the method RMG uses to fill out the trees in the kinetics database. Since not all of the lists or hashMaps are linked, the storing and subsequent reading of the nodes could be different, leading to ever-so-slightly different kinetics from run-to-run. This has never been noticed for species thermochemistry. However, it is the source (99% certain) or RMG predicting a different number of species and reactions from run to run, even though the software, database, and input file are identical. For the pressure-dependent networks, all path reactions are saved. For the net and non-included reactions, the direction that RMG has in memory during its simulation is also stored. The computed micro-canonical rate coefficients, k(T,P), and the fitted Chebyshev polynomial coefficients, are also stored. These are stored because, in general, reading these values are much shorter than having to re-run a fame network (especially as the networks become large).

The restart files have been shown to reproduce successful RMG simulations (meaning, a RMG job completed without error and the restart files were saved. They were then read-in with a new RMG job, with the same input file, and produced the same results). It has also been successful at replicating a prematurely-killed job: a simulation was started, asking for restart files to be saved, and manually stopped before a successful termination. The restart files were then read-in, with the same input file, and were able to successfully restore the last known stable conditions before the first model expansion step took place.

The restart files can also act as a Seed Mechanism. Since the current implementation of "Seed Mechanisms" cannot interpret PLOG or CHEB pressure-dependent rate coefficient expressions, but the Restart files can, it is a convenient way to have a Seed Mechanism containing pressure-dependent kinetics. The restart jobs could also be used to test

266

different reaction systems, where the equivalence ratios were tested. However, this feature is now a standard output of RMG: a list of concentrations may be supplied to the input file and those unique conditions will be crossed with all pressure and temperatures listed by the user in the Temperature and Pressure Model input lines.

7.4.4 CHECKING THE HIGH-P LIMIT KINETICS

Another option available to the user is whether the pressure-dependent simulations should be re-run, with additional grains (decreased grain size). This options checks the computed $k(T,P)$ against the $k_\infty(T)$ for the largest pressure solved by the fame code. If the computed $k(T,P)$ is more than two times the $k_\infty(T)$ value, the number of grains in increased and the fame call is re-run. This is continued until the computed $k(T,P)$ is less than two times the $k_\infty(T)$, or until 1000 grains are reached. After this, the pressure-dependent calculations would take an inordinate amount of time to solve the PES.

Two caveats about this option. The first is that the highest pressure solved for by fame in its calculations may not be the "high-P" limit: for systems such as H2, a pressure of 300 atm is still in the falloff region. Another potential problem can occur if the k vs. P plot does not follow the typical falloff curve. If there is a local maxima, this check is not helpful. Both of these could be reasons why the computed $k(T,P)$ is always greater than 2 times the $k_\infty(T)$ value. At the very least, these extra calculations do not hurt the accuracy of the fame calculations; the only negative is that the runtime will increase.

Note: this check is only performed for the path reactions list. All other reactions have a "zero" high-p limit, because there would be no well hopping.

7.4.5 RUN-TIME AND MEMORY PROFILING

Years ago, I performed a time and memory profiling of RMG. At the time, a typical RMG simulations would spend half of its time in one function: isStructureFordden(). The purpose of the function is the check if any subgraph of the just formed ChemGraph is a forbidden group, as defined in the external RMG database. The purpose of the

forbidden groups is that the thermochemistry of these functional groups is not estimated well by RMG and thus we do not want to include them in our model.

What was surprising (at the time), was that a simulation would spend 50% of its time doing this search. In particular, 7 of the 11 forbidden groups contained at least one oxygen atom; however, for a pyrolysis simulation of 1,3-hexadiene, we were still checking every ChemGraph against every one of the forbidden groups. I updated the code to first check whether each ChemGraph passed to the function has the minimum # of carbons, oxygens, and radicals as the about-to-be-compared-against forbidden group; these values are computed once per simulation, when reading in the forbidden groups. If so, then a full ChemGraph comparison could be performed. This one change drastically reduced the runtime of a typical RMG simulation (approximately by half). Afterwards, the time profiling revealed that comparing ChemGraphs with one another, when RMG is checking whether the ChemGraph already exists in the model, is the function where a simulation spends most of its time.

Another idea that I had (but did not implement; Dr. Richard West implemented this in the Java code) was on addressing this ChemGraph comparison with all other ChemGraphs already present in the model. For instance, if we take the H-abstraction family as an example: when a radical and all core species are passed to the function, many different radicals may be produced (from the stable core species). However, regardless which stable species is the co-reactant, the radical will always produce R-H. Thus, RMG would check the following species against those already present in the model: R-H, R1, R-H, R2, R-H, etc. Thus, I knew that every other species (the R-H, derived from the R radical) already exists in the model. However, we were checking all N# R-H species against the entire SpeciesDictionary. For reaction family templates like H-Abstraction and Disproportionation, this would also be true, for one of the products. The implementation by Dr. West was quite clever: have a small queue in the SpeciesDictionary class that stores the last two new species in the mechanism. Check the proposed species against these two, before checking it against the entire SpeciesDictionary. This fix accomplished my concerns, and cut the runtime down by a factor of 3.

Thus, with these two changes, the runtime for a non-pressure-dependent RMG simulation was cut by a factor of 6!

7.4.6 SEED MECHANISM AND PRIMARY KINETIC LIBRARY

When I joined the group, there was a "Seed Mechanism" option. It was called Primary Reaction Library at the time. The idea is that a user does not have to start a RMG simulation from scratch: they can instead start with an entire mechanism (species and reactions).

CHAPTER 8
RECOMMENDATIONS FOR FUTURE WORK

In addition to the recommendations made at the end of each chapter, here are further thoughts on constructing reaction mechanisms automatically, and on future work on the butanol isomers system.

8.1 BUTANOL

Although all efforts have been made to comprehensively compare our butanol model's predictions against all known datasets, here is a list of the known experimental butanol datasets that the model has not been validated against yet.

Note: The butanol model is either too large, or its kinetics are too stiff, to converge in the CHEMKIN reactor model for flames, including the Flame Speed Calculation, Opposed-Flow Diffusion Flame, and Extinction Strain Rate models. However, recent work by Dr. Ray Speth in the Green Group on a 1-d premixed and opposed-flow flame solver is proving promising: it has been demonstrated by Dr. Speth and me that the solver can solve the mechanism for both the premixed and opposed-flow flame solvers. However, as Dr. Speth's solver utilized the open-source Cantera solver, the mechanism's pressure-dependent rate coefficients (primarily in the form of Chebyshev polynomials, with a few in the pressure-dependent Arrhenius format) must be fit to a modified Arrhenius expression at the pressure-of-interest. Several of the experiments listed below are for flame experiments, and thus refer to this paragraph for the reason behind no model comparisons at this time.

- Extinction strain rates of n-butanol by Veloo et al. [236]: Please see the above paragraph for more details.
- Extinction strain rates of sec-, iso-, and tert-butanol by Veloo et al. [261]: Please see the above paragraph for more details.
- Laminar burning velocities of n- and iso-butanol by Liu et al. [262]: Please see the above paragraph for more details.

271

- Opposed-flow diffusion flame speciation data for tert-butanol [263]: Please see the above paragraph for more details.

- Variable-pressure flow reactor speciation data for tert-butanol [263]: Although this reactor set-up may be modeled in CHEMKIN, particularly with the Plug Flow Reactor model, the initial fuel composition to supply as input is not straightforward. The inlet of the Princeton VPFR is turbulent and the experiments show that reactions occur in this section; the code utilized by the Dryer group in their modeling of the reactor is not available to the public, however their algorithm was recently reported [264].

- Low-pressure speciation data for n- [168] and iso-butanol: The model's predictions and pathway analysis for the n-butanol flames have been presented at the 7th US National Combustion Meeting and will be included in a manuscript in preparation. The iso-butanol flame data is unpublished, but the data and the model predictions and pathway analysis will be included in another manuscript in preparation. As the unpublished data is not mine to present, I will not include it in this document.

- Shock tube ignition delays for all butanol isomers, including OH and H_2O speciation data: The model's predicted ignition delays and pathway analysis for all four butanol isomers will be presented at the 7th International Conference on Chemical Kinetics (ICCK) [231]. As the unpublished data is not mine to present, I will not include it in this document.

- Rapid compression machine ignition delays for 2- and tert-butanol: The predictions for the 2- and tert-butanol isomer will also be presented at the 7th ICCK. As the unpublished data is not mine to present, I will not include it in this document.

- Opposed-flow diffusion flame speciation data for n- and iso-butanol [258]: Please see the above paragraph for more details.

- Pyrolysis of iso-butanol near 1 bar, performed at the Laboratory for Chemical Technology under Prof. Kevin M. Van Geem: The model's predictions and pathway analysis will be included in a manuscript in preparation. As the unpublished data is not mine to present, I will not include it in this document.

Most of this data has been generated by our collaborators in the CEFRC. This is one benefit of having a group of PIs focused on one system of interest: many experimental and theoretical calculations can be generated in a short amount of time. The limiting factor then becomes running dozens of reactor models (normally in CHEMKIN) for a detailed reaction mechanism and analyzing the results.

8.2 CONSTRUCTING REACTION MECHANISMS

In building the butanol reaction mechanism, three non-butanol related issues arose:

The small molecule chemistry

Pressure-dependence

RMG's kinetics estimation routines

8.2.1 PRESSURE DEPENDENCE

Josh Allen in the Green Group has done excellent work on addressing pressure-dependence in RMG. I believe the algorithm to be robust and reliable. In particular, it has helped my modeling efforts with butanol when comparing the results to the low-pressure (15 – 25 torr), laminar, pre-mixed flames of Dr. Nils Hansen. Comparing the model's predictions with the data quickly identified which reactions needed k(T,P) estimates, rather than the k_∞(T) estimates. Chemical activation also helped explain the model's initial failures to capture the ethenol-to-acetaldehyde ratio: the model was initially predicting ratios much higher than observed in experiment. In the original model, ethenol would be formed directly from a radical of n-butanol and would then tautomerize to acetaldehyde. This led to large predictions for ethenol. Once chemical activation was introduced, i.e. ethenol + H = acetaldehyde + H, much more of the ethenol was reacting to acetaldehyde, as expected.

8.2.2 SMALL MOLECULE CHEMISTRY

The most important aspect, moving forward, in constructing kinetic models for any compound is resolving the small molecule chemistry. Each modeling group (the Ranzi

group, the Curran group, the LLNL models, GRI-Mech, etc.) has their own small molecule chemistry, from which to build larger reaction mechanisms. The source of each of these small molecule chemistries is varied, but the commonality of each is that the parameters were "tuned" to match the experiments from the respective groups, i.e. the Curran C_{4-} chemistry predicts their data well, the LLNL C_{4-} chemistry predicts their data well, etc. The problem with this "postdictive" chemistry implementation is that one group's C_{4-} model cannot predict every other group's C_{4-} experiments. This phenomenon clearly indicates that there are deficiencies with the model, the experiments, or possibly both. However, by "tuning" the parameters, everything is swept under the rug and it then becomes the task of all future modelers to explain why their new model cannot reproduce the dataset of group X as well as group X's model.

In our butanol model, the original small molecule chemistry came from the PrIMe Warehouse's recommended kinetics, which essentially was the GRI-Mech 3.0 mechanism. Even for the GRI-Mech 3.0 mechanism, whose parameters were tuned to best predict their 26 validation targets, there are known limitations, e.g. the mechanism does not predict the characteristics of rich flames particularly well. Furthermore, the GRI-Mech 3.0 mechanism was last validated in the late 1990's, leaving the model untested against many new experimental datasets.

In my work on constructing a reaction mechanism for the butanol isomers, I have replaced several dozen rate coefficients from the GRI-Mech 3.0 base chemistry with more recent experimental measurements and quantum chemical calculations; the updated kinetics and citations may be found in the chem.inp file and a summary is provided in Section 5.3.4 of this thesis. Does updating these kinetics invalidate the rest of the GRI-Mech 3.0 mechanism? Technically, yes. However, the first step in using the GRI-Mech 3.0 base chemistry was to remove the C_3H_7 and Nitrogen chemistry, Section 5.3.4. One important thing to remember is that the model was not sensitive to most of the parameters for the reactors simulated; most of the examples discussed in 0 and 0 were high-temperature chemistry, where the concentration of the radical pool is dominated by the $H+O_2=OH+O$ reaction kinetics.

Moreover, the speciation datasets – jet-stirred reactor, opposed-flow diffusion flame, and pyrolysis experiments – were the most beneficial to the model validation process. From experience (i.e. comparing the many different butanol mechanism's thermochemical parameters), I have found that many sets of values for a few key parameters can predict combustion properties, e.g. ignition delay or laminar flame speed, reasonably well. However, when comparing these models to speciation datasets, it becomes clear these models are valid over a narrow range of operating conditions, and can only predict some combustion characteristics accurately (namely, those that were included in the model's validation targets).

Dr. Richard West of the Green Group has clearly demonstrated the effect of utilizing different chemistry models when constructing a reaction mechanism for methyl formate [265]. Using the RMG software to construct a methyl formate kinetic model, using the GRI-Mech 3.0 and Glarborg C_0-C_1 chemistry as Seed Mechanisms, two proposed mechanisms were generated and compared against the high-temperature shock tube ignition delay measurements of Dooley et al. The mechanisms contained different numbers of species and reactions, because the rate coefficients (and thereby the characteristic flux within the RMG simulation) differed between the two models; each contained ~100 species, which is a reasonably sized model for methyl formate (molecular formula $C_2H_4O_2$) combustion. The difference in ignition delay predictions from the two models was drastic, even over a limited temperature and pressure range. This observation was further tested against the variable-pressure flow reactor of Dooley et al., showing differing predicted speciation data as a function of length down the reactor. The conclusion of Dr. West's work was that it is essentially impossible to know which methyl formate chemistry is correct without first knowing the small molecule chemistry.

The Combustion Energy Frontier Research Center (CEFRC) has made resolving the small molecule thermochemistry and kinetics their top priority for the year 2011. Shamel Merchant of the Green Group will be working on the modeling aspect of this work, including extending and improving the small molecule chemistry work from my

275

published butanol mechanism. One example Shamel used in motivating the problem was the HO$_2$+OH=H$_2$O+O$_2$ reaction, see Figure 8-1. Even for a reaction containing only hydrogen and oxygen atoms, there is still a large discrepancy in the rate coefficient. In particular, the Glarborg et al. kinetics is a summation of three modified Arrhenius expressions; this expression is noticeably different from the other three estimates at temperatures above 700 K. Even the difference between the Baulch et al. kinetics and the GRI-Mech 3.0 kinetics can be substantial, if the reaction mechanism is sensitive to this reaction's kinetics; a difference in log$_{10}$k(T) of 0.3 can result in an uncertainty in predicted concentration of a factor 2, if the normalized sensitivity coefficient is O(1). A factor of 2 difference in concentration of the radical OH or HO$_2$ would predict completely different chemistry.
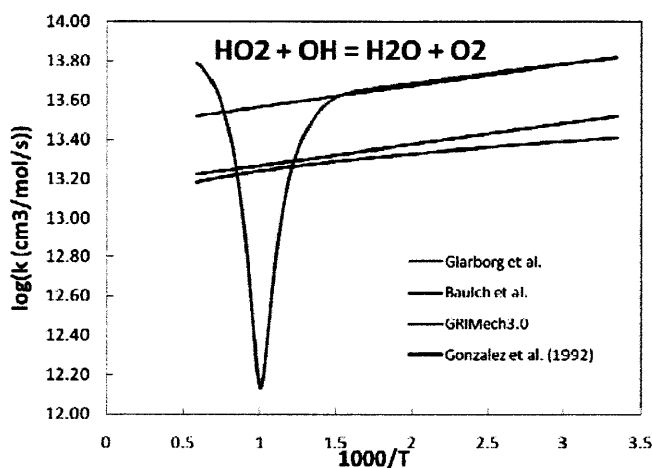
Figure 8-1: Rate coefficient (log$_{10}$ space) of the reaction HO$_2$ + OH = H$_2$O + O$_2$ as a function of temperature, from four different studies.

Another specific example of small molecule chemistry affecting the butanol predictions is for the CO and CO$_2$ mole fraction profile predictions as a function of temperatures in the jet-stirred reactors. The CO$_2$ mole fraction was especially sensitive to the following reactions:

OH + CO = H + CO2

HO2 + CO = OH + CO2
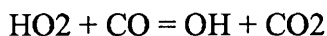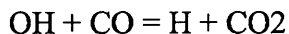
Both of these reaction's rate coefficients come from the GRI-Mech 3.0 mechanism. For both reactions, it is difficult to imagine neither reaction having significant pressure-

276

dependent effects as both are chemically-activated networks; the kinetics reported by GRI-Mech 3.0 may have come from RRKM-ME calculations, but the reported kinetics were for the pressure of interest (probably atmospheric). Thus, it would be beneficial to have a k(T,P) for these reactions. If using RMG to compute the k(T,P), in particular the PopulateReactions module, one could supply the hydrocarboxyl (HO-C*=O) and hydroperoxyoxymethyl (HO-O-C*=O) radicals in the input file. When using RMG's estimates for the species thermochemistry and high-pressure limit rate coefficients (both of which should be scrutinized, as group additivity methods are known to fail for small molecule) in the PopulateReactions class and applying these generated kinetics in the butanol mechanism, drastically different CO and CO_2 curves are predicted, while the remaining species profiles are relatively unchanged.

8.2.3 VALIDATING THE RMG DATABASE

I believe the RMG algorithm is currently sufficient to generate detailed, comprehensive reaction mechanisms for any hydrocarbon or oxygenated hydrocarbon system. Once the small molecule chemistry is resolved, I believe the next step a future RMG student should undertake is continuing to validate the RMG database. From my work on validating the H-abstraction reaction family, most of the discrepancies came from an RMG "estimate," meaning the exact nodes were not found when searching the tree. The H-abstraction reaction family is one of the most highly-populated families, so if a large number of estimates were found for this family, many more will exist for the other reaction families.

I believe the validation method used in my study of the H-Abstraction reaction family, i.e. using the PrIMe Warehouse's kinetic data as a sanity check, will be sufficient for other families as well, especially the R_Addition_MultipleBond (the reverse of β-scission) and intra_H_migration families. Performing quantum chemistry and TST calculations will allow us to fill-in the RMG database gaps, but it will also allow RMG users and developers to know the exact species from which the kinetics were derived. In many instances in the RMG database, it is unclear what species the node name actually refers to.

277

Possible species can be proposed, but if one wanted to implement a group additivity scheme, the entire structure of each reactant must be known.

8.2.4 OTHER "BELLS AND WHISTLES"

One idea I've heard from my fellow developers through group meetings or discussion over tea is adding an ionic charge field for each atom in the ChemGraph. From a software point-of-view, I believe this idea would be relatively straight-forward to implement; an RMG developer could follow the syntax of the "FreeElectron" field as a start. The current reaction family templates would work as is; any new reaction family specifically tailored for ionic chemistry would need to add a new reaction recipe keyword, e.g. "GAIN_ION" and "LOSE_ION." The algorithm for determining resonance structures would also need to be augmented, to include ion chemistry. The biggest challenge in adding ion chemistry, in my humble opinion, would be populating the database with enough parameters to have meaningful results.

8.3   CLOSING REMARKS

As the world looks for alternative fuel sources in the near-future, the possible feedstocks will become increasingly diverse – hydrocarbons have been used extensively in the past, and oxygenated hydrocarbons are now gaining traction as a promising fuel additive and/or alternative. Each of these new feedstocks will bring additional challenges, particularly with emissions – the world's current concerns are with CO_2, NO_x, SO_x, and soot formation.

Many potential fuel alternatives and/or additives will be discovered over the coming years. Quickly screening these potential fuel alternatives will be key in developing a sustainable fuel for the coming decades. Although experimental validation will always have the final say, possessing a model that can accurately predict any fuel's combustion properties and emissions will allow fewer experiments to be run in the laboratory – instead, they will be run on a computer!

This thesis presented my work on upgrading one such tool that constructs reaction mechanisms automatically, the Reaction Mechanism Generator (RMG) software. In January 2006, the RMG software could model any species containing carbon, hydrogen, and oxygen; these elements were hard-coded into the software and the database. Using this software, I constructed a validated kinetic model for the combustion of the butanol isomers. Through my studies, I have updated hundreds of species thermochemistry and reaction kinetics in the RMG database. Although my studies did not include the modeling of NO_x or soot formation, I am leaving the RMG software in a state where both are possible: RMG no longer contains hard-coded chemistry – all of the chemistry is in external files that are easily extensible to any element of interest – and can now recognize, create, and destroy aromatic bonds.

Hopefully, with the additions I have made to the RMG softare over the years, any future modeler can keep pace with the ever-expanding potential fuel alternatives.

CHAPTER 9
BIBLIOGRAPHY

1.   OECD/IEA, Transport, Energy and CO2 - Moving Towards Sustainability, International Energy Agency, Paris, France, 2009.

2.   L. Michaelis; M. L. Menten, Biochemische Zeitschrift 49 (1913) 333-369

3.   H. Lineweaver; D. Burk, Journal of the American Chemical Society 56 (1934) 658-666

4.   A. V. Hill, J. Physiol. (Lond.) 40 (1910) iv-vii

5.   F. O. Rice; K. F. Herzfeld, Journal of the American Chemical Society 56 (1934) 284-289

6.   C. K. Westbrook; W. J. Pitz; J. E. Boercker; H. J. Curran; J. F. Griffiths; C. Mohamed; M. Ribaucour, Proceedings of the Combustion Institute 29 (2003) 1311-1318

7.   C. K. Westbrook; W. J. Pitz; H. J. Curran, Journal of Physical Chemistry A 110 (2006) 6912-6922

8.   C. K. Westbrook; W. J. Pitz; O. Herbinet; H. J. Curran; E. J. Silke, Combustion and Flame 156 (2009) 181-199

9.   C. K. Westbrook; W. J. Pitz; P. R. Westmoreland; F. L. Dryer; M. Chaos; P. Osswald; K. Kohse-Hoinghaus; T. A. Cool; J. Wang; B. Yang; N. Hansen; T. Kasper, Proceedings of the Combustion Institute 32 (2009) 221-228

10.   Lawrence Livermore National Laboratory Mechanisms. https://www-pls.llnl.gov/?url=science_and_technology-chemistry-combustion-mechanisms (December 10, 2010),

11.   S. Dooley; M. P. Burke; M. Chaos; Y. Stein; F. L. Dryer; V. P. Zhukov; O. Finch; J. M. Simmie; H. J. Curran, International Journal of Chemical Kinetics 42 (2010) 527-549

12.   D. Healy; N. S. Donato; C. J. Aul; E. L. Petersen; C. M. Zinner; G. Bourque; H. J. Curran, Combustion and Flame 157 (2010) 1526-1539

13.   D. Healy; N. S. Donato; C. J. Aul; E. L. Petersen; C. M. Zinner; G. Bourque; H. J. Curran, Combustion and Flame 157 (2010) 1540-1551

14.   K. Yasunaga; F. Gillespie; J. M. Simmie; H. J. Curran; Y. Kuraguchi; H. Hoshikawa; M. Yamane; Y. Hidaka, Journal of Physical Chemistry A 114 (2010) 9098-9109

15.   Combustion Chemistry Centre Mechanisms. http://c3.nuigalway.ie/mechanisms.html (December 10, 2010),

16.   H. Wang; X. You; A. V. Joshi; S. G. Davis; A. Laskin; F. Egolfopoulos; C. K. Law USC Mech Version II. High-Temperature Combustion Reaction Model of H2/CO/C1-C4 Compounds. http://ignis.usc.edu/USC_Mech_II.htm (December 10, 2010),

17.   H. Wang; E. Dames; B. Sirjean; D. A. Sheen; R. Tangko; A. Violi; J. Y. W. Lai; F. N. Egolfopoulos; D. F. Davdison; R. K. Hanson; C. T. Bowman; C. K. Law; W. Tsang; N. P. Cernansky; D. L. Miller; R. P. Lindstedt A high-temperature chemical kinetic model of n-alkane (up to n-dodecane), cyclohexane, and methyl-, ethyl-, n-propyl and n-butyl-cyclohexane oxidation at high temperatures, JetSurF version 2.0. http://melchior.usc.edu/JetSurF/JetSurF2.0

18. F. Battin-Leclerc EXGAS. http://www.ensic.inpl-nancy.fr/DCPR/Anglais/GCR/softwaresdescription/exgas.htm (December 10, 2010),

19. M. H. Hakka; H. Bennadji; J. Biet; M. Yahyaoui; B. Sirjean; V. Warth; L. Coniglio; O. Herbinet; P. A. Glaude; F. Billaud; F. Battin-Leclerc, International Journal of Chemical Kinetics 42 (2010) 226-252

20. H. Wang; S. J. Warner; M. A. Oehlschlaeger; R. Bounaceur; J. Biet; P. A. Glaude; F. Battin-Leclerc, Combustion and Flame 157 (2010) 1976-1988

21. P. A. Glaude; O. Herbinet; S. Bax; J. Biet; V. Warth; F. Battin-Leclerc, Combustion and Flame 157 (2010) 2035-2050

22. E. Ranzi MAMOX. http://creckmodeling.chem.polimi.it/kinetic.html (December 10, 2010),

23. E. Ranzi; A. Frassoldati; T. Faravelli; A. Cuoci, Energy & Fuels 23 (2009) 5287-5289

24. A. Frassoldati; A. Cuoci; T. Faravelli; U. Niemann; E. Ranzi; R. Seiser; K. Seshadri, Combustion and Flame 157 (2010) 2-16

25. A. Frassoldati; A. Cuoci; T. Faravelli; E. Ranzi, Combustion Science and Technology 182 (2010) 653-667

26. E. S. Blurock, Journal of Chemical Information and Computer Sciences 35 (1995) 607-616

27. E. S. Blurock, Journal of Chemical Information and Computer Sciences 44 (2004) 1336-1347

28. E. S. Blurock, Journal of Chemical Information and Computer Sciences 44 (2004) 1348-1357

29. G. Moreac; E. S. Blurock; F. Mauss, Combustion Science and Technology 178 (2006) 2025-2038

30. Y. Muharam; J. Warnatz, Physical Chemistry Chemical Physics 9 (2007) 4218-4229

31. L. J. Broadbelt; S. M. Stark; M. T. Klein, Industrial & Engineering Chemistry Research 33 (1994) 790-799

32. L. J. Broadbelt; S. M. Stark; M. T. Klein, Industrial & Engineering Chemistry Research 34 (1995) 2566-2573

33. L. J. Broadbelt; S. M. Stark; M. T. Klein, Computers & Chemical Engineering 20 (1996) 113-129

34. R. J. Quann; S. B. Jaffe, Industrial & Engineering Chemistry Research 31 (1992) 2483-2497

35. R. J. Quann; S. B. Jaffe, Industrial & Engineering Chemistry Research 32 (1993) 1800-1800

36. R. J. Quann; S. B. Jaffe, Chemical Engineering Science 51 (1996) 1615-&

37. T. Ogura; Y. Nagumo; A. Miyoshi; M. Koshi, Energy & Fuels 21 (2007) 130-135

38. T. Ogura; Y. Sakai; A. Miyoshi; M. Koshi; P. Dagaut, Energy & Fuels 21 (2007) 3233-3239

39. Y. Sakai; A. Miyoshi; M. Koshi; W. J. Pitz, Proceedings of the Combustion Institute 32 (2009) 411-418

40. A. Miyoshi, International Journal of Chemical Kinetics 42 (2010) 273-288

41. E. R. Ritter; J. W. Bozzelli, International Journal of Chemical Kinetics 23 (1991) 767-778

42.   S. Pierucci; E. Ranzi, Computers & Chemical Engineering 32 (2008) 805-826
43.   S. Rangarajan; A. Bhan; P. Daoutidis, Industrial & Engineering Chemistry Research 49 (2010) 10459-10470
44.   A. J. Adamczyk; M. F. Reyniers; G. B. Marin; L. J. Broadbelt, Journal of Physical Chemistry A 113 (2009) 10933-10946
45.   A. J. Adamczyk; M. F. Reyniers; G. B. Marin; L. J. Broadbelt, Physical Chemistry Chemical Physics 12 (2010) 12676-12696
46.   A. J. Adamczyk; M. F. Reyniers; G. B. Marin; L. J. Broadbelt, CHEMPHYSCHEM 11 (2010) 1978-1994
47.   IUPAC: Subcommittee for Gas Kinetics Data Evaluation. http://www.iupac-kinetic.ch.cam.ac.uk/ (December 10, 2010),
48.   The Master Chemical Mechanism. http://www.iupac-kinetic.ch.cam.ac.uk/projects.html (December 10, 2010),
49.   J. Song. Building robust chemical reaction mechanisms: Next generation of automatic model construction software, Ph.D. thesis. Massachusetts Institute of Technology, Cambridge, MA, 2004.
50.   D. M. Matheu. Integrated pressure-dependence in automated mechanism generation: a new tool for building gas-phase kinetic models. Massachusetts Institute of Technology, Cambridge, 2003.
51.   P. E. Yelvington. Design of a viable homogenous-charge compression-ignition (HCCI) engine: a computation study with detailed chemical kinetics. Massachusetts Institute of Technology, Cambridge, MA, 2005.
52.   J. Yu. Estimation method for the thermochemical properties of polycyclic aromatic molecules. Massachusetts Institute of Technology, Cambridge, MA, 2005.
53.   S. V. Petway. Uncertainty analysis in automatic reaction mechanism generation: neopentyl + O2. Massachusetts Institute of Technology, Cambridge, MA, 2006.
54.   R. W. Ashcraft. Ab initio modeling of complex aqueous and gaseous systems containing nitrogen. Massachusetts Institute of Technology, Cambridge, MA, 2008.
55.   S. Sharma. Predictive modeling of combustion processes, Ph.D. thesis. Massachusetts Institute of Technology, Cambridge, MA, 2009.
56.   C. F. Goldsmith. Predicting combustion properties of hydrocarbon fuel mixtures. Massachusetts Institute of Technology, Cambridge, MA, 2008.
57.   R. G. Susnow; A. M. Dean; W. H. Green; P. Peczak; L. J. Broadbelt, J. Phys. Chem. A 101 (1997) 3731-3740
58.   S. W. Benson, Thermochemical kinetics : methods for the estimation of thermochemical data and rate parameters, Wiley, New York, 1976.
59.   K. J. Hughes; T. Turanyi; A. R. Clague; M. J. Pilling, International Journal of Chemical Kinetics 33 (2001) 513-538
60.   NIST, "Chemical Kinetics Database on the Web: Standard Reference Database 17, Version 7.0 (Web Version), Release 1.5" (2000)
61.   E. Bolton; Y. Wang; T. P. A.; S. H. Bryant, Annual Reports in Computational Chemistry 4 (2008)
62.   M. Frenklach; A. Packard; Z. M. Djurisic; D. M. Golden; C. T. Bowman; W. H. Green, Jr.; G. J. McRae; T. C. Allison; G. J. Rosasco; M. J. Pilling, Abstracts of Papers, 231st ACS National Meeting, Atlanta, GA, United States, March 26-30, 2006 (2006) CINF-036

63.   M. Frenklach, "PrIMe: Process Informatics Model http://www.primekinetics.org/" (2006-2009)

64.   "CHEMKIN-MFC 4.0" (2009)

65.   M. R. Nyden; G. A. Petersson, Journal of Chemical Physics 75 (1981) 1843-1862

66.   G. A. Petersson; M. A. Allaham, Journal of Chemical Physics 94 (1991) 6081-6090

67.   G. A. Petersson; T. G. Tensfeldt; J. A. Montgomery, Journal of Chemical Physics 94 (1991) 6091-6101

68.   J. A. Montgomery; J. W. Ochterski; G. A. Petersson, J. Chem. Phys. 101 (1994) 5900-5909

69.   M. J. Frisch; G. W. Trucks; H. B. Schlegel; G. E. Scuseria; M. A. Robb; J. R. Cheeseman; J. Montgomery, J. A.; T. Vreven; K. N. Kudin; J. C. Burant; J. M. Millam; S. S. Iyengar; J. Tomasi; V. Barone; B. Mennucci; M. Cossi; G. Scalmani; N. Rega; G. A. Petersson; H. Nakatsuji; M. Hada; M. Ehara; K. Toyota; R. Fukuda; J. Hasegawa; M. Ishida; T. Nakajima; Y. Honda; O. Kitao; H. Nakai; M. Klene; X. Li; J. E. Knox; H. P. Hratchian; J. B. Cross; V. Bakken; C. Adamo; J. Jaramillo; R. Gomperts; R. E. Stratmann; O. Yazyev; A. J. Austin; R. Cammi; C. Pomelli; J. W. Ochterski; P. Y. Ayala; K. Morokuma; G. A. Voth; P. Salvador; J. J. Dannenberg; V. G. Zakrzewski; S. Dapprich; A. D. Daniels; M. C. Strain; O. Farkas; D. K. Malick; A. D. Rabuck; K. Raghavachari; J. B. Foresman; J. V. Ortiz; Q. Cui; A. G. Baboul; S. Clifford; J. Cioslowski; B. B. Stefanov; G. Liu; A. Liashenko; P. Piskorz; I. Komaromi; R. L. Martin; D. J. Fox; T. Keith; M. A. Al-Laham; C. Y. Peng; A. Nanayakkara; M. Challacombe; P. M. W. Gill; B. Johnson; W. Chen; M. W. Wong; C. Gonzalez; J. A. Pople, "Gaussian 03, Version 6.0" (2004)

70.   J. A. Montgomery; M. J. Frisch; J. W. Ochterski; G. A. Petersson, Journal of Chemical Physics 110 (1999) 2822-2827

71.   C. Eckart, Physical Review 35 (1930) 1303-1309

72.   H. S. Johnston; J. Heicklen, Journal of Physical Chemistry 66 (1962) 532-533

73.   B. C. Garrett; D. G. Truhlar, Journal of Physical Chemistry 83 (1979) 2921-2926

74.   S. Sharma; M. R. Harper; W. H. Green, "CanTherm" http://sourceforge.net/projects/cantherm/ (2010)

75.   A. L. L. East; L. Radom, J. Chem. Phys. 106 (1997) 6655-6674

76.   T. Berces; A. F. Trotman-Dickenson, Journal of the Chemical Society (1961) 348-350

77.   J. A. Kerr; S. J. Moss, CRC handbook of bimolecular and termolecular gas reactions, CRC Press, Boca Raton, Fla., 1981.

78.   W. Tsang, Journal of Physical and Chemical Reference Data 19 (1990) 1-68

79.   R. Shaw; A. F. Trotman-Dickenson, Journal of the Chemical Society (1960) 3210-3215

80.   L. Batt; G. N. Rattray, International Journal of Chemical Kinetics 11 (1979) 1183-1196

81.   R. Atkinson; D. L. Baulch; R. A. Cox; R. F. Hampson; J. A. Kerr; M. J. Rossi; J. Troe, Journal of Physical and Chemical Reference Data 26 (1997) 521-1011

82.   F. P. Tully; J. E. M. Goldsmith; A. T. Droege, Journal of Physical Chemistry 90 (1986) 5932-5937

83.   W. G. Alcock; B. Mile, Combustion and Flame 24 (1975) 125-128

84. R. S. Konar; R. M. Marshall; J. H. Purnell, International Journal of Chemical Kinetics 5 (1973) 1007-21

85. W. Tsang, Journal of Physical and Chemical Reference Data 17 (1988) 887-952

86. H. X. Zhang; M. H. Back, International Journal of Chemical Kinetics 22 (1990) 21-35

87. W. M. Jackson; B. D. Darwent; J. R. Mcnesby, Journal of Chemical Physics 37 (1962) 1610-1615

88. S. I. Ahonkhai; X. H. Lin; M. H. Back, International Journal of Chemical Kinetics 21 (1989) 1-20

89. E. Goos; H. Hippler; K. Hoyermann; B. Jurges, International Journal of Chemical Kinetics 33 (2001) 732-740

90. Y. P. Yampolskii, Reaction Kinetics and Catalysis Letters 2 (1975) 449-455

91. Y. P. Yampolskii; V. M. Rybin, Reaction Kinetics and Catalysis Letters 1 (1974) 321-325

92. D. R. Blackmore; C. Hinshelwood, Proceedings of the Royal Society of London Series a-Mathematical and Physical Sciences 268 (1962) 36-45

93. M. I. Sway, Indian Journal of Chemistry Section a-Inorganic Bio-Inorganic Physical Theoretical & Analytical Chemistry 29 (1990) 748-752

94. J. A. Kerr; M. J. Parsonage, Evaluated kinetic data on gas phase hydrogen transfer reactions of methyl radicals, Butterworths, London ; Boston, 1976.

95. Y. P. Yampol'skii; V. Tsikhlinski, Neftekhimiya 16 (1976) 560-8

96. C. Anastasi, Journal of the Chemical Society-Faraday Transactions I 79 (1983) 741-747

97. R. M. Marshall; G. Shahkar, Journal of the Chemical Society-Faraday Transactions I 79 (1983) 1891-1900

98. R. R. Baldwin; R. W. Walker, Journal of the Chemical Society-Faraday Transactions I 75 (1979) 140-154

99. R. M. Marshall; H. Purnell; P. W. Satchell, Journal of the Chemical Society-Faraday Transactions I 80 (1984) 2395-2403

100. R. M. Marshall; H. Purnell; A. Sheppard, Journal of the Chemical Society-Faraday Transactions II 82 (1986) 929-935

101. A. Lifshitz; H. Ben-Hamou, Journal of Physical Chemistry 87 (1983) 1782-1787

102. R. R. Baldwin; A. Keen; R. W. Walker, Journal of the Chemical Society-Faraday Transactions I 80 (1984) 435-456

103. W. Tsang, Journal of Physical and Chemical Reference Data 16 (1987) 471-508

104. U. Loser; K. Scherzer; K. Weber, Zeitschrift Fur Physikalische Chemie-Leipzig 270 (1989) 237-245

105. L. Szirovicza; F. Marta, International Journal of Chemical Kinetics 8 (1976) 897-910

106. D. M. Golden; Piszkiew.Lw; M. J. Perona; P. C. Beadle, Journal of the American Chemical Society 96 (1974) 1645-1653

107. S. J. Klippenstein; Y. Georgievskii; L. B. Harding, Physical Chemistry Chemical Physics 8 (2006) 1133-1147

108. W. Tsang, Journal of Physical and Chemical Reference Data 20 (1991) 221-273

109. E. Goos; A. Burcat; B. Ruscic, "Third Millennium Thermodynamic Database for Combustion and Air-Pollution Use with updates from Active Thermochemical Tables" (2010)

110. Y. Hidaka; S. Shiba; H. Takuma; M. Suga, International Journal of Chemical Kinetics 17 (1985) 441-453

111. W. Tsang; R. F. Hampson, Journal of Physical and Chemical Reference Data 15 (1986) 1087-1279

112. M. P. Halstead; C. P. Quinn, Transactions of the Faraday Society 64 (1968) 103-118

113. K. Scherzer; U. Loser; W. Stiller, Zeitschrift Fur Chemie 27 (1987) 300-301

114. I. R. Slagle; J. Y. Park; M. C. Heaven; D. Gutman, Journal of the American Chemical Society 106 (1984) 4356-4361

115. P. J. Boddy; E. W. R. Steacie, Canadian Journal of Chemistry-Revue Canadienne De Chimie 38 (1960) 1576-1589

116. Y. Z. He; W. G. Mallard; W. Tsang, Journal of Physical Chemistry 92 (1988) 2196-2201

117. D. L. Baulch; C. J. Cobos; R. A. Cox; C. Esser; P. Frank; T. Just; J. A. Kerr; M. J. Pilling; J. Troe; R. W. Walker; J. Warnatz, Journal of Physical and Chemical Reference Data 21 (1992) 411-734

118. K. T. Oganesyan; A. B. Nalbandyan, Izvestiya Akademii Nauk Armyanskoi SSR, Khimicheskie Nauki 18 (1965) 237-43

119. M. G. Bryukov; I. R. Slagle; V. D. Knyazev, Journal of Physical Chemistry A 105 (2001) 6900-6909

120. J. A. Kerr; A. F. Trotman-Dickenson, Transactions of the Faraday Society 55 (1959) 921-928

121. K. Selby; D. J. Waddington, Journal of the Chemical Society-Perkin Transactions 2 (1979) 1259-1263

122. R. W. Walker, in: Reaction Kinetics, The Chemical Society, Burlington House: London, 1975; Vol. 1.

123. H. Knoll; A. Nacsa; S. Forgeteg; T. Berces, Reaction Kinetics and Catalysis Letters 15 (1980) 481-485

124. J. A. Kerr; A. F. Trotman-Dickenson, Progress in Reaction Kinetics and Mechanism 1 (1961) 105-127

125. J. A. Kerr; A. F. Trotman-Dickenson, Transactions of the Faraday Society 55 (1959) 572-580

126. S. Forgeteg; T. Berces; S. Dobe, International Journal of Chemical Kinetics 11 (1979) 219-237

127. Y. Zhang; S. W. Zhang; Q. S. Li, Chemical Physics 306 (2004) 51-56

128. H. B. Xie; Y. H. Ding; C. C. Sun, Journal of Physical Chemistry A 109 (2005) 8419-8423

129. N. Y. Al Akeel; K. Selby; D. J. Waddington, Journal of the Chemical Society-Perkin Transactions 2 (1981) 1036-1040

130. M. Buback; M. Kling; S. Schmatz, Zeitschrift Fur Physikalische Chemie-International Journal of Research in Physical Chemistry & Chemical Physics 219 (2005) 1205-1222

131.   H. J. Curran, International Journal of Chemical Kinetics 38 (2006) 250-275 Doi 10.1002/Kin.20153.

132.   J. F. Foucaut; R. Martin, Journal De Chimie Physique Et De Physico-Chimie Biologique 75 (1978) 132-144

133.   C. Faubel; K. Hoyermann; E. Strofer; H. G. Wagner, Berichte Der Bunsen-Gesellschaft-Physical Chemistry Chemical Physics 83 (1979) 532-538

134.   K. M. Bansal; G. R. Freeman, Journal of the American Chemical Society 90 (1968) 7183-7189

135.   Cvetanov.Rj; R. S. Irwin, Journal of Chemical Physics 46 (1967) 1694-1702

136.   P. Gray; A. A. Herod, Transactions of the Faraday Society 64 (1968) 1568-1576

137.   Z. F. Xu; J. Park; M. C. Lin, Journal of Chemical Physics 120 (2004) 6593-6599

138.   A. F. Trotman-Dickenson, Advan. Free Radical Chem. 1 (1965) 1

139.   W. K. Aders; H. G. Wagner, Berichte Der Bunsen-Gesellschaft-Physical Chemistry Chemical Physics 77 (1973) 712-718

140.   J. Park; Z. F. Xu; M. C. Lin, Journal of Chemical Physics 118 (2003) 9990-9996

141.   J. L. Brokenshire; A. Nechvatal; J. M. Tedder, Transactions of the Faraday Society 66 (1970) 2029-2037

142.   M. I. Sway; D. J. Waddington, Journal of the Chemical Society-Perkin Transactions 2 (1984) 63-69

143.   L. J. Kirsch; D. A. Parkes, Journal of the Chemical Society-Faraday Transactions I 77 (1981) 293-307

144.   P. Mulder; R. Louw, Recueil Des Travaux Chimiques Des Pays-Bas-Journal of the Royal Netherlands Chemical Society 103 (1984) 148-152

145.   K. C. Ferguson; J. T. Pearson, Transactions of the Faraday Society 66 (1970) 910-919

146.   N. L. Arthur; P. J. Newitt, Australian Journal of Chemistry 32 (1979) 1697-1708

147.   N. L. Arthur; P. J. Newitt, Australian Journal of Chemistry 34 (1981) 727-735

148.   D. L. Baulch; C. J. Cobos; R. A. Cox; P. Frank; G. Hayman; T. Just; J. A. Kerr; T. Murrells; M. J. Pilling; J. Troe; R. W. Walker; J. Warnatz, Journal of Physical and Chemical Reference Data 23 (1994) 847-1033

149.   M. Scott; R. W. Walker, Combustion and Flame 129 (2002) 365-377

150.   K. H. Ebert; H. J. Ederer; P. S. Schmidt, in: ACS Symposium Series 65, V. W. Weekman Jr.; D. Luss, (Eds.) Chemical Reaction Engineering-Houston: Washington, DC, 1978;

151.   W. Muller-Markgraf; J. Troe, Journal of Physical Chemistry 92 (1988) 4914-4922

152.   C. Ellis; M. S. Scott; R. W. Walker, Combustion and Flame 132 (2003) 291-304

153.   M. F. R. Mulcahy; B. G. Tucker; D. J. Williams; J. R. Wilmshur, Australian Journal of Chemistry 20 (1967) 1155-1171

154.   H. Hippler; S. Seisel; J. Troe, Symposium (International) on Combustion, [Proceedings] 25th (1994) 875-82

155.   R. J. Akers; J. J. Throssell, Chemical Communications (1966) 432-433

156.   J. J. Throssell, International Journal of Chemical Kinetics 4 (1972) 273-6

157.   A. B. Trenwith, Transactions of the Faraday Society 66 (1970) 2805-2811

158.   R. Louw, Recueil Des Travaux Chimiques Des Pays-Bas 90 (1971) 469-476

159.   A. B. Lovell; K. Brezinsky; I. Glassman, International Journal of Chemical Kinetics 21 (1989) 547-560

160.   J. C. J. Thynne, Transactions of the Faraday Society 58 (1962) 676-684

161.   T. R. Donovan; W. Dorko; A. G. Harrison, Canadian Journal of Chemistry 49 (1971) 828-832

162.   D. A. Good; J. S. Francisco, Journal of Physical Chemistry A 106 (2002) 1733-1738

163.   K. Al-Niami; K. A. Holbrook; G. A. Oldershaw, Journal of the Chemical Society-Faraday Transactions II 85 (1989) 1601-1608

164.   D. G. L. James; E. W. R. Steacie, Proceedings of the Royal Society of London Series a-Mathematical and Physical Sciences 244 (1958) 289-296

165.   J. T. Jodkowski; M. T. Rayez; J. C. Rayez; T. Berces; S. Dobe, Journal of Physical Chemistry A 103 (1999) 3750-3765

166.   M. R. Harper; K. M. Van Geem; S. P. Pyl; G. B. Marin; W. H. Green, Combust. Flame (accepted) doi: 10.1016/j.combustflame.2010.06.002 (2010)

167.   M. R. Harper; K. M. Van Geem; S. P. Pyl; S. M. Merchant; G. B. Marin; W. H. Green, Combust. Flame (2011) in press http://dx.doi.org/10.1016/j.combustflame.2011.02.023

168.   N. Hansen; M. R. Harper; H. Green William, *7th US National Combustion Meeting*, Atlanta, GA, 2011; p Paper 1B09.

169.   P. Durre, Biotechnol. J. 2 (2007) 1525-34

170.   J. A. Barnard, Trans. Faraday Soc. 53 (1957) 1423-1430

171.   S. R. Smith; A. S. Gordon; M. H. Hunt, J. Phys. Chem. 61 (1957) 553-558

172.   C. S. McEnally; L. D. Pfefferle, Proceedings of the Combustion Institute 30 (2005) 1363-1370

173.   B. Yang; P. Osswald; Y. Y. Li; J. Wang; L. X. Wei; Z. Y. Tian; F. Qi; K. Kohse-Hoinghaus, Combustion and Flame 148 (2007) 198-209

174.   C. A. Taatjes; N. Hansen; A. McIlroy; J. A. Miller; J. P. Senosiain; S. J. Klippenstein; F. Qi; L. S. Sheng; Y. W. Zhang; T. A. Cool; J. Wang; P. R. Westmoreland; M. E. Law; T. Kasper; K. Kohse-Hoinghaus, Science 308 (2005) 1887-1889

175.   X. Gu; Z. Huang; Q. Li; C. Tang, Energy Fuels 23 (2009) 4900-4907

176.   P. Dagaut; C. Togbe, Fuel 87 (2008) 3313-3321

177.   P. Dagaut; C. Togbe, Energy Fuels 23 (2009) 3527-3535

178.   P. Dagaut; S. M. Sarathy; M. J. Thomson, Proc. Combust. Inst. 32 (2009) 229-237

179.   S. M. Sarathy; M. J. Thomson; C. Togbe; P. Dagaut; F. Halter; C. Mounaim-Rousselle, Combustion and Flame 156 (2009) 852-864

180.   J. T. Moss; A. M. Berkowitz; M. A. Oehlschlaeger; J. Biet; V. Warth; P. A. Glaude; F. Battin-Leclerc, Journal of Physical Chemistry A 112 (2008) 10843-10855

181.   G. Black; H. J. Curran; S. Pichon; J. M. Simmie; V. Zhukov, Combustion and Flame 157 (2010) 363-373

182.   D. F. Davidson; S. C. Ranganath; K. Y. Lam; M. Liaw; Z. Hong; R. K. Hanson, Journal of Propulsion and Power 26 (2010) 280-287

183.   W. H. Green; J. W. Allen; R. W. Ashcraft; G. J. Beran; C. F. Goldsmith; M. R. Harper; A. Jalan; G. R. Magoon; D. M. Matheu; S. Petway; S. Raman; S. Sharma; K. M. Van Geem; J. Song; J. Wen; R. H. West; A. Wong; H.-W. Wong; P. E. Yelvington; J. Yu, "RMG - Reaction Mechanism Generator v3.1 http://rmg.sourceforge.net/" http://rmg.sourceforge.net/ (2009)

184. N. J. B. Green; Z. A. Bhatti, Physical Chemistry Chemical Physics 9 (2007) 4275-4290
185. A. Y. Chang; J. W. Bozzelli; A. M. Dean, Zeitschrift Fur Physikalische Chemie-International Journal of Research in Physical Chemistry & Chemical Physics 214 (2000) 1533-1568
186. P. K. Venkatesh; A. Y. Chang; A. M. Dean; M. H. Cohen; R. W. Carr, Aiche Journal 43 (1997) 1331-1340
187. K. M. Van Geem; M. F. Reyniers; G. B. Marin; J. Song; W. H. Green; D. M. Matheu, Aiche Journal 52 (2006) 718-730
188. G. J. Beran; W. H. Green, Abstracts of Papers, 231st ACS National Meeting, Atlanta, GA, United States, March 26-30, 2006 (2006) PHYS-140
189. S. V. Petway; H. Ismail; W. H. Green; E. G. Estupinan; L. E. Jusinski; C. A. Taatjes, Journal of Physical Chemistry A 111 (2007) 3891-3900
190. S. Sharma; M. R. Harper; W. H. Green, Combustion and Flame 157 (2010) 1331-1345
191. G. P. Smith; D. M. Golden; M. Frenklach; N. W. Moriarty; B. Eiteneer; M. Goldenberg; C. T. Bowman; R. K. Hanson; S. Song; W. C. Gardiner Jr.; V. V. Lissianski; Z. Qin, "GRI-Mech 3.0" (1999)
192. N. M. Marinov, Int. J. Chem. Kinet. 31 (1999) 183-220
193. Chemkin-Pro,
194. Q. Chen; G. F. Froment, Journal of Analytical and Applied Pyrolysis 21 (1991) 27-50
195. R. H. Wilhelm; L. Lapidus; N. R. Amundson, Chemical reactor theory : a review : dedicated to the memory of Richard H. Wilhelm, Prentice-Hall, Englewood Cliffs, N.J., 1977.
196. J. C. Lee; R. A. Yetter; F. L. Dryer; A. G. Tomboulides; S. A. Orszag, Combustion Science and Technology 159 (2000) 199-212
197. A. H. Cutler; M. J. Antal; M. Jones, Industrial & Engineering Chemistry Research 27 (1988) 691-697
198. B. A. V. Bennett; C. S. McEnally; L. D. Pfefferle; M. D. Smooke, Combustion and Flame 123 (2000) 522-546
199. C. S. McEnally; D. M. Ciuparu; L. D. Pfefferle, Combustion and Flame 134 (2003) 339-353
200. C. S. McEnally; L. D. Pfefferle, Combustion and Flame 152 (2008) 469-481
201. W. E. Schiesser, The numerical method of lines : integration of partial differential equations, Academic Press, San Diego, 1991.
202. L. Petzold; S. T. Li; Y. Cao; R. Serban, Comput. Chem. Eng. 30 (2006) 1553-1559
203. Chemkin-MFC, "Chemkin-MFC" (2008)
204. S. M. Sarathy; M. J. Thomson; C. Togbe; P. Dagaut; F. Halter; C. Mounaim-Rousselle, Combustion and Flame 157 (2010) 837-838
205. R. J. Kee; F. M. Rupley; J. A. Miller, 1991.
206. R. J. Kee; G. Dixon-Lewis; J. Warnatz; M. E. Coltrin; J. A. Miller, 1986.
207. J. R. Welty; C. E. Wicks; R. E. Wilson; G. L. Rorrer, Fundamentals of Momentum, Heat, and Mass Transfer, John Wiley & Sons, Inc., 2001.

208. K. G. Joback. A unified approach to physical property estimation using multivariate statistical techniques, M.S. thesis. Massachusetts Institute of Technology, Cambridge, MA, 1984.

209. J. A. Miller; M. J. Pilling; E. Troe, Proceedings of the Combustion Institute 30 (2005) 43-88

210. J. P. Senosiain; S. J. Klippenstein; J. A. Miller, Journal of Physical Chemistry A 110 (2006) 5772-5781

211. N. K. Srinivasan; M. C. Su; J. W. Sutherland; J. V. Michael, Journal of Physical Chemistry A 109 (2005) 1857-1863

212. A. W. Jasper; S. J. Klippenstein; L. B. Harding, Proceedings of the Combustion Institute 32 (2009) 279-286

213. Q. S. Li; X. Zhang; S. W. Zhang, Journal of Physical Chemistry A 109 (2005) 12027-12035

214. N. M. Marinov; W. J. Pitz; C. K. Westbrook; A. M. Vincitore; M. J. Castaldi; S. M. Senkan; C. F. Melius, Combust. Flame 114 (1998) 192-213

215. H. S. Johnston; J. Heicklen, Journal of Physical Chemistry 66 (1962) 532-&

216. J. W. Ochterski; G. A. Petersson; J. A. Montgomery, J. Chem. Phys. 104 (1996) 2598-2619

217. J. A. Montgomery; M. J. Frisch; J. W. Ochterski; G. A. Petersson, J. Chem. Phys. 112 (2000) 6532-6542

218. G. A. Petersson; D. K. Malick; W. G. Wilson; J. W. Ochterski; J. A. Montgomery; M. J. Frisch, J. Chem. Phys. 109 (1998) 10570-10579

219. J. Moc; J. M. Simmie; H. J. Curran, Journal of Molecular Structure 928 (2009) 149-157

220. G. da Silva; C. H. Kim; J. W. Bozzelli, J. Phys. Chem. A 110 (2006) 7925-7934

221. T. Yamada; J. W. Bozzelli; T. Lay, J. Phys. Chem. A 103 (1999) 7646-7655

222. J. J. C. Teixeira-Dias; T. R. Furlani; K. S. Shores; J. F. Garvey, Phys. Chem. Chem. Phys. 5 (2003) 5063-5069

223. J. Pardo; M. C. Lopez; J. Santafe; F. M. Royo; J. S. Urieta, Fluid Phase Equilib. 109 (1995) 29-37

224. N. Cohen, International Journal of Chemical Kinetics 23 (1991) 397-417

225. A. M. Mebel; E. W. G. Diau; M. C. Lin; K. Morokuma, Journal of the American Chemical Society 118 (1996) 9759-9771

226. M. A. Weissman; S. W. Benson, Journal of Physical Chemistry 92 (1988) 4080-4084

227. K. E. Noorani; B. Akih-Kumgeh; J. M. Bergthorson, Energy & Fuels 24 (2010)

228. K. A. Heufer; R. X. Fernandes; H. Olivier; J. Beeckmann; O. Rohl; N. Peters, Proceedings of the Combustion Institute 33 (2011) 359-366 DOI 10.1016/j.proci.2010.06.052.

229. S. Vranckx; K. A. Heufer; C. Lee; H. Olivier; L. Schill; W. A. Kopp; K. Leonhard; C. A. Taatjes; R. X. Fernandes, Combustion and Flame (2011) in press http://dx.doi.org/10.1016/j.combustflame.2010.12.028.

230. B. W. Weber; K. Kumar; Y. Zhang; C.-J. Sung, Combustion and Flame 158 (2011) 808-819

231.   M. R. Harper; H. Green William; K. M. Van Geem; B. W. Weber; C.-J. Sung; I. Stranic; D. F. Davdison; R. K. Hanson, *7th International Conference on Chemical Kinetics*, Cambridge, MA, 2011.

232.   S. S. Vasu; D. F. Davidson; R. K. Hanson; D. M. Golden, Chem Phys Lett 497 (2010) 26-29 DOI 10.1016/j.cplett.2010.08.001.

233.   C. W. Zhou; J. M. Simmie; H. J. Curran, Combustion and Flame 158 (2011) 726-731 DOI 10.1016/j.combustflame.2010.11.002.

234.   S. Sharma; S. Raman; W. H. Green, Journal of Physical Chemistry A 114 (2010) 5689-5701 Doi 10.1021/Jp9098792.

235.   J. Zador; J. A. Miller, *7th US National Combustion Meeting*, Atlanta, GA, 2011; p Paper 2B06.

236.   P. S. Veloo; Y. L. Wang; F. N. Egolfopoulos; C. K. Westbrook, Combustion and Flame 157 (2010) 1989-2004 DOI 10.1016/j.combustflame.2010.04.001.

237.   K. M. Van Geem; S. P. Pyl; G. B. Marin; M. R. Harper; W. H. Green, Industrial & Engineering Chemistry Research 49 (2010) 10399-10420 Doi 10.1021/Ie1005349.

238.   P. M. Plehiers; G. F. Froment, Chemical Engineering Communications 80 (1989) 81-99

239.   R. F. Schultz; G. B. Kistiakowsky, Journal of the American Chemical Society 56 (1934) 395-398

240.   J. A. Barnard, Transactions of the Faraday Society 55 (1959) 947-951

241.   G. F. Froment; K. B. Bischoff, Chemical reactor design and analysis, John Wiley & Sons, Inc., New York, 1990.

242.   B. A. V. Bennett; M. D. Smooke, Combustion Theory and Modelling 2 (1998) 221-258

243.   C. T. Bowman; R. K. Hanson; D. F. Davidson; W. C. Gardiner Jr.; V. Lissianski; G. P. Smith; D. M. Golden; M. Frenklach; M. Goldenberg, "GRI-Mech 2.11" (1995)

244.   R. J. Kee; F. M. Rupley; J. A. Miller; M. E. Coltrin; J. F. Grcar; E. Meeks; H. K. Moffat; A. E. Lutz; G. Dixon-Lewis; M. D. Smooke; J. Warnatz; G. H. Evans; R. S. Larson; R. E. Mitchell; L. R. Petzold; W. C. Reynolds; M. Caracotsios; W. E. Stewart; P. Glarborg; C. Wang; C. L. McLellan; O. Adigun; W. G. Houf; C. P. Chou; S. F. Miller; P. Ho; P. D. Young; D. J. Young; D. W. Hodgson; M. V. Petrova; K. V. Puduppakkam, (2007)

245.   C. D. Wijaya. Developing fundamentally based models for autoignition, Ph.D. thesis. Massachusetts Institute of Technology, Cambridge, MA, 2005.

246.   K. Yasunaga; Y. Kuraguchi; R. Ikeuchi; H. Masaoka; O. Takahashi; T. Koike; Y. Hidaka, Proceedings of the Combustion Institute 32 (2009) 453-460 DOI 10.1016/j.proci.2008.06.144.

247.   G. F. Froment, Chemical Engineering Science 47 (1992) 2163-2177

248.   K. M. Van Geem; M. F. Reyniers; G. B. Marin, Industrial & Engineering Chemistry Research 44 (2005) 3402-3411

249.   J. A. Miller; S. J. Klippenstein, Journal of Physical Chemistry A 105 (2001) 7254-7266

250.   J. Pardo; M. C. Lopez; J. A. Mayoral; F. M. Royo; J. S. Urieta, Fluid Phase Equilibria 134 (1997) 133-140

251.   J. Pardo; A. M. Mainar; M. C. Lopez; F. Royo; J. S. Urieta, Fluid Phase Equilibria 155 (1999) 127-137

252. A. Fahr; A. Laufer; R. Klein; W. Braun, Journal of Physical Chemistry 95 (1991) 3218-3224

253. C. Togbe; A. Mze-Ahmed; P. Dagaut, Energy & Fuels 24 (2010) 5244-5256 Doi 10.1021/Ef1008488.

254. P. Osswald; H. Guldenberg; K. Kohse-Hoinghaus; B. Yang; T. Yuan; F. Qi, Combustion and Flame 158 (2011) 2-15 DOI 10.1016/j.combustflame.2010.06.003.

255. H. J. Curran; P. Gaffuri; W. J. Pitz; C. K. Westbrook, Combustion and Flame 129 (2002) 253-280

256. A. W. Jasper; S. J. Klippenstein; L. B. Harding; B. Ruscic, Journal of Physical Chemistry A 111 (2007) 3932-3950

257. S. G. Davis; C. K. Law; H. Wang, Journal of Physical Chemistry A 103 (1999) 5889-5899

258. R. Grana; A. Frassoldati; T. Faravelli; U. Niemann; E. Ranzi; R. Seiser; R. Cattolica; K. Seshadri, Combustion and Flame 157 (2010) 2137-2154 DOI 10.1016/j.combustflame.2010.05.009.

259. M. P. Dunphy; J. M. Simmie, Journal of the Chemical Society-Faraday Transactions 87 (1991) 1691-1696

260. M. P. Dunphy; P. M. Patterson; J. M. Simmie, Journal of the Chemical Society-Faraday Transactions 87 (1991) 2549-2559

261. P. S. Veloo; F. N. Egolfopoulos, Proceedings of the Combustion Institute 33 (2011) 987-993 DOI 10.1016/j.proci.2010.06.163.

262. W. Liu; A. P. Kelley; C. K. Law, Proceedings of the Combustion Institute 33 (2011) 995-1002 DOI 10.1016/j.proci.2010.05.084.

263. J. S. Heyne; J. K. Lefkowitz; F. M. Haas; S. H. Won; S. Dooley; H. H. Kim; S. Jahangirian; F. L. Dryer; Y. Ju, *7th US National Combustion Meeting*, 2011; p Paper 3C03.

264. Z. Zhao; M. Chaos; A. Kazakov; F. L. Dryer, International Journal of Chemical Kinetics 40 (2008) 1-18

265. R. H. West; C. F. Goldsmith; M. R. Harper; W. H. Green; L. Catoire; N. Chaumeix, *7th US National Combustion Meeting*, Atlanta, GA, 2011; p Paper 1A06.